Research of experimental methods to simulate propagation channels in mode-stirred reverberation chamber

Mihai Ionut Andries

Thèse

THÈSE INSA Rennes
sous le sceau de l'Université Européenne de Bretagne
pour obtenir le grade de
DOCTEUR DE L'INSA DE RENNES
Spécialité : Électronique et Télécommunications

présentée par
Mihai Ionut Andries
ÉCOLE DOCTORALE : MATISSE
LABORATOIRE : IETR

Research of experimental methods to simulate propagation channels in mode-stirred reverberation chamber

Thèse soutenue le 04.04.2013
devant le jury composé de :

Bernard UGUEN
Professeur à l'Université de Rennes 1 / *président*

Martine LIÉNARD
Professeur à l'Université de Lille, USTL - TELICE / *rapporteur*

Cyril LUXEY
Professeur à l'Université de Nice Sophia-Antipolis,
Chercheur à l'IM2NP / *rapporteur*

Divitha SEETHARAMDOO
Chargée de Recherche à l'IFSTTAR, Lille / *examinateur*

Luk ARNAUT
Chargé de recherche à GGIEMR, University of Notthingam / *membre invité*

Christophe LEMOINE
Maître de conférences, INSA de Rennes / *Co-encadrant de thèse*

Philippe BESNIER
Chargé de recherche CNRS / *Directeur de thèse*

Research of experimental methods to simulate propagation channels in mode-stirred reverberation chamber

Recherche de méthodes expérimentales de simulation de canaux de propagation en chambre réverbérante à brassage de modes

Mihai Ionut Andries

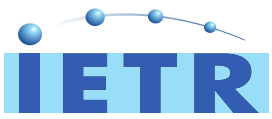

It is far better to grasp the universe as it really is
than to persist in delusion, however satisfying and reassuring.
Carl Sagan

Remerciements

Je tiens en premier lieu à remercier la Région Bretagne pour le financement de cette thèse.

Je souhaite remercier aussi mes encadrants M. Philippe Besnier, Chargé de recherches CNRS à l'IETR, directeur de thèse, et M. Christophe Lemoine, maître de conférences à INSA de Rennes et co-encadrant de cette thèse. Je les remercie pour leur patience et conseils pendant les trois années de thèse et de m'avoir donné la chance de réaliser cette thèse. Une thèse est ponctuée de moments plus ou moins difficiles et mes encadrants ont toujours été là pour moi et m'ont aidé à surmonter ces épreuves.

Je remercie M. Bernard Uguen, Professeur à l'Université de Rennes 1, d'avoir présidé le jury de la soutenance de cette thèse. J'adresse aussi mes remerciements à Mme Martine Liénard, Professeur à l'Université de Lille, USTL - TELICE, et à M. Cyril Luxey, Professeur à l'Université de Nice Sophia-Antipolis, qui ont accepté d'être rapporteurs de cette thèse. Je remercie également Mme Divitha Seetharamdoo, Chargée de recherche à l'IFSTTAR, et M. Luk Arnaut, Chargé de recherche à George Green Institute for Electromagnetics Research, University of Notthingam, d'avoir examiné ma thèse.

Je remercie les membres du projet METAPHORT, tous les collègues de l'IETR et en particulier Jérôme Sol, avec lequel j'ai préparé de nombreuses mesures exploitées dans cette thèse. Je remercie enfin ma famille pour son soutien dans cette aventure.

Une thèse est une expérience personnelle et pour moi cette thèse m'a donné la possibilité de développer des compétences théoriques et pratiques. En outre, la gestion de projet et en particulier la gestion du temps, sont deux compétences essentielles que j'ai pu développer pendant ces annèes de thèse.

Par ailleurs, une thèse représente une étape importante qui permet des échanges dans un contexte international.

Je me souviens avec plaisir des conférences à l'étranger, des réunions de travail du projet METAPHORT, des discussions diverses sur des sujets scientifiques ou thèmes plus généraux, avec différentes personnes que j'ai rencontrées pendant les trois années. Sans aucun doute, réaliser cette thèse a été un très bon choix.

Résumé

Les tests de dispositifs de communication sans fil peuvent être réalisés en utilisant des simulations numériques ou des sondeurs de canaux. Bien que ne reflétant pas un environnement électromagnétique réaliste, une chambre réverbérante peut néanmoins émuler un canal de propagation comparable à un cas réel si l'on modifie convenablement ses propriétés. Les propriétés des signaux générés dans une chambre réverbérante sont fonction de différents paramètres. Au cours des trois années de thèse, nous avons analysé et mis en œuvre plusieurs techniques pour mesurer et contrôler ces paramètres à l'intérieur d'une chambre réverbérante.

D'abord, différents estimateurs du facteur K sont testés et leurs propriétés sont évaluées. Nous présentons les limites de fonctionnement utiles dans lesquelles différents estimateurs peuvent être utilisés. Ensuite, nous proposons deux nouveaux estimateurs qui utilisent comme données d'entrée seulement l'enveloppe du signal. Ils apportent en outre des améliorations sur la gamme des valeurs détectables du facteur K.

Une des possibilités pour contrôler un canal de propagation à l'intérieur d'une chambre réverbérante est d'utiliser des matériaux absorbants. Nous présentons une méthode pour estimer la surface équivalente moyenne d'absorption en utilisant une seule antenne. Cette méthode exploite la mesure de la bande de cohérence du canal de propagation. Ensuite, nous étendons notre analyse à la prédiction de la surface équivalente moyenne d'absorption lorsque les dimensions géométriques et les propriétés électromagnétiques des absorbants sont connues.

On crée ensuite un modèle de canal de propagation en exploitant les régimes transitoire et permanent du signal. Avec ce modèle, selon les informations disponibles, on peut extraire le facteur K, la surface équivalente moyenne d'absorption et différents paramètres temporels (i.e., profil de l'étalement des retards).

Nous poursuivons avec deux applications possibles des chambres réverbérantes. Tout d'abord, on évalue le gain d'une antenne à partir de mesures du coefficient de réflexion de cette antenne. Nous étendons notre analyse à l'évaluation du diagramme de rayonnement de l'antenne et de son erreur d'estimation. Nous estimons aussi la désadaptation de l'antenne et son ouverture à 3 dB. La deuxième application porte sur l'évaluation du gain de diversité dans la chambre réverbérante. Nous isolons les influences des efficacités des antennes, des puissances des composantes brassées, et des facteurs K sur l'évaluation du gain de diversité. On obtient une relation simple de la corrélation de puissance en fonction de la corrélation complexe lorsque les facteurs K sur différents branches ne sont pas identiques. Nous montrons que lors d'un fort déséquilibre de facteur K il est impossible de conclure sur le gain de diversité à partir de la seule évaluation de la corrélation d'enveloppe ou de puissance. À l'aide de simulations statistiques on compare le gain de diversité mesuré avec les valeurs simulées.

Résumé étendu

Introduction

Les applications sans fil sont devenues de plus en plus présentes dans le quotidien de la population. Différents types d'environnements, i.e., maison, bureau, parc, place publique, etc. influencent la propagation sans fil et par conséquent la qualité de transmission. La qualité d'une liaison de communication nécessite une bonne connaissance des canaux de propagation. Pour qu'un système de communication fonctionne bien il a toujours besoin de mesurer différents paramètres de contrôle pour s'adapter aux conditions de la transmission. Quelques-uns de ces paramètres sont le rapport signal sur bruit, les temps caractéristiques associés au profil des retards, la bande de cohérence, le spectre Doppler, le facteur K, etc. Pour une mise en œuvre réussie d'un système de communication, les tests et les optimisations sont deux facteurs clés. Plusieurs paramètres de la transmission doivent être étudiés correctement avant que le produit puisse être validé. Une première façon de tester le système de communication peut se faire en utilisant des simulations numériques ou des sondeurs de canal. Une autre solution exige un environnement fiable, contrôlable et répétable qui a des caractéristiques semblables à celles trouvées dans un canal de propagation réel. Un environnement tel qu'une chambre réverbérante (RC en anglais) constitue potentiellement un de ces moyens d'essai.

Description de la thèse

Cette thèse est traitée dans le contexte d'un projet ANR et concerne l'émulation de canaux de propagation en chambre réverbérante, spécifiquement les canaux typiques d'environnements urbains et intérieurs. Ces environnements sont fortement affectés par l'évanouissement des signaux dû aux réflexions multiples avec les bâtiments, voitures, arbres, etc. et un haut degré d'absorption électromagnétique. Les objectifs de la thèse sont de caractériser la propagation sans fil dans la chambre réverbérante, modéliser cette propagation, surtout pour les systèmes de multi-antennes, et finalement comparer les canaux de propagation mesurés dans la chambre réverbérante avec les canaux mesurés dans des environnements réels de propagation. Pour considérer la chambre réverbérante comme un moyen de reproduction des caractéristiques d'un canal sans fil réaliste est important d'identifier les paramètres de canaux contrôlables. Pendant cette thèse, plusieurs paramètres sont successivement analysés. Les modèles proposés sont systématiquement confrontés aux résultats de mesure dans la chambre.

Vue d'ensemble de la chambre réverbérante

Une chambre réverbérante est une cage de Faraday (i.e., faites d'acier ou aluminium) dans laquelle la distribution du champ électromagnétique correspond à un modèle d'ondes stationnaires dépendant de l'excitation plus ou moins importante de plusieurs modes de propagation dans la chambre. La propriété principale de la chambre réverbérante est l'uniformité statistique et isotrope du champ électrique moyen dans le volume de travail de la cavité [1]. Cette uniformité est assurée par une haute densité de modes au-delà d'une fréquence, imparfaitement définie et dénommée fréquence minimale d'utilisation (LUF en anglais). Pour la chambre réverbérante que nous utilisons dans cette thèse la LUF est autour de 250 MHz. Cependant les tests statistiques ont montré que les statistiques d'une composante rectangulaire du champ électrique suivent une distribution Rayleigh après une fréquence de 750 MHz [2]. En dessous de cette fréquence la distribution devient une loi de Weibull (qui est un cas plus général que Rayleigh). Le comportement aléatoire de la distribution du champ électromagnétique dans un point du volume de test de la chambre peut être obtenu à travers un processus de brassage qui utilise des plaques métalliques tournantes soit de façon continue ou pas à pas. D'autres solutions de brassage consistent à déplacer les antennes, changer la polarisation, varier la fréquence, etc. Le processus de brassage est assimilable à un changement de fréquences résonantes dû à la modification de conditions limites, augmentant le nombre de modes excités. Dans cette thèse nous utilisons une grande chambre réverbérante, Fig. 1, qui a les dimensions suivantes : 8.7 m de longueur, 3.7 m de largeur et 2.9 m en hauteur. Le brasseur mécanique est utilisé dans cette thèse pour créer la statistique du champ électromagnétique et le brassage fréquentiel pour augmenter le nombre de réalisations de cette distribution. Quand on utilise le brasseur en mode continu, les canaux de propagation deviennent variables en temps. Pour notre chambre, la durée minimale pour une rotation complète du brasseur (qui correspond à la vitesse maximale du brasseur) est de 30 s. Il résulte que l'effet Doppler devient presque insignifiant pour le signal, il est donc négligé. De plus, le brasseur est utilisé dans le mode pas à pas pour lequel les canaux de propagation sont invariants en temps. Les fréquences de mesures vont de 1 GHz jusqu'à 9 GHz. À l'origine, les chambres réverbérantes ont été utilisées comme installations de test pour la compatibilité électromagnétique [3]. Sur une rotation complète de brasseur, les propriétés statistiques de la chambre réverbérante correspondent aux environnements avec trajets multiples (i.e., Rice, Rayleigh, etc.). Comme la chambre réverbérante est un moyen de créer un champ électromagnétique diffus, plusieurs nouvelles fonctionnalités de cet environnement ont été proposées telle que : caractériser les antennes (i.e., l'efficacité de l'antenne, le gain de l'antenne, etc.) [4–8], émuler les canaux sans fils avec évanouissements de type Rayleigh et Rice [3, 9–14], évaluer les performances de systèmes MIMO et le gain de diversité [15–20], caractériser les appareils sans fil et leur qualité d'émission [21–25], analyser les taux de l'erreur (BER an anglais) [26–28], l'effet Doppler [29–32], mesurer le facteur K [18, 33–35] et les temps caractéristiques associés au profil des retards [36, 37], tester l'exposition du corps humain aux ondes électromagnétiques [38–40], etc. De plus, le confinement du champ électromagnétique assuré par la chambre permet d'isoler les signaux créés d'éventuelles interférences.

Avec les modifications nécessaires, il résulte que les chambres réverbérantes sont des environnements simples, de coût modéré, qui peuvent être utilisés pour la reproduction artificielle de canaux de propagation surtout pour les systèmes sans fil affectés par l'évanouissement [12, 16, 41].

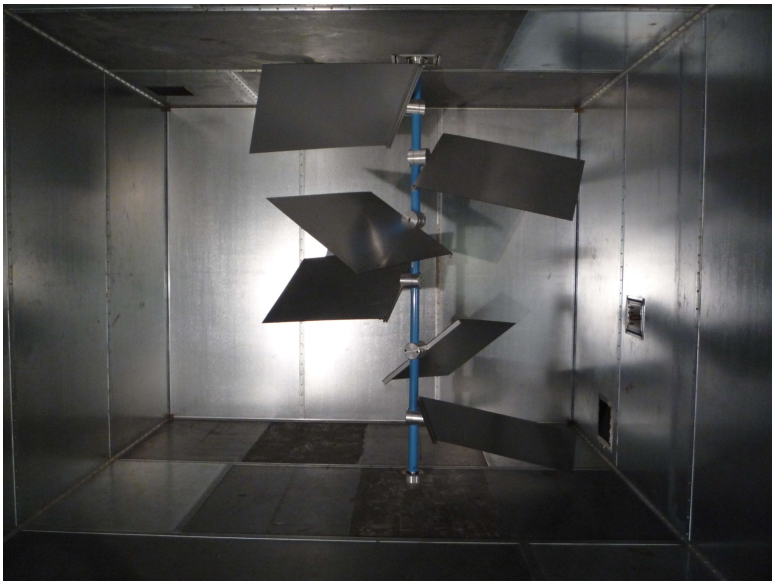

Figure 1: Le brasseur de la chambre réverbérante de l'IETR.

Vue d'ensemble sur les canaux de propagation dans la chambre réverbérante

Entre l'émetteur et le récepteur, les signaux subissent des réflexions/diffractions multiples. Le signal reçu est alors composé d'une somme de signaux complexes avec différentes amplitudes, phases et changements de fréquences causés par l'effet Doppler. L'effet direct sur l'enveloppe et la phase du signal reçu est identifiable par les variations rapides qui sont appelées évanouissements Fig. 2. Les variations de l'enveloppe sont par exemple modélisées comme un processus aléatoire suivant une distribution de Rayleigh (ou plus généralement une distribu-

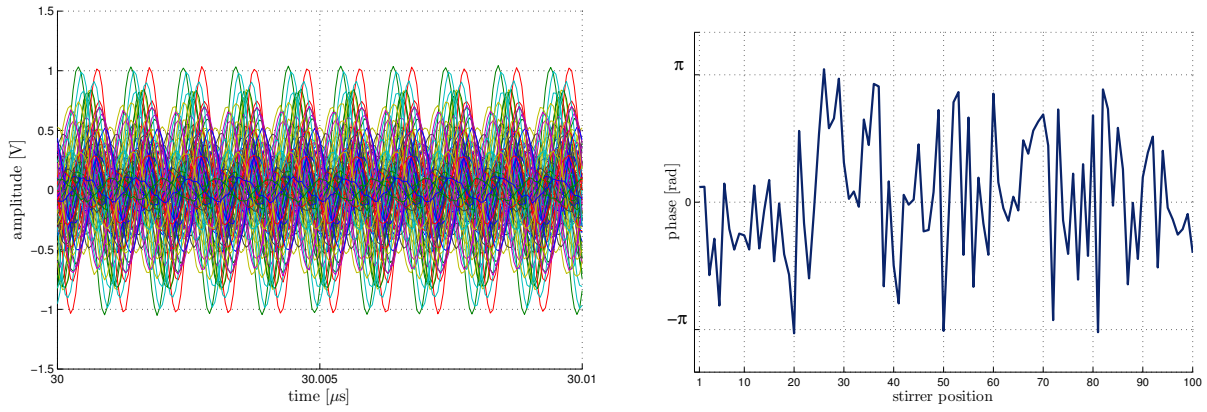

(a) (b)

Figure 2: L'amplitude r du signal reçu en régime permanent (a) et sa phase Θ (b) pour 100 positions du brasseur (le signal émis est une onde sinusoïdale entretenue à la fréquence de 1.5 GHz).

tion de Weibull) quand il n'y a pas de composantes spéculaires, ou selon une distribution de Rice (ou plus généralement Rice-Nakagami) en présence de composantes spéculaires [42, 43]. Nous identifions trois types de composantes dans la chambre réverbérante, Fig. 3 :

- composantes non-brassées (spéculaires) directes, Fig. 3 (a), et composantes non-brassées secondaires, Fig. 3 (b), qui sont réfléchies par les murs de la chambre mais pas par le brasseur. Ces composantes sont invariantes dans le temps. Dans cette thèse elles sont nommées composantes "unstirred" ;

- composantes brassées Fig. 3 (c). Elles sont réfléchies par le brasseur et sont variables dans le temps via le mouvement du brasseur. Ces composantes sont nommées "stirred".

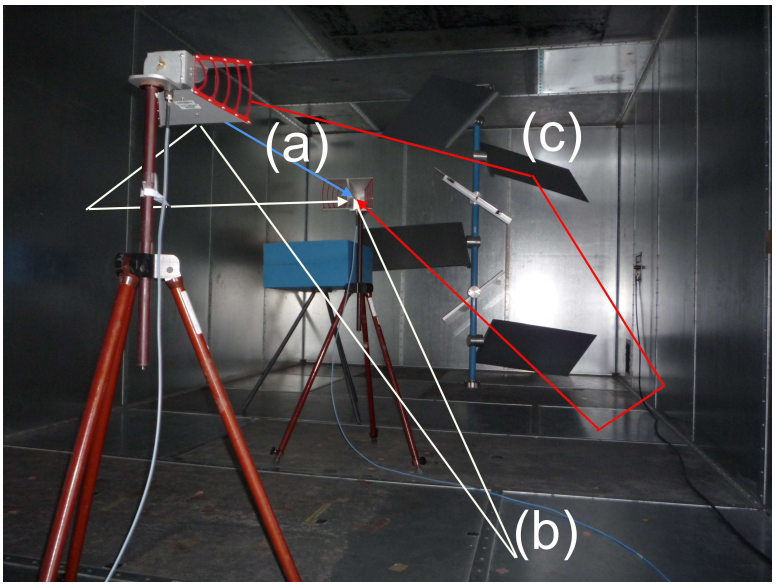

Figure 3: Les composantes des signaux mesurés dans la chambre réverbérante : (a) composantes non-brassées, (b) composantes non-brassées secondaires, (c) composantes brassées.

Nous présentons en Fig. 4, 100 réponses du canal de transmission (qui correspondent à 100 positions du brasseur) mesurées dans la chambre réverbérante. À partir de ces signaux nous pouvons identifier deux régions. Dans la première partie du signal les 100 signaux sont identiques. Cette partie du signal correspond à la plus courte distance de propagation entre antennes et aux réflexions avec les murs métalliques qui ne sont pas affectées par le brasseur. Dans la deuxième région les signaux sont mélangés dû aux réflexions multiples avec le brasseur qui modifie les amplitudes et les phases des signaux reçus. Analyser un signal dans le domaine temporel permet d'analyser le régime transitoire et aussi le régime permanent. Plutôt que de travailler dans le domaine temporel, nous pouvons utiliser un analyseur de réseau vectoriel (VNA en anglais) et faire les mesures dans le domaine fréquentiel. On peut mesurer des amplitudes, des phases ou extraire le comportement d'un canal de communication en mesurant différents paramètres du temps.

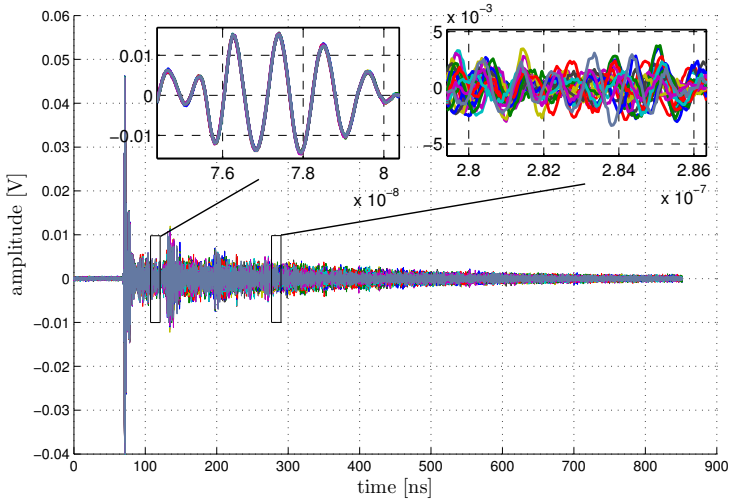

Figure 4: 100 réponses à une impulsion émise dans la chambre réverbérante mesurées à l'oscilloscope numérique.

Le facteur K

Un paramètre important pour caractériser la sévérité de l'évanouissement du signal reçu est le facteur K. Une estimation fiable du facteur K est nécessaire dans beaucoup d'applications. Il est défini comme le rapport de la puissance moyenne des composantes non-brassées (composantes invariantes pendant de grands intervalles de temps) sur la puissance moyenne des composantes brassées (composantes aléatoires selon les statistiques du canal) [12, 44–47].

Méthodes pour estimer le facteur K

En général, nous pouvons classer les estimations du facteur K dans deux catégories. La première concerne les méthodes dites du maximum de vraisemblance. La seconde repose sur les méthodes basées sur les moments (de la densité de probabilité). Pour chacune de ces techniques les signaux mesurés peuvent être l'amplitude complexe, le module, la phase, etc.

Il y a des nombreuses méthodes pour estimer le facteur K. Nous choisissons les méthodes qui fournissent un résultat rapidement (i.e., ces méthodes n'ont pas besoin d'un algorithme itératif pour arriver à un résultat) et peuvent être appliquées dans la chambre réverbérante. Pour chacune d'elles nous analysons leurs performances avec des méthodes statistiques. Les premières méthodes utilisent des signaux complexes. En comparaison avec les méthodes qui utilisent seulement le module ou la phase du signal, ces méthodes sont plus robustes. Une première méthode choisie, parmi celles-ci, utilise l'enveloppe et la phase du signal sujet à l'évanouissement [48] (estimateur noté K_{a}). Un second estimateur repose sur les travaux de [12], et les développements récents en [34, 49]. Les travaux menés par C. Lemoine et al. [34] reposent notamment sur la faculté d'augmenter le nombre de réalisations en chambre réverbérante. D'autres méthodes, plus simples que les précédentes, utilisent seulement la phase [48] (K_{c}) ou l'amplitude de l'évanouissement [46] ($\widehat{K}_{\mathrm{d}}$ et K_{e}) et [45, 47] (noté $\widehat{K}_{\mathrm{f}}$).

Validation des méthodes

Pour caractériser les méthodes sélectionnées, nous réalisons plusieurs simulations de type Monte Carlo et aussi de mesures dans la chambre réverbérante. L'analyse de ces méthodes est basée sur trois indicateurs de la qualité de l'estimation : le taux de rejet constitué de valeurs d'estimation absurdes, le biais entre la valeur vraie et l'estimation, et l'intervalle de la confiance calculé pour un niveau de confiance de 95%. Si on accepte un taux de rejet de 10%, un biais maximal de 3 dB, et un intervalle de confiance de 6 dB le choix d'un estimateur se fait d'après les résultats présentés dans le tableau 1.

Table 1: Intervalles utiles de K pour 10% taux de rejet, 3 dB de biais, et un intervalle de confiance de 6 dB.

Type d'estimateur	**Gamme de K[dB]**
$\widehat{K}_{\mathrm{a}}$ [48]	> -20
$\widehat{K}_{\mathrm{b}}$ [34, 49]	> -24.75
$\widehat{K}_{\mathrm{c}}$ [48]	> -1.75
$\widehat{K}_{\mathrm{d}}$ [46]	$[-2.75, 16.15]$
$\widehat{K}_{\mathrm{e}}$ [46]	$[-3.90, 17.75]$
$\widehat{K}_{\mathrm{f}}$ [45, 47]	≥ 2.40

La nécessité de nouveaux estimateurs : deux situations extrêmes

En fonction de l'environnement de transmission, le facteur K peut évoluer typiquement sur une gamme importante de valeurs et certains estimateurs deviennent inutilisables au-delà d'une limite [50], (Fig. 5). L'estimation de K peut être instable et la qualité de cette estimation dépend de la méthode sélectionnée. D'après le tableau 1 nous observons que les estimateurs

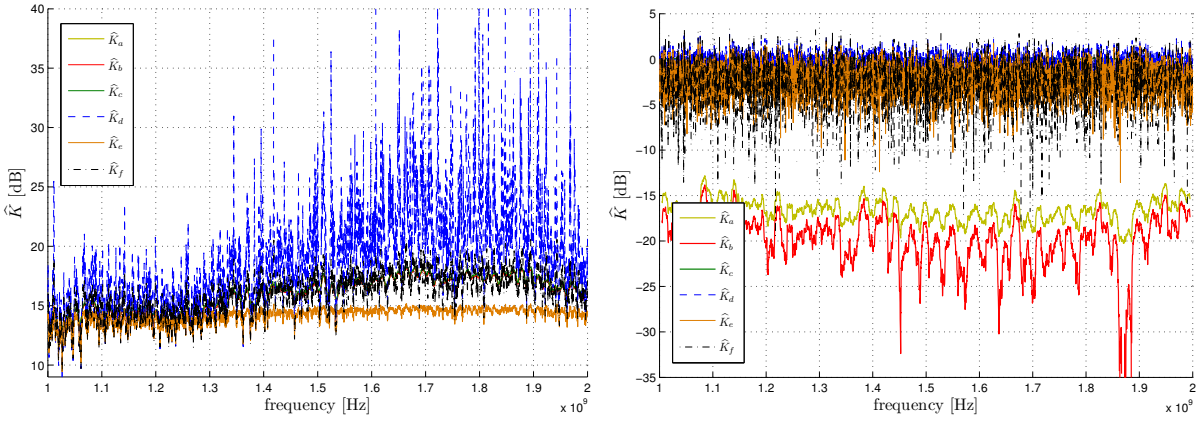

(a) (b)

Figure 5: Le facteur K mesuré dans la chambre réverbérante pour une distance entre les antennes de 0.5 m en présence d'absorbants (a) et pour une distance entre antennes de 6 m en l'absence d'absorbants (b).

analysés peuvent fournir des résultats acceptables seulement dans une gamme plus ou moins limitée de valeurs : les moins intéressants sont les estimateurs basés sur l'enveloppe du signal (ou la phase). D'où le besoin de méthodes plus fiables pour estimer le facteur K dans une grande gamme de valeurs plus large si on ne bénéficie que de la mesure de l'enveloppe du signal.

Notre proposition de nouveaux estimateurs du facteurs K

Un approche simple

Un premier estimateur est proposé à partir d'une méthode rapide et facile à mettre en œuvre. Il utilise le deuxième moment de l'enveloppe et le deuxième moment de la différence entre des données consécutives :

$$\widehat{K} = \frac{\widehat{A^2}}{\widehat{2\sigma^2}^*} = \frac{\left(\widehat{A^2}\right)^2}{\langle r^2\rangle_N \times \frac{1}{N-1}\sum_{i=1}^{N-1}\left(r_{i+1}-r_i\right)^2}, \tag{1}$$

et

$$\widehat{A^2} \approx \langle r^2\rangle_N - \frac{1}{N-1}\sum_{i=1}^{N-1}\left(r_{i+1}-r_i\right)^2. \tag{2}$$

Il n'est pas influencé par des valeurs absurdes et il donne des résultats acceptables comparativement aux autres estimateurs d'enveloppe. Cet estimateur est particulièrement utile quand la taille de l'échantillon est réduite (i.e., 100 réalisations dans la chambre réverbérante).

Une approximation qui utilise le maximum de vraisemblance

Le deuxième nouvel estimateur que nous suggérons ici est calculé avec une méthode de maximum de vraisemblance basée sur une approximation de la fonction Bessel modifiée du premier degré.

$$\widehat{K} = \frac{\widehat{A}^2}{2\widehat{\sigma}^{2*}} = \frac{1}{4}\frac{\widehat{A}}{\widehat{\mu}_1 - \widehat{A}}\mathcal{E}\left(\frac{4\widehat{A}\left(\widehat{\mu}_1 - \widehat{A}\right)}{\widehat{\mu}_2}\right). \tag{3}$$

avec

$$\widehat{A} = \frac{2\widehat{\mu}_1 + \sqrt{4\widehat{\mu}_1^2 - 3\widehat{\mu}_2}}{3}, \tag{4}$$

L'operateur $\mathcal{E}(x)$ est une fonction de correction définie comme :

$$\mathcal{E}(x) = -0.145e^{4.9x^2+1.95x} + 1.12, \tag{5}$$

et l'estimateur de la puissance des composantes brassés est décrit par :

$$2\widehat{\sigma}^{2*} = \frac{1}{\mathcal{E}\left(\frac{\widehat{2}\sigma^2}{\widehat{\mu}_2}\right)} 2\widehat{\sigma}^2 \approx 2\sigma^2. \tag{6}$$

Les estimateurs $\widehat{\mu}_1$ et $\widehat{\mu}_2$ sont respectivement les moments d'ordre 1 et 2 de l'enveloppe du signal.
Comme dans l'analyse précédente, on présente dans le tableau 2 les limites de ces estimateurs dans les mêmes conditions : un biais de 3 dB, un intervalle de confiance à 95% de 6 dB, et un taux de rejet de 10%.

Table 2: Intervalles utiles de K pour 10% de taux de rejet, 3 dB de biais, et 6 dB pour l'intervalle de confiance.

Type d'estimateur	**Gamme de** K[dB]
estimateur, (1)	≥ -2.20
estimateur, (3)	≥ -5.10

Validation expérimentale

Une validation expérimentale incluant l'analyse du deuxième estimateur proposé (3) est faite avec des mesures en chambre réverbérante. Ces expériences mettent en valeur les avantages de cet estimateur et confirment l'augmentation de la gamme des valeurs du facteur K correctement estimées.

La première configuration teste la limite supérieure des estimateurs. Les antennes sont placées en ligne de vue, à une distance de 1 m l'une de l'autre. Fig. 6(a) présente un zoom sur 40 MHz de bande des facteur K mesurés. Quelques valeurs pour les estimateurs de $\widehat{K}_{\mathrm{d}}$ doivent être abandonnées puisque sont des valeurs négatives ou complexe (valeurs qualifiées d'absurdes). L'estimateur le moins performant est $\widehat{K}_{\mathrm{e}}$. Les résultats pour l'estimateur $\widehat{K}_{\mathrm{f}}$ et la nouvelle méthode se ressemblent.

Dans la deuxième expérience, les composantes non-brassées sont réduites en augmentant la distance entre les antennes à 4 m. Le niveau du signal fluctue fortement avec la fréquence. Comme le niveau de facteur K est réduit, les estimateurs $\widehat{K}_{\mathrm{d}}$ et $\widehat{K}_{\mathrm{e}}$ sont fortement influencés. Le nouvel estimateur est affecté légèrement par les valeurs absurdes, tandis que pour $\widehat{K}_{\mathrm{f}}$ le nombre de ces valeurs erronées est cinq fois plus élevé.

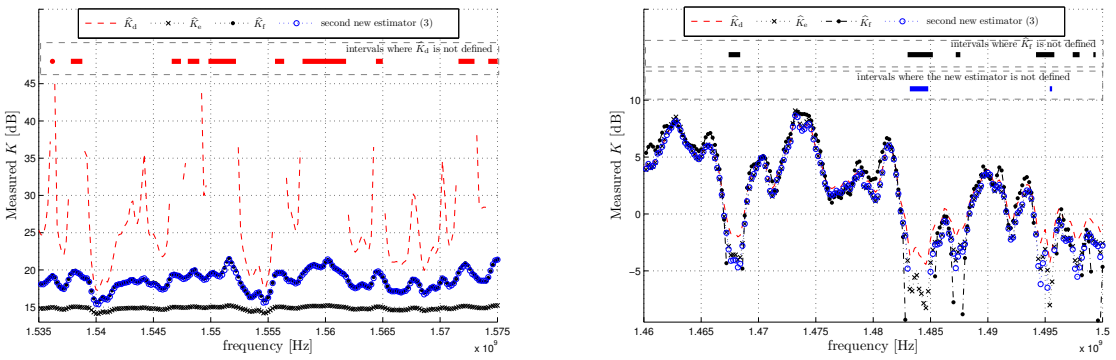

(a) (b)

Figure 6: Facteurs K mesurés dans la chambre réverbérante quand on utilise des absorbants et des antennes cornet placées face à face à une distance de 1 m (a) et une distance de 4 m (b).

Estimer la surface équivalente moyenne d'absorption pour contrôler les canaux de propagation

Dans les plupart d'applications de compatibilité électromagnétique ou de communications sans fil, les chambres réverbérantes sont chargées avec des matériaux absorbants. Ces objets modifient les canaux de propagation puisqu'ils absorbent et modifient le facteur de qualité de la cavité [51]. Quand une "cible" est éclairée par une onde, elle va à la fois réfléchi et absorber une fraction de l'énergie de l'onde. La surface d'absorption est une aire équivalente qui multipliée par la densité de puissance de l'onde incidente donne la puissance absorbée et dissipée par la "cible". La surface équivalente moyenne d'absorption (AACS en anglais) est obtenu en faisant la moyenne des surfaces absorbantes pour toutes les directions des ondes et toutes les polarisations possibles. La bande de cohérence change avec le degré d'absorption et peut affecter la qualité du signal à la réception.

Estimer la surface équivalente moyenne d'absorption dans la chambre réverbérante

Le coefficient $S_{11_{\mathrm{RC}}}$ mesuré dans la chambre réverbérante avec un VNA est une combinaison des composantes déterministes et des composantes spécifiques aux canaux de propagation à l'intérieur de la cavité. La bande de cohérence (CB en anglais) est définie comme la bande de fréquence pour laquelle la fonction d'autocorrélation calculée atteint un seuil de corrélation, i.e., 0.5, ou 0.7, ou 0.9, de l'enveloppe ou du signal complexe.
La distribution des modes dans la chambre réverbérante change avec le degré d'absorption et influence la bande de cohérence et donc le facteur de qualité ou encore la bande passante à 3 dB (en puissance) du mode de propagation. Utilisant [52], cette dernière bande est proportionnelle avec la bande de cohérence calculée en utilisant des signaux complexes pour un niveau de corrélation de 0.7. Alors, la surface équivalente moyenne d'absorption est évaluée en fonction de la bande de cohérence selon :

$$\overset{\blacktriangle}{\sigma}_{\mathrm{A,mes}} \approx \frac{V\pi\sqrt{3}}{c}\left(CB_{\mathrm{L}}^{\mathrm{cpx},0.7} - CB_{\mathrm{E}}^{\mathrm{cpx},0.7}\right), \tag{7}$$

Réciproquement, à partir de (7) il résulte que les modifications du canal de propagation en terme de bande de cohérence dues à la présence d'absorption peuvent être a priori estimées si on connaît la surface équivalente moyenne d'absorption et la bande de cohérence du canal de communication en l'absence des absorbants.

Prédiction de la surface équivalente moyenne d'absorption des absorbants parallélépipédiques

Nous obtenons une évaluation théorique approximative de la surface équivalente moyenne d'absorption des absorbants parallélépipédiques. Ce calcul est effectué dans l'hypothèse où les ondes dans la chambre peuvent être représentées par un spectre d'ondes planes (d'angles d'incidences et de polarisations aléatoires et uniformément répartis). De plus, nous considérons qu'une face d'un absorbant ne masque pas partiellement une autre face de l'absorbant. La surface équivalente moyenne d'absorption estimée devient alors :

$$\overset{\blacktriangle}{\sigma}_{\mathrm{A,theo}} \approx \overline{T} S_{\mathrm{APS,corr}}. \tag{8}$$

où

$$S_{\mathrm{APS,corr}} = S_{\mathrm{APS}} - \frac{6\delta(l+L) - 3\delta^2}{\pi}, \tag{9}$$

est la surface projetée moyenne corrigée (APS en anglais) d'un absorbant parallélépipédique (et dépend de ses paramètres géométriques), et le paramètre $\overline{T}$ correspond à la moyenne du coefficient de transmission de l'onde plane et est calculé en faisant la moyenne sur tous les angles θ des coefficients de transmission (lesquels dépendent de propriétés électromagnétiques du matériau et la fréquence du signal) et les polarisations H et V, [53]. Le paramètre δ est l'épaisseur de peau, et L et l sont les dimensions physiques de l'absorbant parallélépipédique. Nous incluons les effets de l'absorption partielle des ondes électromagnétiques après qu'elles aient traversé l'absorbant. Pour ce faire on suppose que si la distance parcourue par une onde dans un absorbant est plus grande que la profondeur de peau δ de l'absorbant, l'onde est dissipée en totalité. Aussi on considère que les dimensions géométriques de l'absorbant (largeur, longueur et hauteur) sont toutes plus grandes que la profondeur de peau.

Validation de la méthode

Pour la validation de la méthode on donne quelques résultats. Par exemple, les bandes de cohérence quand on change le nombre d'absorbants de 1 jusqu'au 4 sont présentés en Fig. 7(a). Comme attendu, le niveau de la bande de cohérence augmente avec le nombre d'absorbants dans la chambre.
En utilisant (7) pour estimer la surface équivalente moyenne d'absorption et avec (8) et (9) pour simuler cette surface, on compare les résultats en Fig. 7(b). La valeur de la surface équivalente moyenne d'absorption correspond à une moyenne pondérée par la densité de modes de la chambre dans la bande d'évaluation (i.e., 10 MHz). Nous présentons également la surface équivalente moyenne d'absorption quand on utilise la méthode expérimentale classique [51]. La comparaison des résultats de mesures et de simulations est satisfaisante même si il y a

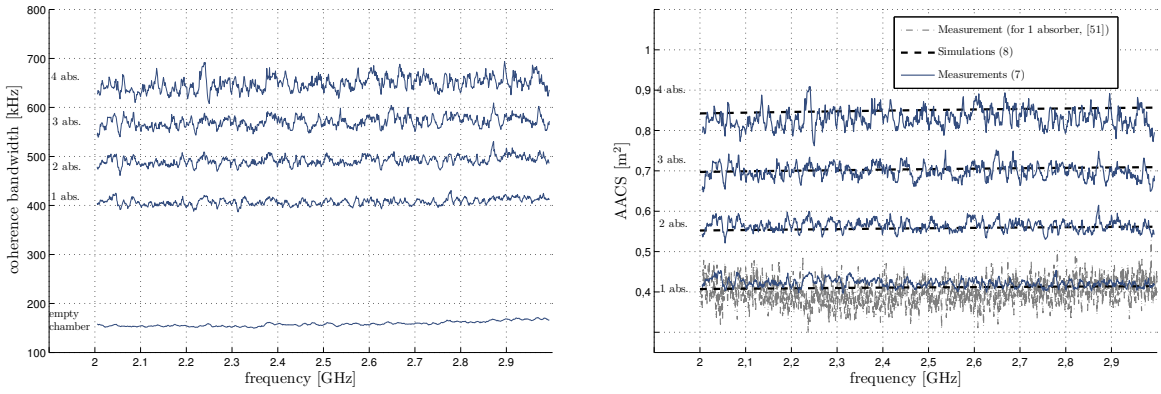

(a) (b)

Figure 7: Les bandes de cohérences calculées entre 2 – 3 GHz dans des sous-bandes de fréquence de 10 MHz (a), et les surfaces équivalentes moyennes d'absorption mesurées et simulées en fonction du nombre d'absorbants dans la chambre dans la bande de fréquence 2 – 3 GHz pour des absorbants de type P150 (b).

certaines différences.

Fig. 8 présente un exemple de mesure de la variation de la surface équivalente moyenne d'absorption à une fréquence centrale de 2.5 GHz pour un absorbant parallélépipédique P150 en fonction de la bande de cohérence. Ce résultat peut être utilisé comme une abaque pour déterminer la quantité d'absorbants nécessaire afin d'obtenir la bande de cohérence désirée.

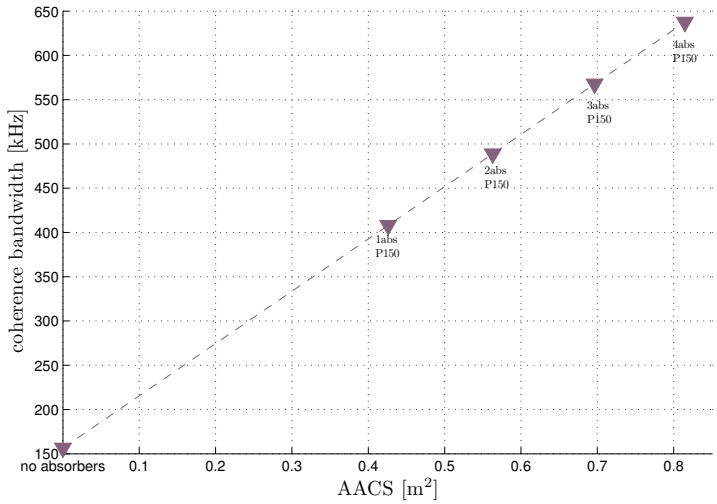

Figure 8: La bande de cohérence en fonction de la surface équivalente moyenne d'absorption à une fréquence centrale de 2.5 GHz.

Contrôle simultané de paramètres du canal de propagation

Nous proposons une façon rapide de contrôler simultanément le canal de propagation à l'intérieur de chambre réverbérante en fonction du facteur K, des paramètres de temps et du degré d'absorption, en utilisant un modèle statistique simple du profil de puissance du canal de propagation pour un signal d'émission de type sinusoïdal.

Modèle du signal

Les constantes de temps suivantes sont utilisées pour décrire les caractéristiques d'une chambre réverbérante en régime transitoire :

- τ est le temps caractéristique de la chambre ;
- t_{unSti} est le temps mis par le signal non-brassé pour parvenir au récepteur. La transmission commence à $t = 0$;
- t_{Sti} est défini comme le moment à partir duquel des composantes brassées apparaissent au niveau du récepteur ;
- t_{Ss} est défini comme le temps nécessaire pour atteindre un niveau $\alpha\%$ de la puissance du signal à la réception en régime permanent.

Quand le signal reçu contient des composantes brassées et non-brassées l'enveloppe du champ électrique en régime permanent suit une loi de distribution de Rice. Le profil de puissance du signal total pour la $i$ème réalisation $p_{\text{total},i}(t)$ (e.g., la $i$ème position du brasseur) est décrit par une loi du χ^2. La moyenne sur plusieurs réalisations est alors modélisée par :

$$P_{\text{total}}(t) = E\left[p_{\text{total},i}(t)\right] \approx A_{\text{unSti}}^2 u(t - t_{\text{unSti}}) + 2\sigma^2\left[1 - e^{-(t-t_{\text{Sti}})/\tau}\right]u(t - t_{\text{Sti}}), \tag{10}$$

où A_{unSti} est le niveau maximal de l'enveloppe du champ électrique des composantes non-brassées, le paramètre σ^2 est la variance de la composante brassée [54], $u(t - t_{\text{unSti}})$ est la fonction échelon définie au moment $t = t_{\text{unSti}}$, et $\theta_{\text{Sti},i}$ est la phase en régime permanent pour la $i$ème réalisation.
Des relations analytiques pour différents paramètres de canal sont extraites : le facteur K est décrit comme une fonction de temps caractéristiques et le niveau de puissance normalisé de l'enveloppe du signal :

$$K = \frac{1}{1-\alpha} e^{-(t_{\text{Ss}} - t_{\text{Sti}})/\tau} - 1. \tag{11}$$

Les différentes grandeurs temporelles décrivant l'étalement du signal (retard moyen τ_μ, étalement de délai τ_{rms}) sont aussi définies comme fonctions de plusieurs paramètres :

- le facteur K qui est influencé par le volume de la chambre et son facteur de qualité, la fréquence du signal, la distance entre les antennes, et la directivité des antennes [12] ;
- le temps caractéristique de la chambre τ qui dépend de la distance caractéristique L de la cavité et le coefficient d'absorption moyen $\overline{T}$;
- le paramètre t_{unSti} qui dépend directement de la distance entre antennes ;
- le temps t_{Sti} qui dépend du temps caractéristique de la chambre ;
- la limite α, sélectionnée pour prendre en considération le maximum d'énergie pour assurer que la distribution dans le régime permanent est bien déterminée.

Les paramètres présentés dépendent du facteur de qualité de la chambre. Ce facteur peut être ajusté en utilisant des absorbants. Nous présentons plusieurs relations entre la surface équivalente moyenne d'absorption, le temps caractéristique de la chambre et le facteur K. On considère l'hypothèse dans laquelle les absorbants sont placés dans la chambre réverbérante de telle manière qu'ils absorbent essentiellement les composantes brassées. Deux situations générales sont analysées :
1) dans la première situation, les temps caractéristiques pour la chambre vide et chargée avec des absorbants, respectivement τ_{E} et τ_{L}, sont supposés être connus. Les puissances des composantes brassées, $2\sigma_{\text{E}}^2$ et $2\sigma_{\text{L}}^2$, sont aussi connues. Dans ces conditions la surface équivalente moyenne d'absorption $\overset{\blacktriangle}{\sigma}_{\text{A}}$ est calculée par :

$$\overset{\blacktriangle}{\sigma}{}'_{\text{A}} = \frac{V}{c\tau_{\text{L}}}\left(\frac{\sigma_{\text{E}}^2}{\sigma_{\text{L}}^2} - 1\right) - \underbrace{\pm\delta\frac{V}{c\tau_{\text{L}}}}_{\substack{\text{erreur de} \\ \text{l'estimation}}}, \tag{12a}$$

et

$$\overset{\blacktriangle}{\sigma}{}'_{\mathrm{A}} = \frac{V}{c\tau_{\mathrm{E}}}\left(\frac{\sigma_{\mathrm{E}}^2}{\sigma_{\mathrm{L}}^2} - 1\right) - \underbrace{\frac{\pm\delta}{1\pm\delta}\frac{V}{c\tau_{\mathrm{E}}}\frac{\sigma_{\mathrm{E}}^2}{\sigma_{\mathrm{L}}^2}}_{\substack{\text{erreur de} \\ \text{l'estimation}}}. \tag{12b}$$

Où δ est l'erreur d'estimation de la puissance non-brassée ($A_{\mathrm{unSti,E}}/A_{\mathrm{unSti,L}} = 1\pm\delta$). Une erreur de $+\delta\%$ peut correspondre à la situation pour laquelle l'énergie des composantes spéculaires est absorbée partiellement ou quand $A_{\mathrm{unSti,L}}$ est sous-estimé, tandis qu'une erreur de $-\delta\%$ caractérise le cas où $A_{\mathrm{unSti,L}}$ est surestimé.
Quand le temps caractéristique initial τ_{E}, le facteur K pour la chambre vide K_{E}, et la surface équivalente moyenne d'absorption $\overset{\blacktriangle}{\sigma}_{\mathrm{A}}$ sont connus, alors à partir de (12b) il résulte une façon rapide d'estimer le facteur K quand la chambre est chargée :

$$K_{\mathrm{L}} = K_{\mathrm{E}} \underbrace{\left(\frac{c\tau_{\mathrm{E}}\,\overset{\blacktriangle}{\sigma}_{\mathrm{A}}}{V} + 1\right)}_{\text{facteur d'absorption}}. \tag{13}$$

2) pour la deuxième situation, on connaît la surface équivalente moyenne d'absorption $\overset{\blacktriangle}{\sigma}_{\mathrm{A}}$ et les conditions initiales (i.e., la puissance des composantes brassées σ_{E}^2, et le temps caractéristique de la chambre vide τ_{E}). Dans cette situation on calcule σ_{L} et le temps τ_{L} quand la chambre est chargée, selon :

$$\sigma_{\mathrm{L}} = \sigma_{\mathrm{E}} \sqrt{\frac{1}{c\tau_{\mathrm{E}}\dfrac{\overset{\blacktriangle}{\sigma}_{\mathrm{A}}}{V} + 1}}, \tag{14}$$

et

$$\tau_{\mathrm{L}} = \frac{1}{c\dfrac{\overset{\blacktriangle}{\sigma}_{\mathrm{A}}}{V} + \dfrac{1}{\tau_{\mathrm{E}}}}. \tag{15}$$

Validation

La Fig. 9(a) présente une comparaison entre la valeur simulée et la valeur mesurée du temps caractéristique de la chambre.
En exploitant (11) pour calculer le facteur K, la Fig. 9(b) montre les valeurs mesurées et simulées du facteur K en fonction de la distance entre antennes d'émission et de réception. Les paramètres τ_{μ} et τ_{rms} sont aussi estimés et quelques résultats sont présentés en Fig. 10 Une analyse plus détaillée de ces résultats est présentée en section 5.4.2.

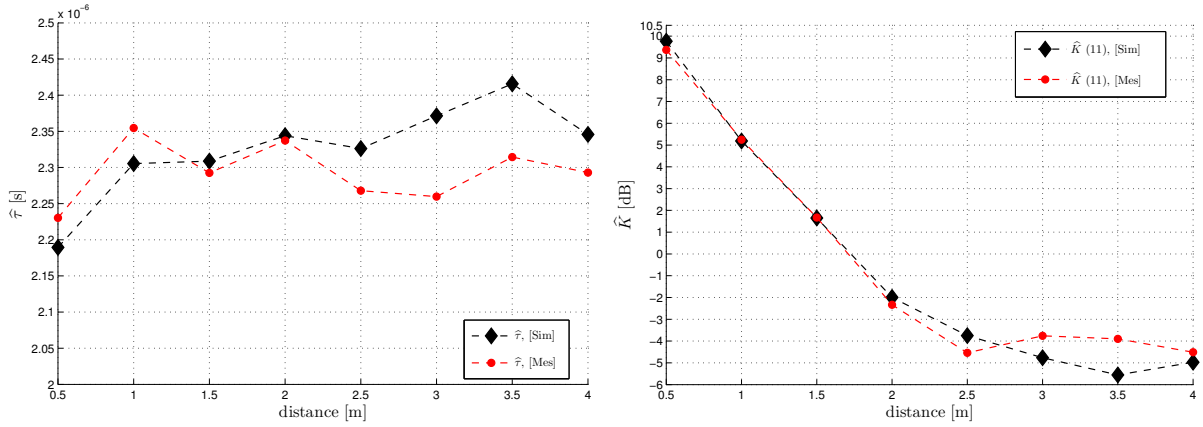

(a) (b)

Figure 9: La variation du temps caractéristique de la chambre (a), et la variation de facteur K obtenu en utilisant des paramètres du temps (b). La distance entre les antennes varie de 0.5 à 4 m (la chambre est vide).

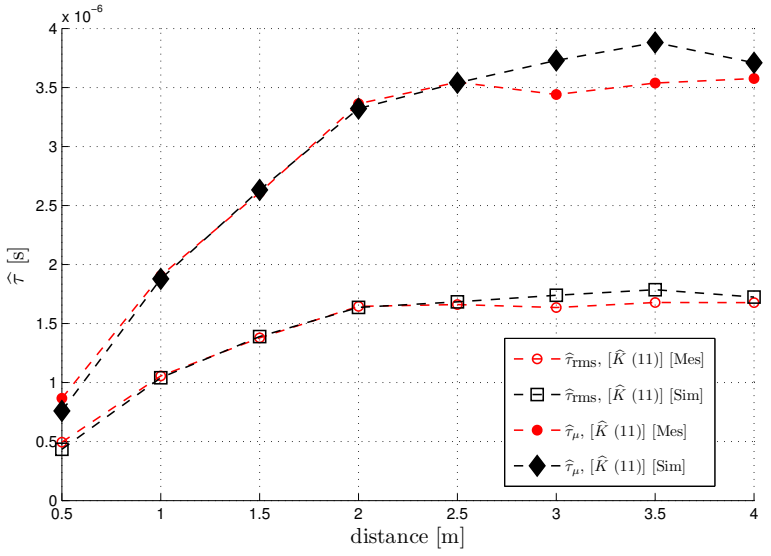

Figure 10: La variation de τ_{μ} et τ_{rms}. La distance entre les antennes varie de 0.25 à 4 m (chambre vide).

Évaluation de paramètres d'une antenne dans la chambre réverbérante

Une alternative aux moyens d'essai classiques (e.g., chambres anéchoïques) pour caractériser différents paramètres d'une antenne est d'utiliser un simple réflecteur métallique. Par exemple, une méthode pour calculer le gain d'une antenne quand celle-ci est placée devant un grand mur métallique a été introduit en [55]. Cette méthode consiste à analyser le coefficient de réflexion résultant. Cette méthode a été repris en [56, 57]. En utilisant le paramètres mesuré S_{11} de l'antenne nous proposons dans cette thèse d'estimer plusieurs paramètres par une approche plus détaillée comprenant l'analyse des incertitudes associées. Un premier paramètre estimé est la désadaptation de l'antenne. Ensuite, nous examinons l'estimation de la distance de propagation. Une analyse de l'incertitude de la distance de propagation en espace-libre montre les conditions dans lesquelles ce paramètre est estimé. Finalement, on présente des résultats pour le diagramme de rayonnement et l'ouverture à 3 dB d'une antenne.

La méthode

Le gain d'une antenne peut être calculé à partir de l'équation de Friis :

$$G(\theta,\varphi) = \left(1 - |S_{11_{\mathrm{FS}}}|^2\right)\eta |H_{\mathrm{FS}}(\theta,\varphi)| \left(\frac{8\pi d}{\lambda}\right), \tag{16}$$

où d est la distance de propagation en espace libre. La fonction de transfert H_{FS} est calculée à partir de mesures du coefficient de réflexion $S_{11_{\mathrm{RC}}}$ dans la chambre réverbérante. Ce signal est une combinaison des signaux liés à l'antenne et des signaux spécifiques à la propagation à l'intérieur de la chambre :

$$S_{11_{\mathrm{RC}}}(\theta,\varphi) = S_{11_{\mathrm{FS}}} + \left(1 - |S_{11_{\mathrm{FS}}}|^2\right)\eta \cdot \left(H_{\mathrm{FS}}(\theta,\varphi) + H^{\mathrm{sec}}_{\mathrm{unSti}}(\theta,\varphi) + H_{\mathrm{Sti}}(\theta,\varphi)\right), \tag{17}$$

où $S_{11_{\mathrm{FS}}}$ représente le coefficient de désadaptation de l'antenne et $H^{\mathrm{sec}}_{\mathrm{unSti}}$ et H_{Sti} sont les fonctions de transfert complexes des composantes non-brassées secondaires et brassées.

Estimation de la distance de propagation d

L'extraction du gain de l'antenne à partir de la relation (16), nécessite la connaissance de la distance de propagation en espace libre d. La qualité de l'estimation de ce paramètre a un impact direct sur l'estimation du gain de l'antenne. Avec la diminution de la distance entre antennes cette erreur augmente. Nous pouvons mesurer facilement la distance physique entre le mur métallique de la chambre et le support de l'antenne mais la véritable distance de propagation diffère de cette valeur. Une longueur inconnue résiduelle d_{x} peut influencer l'estimation de cette distance de propagation, Fig. 11. De plus, la distance de propagation en espace libre change avec la position angulaire de l'antenne (i.e., avec l'angle θ) et il est difficile de la mesurer physiquement pour chaque angle de l'antenne. Pour trouver la distance de propagation en espace libre, une solution est d'extraire le temps qui correspond au maximum d'amplitude du signal mesuré et qui correspond à une distance de propagation totale d_{IR} :

$$d_{\mathrm{IR}}(\theta) = \underbrace{2\left[d(0) + (1-\cos\theta)d_{\mathrm{x}}\right]}_{\substack{\text{distance de propagation} \\ \text{en espace libre}=2d(\theta)}} + 2d_{\mathrm{a}}, \tag{18}$$

Ce paramètre représente deux fois la distance de propagation totale. Cette distance totale est composée d'une distance de propagation en espace libre d et une distance guidée dans l'antenne, d_a calculée par :

$$d_a = \frac{1}{2}\frac{d_{IR,1}(0)|H_{FS,1}| - d_{IR,2}(0)|H_{FS,2}|}{|H_{FS,1}| - |H_{FS,2}|}. \tag{19}$$

et "1 "et "2 " représentent deux distances entre l'antenne et le réflecteur métallique pour un angle $\theta = 0$.

Résultats

Fig. 12(a) montre la désadaptation de l'antenne mesurée dans la bande de fréquence 2 – 6 GHz en utilisant le filtrage en temps pour une antenne de type cornet (modèle ETS 3115). Les deux autres résultats (en utilisant la moyenne sur plusieurs mesures, et mesurée dans la base champ proche) sont donnés pour comparaison (voir section 6.3.1).
Fig. 12(b) présente une comparaison entre le module de la fonction du transfert en espace libre évalué à partir du gain mesuré dans la base champ proche (NFC en anglais) de l'IETR et la mesure en chambre réverbérante, dans la bande passante 2–6 GHz, pour plusieurs intervalles de filtrage temporel. Le paramètre $t_{maximum}$ correspond au maximum d'amplitude de la première réflexion. Cette durée dépend seulement de la forme d'onde du signal et non de la chambre.

Estimation du gain maximal Le gain maximal est présenté à la Fig. 13. Un facteur d'erreur important est l'erreur associée à l'estimation de la distance de propagation. Les incertitudes augmentent lorsque le gain de l'antenne est plus petit, parce que l'amplitude du signal est beaucoup plus réduite. Il est donc plus difficile d'extraire le maximum du signal dans cette situation. Dans cette analyse toutes les mesures ont été faites manuellement. Cela cause inévitablement des incertitudes de positionnement de l'antenne. Néanmoins, les résultats de mesure en champ proche sont aussi affectées par les incertitudes de mesure.

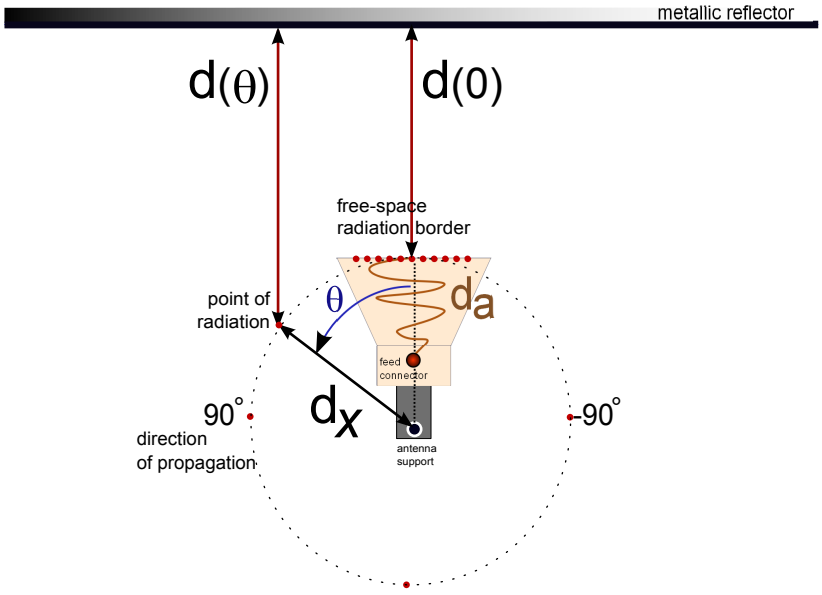

Figure 11: Les distances de propagation quand l'antenne tourne pour $\theta \in [0, 2\pi[$.

Estimation du diagramme de rayonnement Pour une analyse plus détaillée nous estimons le gain en fonction de l'angle $\theta \in [-30\,°, 30\,°]$ (voir section 6.3.3). Ensuite, on compare les valeurs trouvées dans la chambre réverbérante avec celles mesurées dans la base champ proche. Nous calculons l'écart relatif des mesures en chambre réverbérante et base champ proche par rapport à la mesure en base champ proche. On poursuit avec l'analyse pour tout le diagramme de rayonnement. Nous présentons quatre diagrammes de rayonnement de l'antenne (i.e., deux pour chaque polarisation à deux fréquences différentes, 3 et 5 GHz), Fig. 14 et 15 (pour plus de details voir section 6.3.4).

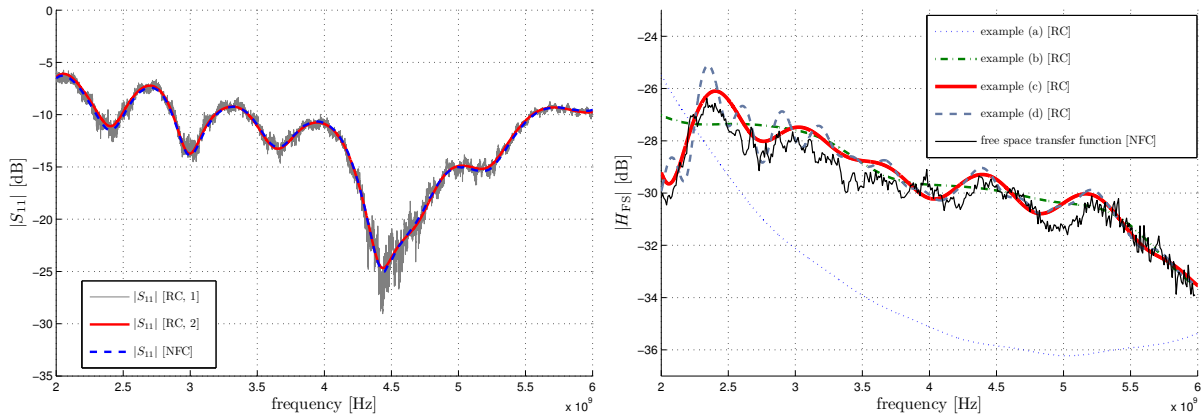

(a) (b)

Figure 12: Désadaptation de l'antenne : [RC, 1] - en utilisant la moyenne sur plusieurs mesures, [RC, 2] - en utilisant le filtrage en temps, [NFC] - mesure dans NFC (a). Comparaison entre la fonction de transfert estimée dans la direction ($\theta = 0$, $\varphi = 0$) dans la NFC et la valeur mesurée dans la chambre réverbérante pour différents intervalles de troncature : (a) $[7\,\text{ns}, t_{\text{maximum}}]$, (b) $[7\,\text{ns}, t_{\text{maximum}} + 1\,\text{ns}]$, (c) $[7\,\text{ns}, t_{\text{maximum}} + 2\,\text{ns}]$, (d) $[7\,\text{ns}, t_{\text{maximum}} + 4\,\text{ns}]$ (b).

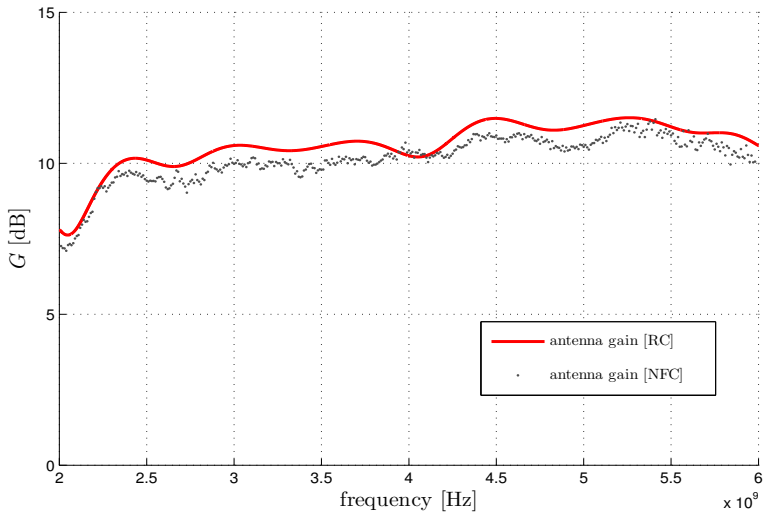

Figure 13: Comparaison entre les valeurs de gain, dans la direction ($\theta = 0$, $\varphi = 0$), mesures en chambre réverbérante et dans la base champ proche.

Évaluation de l'ouverture de l'antenne à 3 dB

Précédemment, nous avons discuté la possibilité d'extraire le diagramme de l'antenne à partir de mesures en chambre réverbérante. Nous réduisons l'intervalle d'analyse pour la gamme où le gain de l'antenne est élevé pour extraire l'ouverture à 3 dB. Pour cela, on réalise des mesures pour un angle $\theta \in [-30\,°, 30\,°]$ avec un pas de 5 °. Dans les Fig. 16(a) et Fig. 16(b) nous présentons les ouvertures à 3 dB pour la polarisation horizontale et verticale.

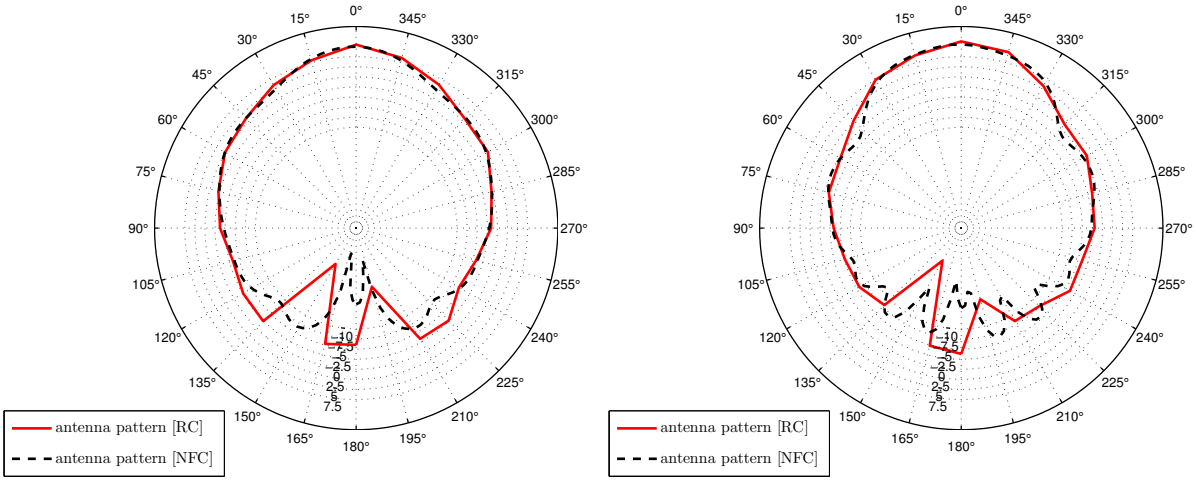

(a) (b)

Figure 14: Comparaison entre les diagrammes de rayonnement de l'antenne (polarisée horizontalement) mesurés dans la chambre réverbérante et la base champ proche à $f = 3\,\text{GHz}$ (a), et $f = 5\,\text{GHz}$ (b).

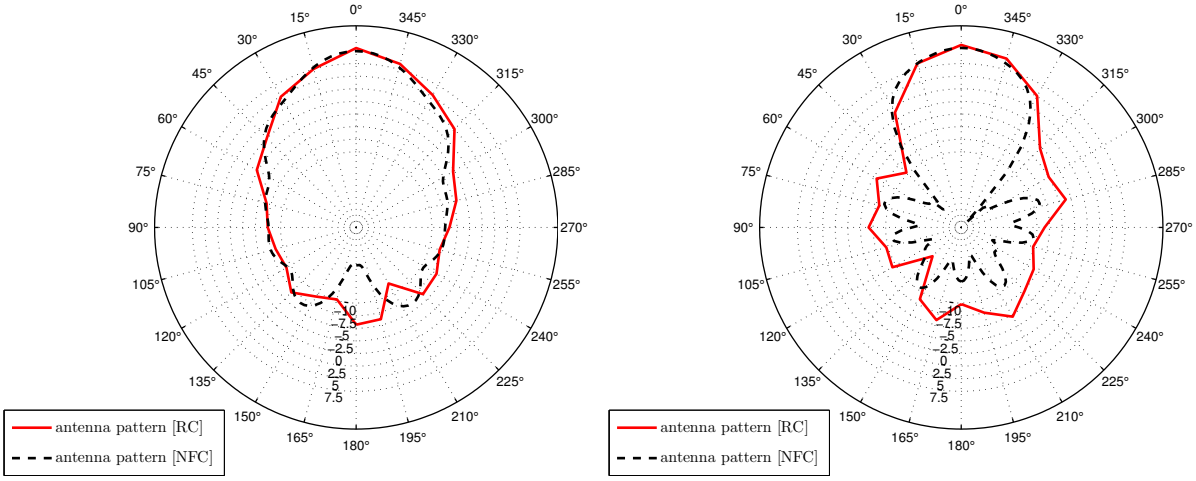

(a) (b)

Figure 15: Comparaison entre les diagrammes de rayonnement de l'antenne (polarisée verticalement) mesurés dans la chambre réverbérante et la base champ proche à $f = 3\,\text{GHz}$ (a), et $f = 5\,\text{GHz}$ (b).

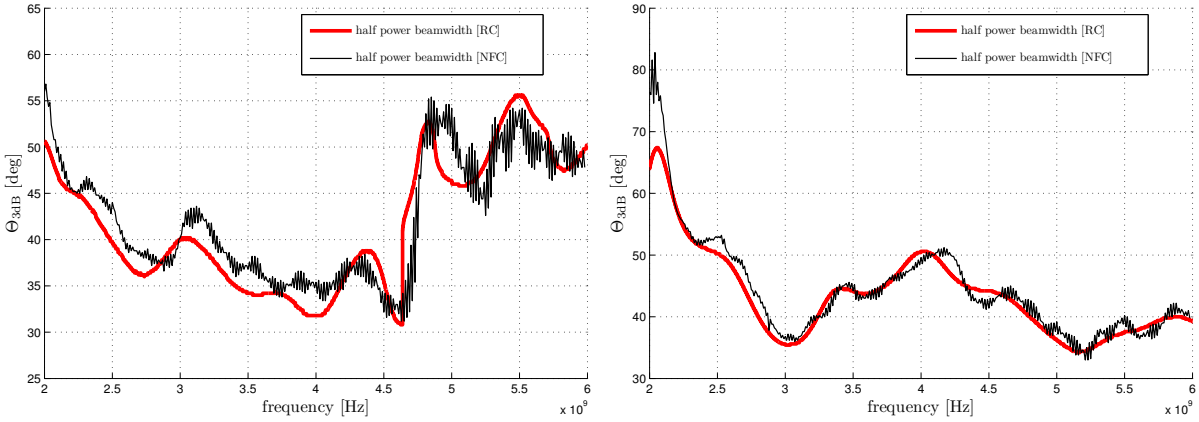

(a) (b)

Figure 16: L'ouverture à 3 dB mesurée en RC et NFC : polarisation horizontale (a), et polarisation verticale (b).

Le gain de diversité pour des environnements de type Rice et Rayleigh en chambre réverbérante

La diversité a le rôle d'augmenter la puissance du signal reçu (i.e., envoyer le même signal sur des canaux différents), et la capacité de canal de transmission (i.e., envoyer des données diverses en parallèle sur des canaux différents). On analyse la diversité pour un canal sans fil émulé en chambre réverbérante. Le but est d'analyser et d'obtenir des résultats relatifs à l'apport de la diversité en présence d'évanouissements, similaires à ce que l'on obtiendrait en environnement réel. Les signaux mesurés peuvent être des tensions ou des puissances avec ou sans mesure de phase des signaux (selon le type d'instrumentation disponible : VNA, oscilloscope, analyseur du spectre, etc.).
Dans une première étape, nous identifions les facteurs qui peuvent influencer les résultats. Ces facteurs nous permettent de déterminer les plages de gains de diversité que l'on doit pouvoir retrouver en mesurés. Nous étendons l'analyse de gain pour le cas où les canaux sont caractérises par une distribution de Rice et nous examinons le cas où les puissances dues aux composantes non-brassées sont différentes pour chaque antenne. Cette étude est réalisée en utilisant des simulations de type Monte Carlo. Les mesures dans la chambre réverbérante valident ces résultats théoriques. Nous montrons que dans les environnements caractérisés par une distribution de Rice, la diversité est influencée par la présence de composantes du signal non-brassées et aussi par le déséquilibre de puissance dû à ces composantes. Dans ces environnements, l'usage de la corrélation d'enveloppe ou de puissance pour caractériser la qualité de la diversité n'est pas recommandé.

Techniques de diversité

Il y a plusieurs mécanismes pour exploiter la diversité [58]. Un premier mécanisme utilise les propriétés de l'antenne. Parmi ces techniques, on identifie la diversité spatiale, la diversité de polarisation et la diversité de rayonnement ou d'angle (d'arrivée). Un autre mécanisme utilise les propriétés du système (ou le signal) : diversité de fréquence et diversité de temps.

Calcul du gain de diversité

Le gain de diversité mesure l'amélioration du SNR d'un signal qui est obtenu par la combinaison de plusieurs signaux reçus. Par exemple, si les deux signaux reçus sont combinés d'après une certaine règle, la fonction de répartition résultante (CDF en anglais) pour le signal combiné est localisée à la droite de chaque CDF du signal correspondant à chaque branche (ou des antennes prises individuellement). Dans ces conditions, le gain de diversité (en dB) est défini comme la différence de puissance entre le niveau d'un signal de référence et le signal combiné, Fig 17. En général ce paramètre est mesuré à différents niveaux de précision : 99%, 95% ou 90% : Selon le signal pris comme référence, il existe différentes définitions du gain

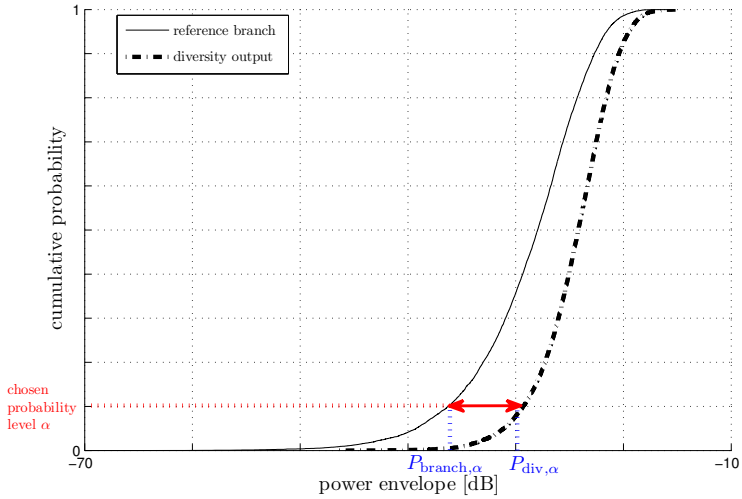

Figure 17: Définition du gain de diversité à partir des CDF des signaux.

de diversité [59] : gain de diversité apparente, gain de diversité effective et gain de diversité réelle. Le signal résultant peut être calculé avec plusieurs techniques.

Paramètres qui peuvent influencer le gain de diversité

Le gain de diversité est une fonction de la corrélation du signal entre branches, du couplage entre antennes, du déséquilibre de puissance entre les branches et des niveaux de puissances non-brassées. Pour un système avec deux antennes, nous pouvons exprimer le déséquilibre de puissance de la manière suivante :

$$PI = \frac{\eta_1}{\eta_2} \times \frac{2\sigma_1^2}{2\sigma_2^2} \times \frac{K_1 + 1}{K_2 + 1} = PI_\eta \times PI_{\text{Sti}} \times PI_K \tag{20}$$

où l'indice "1" dénote la première branche et "2" la deuxième, et $PI_\eta\times$, PI_{Sti} et PI_K sont les déséquilibres de puissance due à l'efficacité de l'antenne, aux composantes brassées et aux différents facteurs K.

Résultats

Un premier résultat pour un cas particulier est le gain de diversité (calculé avec la technique de combinaison à gain maximal) quand les signaux sur les deux antennes ne sont pas corrélés (voir section 7.7.1). La Fig. 18 représente l'évolution du gain de diversité en fonction de K et du déséquilibre de puissance. Cette situation peut correspondre au cas où les antennes ont des polarisations différentes ou quand les antennes sont localisées loin l'une de l'autre. Un autre exemple sélectionné, concerne le cas où il n'y a aucun déséquilibre de puissance dû aux facteurs K, PI_K = 0 dB. C'est le cas quand, dans un environnement réel, les deux antennes reçoivent la même puissance non-brassée. La corrélation complexe varie entre 0 et 1, Fig. 19(a) :
Un troisième exemple sélectionné est présenté à la Fig. 19(b). Il représente la situation pour laquelle le facteur K d'une antenne est très faible (−20 dB) tandis qu'il est très élevé pour l'autre. En conséquence, le déséquilibre de puissance PI_K va augmenter (le facteur K sur une branche est −20 dB et sur l'autre branche change de −20 à 3.5 dB).

Le gain de diversité simulé et mesuré

On compare finalement les résultats de gain de diversité mesurés avec ceux obtenus par simulation. Les paramètres d'entrée pour les simulations, évalués par les mesures, sont les puissances brassées et non-brassées, la corrélation complexe et les efficacités de rayonnement. Comme ces valeurs sont affectées par des incertitudes et les simulations ne sont pas basées sur un modèle exact de l'environnement les résultats de simulations peuvent être légèrement différents de ceux mesurés. Fig. 20(a) présente la comparaison pour une configuration en l'absence de ligne-de-vue directe, tandis que la Fig. 20(b) illustre les résultats pour une configuration en ligne-de-vue directe.

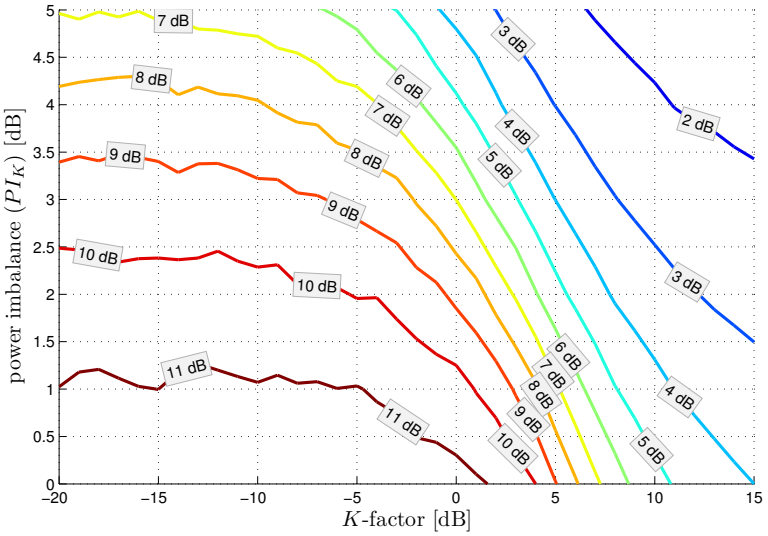

Figure 18: Simulation de gain de diversité quand ρ_{cpx} = 0 pour la technique de combinaison à gain maximal.

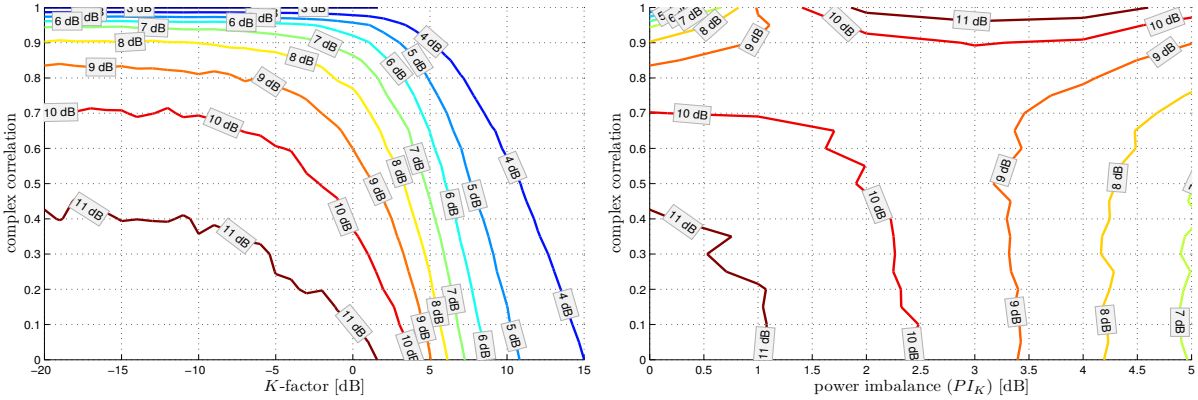

(a) (b)

Figure 19: Simulation de gain de diversité pour la technique de combinaison à gain maximal quand $PI_K = 0\,\text{dB}$ (a), et quand le facteur K d'une antenne est $-20\,\text{dB}$ (b).

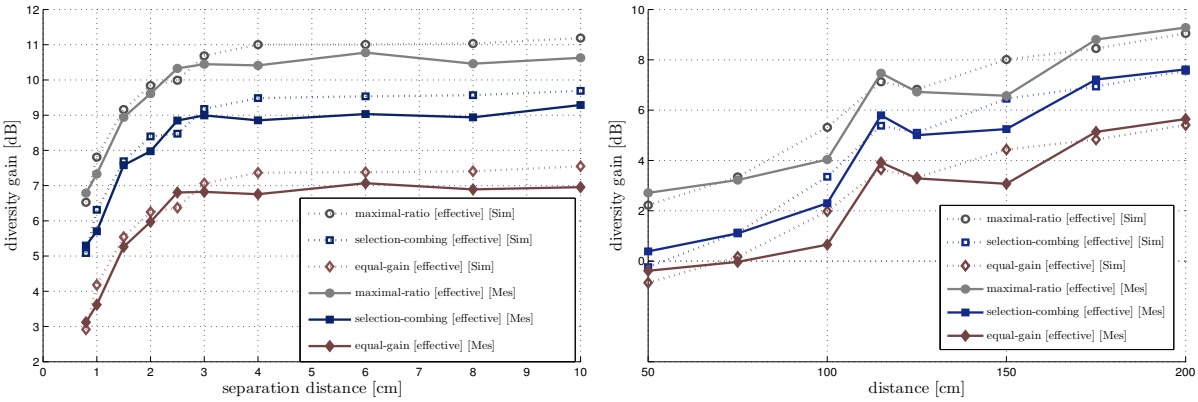

(a) (b)

Figure 20: Comparaisons entre les diversités mesurées et simulées en cas d'absence de ligne-de-vue directe quand on change la distance entre les antennes du réseau de réception, et pour le cas de ligne-de-vue directe quand on change la distance de propagation entre l'antenne d'émission et le réseau d'antennes. La fréquence est de 2.9 GHz.

Conclusions

Dans la plupart des situations, les propriétés du milieu de propagation sont à l'origine de phénomènes d'évanouissement des signaux qui affectent la qualité de transmission, le débit et d'autres paramètres significatifs de la qualité de la liaison. Le développement d'un système de communication performant nécessite des testes préalables et l'optimisation du système. Ces essais peuvent être faits en utilisant des simulations numériques ou des sondeurs de canal. La chambre réverbérante est un environnement qui peut aussi être utilisé pour imiter des canaux des propagation car ses propriétés peuvent être modifiées et contrôlées convenablement. Le contrôle de la transmission peut être réalisé au moyen de plusieurs paramètres. Au cours de ces travaux de thèse nous avons analysé et obtenu plusieurs techniques pour mesurer et

contrôler ces paramètres à l'intérieur de la chambre réverbérante.

Un premier paramètre que nous avons analysé est le facteur K. Ce paramètre est obtenu en appliquant différentes méthodes dont les résultats peuvent être influencés par plusieurs facteurs. En fonction de la méthode utilisée, les résultats obtenus pour calculer le facteur K sont plus ou moins exploitable. En effet, une méthode I/Q fonctionne bien, mais il est nécessaire de connaître l'amplitude et la phase du signal ; la méthode qui utilise l'enveloppe est plus simple et donne des résultats plus rapides, mais pour des faibles valeurs de facteur K cette méthode fournit des résultats fortement biaisés et/ou faux. Nous avons analysé plusieurs estimateurs et identifié les limites utiles dans lesquelles ils peuvent être utilisés. Aussi, parce que les estimateurs qui nécessitent de connaître seulement l'enveloppe du signal sont les plus affectés par les incertitudes d'estimation, nous proposons deux nouvelles méthodes qui augmentent la gamme utile de valeurs de K correctement détectées en gardant une formulation mathématique simple.

Une manière de contrôler un canal de propagation à l'intérieur de la chambre réverbérante est de modifier le degré d'absorption. Cela modifie le facteur de qualité de la chambre et par conséquent le temps caractéristique de l'environnement. Ce paramètre est évalué facilement à partir de mesures de la bande de cohérence, réalisées en utilisant une seule antenne. Pour des absorbants parallélépipédiques et des absorbants qui ont des formes géométriques simples la surface équivalente moyenne d'absorption peut être simulée si on connaît les dimensions physiques et les propriétés électromagnétiques du matériau.

Le contrôle de canaux de propagation émulés dans la chambre réverbérante nécessite la connaissance de relations entre différents paramètres du canal de propagation. À partir d'un modèle statistique basé sur le profil de puissance d'un signal sinusoïdal plusieurs paramètres sont calculés : le facteur K, la surface équivalente moyenne d'absorption et différents paramètres d'étalement. Le facteur K est décrit comme une fonction de moments caractéristique du temps et du niveau normalisé de la puissance reçue. Des relations analytiques pour τ_{μ} et τ_{rms} sont présentées. La surface équivalente moyenne d'absorption est estimée comme une fonction de K. Nous discutons aussi la dispersion des composantes du signal non-brassées secondaires avec le temps et les effets sur ce modèle. Les simulations et les mesures valident et montrent l'utilité de cette méthode.

Nous montrons qu'il est également possible de mesurer les caractéristiques d'une antenne dans une chambre réverbérante. En utilisant un filtrage dans le domaine temporel, plusieurs paramètres de l'antenne peuvent être évalués directement. Cette méthode n'est pas nouvelle mais nous étendons l'analyse pour tout le diagramme de rayonnement de l'antenne. Nous discutons les erreurs d'évaluation dues à l'estimation de la distance de propagation en espace libre, ainsi que de la distance de propagation guidée au sein de l'antenne. Nous présentons des résultats pour la désadaptation de l'antenne, l'ouverture à 3 dB, et on compare ces résultats avec ceux évalués dans une base de mesure de champ proche.

A la fin de cette thèse, nous étendons notre travail aux réseaux d'antennes et aux améliorations de la transmission dues à la diversité. Nous évaluons les limites d'une estimation du gain de diversité pour différentes techniques et différentes configurations de canaux de transmission. Nous discutons surtout la situation d'un canal de type Rice. Nous montrons que selon le niveau du facteur K mesuré par les antennes de réception le gain de diversité peut être affecté. De plus, nous montrons qu'en présence de composantes du signal non-brassées et d'un haut déséquilibre de puissance pour différentes branches, les corrélations d'enveloppe et de puissance peuvent être très faibles bien que le signal sur les différents branches soit très corrélé.

Bibliography

[1] D. A. Hill, *Electromagnetic Fields in Cavities: Deterministic and Statistical Theories*, I. Press, Ed. Wiley/IEEE Press, Piscataway, NJ, 2009.

[2] C. Lemoine, P. Besnier, and M. Drissi, "Investigation of reverberation chamber measurements through high-power goodness-of-fit tests," *Electromagnetic Compatibility, IEEE Transactions on*, vol. 49, no. 4, pp. 745–755, Nov. 2007.

[3] G. Koepke and J. Ladbury, "New electric field expressions for EMC testing in a reverberation chamber," in *Digital Avionics Systems Conference, 1998. Proceedings., 17th DASC. The AIAA/IEEE/SAE*, vol. 1, Oct. 1998, p. 53.

[4] M. Piette, "Antenna radiation efficiency measurements in a reverberation chamber," in *Radio Science Conference, 2004. Proceedings. 2004 Asia-Pacific*, Aug. 2004, pp. 19–22.

[5] K. Rosengren and P.-S. Kildal, "Radiation efficiency, correlation, diversity gain and capacity of a six-monopole antenna array for a MIMO system: theory, simulation and measurement in reverberation chamber," *Microwaves, Antennas and Propagation, IEE Proceedings*, vol. 152, no. 1, pp. 7–16, Feb. 2005.

[6] G. Le Fur, P. Besnier, and A. Sharaiha, "Efficiency measurement of UWB antennas using time reversal in reverberation chambers," *Electronics Letters*, vol. 44, no. 17, pp. 1002–1003, 2008.

[7] C. Rizzo, M. Franzen, and M. Andersson, "Fast measurements with high repeatability of antenna efficiency and over the air (ota) parameters in reverberation chambers," in *Antennas Propagation Conference, 2009. LAPC 2009. Loughborough*, Nov. 2009, pp. 777–780.

[8] H. Krauthauser and M. Herbrig, "Yet another antenna efficiency measurement method in reverberation chambers," in *Electromagnetic Compatibility (EMC), 2010 IEEE International Symposium on*, Jul. 2010, pp. 536–540.

[9] D. A. Hill, "Electromagnetic theory of reverberation chambers," National Institute of Standards and Technology (NIST), Note 1506, 1998.

[10] J. M. Ladbury, G. H. Koepke, and D. Camell, "Evaluation of the NASA Langley Research Center mode-stirredchamber facility," United States Department of Commerce, NIST Tech. Note 1508, Jan. 1999.

[11] K. Rosengren, P. Bohlin, and P.-S. Kildal, "Multipath characterization of antennas for MIMO systems in reverberation chamber including effects of coupling and efficiency," in *Antennas and Propagation Society International Symposium, 2004. IEEE*, vol. 2, Jun. 2004, pp. 1712–1715.

[12] C. Holloway, D. Hill, J. Ladbury, P. Wilson, G. Koepke, and J. Coder, "On the use of reverberation chambers to simulate a Rician radio environment for the testing of wireless devices," *Antennas and Propagation, IEEE Transactions on*, vol. 54, no. 11, pp. 3167–3177, Nov. 2006.

[13] J. F. Valenzuela-Valdes, M. A. Garcia-Fernandez, A. M. Martinez-Gonzalez, and D. Sanchez-Hernandez, "Non-isotropic scattering environments with reverberation chambers," in *Antennas and Propagation, 2007. EuCAP 2007. The Second European Conference on*, Edinburgh, 2007, pp. 1–4.

[14] O. Delangre, P. De Doncker, F. Horlin, M. Lienard, and P. Degauque, "Reverberation chamber environment for testing communication systems: Applications to ofdm and sc-fde," in *Vehicular Technology Conference, 2008. VTC 2008-Fall. IEEE 68th*, 2008, pp. 1–5.

[15] P.-S. Kildal and K. Rosengren, "Correlation and capacity of MIMO systems and mutual coupling, radiation efficiency, and diversity gain of their antennas: simulations and measurements in a reverberation chamber," *IEEE Communications Magazine*, vol. 2, pp. 104–112, Dec. 2004.

[16] J. F. Valenzuela-Valdes, A. M. Martinez-Gonzalez, and D. A. Sanchez-Hernandez, "Emulation of MIMO nonisotropic fading environments with reverberation chambers," *IEEE Antennas and Wireless Propagation Letters*, vol. 7, pp. 325–328, 2008.

[17] K. Remley, H. Fielitz, H. Shah, and C. Holloway, "Simulating MIMO techniques in a reverberation chamber," in *Electromagnetic Compatibility (EMC), 2011 IEEE International Symposium on*, Aug. 2011, pp. 676–681.

[18] J. Sanchez-Heredia, J. Valenzuela-Valdes, A. Martinez-Gonzalez, and D. Sanchez-Hernandez, "Emulation of MIMO Rician-fading environments with mode-stirred reverberation chambers," *Antennas and Propagation, IEEE Transactions on*, vol. 59, no. 2, pp. 654–660, Feb. 2011.

[19] P. Kildal, A. Hussain, X. Chen, C. Orlenius, A. Skarbratt, J. Asberg, T. Svensson, and T. Eriksson, "Threshold receiver model for throughput of wireless devices with MIMO and frequency diversity measured in reverberation chamber," *Antennas and Wireless Propagation Letters, IEEE*, vol. 10, pp. 1201–1204, 2011.

[20] C. Orlenius, C. Patane, A. Skarbratt, J. Asberg, and M. Franzen, "Analysis of MIMO OTA measurements for LTE terminals performed in reverberation chamber," in *Antennas and Propagation (EUCAP), 2012*

6th European Conference on, Mar. 2012, pp. 1934–1938.

[21] K. Rosengren, P.-S. Kildal, C. Carlsson, and J. Carlsson, "Characterization of antennas for mobile and wireless terminals in reverberation chambers: improved accuracy by platform stirring," *Microwave and Optical Technology Letters*, vol. 30, pp. 391–397, Sep. 2001.

[22] A. Azoulay, T. Letertre, V. Monebhurrun, J. Bolomey, and B. Despres, "Characterization of spurious emissions of wireless devices in a reverberation chamber," in *Electromagnetic Compatibility, 2004. EMC 2004. 2004 International Symposium on*, vol. 1, Aug. 2004, pp. 128–132.

[23] P.-S. Kildal and C. Orlenius, "Characterization of mobile terminals in Rayleigh fading by using reverberation chamber," in *Applied Electromagnetics and Communications, 2005. ICECom 2005. 18th International Conference on*, Oct. 2005, pp. 1–4.

[24] J. Chen, A. McKernan, G. W. Irwin, and W. G. Scanlon, "Experimental characterisation and analysis of wireless network control systems," in *Signals and Systems Conference, 208. (ISSC 2008). IET Irish*, Jun. 2008, pp. 238–243.

[25] P. Kildal, X. Chen, C. Orlenius, M. Franzen, and C. Patane, "Characterization of reverberation chambers for OTA measurements of wireless devices: Physical formulations of channel matrix and new uncertainty formula," *Antennas and Propagation, IEEE Transactions on*, vol. 60, no. 8, pp. 3875–3891, Aug. 2012.

[26] G. Ferrara, M. Migliaccio, and A. Sorrentino, "Characterization of GSM non-line-of-sight propagation channels generated in a reverberating chamber by using bit error rates," *Electromagnetic Compatibility, IEEE Transactions on*, vol. 49, no. 3, pp. 467–473, Aug. 2007.

[27] S. Floris, K. Remley, and C. Holloway, "Bit error rate measurements in reverberation chambers using real-time vector receivers," *Antennas and Wireless Propagation Letters, IEEE*, vol. 9, pp. 619–622, 2010.

[28] E. Genender, C. Holloway, K. Remley, J. Ladbury, G. Koepke, and H. Garbe, "Simulating the multipath channel with a reverberation chamber: Application to bit error rate measurements," *Electromagnetic Compatibility, IEEE Transactions on*, vol. 52, no. 4, pp. 766–777, Nov. 2010.

[29] P. Hallbjorner and A. Rydberg, "Maximum doppler frequency in reverberation chamber with continuously moving stirrer," in *Antennas and Propagation Conference, 2007. LAPC 2007. Loughborough*, Apr. 2007, pp. 229–232.

[30] K. Karlsson, X. Chen, P.-S. Kildal, and J. Carlsson, "Doppler spread in reverberation chamber predicted from measurements during step-wise stationary stirring," *Antennas and Wireless Propagation Letters, IEEE*, vol. 9, pp. 497–500, 2010.

[31] J.-H. Choi, J.-H. Lee, and S.-O. Park, "Characterizing the impact of moving mode-stirrers on the doppler spread spectrum in a reverberation chamber," *Antennas and Wireless Propagation Letters, IEEE*, vol. 9, pp. 375–378, 2010.

[32] X. Chen, P.-S. Kildal, and J. Carlsson, "Determination of maximum doppler shift in reverberation chamber using level crossing rate," in *Antennas and Propagation (EUCAP), Proceedings of the 5th European Conference on*, Apr. 2011, pp. 62–65.

[33] X. Chen, P.-S. Kildal, and S.-H. Lai, "Estimation of average Rician K-factor and average mode bandwidth in loaded reverberation chamber," *Antennas and Wireless Propagation Letters, IEEE*, vol. 10, pp. 1437–1440, 2011.

[34] C. Lemoine, E. Amador, and P. Besnier, "On the K-factor estimation for Rician channel simulated in reverberation chamber," *Antennas and Propagation, IEEE Transactions on*, vol. 59, no. 3, pp. 1003–1012, Mar. 2011.

[35] C. Lemoine, E. Amador, P. Besnier, J. Sol, J.-M. Floc'h, and A. Laisne, "Statistical estimation of antenna gain from measurements carried out in a mode-stirred reverberation chamber," in *General Assembly and Scientific Symposium, 2011 XXXth URSI*, Aug. 2011, pp. 1–4.

[36] X. Chen and P.-S. Kildal, "Comparison of RMS delay spread and decay time measured in reverberation chamber," in *Antennas and Propagation (EuCAP), 2010 Proceedings of the Fourth European Conference on*, Apr. 2010, pp. 1–3.

[37] C. Holloway, H. Shah, R. Pirkl, K. Remley, D. Hill, and J. Ladbury, "Early time behavior in reverberation chambers and its effect on the relationships between coherence bandwidth, chamber decay time, RMS delay spread, and the chamber buildup time," *Electromagnetic Compatibility, IEEE Transactions on*, vol. 54, no. 4, pp. 714–725, Aug. 2012.

[38] A. Coates, A. Duffy, K. Hodge, and A. Willis, "Investigating electromagnetic exposure of communication cables in reverberant chambers," in *Electromagnetic Compatibility, 2002. EMC 2002. IEEE International Symposium on*, vol. 1, Aug. 2002, pp. 233–237.

[39] R. De Leo, V. Primiani, F. Moglie, and A. Pastore, "SAR numerical analysis of the whole human body exposed to a random field," in *Electromagnetic Compatibility, 2009. EMC 2009. IEEE International*

Symposium on, Aug. 2009, pp. 81–86.

[40] K. Harima, "Estimation of power absorbed by human body using reverberation chamber," in *Electromagnetic Compatibility (EMC), 2012 IEEE International Symposium on*, Aug. 2012, pp. 39–43.

[41] E. Genender, C. Holloway, K. Remley, J. Ladbury, G. Koepke, and H. Garbe, "Use of reverberation chamber to simulate the power delay profile of a wireless environment," in *Electromagnetic Compatibility-EMC Europe, 2008 International Symposium on*, Sep. 2008, pp. 1–6.

[42] G. L. Stüber, *Principles of Mobile Communication (2nd Edition)*. Boston: Kluwer Academic, 2001.

[43] R. Vaughan and J. B. Andersen, *Channels, propagation and antennas for mobile communications*. London, UK: IEE electromagnetic wave series, No. 50, 2003.

[44] J. D. Parsons, *The Mobile Radio Propagation Channel, 2nd*. New York: John Wiley & Sons, 2000.

[45] L. Greenstein, D. Michelson, and V. Erceg, "Moment-method estimation of the Ricean K-factor," *Communications Letters, IEEE*, vol. 3, no. 6, pp. 175–176, Jun. 1999.

[46] G. Azemi, B. Senadji, and B. Boashash, "Estimating the Ricean K-factor for mobile communication applications," in *Signal Processing and Its Applications, 2003. Proceedings. Seventh International Symposium on*, vol. 2, Jul. 2003, pp. 311–314.

[47] C. Tepedelenlioglu, A. Abdi, and G. Giannakis, "The Ricean K factor: estimation and performance analysis," *Wireless Communications, IEEE Transactions on*, vol. 2, no. 4, pp. 799–810, Jul. 2003.

[48] Y. Chen and N. C. Beaulieu, "Maximum likelihood estimation of the K factor in Ricean fading channels," *IEEE Communications Letters*, vol. 9, no. 12, pp. 1040–1042, 2005.

[49] K. Baddour and T. Willink, "Improved estimation of the Ricean K-factor from I/Q fading channel samples," *IEEE Transactions on Wireless Communications*, vol. 7, no. 12, pp. 5051–5057, 2008.

[50] M. Andries, P. Besnier, and C. Lemoine, "Rician channels in a RC: Statistical uncertainty of K estimations versus K fluctuations due to unstirred paths," in *Antennas and Propagation (EUCAP), Proceedings of the 5th European Conference on*, Apr. 2011, pp. 1758–1762.

[51] D. A. Hill, M. T. Ma, A. R. Ondrejka, B. F. Riddle, M. Crawford, and R. T. Johnk, "Aperture excitation of electrically large, lossy cavities," *IEEE Transactions on Electromagnetic Compatibility*, vol. 36, no. 3, pp. 169–178, Aug. 1994.

[52] X. Chen and P.-S. Kildal, "Theoretical derivation and measurements of the relationship between coherence bandwidth and RMS delay spread in reverberation chamber," in *Antennas and Propagation, 2009. EuCAP 2009. 3rd European Conference on*, Mar. 2009, pp. 2687–2690.

[53] J. A. Stratton, *Electromagnetic Theory*. McGraw-Hill, 2006, vol. 51, no. 1312. [Online]. Available: http://usir.salford.ac.uk/3420/

[54] A. Papoulis and S. Pillai, *Probability, random variables, and stochastic processes*, ser. McGraw-Hill electrical and electronic engineering series. McGraw-Hill, 2002. [Online]. Available: http://books.google.fr/books?id=YYwQAQAAIAAJ

[55] E. M. Purcell, "A method for measuring the absolute gain of microwave antennas," Radiation Laboratory, Massachusetts Institute of Technology, Tech. Rep. 41-9, 1943.

[56] Z. Wu, "Effect of mismatch on antenna gain measurement by purcell's method," *Electronics Letters*, vol. 22, no. 10, pp. 522–524, Aug. 1986.

[57] J. Glimm, R. Harms, K. Munter, M. Spitzer, and R. Pape, "A single-antenna method for traceable antenna gain measurement," *Electromagnetic Compatibility, IEEE Transactions on*, vol. 41, no. 4, pp. 436–439, Nov. 1999.

[58] M. Schwartz, W. R. Bennett, and S. Stein, *Communication systems and techniques*. McGraw-Hill, New York, 1966.

[59] P.-S. Kildal, K. Rosengren, J. Byun, and J. Lee, "Definition of effective diversity gain and how to measure it in a reverberation chamber," *Microwave and Optical Technology Letters*, vol. 34, pp. 56–59, Jul. 2002.

Abstract

The testing of wireless devices is generally done using numerical simulations or channel sounders. Though a reverberation chamber does not reflect a real transmission environment, its properties can also be appropriately modified to emulate one. This emulation may be achieved thanks to various parameters. Our PhD thesis has been devoted to analyze and implement several techniques to measure and control these parameters inside reverberation chambers.

First we evaluate different K-factor estimators and their capabilities. We present the useful limits in which several complex, phase and envelope K-factor estimators can be used. Then, we propose two new envelope-based estimators improving the useful range of detectable values of K-factor.

One of the possibilities to control a propagation channel inside a reverberation chamber is to use absorbing materials. We present a method to estimate the average absorbing cross section by using only one antenna. This is done with measurements of coherence bandwidth of the channel. Then, we extend our analysis to predict the average absorbing cross section when we know the physical dimensions of a parallelepiped absorber as well its electromagnetic properties.

Next, we create a model of the reverberation chamber propagation channel using the transient regime and steady state of the signal. With this model, depending on the available information, we can extract the K-factor, the average absorbing cross section and different time spreads parameters (i.e., mean delay spread and the root mean square delay spread).

We continue with two possible applications of the reverberation chamber. First, we evaluate the gain of an antenna from only the measurement of reflection coefficient. We extend our analysis to the evaluation of antenna pattern and its estimation errors. We also estimate the antenna mismatch and half power beamwidth. The second application deals with the evaluation of the diversity gain in reverberation chamber. We isolate the effects on the diversity gain due to different antenna efficiencies, stirred powers and K-factors. Then, we estimate a simple relation of the power correlation as a function of the complex correlation when the K-factors on different branches are not identical. We show that using an envelope/power correlation as a criterion to characterize the diversity may bias the conclusions without taking into account other parameters. Using statistical simulations we compare the measured diversity gain with the simulated values.

List of acronyms and abbreviations

AACS	average absorbing cross section
AoA	angles-of-arrival
APS	average projected surface
AR	autoregressive
AUT	antenna under test
AWG	arbitrary waveform generator
BER	bit error rate
CB	coherence bandwidth
CI	confidence interval
CLT	central limit theorem
CRLB	Cramer Rao lower bound
CZT	Chirp Z transform
DOF	degrees of freedom
DSO	digitally storage oscilloscope
DSP	digital signal processor
EM	electromagnetic
EMC	electromagnetic compatibility
EPC	emulation of propagation channels
FFT	Fast Fourier Transform
I	imaginary component

i.i.d.	independent and identically distributed
IR	impulse response
LUF	lowest usable frequency
MLE	maximum likelihood estimation
MSE	Mean squared error
NFC	near field chamber
pdf	probability density function
PDP	power delay profiles
R	real component
RC	reverberation chamber
RMS	root mean square
RMSE	root mean square error
SNR	signal to noise ratio
VNA	vector network analyzer

Contents

I Introduction and channel description in reverberation chamber 1

1 Introduction and description of the work 3
- 1.1 Introduction . . . 3
- 1.2 Working context . . . 4
- 1.3 Overview of reverberation chambers . . . 4
- 1.4 Description of this thesis . . . 8
- References . . . 10

2 Overview of propagation channels inside the mode-stirred reverberation chamber 13
- 2.1 Friis propagation model . . . 15
- 2.2 Two fading models . . . 15
  - 2.2.1 Representation of a signal with Rayleigh fading . . . 15
  - 2.2.2 Representation of a Rician fading signal . . . 16
- 2.3 Overview on channel measurements in reverberation chamber . . . 18
- 2.4 Conclusions . . . 26
- References . . . 28

II Estimating channel parameters 29

3 Rician K-factor estimators 33
- 3.1 Introduction . . . 33
- 3.2 Methods to estimate K-factor . . . 34
  - 3.2.1 Classification of methods . . . 34
  - 3.2.2 Selection of different methods to compute K-factor . . . 35
  - 3.2.3 Validation of the methods . . . 37
  - 3.2.4 The necessity of new estimators: two extreme situations . . . 45
- 3.3 Our proposal for new K-factor estimators . . . 46
  - 3.3.1 A simple approximation . . . 47
  - 3.3.2 A maximum-likelihood approximation . . . 51
  - 3.3.3 Conclusion . . . 60
- References . . . 62

4 Estimating the average absorbing cross section to control propagation channels 65
- 4.1 Introduction . . . 65
- 4.2 Estimating the average absorbing cross section from measurements in reverberation chamber . . . 67
  - 4.2.1 Transfer function of the channel used as input data . . . 67
  - 4.2.2 Average absorbing cross section in frequency domain from the coherence bandwidth . . . 68
- 4.3 Prediction of the average absorbing cross section of the parallelepiped absorbers . . . 69
- 4.4 Validation of the method . . . 73
  - 4.4.1 Experimental setup . . . 73

4.4.2 Data processing and results . . . 74
4.5 Conclusions . . . 79
References . . . 80

5 Simultaneous control of emulated propagation channel parameters 81
5.1 Introduction . . . 81
5.2 Signal model . . . 81
5.2.1 Hypothesis . . . 81
5.2.2 Defining the "steady state time" . . . 85
5.3 Relating K-factor with various time parameters . . . 86
5.3.1 K-factor as a function of time parameters . . . 86
5.3.2 Time parameters: τ_{μ} and τ_{rms} as functions of K-factor . . . 86
5.3.3 Parameters for a loaded chamber . . . 88
5.4 Validation . . . 91
5.4.1 Measurements and Simulations scenario . . . 91
5.4.2 Results . . . 96
5.5 Conclusions . . . 101
References . . . 102

III Applications 103

6 Evaluation of antenna parameters in reverberation chamber 107
6.1 Introduction . . . 107
6.2 The Method . . . 108
6.2.1 Gain estimation from a single transmitting-receiving antenna . . . 108
6.2.2 Estimating propagation distance . . . 109
6.3 Data processing and Results . . . 113
6.3.1 Extracting antenna mismatch $S_{11_{\text{FS}}}$ . . . 113
6.3.2 Estimating the free-space transfer function of the channel $H_{\text{FS}}(0,0)$ . . . 116
6.3.3 Estimating antenna gain G . . . 117
6.3.4 Evaluation of antenna pattern . . . 121
6.4 Conclusions . . . 123
References . . . 125

7 Diversity gain for Rician and Rayleigh environments in reverberation chamber 127
7.1 Introduction . . . 127
7.2 Computing the diversity gain . . . 128
7.3 Linear diversity combining techniques . . . 129
7.4 Definitions of the diversity gain . . . 130
7.5 Methods to combine the signals for diversity gain . . . 131
7.5.1 For maximal-ratio combining . . . 131
7.5.2 For selection combining . . . 131
7.5.3 For equal-gain combining . . . 132
7.5.4 Other algorithms . . . 132
7.6 Parameters which may influence diversity gain . . . 132
7.6.1 Mutual coupling between antennas: radiation efficiency and mismatch . . . 132
7.6.2 The Ricean parameter K . . . 133
7.6.3 Power Imbalance . . . 133
7.6.4 Branch correlation . . . 134
7.7 Results . . . 137
7.7.1 Simulations . . . 137
7.7.2 Measurements . . . 144
7.7.3 Diversity gain in simulations and measurements . . . 156
7.8 Conclusions . . . 158

References . . . 159

IV Conclusions and future work 161

8 General conclusion and future work 163
8.1 General Conclusion . . . 163
8.2 Future work . . . 164
8.2.1 Better separation between the direct unstirred components and secondary unstirred components . . . 164
8.2.2 Shadowing control in reverberation chamber . . . 164
8.2.3 Clusters control in reverberation chamber . . . 165
8.2.4 Methodology for a complete communication link testing in reverberation chamber 165

Publications 167

Appendix 171

Appendix A About random variables and some distribution functions. 173
A.1 The joint probability density function of the fading envelope and the fading phase . . . 174
A.2 The probability density function of the fading phase . . . 174
A.3 Rayleigh distribution . . . 175
A.4 Rician distribution . . . 175
A.5 The probability density function of the fast varying instantaneous power . . . 176
A.6 The probability density function of the shadowing fading envelope . . . 176
A.7 Gaussian Distribution . . . 177
A.8 Weibull Distribution . . . 177
A.9 Chi-square Distribution . . . 178
A.10 F-distribution . . . 178
A.11 Relations between distributions . . . 178

Appendix B Basic elements of the statistical estimation 181
B.1 Correlation and covariance . . . 181
B.2 Central Limit Theorem . . . 182
B.3 Independent variables . . . 182
B.4 Biased/Unbiased estimators . . . 183
B.5 (Root) Mean Squared Error . . . 183
B.6 Asymptotic Variance of an Estimator . . . 184
B.7 Cramer-Rao bound . . . 184
B.8 Maximum Likelihood Estimation . . . 184

Appendix C Standard Functions 185
C.1 Bessel Functions . . . 185
C.2 Gamma Function . . . 186
C.3 Gauss error function . . . 187
C.4 Laguerre polynomials . . . 187

Appendix D Frequency to time transformation 189
D.1 Basics of samplings in frequency and time domain . . . 189
D.2 Inverse CZT transform function . . . 189

Appendix E 3D generation of the absorbers 195

References 198

List of Figures 199

List of Tables 203

Part I

Introduction and channel description in reverberation chamber

CHAPTER 1

Introduction and description of the work

1.1 Introduction

In the past decade wireless applications have become more and more present in everyday life. Different types of environments, e.g., home, offices, parks, public places, etc. influence the propagation channels and in consequence the quality of transmission. Due to the multiple paths links between transmitter and receiver caused by reflections, diffraction and scatterings, the received signal is composed of a sum of complex signals with various amplitudes, phases, and Doppler frequency shifts. The direct effect over the envelope and the phase of the received signal is constituted by rapid fluctuations, which are called multipath fading. The envelope fluctuations are modeled as a random process with Rayleigh distribution for example (or more generally Weibull distribution) when a specular component does not exist, or with Rice distribution (or Rice-Nakagami distribution in a more general case) in the presence of a specular component [1, 2]. Even if the transmitter is out of sight, the around motionless objects may scatter the waves, generating specular components at receiver site. We consider as specular components all the paths which are not affected by the statistics of the fading and which remain constant for large time intervals. In most of the cases the fading will negatively influence the quality of a wireless transmission. The quality of communication link requires a good knowledge of propagation channels. A well operating communication system always need controlled parameters to adapt itself to transmission conditions. Some of these parameters are signal to noise ratio, mean and delay spread, coherence bandwidth, coherence time, Doppler spectrum, K-factor, etc.
For a successful implementation of an integrated communication system testing and optimization are two key factors. Several transmission parameters have to be accurately studied before any final product can be validated. Designing and testing wireless devices used in any type of environment can be done using numerical simulations or channel sounders. Another solution requires a reliable, controllable, and repeatable facility having similar characteristics as those found in a real propagation channel. One such environment is the reverberation chamber (RC).

1.2 Working context

This thesis deals with the emulation of propagation channels in reverberation chamber, in particular typical urban and indoor femto-cell channels. It is done in the framework of the ANR project METAPHORT involving several laboratories from France (IFSTTAR Lille, LABSTIC Brest, XLIM Poitiers, IEF Paris, IETR Rennes) associated with ALSTOM, and whose aim is to improve the communication links between the base stations and trains during their passage through tunnels [3, 4]. This environment is strongly affected by fading due to reflections with the tunnel walls and high degree of electromagnetic absorption [5, 6]. In this context, the reverberation chamber has the role to emulate the multifading absorbing environment found in tunnels [7].

1.3 Overview of reverberation chambers

Reverberation chambers consist of an oversized metallic shielded enclosure (i.e., made from steel or aluminum) in which the field distribution corresponds to a standing wave pattern according to the excitation of resonant cavity modes.

Resonance frequency

The resonant cavity modes of a parallelepiped chamber are characterized by their bandwidth and resonant frequencies. For an empty cavity, these modes are present whenever [8]:

$$k = \pi\sqrt{\left(\frac{m}{d_1}\right)^2 + \left(\frac{n}{d_2}\right)^2 + \left(\frac{p}{d_3}\right)^2}, \tag{1.1}$$

where the parameter k is the wavenumber:

$$k = \frac{2\pi}{\lambda}, \tag{1.2}$$

and the parameters $m = 0, 1, 2, \cdots$, $n = 0, 1, 2, \cdots$ and $p = 0, 1, 2, \cdots$ (at least two of these parameters are different from zero) while d_1, d_2, and d_3 are the dimensions of the chamber. The parameter c is the speed of light and λ is the wavelength. Equivalent to (1.1), the resonant frequency f_{mnp} is defined by:

$$f_{mnp} = \frac{c}{2}\sqrt{\left(\frac{m}{d_1}\right)^2 + \left(\frac{n}{d_2}\right)^2 + \left(\frac{p}{d_3}\right)^2}. \tag{1.3}$$

Operating modes in reverberation chamber are TE or TM. The first resonant frequency corresponds to mode TM_{110}, TE_{011} or TE_{101}. The excitation of a set of cavity modes result in a particular pattern of standing waves.
Compared to an ideal reverberation chamber with perfectly conducting walls, due to conductivity losses in chamber (i.e., on walls, antennas, cables, etc.) the modes are no more discrete but defined in a frequency bandwidth Δf. It results that every resonances have a finite Q factor corresponding to a finite bandwidth Δf. The quality factor of the ith mode is then computed as $Q_i = f_i/\Delta f_i$. For an appropriate excitation of resonant modes in a reverberation chamber, the signal frequency should be higher than the lowest cutoff frequency of the nearest

TE or TM mode (ideally it should be the resonant frequency of the mode). It means that all the resonances which are in the range $\left[f_{mnp} - \frac{\Delta f}{2}; f_{mnp} + \frac{\Delta f}{2}\right]$ will be excited in a significant way by this wave [9]. If the chamber is operated at a frequency less than the cutoff frequency of the chamber mode then the wave is more or less spread in the vicinity of the source. For the same resonant frequency it may be several modes, resulting in overlapped modes.

Density of modes

For a general reverberating cavity whose volume is $V = d_1 d_2 d_3$, a smoothed approximation of the total number of modes starting from the first resonant frequency until a frequency f may be approximated with [10]:

$$N(f) \approx \frac{8\pi V}{3\lambda^3}, \tag{1.4}$$

For the parallelepiped cavity as the one we use in our measurements, the smoothed approximation of the number of modes N becomes [10]:

$$N(f) \approx \frac{8\pi V}{3\lambda^3} - (d_1 + d_2 + d_3)\frac{1}{\lambda} + \frac{1}{2}. \tag{1.5}$$

For high frequencies and dimensions of the chamber greater than a half wavelength (1.5) converges to (1.4). When the number of modes is small the accuracy (the repeatability) of measurements is low [9]. It is possible to increase the number of modes by increasing the working frequency or the chamber volume. With (1.4) the mode density, which indicates the number of modes that can be excited over a unit bandwidth and is an indicator of the separation between the modes, is given by:

$$n(f) \approx \frac{\mathrm{d}\,N(f)}{\mathrm{d}\,f} \approx \frac{8\pi f^2 V}{c^3} - \frac{d_1 + d_2 + d_3}{c} \overset{\text{at high frequencies}}{=} \frac{8\pi f^2 d_1 d_2 d_3}{c^3}, \tag{1.6}$$

In a high mode density region, it is highly probable to excite several of modes through a stirring process. The random weighting of a number of these modes provides the random-like field.

Random field

The random behavior of the electromagnetic field distribution at one point in the test volume of the chamber can be obtained through a mechanical stirring process using a rotating metallic paddle moving either continuously or in a stepped-mode. Other solutions are to move the antennas, to change the polarization, to vary the frequency in a small bandwidth, etc. The stirring process will cause the change of modal excitations due to modification of boundary conditions (either if it is due to modifications of the physical dimensions of the chamber or varying the frequency of the source), thus increasing the number and configuration of excited modes. The average field in a well operated reverberation chamber (over the stirring process) is considered as being statistically isotropic and homogeneous in a limited volume of the chamber. The field inside reverberation chamber can be described in terms of its plane wave spectrum [8].

Utility of reverberation chambers

Originally, reverberation chambers were used as test facilities for electromagnetic compatibility (EMC) testing [11]. In a stirred configuration, the statistical properties of reverberation chamber correspond to propagation environments with multipath fading (i.e., Rician, Rayleigh, etc.). As the reverberation chamber is a tool to create a diffuse electromagnetic field, new functionalities of this environment were found such as: antenna characterization (i.e., antenna efficiency, antenna gain, etc.) [12–16], the emulation of wireless environments with Rayleigh and Rician fading are analyzed in [11, 17–22], the evaluation of the performances of MIMO systems and the diversity gain [23–28], characterization of wireless devices and their quality of emission [29–33], bit error rate (BER) measurements [34–36], Doppler effect [37–40], measurement of K-factor [26, 41–43], channel time parameter [44, 45], human body exposure to electromagnetic waves [46–48], etc. Moreover, because it is a closed environment the reverberation chamber can isolate the artificial propagation channels from other issues (i.e., slow fading, Doppler effect, etc.). It results that a reverberation chamber is a simple low cost controllable environment which can be used for the artificial reproduction of propagation channels giving the capacity to test wireless systems especially those affected by strong fading [20, 24, 49].

As for a real environment, the rich density of multipath reflections inside reverberation chamber creates a power delay profile (PDP) which decays exponentially with time. Still, reverberation chambers can be seen as a very special case of indoor environment since chamber metallic walls are made up of highly conducting materials (very high reflection coefficient) whereas various elements (walls, vegetation, etc.) in realistic scenarios introduce losses. Modifications into reverberation chambers are therefore necessary to introduce losses. Also, in real environments (i.e., where reflecting structures may be located far from the receiver, or when there is a high degree of loss) it is possible to find clusters of discrete reflections or specular components that are not present in reverberation chamber. It results that the wireless channels created in reverberation chamber under a conventional configuration, as for EMC testing, may not be appropriate to emulate some propagation environments. However, a simple way to modify the properties of reverberation chamber is to use absorbing materials [36]. Also, components that cannot be obtained directly in reverberation chamber may be added artificially using fading simulators [50, 51].

Comparison between electromagnetic compatibility testing and emulation of propagation channels in reverberation chamber

Comparing the functionality of reverberation chambers for EMC testing and for emulation of propagation channels (EPC) some differences can be identified:

- The distribution of energy in the chamber: For an EMC testing all the energy injected into the chamber is contained in the scattered component, while for EPC, in general, the energy is distributed between specular and scattered components.

- The working frequency bandwidth: In EMC testing the measurements are done in a narrow bandwidth and at various frequencies with a step of some MHz. Depending on the transmission system, the measurements for EPC may be done in a narrow or broad frequency bandwidth.

- Domain of measures: The EMC analyses are usually done in a frequency domain, while for the EPC one may use the frequency or time domain to characterize a propagation channel.

- Reverberation chamber electromagnetic model: For an EMC environment, the model to characterize the reverberation chamber is often an ideal model in which the density of modes of the cavity is infinite requesting that the working frequency should be high (see 1.6). In EPC, due to complexity of environments it is necessary to include various parameters to recreate a transmission environment.

- Experiments independence: In order to have results with the lowest uncertainty, the EMC testings must use independent measurements between successive observations (see annex B.3). For the EPC the temporal autocorrelation is an important feature of the channel and it may become necessary to have a partial correlation between realizations.

In this thesis we use a large reverberation chamber whose dimensions are: 8.7 m length, 3.7 m wide, 2.9 m high made from anodized aluminum, for various configurations. The mechanical stirrer is used to create a statistical distribution of the electromagnetic field, while frequency stirring expands this distribution increasing the number of trials. In some situations several antenna positions are also used to increase the number of realizations.

Statistics of reverberating environments without any specular components

The main property of the reverberation chamber is the statistical uniformity and isotropy of the average electric field in the working volume of the cavity. This uniformity is assured by a high density of modes which for any chamber is guaranteed over a, not always well defined, minimum lowest usable frequency (LUF). For the reverberation chamber we use in this thesis the LUF is around 250 MHz. Even so, high power goodness-of-fit tests in this reverberation chamber have shown that the statistics of a rectangular component of the electric field follow a Rayleigh distribution (in a non-line-of-sight configuration) above a frequency of 750 MHz [52] while below this frequency the distribution becomes Weibull which is a more general case than Rayleigh. In this thesis the reverberation chamber is used from 1 GHz up to 9 GHz.
In Table 1.1 are presented the ideal distributions of several parameters when there is no line-of-sight between the transmitter and the receiver [53]. Any deviation from these distributions may be due to the modifications of measurements (e.g., using a line-of-sight configuration) or because the quality factor is highly modified (and the uniformity of the field is no more guaranteed).
In this table,

- $\star$ corresponds to real (R) or imaginary component (I);

- $\star$ represents a rectangular component of the field which can be x, y or z;

- $E_{\star,\mathrm{R}}$ and $E_{\star,\mathrm{I}}$ represents the real and imaginary parts of a rectangular component of the electric field, which may be the electric field on the axis x, y or z;

- $E_{\star} = \sqrt{E_{\star,\mathrm{R}}^2 + E_{\star,\mathrm{I}}^2}$ is the absolute value of a rectangular component of the electric field in direction x, y or z;

- $E_{\mathrm{T}} = \sqrt{E_{\mathrm{x}}^2 + E_{\mathrm{y}}^2 + E_{\mathrm{z}}^2}$ represents the total electric field component.

With the emergence of specular components (e.g., due to a line-of-sight configuration), the statistics of electric field will change to noncentral distributions or to other distributions than the one presented in Table 1.1 as they will be presented later in this thesis.

Table 1.1: Statistical distributions of several electric field components and their pdf measured in reverberation chamber in an EMC configuration.

Parameter	**Statistical distribution and pdf**
$E_{\star,\mathrm{R}}$ and $E_{\star,\mathrm{I}}$	Gaussian, $f(E_{\star,\star}) = \frac{1}{\sigma\sqrt{2\pi}} e^{-\frac{1}{2}\frac{E_{\star,\star}^2}{\sigma^2}}$
$E_\star$	Rayleigh $(\chi, 2\,\mathrm{DOF}^1)$, $f(E_\star) = \frac{E_\star}{\sigma^2} e^{-\frac{E_\star^2}{2\sigma^2}}$
$E_\star^2$	exponential $(\chi^2, 2\,\mathrm{DOF})$, $f(E_\star^2) = \frac{1}{2\sigma^2} e^{-\frac{E_\star^2}{2\sigma^2}}$
E_T	chi $(\chi, 6\,\mathrm{DOF})$, $f(E_\mathrm{T}) = \frac{E_\mathrm{T}^5}{8\sigma^6} e^{-\frac{E_\mathrm{T}^2}{2\sigma^2}}$
E_T^2	chi square $(\chi^2, 6\,\mathrm{DOF})$, $f(E_\mathrm{T}) = \frac{E_\mathrm{T}^4}{16\sigma^6} e^{-\frac{E_\mathrm{T}^2}{2\sigma^2}}$

[1] degrees of freedom.

1.4 Description of this thesis

The objectives of this thesis are to characterize the wireless propagation channels in reverberation chamber, to model these channels, especially for multi-antenna systems, and finally to emulate propagation channels as found in real environments. In order to consider the reverberation chamber as a mean to reproduce the characteristics of a wireless channel found in a real environment it is important to identify the adjustable parameters in the reverberation chamber. These parameters are successively investigated making comparisons between the proposed models and measurement results in reverberation chamber.
The first part of this thesis gives a short introduction about the working environment (the reverberation chamber) and the statistics of different parameters as they are usually measured in reverberation chamber. In chapter 2 we extend our analysis to propagation channels. First, we describe the basics of the propagation in free-space (which may be used to characterize the propagation of specular components) and two fading models which are later used in this thesis. Next we present an overview over different types of measurements in reverberation chamber in time and frequency domains, to give an idea on the propagation channels measured in this environment.
The second part of this thesis analyzes different channel parameters and the solution to estimate, measure and control them. Chapter 3 discusses different methods to estimate K-factor and their limitations. We propose two new estimators which increase the useful range of K values. Next, in chapter 4 the degree of absorption for parallelepiped absorbers is analyzed.

Then, a method to estimate the average absorbing cross section from the coherence bandwidth and a simple model to predict this parameter are presented. In the last chapter of this part, chapter 5, we propose a model in time domain in order to extract different channel parameters and control them simultaneously. We test different measurement configurations, considering different levels of K-factor and degrees of absorption.
In the third part of this thesis we present two applications. The first application is an evaluation of antenna parameters in reverberation chamber. The second application analyzes the improvements, when using diversity techniques, over the propagation channels for the multiple-antennas systems. We examine the diversity gain in the presence of power imbalance and correlation especially for the Rician fading situation.
This thesis ends with some conclusions and work perspectives. Moreover, a list of publications associated with these the three years of thesis is presented and an annex describes different parameters used in this manuscript.

Bibliography

[1] G. L. Stüber, *Principles of Mobile Communication (2nd Edition)*. Boston: Kluwer Academic, 2001.

[2] R. Vaughan and J. B. Andersen, *Channels, propagation and antennas for mobile communications*. London, UK: IEE electromagnetic wave series, No. 50, 2003.

[3] M. Lienard, P. Degauque, and P. Laly, "Communication and distance measurement in subway tunnels using natural propagation," in *Devices, Circuits and Systems, 2004. Proceedings of the Fifth IEEE International Caracas Conference on*, vol. 1, 2004, pp. 240–243.

[4] D. Dudley, M. Lienard, S. Mahmoud, and P. Degauque, "Wireless propagation in tunnels," *Antennas and Propagation Magazine, IEEE*, vol. 49, no. 2, pp. 11–26, 2007.

[5] M. Lienard, S. Betrencourt, and P. Degauque, "Theoretical and experimental approach of the propagation at 2.5 ghz and 10 ghz in straight and curved tunnels," in *Vehicular Technology Conference, 1999. VTC 1999 - Fall. IEEE VTS 50th*, vol. 4, 1999, pp. 2268–2271 vol.4.

[6] M. Lienard and P. Degauque, "Propagation in road tunnels: from modeling to experiments," in *Devices, Circuits and Systems, 2002. Proceedings of the Fourth IEEE International Caracas Conference on*, 2002, pp. T011–1–T011–4.

[7] O. Delangre, P. De Doncker, M. Lienard, D. Gaillot, and P. Degauque, "Mimo channel emulator based on reverberation chambers," in *Intelligent Transport Systems Telecommunications,(ITST),2009 9th International Conference on*, 2009, pp. 42–44.

[8] D. A. Hill, *Electromagnetic Fields in Cavities: Deterministic and Statistical Theories*, I. Press, Ed. Wiley/IEEE Press, Piscataway, NJ, 2009.

[9] K. Rosengren and P.-S. Kildal, "Study of distributions of modes and plane waves in reverberation chambers for the characterization of antennas in a multipath environment," *Microwave and Optical Technology Letters*, vol. 30, no. 6, pp. 386–391, 2001. [Online]. Available: http://dx.doi.org/10.1002/mop.1323

[10] B. Liu, D. Chang, and M. Ma, *Eigenmodes and the Composite Quality Factor of a Reverberating Chamber*, ser. NBS Technical Note. National Bureau of Standards, 1983. [Online]. Available: http://books.google.fr/books?id=e70AHAAACAAJ

[11] G. Koepke and J. Ladbury, "New electric field expressions for EMC testing in a reverberation chamber," in *Digital Avionics Systems Conference, 1998. Proceedings., 17th DASC. The AIAA/IEEE/SAE*, vol. 1, Oct. 1998, p. 53.

[12] M. Piette, "Antenna radiation efficiency measurements in a reverberation chamber," in *Radio Science Conference, 2004. Proceedings. 2004 Asia-Pacific*, Aug. 2004, pp. 19–22.

[13] K. Rosengren and P.-S. Kildal, "Radiation efficiency, correlation, diversity gain and capacity of a six-monopole antenna array for a MIMO system: theory, simulation and measurement in reverberation chamber," *Microwaves, Antennas and Propagation, IEE Proceedings*, vol. 152, no. 1, pp. 7–16, Feb. 2005.

[14] G. Le Fur, P. Besnier, and A. Sharaiha, "Efficiency measurement of UWB antennas using time reversal in reverberation chambers," *Electronics Letters*, vol. 44, no. 17, pp. 1002–1003, 2008.

[15] C. Rizzo, M. Franzen, and M. Andersson, "Fast measurements with high repeatability of antenna efficiency and over the air (ota) parameters in reverberation chambers," in *Antennas Propagation Conference, 2009. LAPC 2009. Loughborough*, Nov. 2009, pp. 777–780.

[16] H. Krauthauser and M. Herbrig, "Yet another antenna efficiency measurement method in reverberation chambers," in *Electromagnetic Compatibility (EMC), 2010 IEEE International Symposium on*, Jul. 2010, pp. 536–540.

[17] D. A. Hill, "Electromagnetic theory of reverberation chambers," National Institute of Standards and Technology (NIST), Note 1506, 1998.

[18] J. M. Ladbury, G. H. Koepke, and D. Camell, "Evaluation of the NASA Langley Research Center mode-stirredchamber facility," United States Department of Commerce, NIST Tech. Note 1508, Jan. 1999.

[19] K. Rosengren, P. Bohlin, and P.-S. Kildal, "Multipath characterization of antennas for MIMO systems in reverberation chamber including effects of coupling and efficiency," in *Antennas and Propagation Society International Symposium, 2004. IEEE*, vol. 2, Jun. 2004, pp. 1712–1715.

[20] C. Holloway, D. Hill, J. Ladbury, P. Wilson, G. Koepke, and J. Coder, "On the use of reverberation chambers to simulate a Rician radio environment for the testing of wireless devices," *Antennas and Propagation, IEEE Transactions on*, vol. 54, no. 11, pp. 3167–3177, Nov. 2006.

[21] J. F. Valenzuela-Valdes, M. A. Garcia-Fernandez, A. M. Martinez-Gonzalez, and D. Sanchez-Hernandez, "Non-isotropic scattering environments with reverberation chambers," in *Antennas and Propagation, 2007. EuCAP 2007. The Second European Conference on*, Edinburgh, 2007, pp. 1–4.

[22] O. Delangre, P. De Doncker, F. Horlin, M. Lienard, and P. Degauque, "Reverberation chamber envi-

ronment for testing communication systems: Applications to ofdm and sc-fde," in *Vehicular Technology Conference, 2008. VTC 2008-Fall. IEEE 68th*, 2008, pp. 1–5.

[23] P.-S. Kildal and K. Rosengren, "Correlation and capacity of MIMO systems and mutual coupling, radiation efficiency, and diversity gain of their antennas: simulations and measurements in a reverberation chamber," *IEEE Communications Magazine*, vol. 2, pp. 104–112, Dec. 2004.

[24] J. F. Valenzuela-Valdes, A. M. Martinez-Gonzalez, and D. A. Sanchez-Hernandez, "Emulation of MIMO nonisotropic fading environments with reverberation chambers," *IEEE Antennas and Wireless Propagation Letters*, vol. 7, pp. 325–328, 2008.

[25] K. Remley, H. Fielitz, H. Shah, and C. Holloway, "Simulating MIMO techniques in a reverberation chamber," in *Electromagnetic Compatibility (EMC), 2011 IEEE International Symposium on*, Aug. 2011, pp. 676–681.

[26] J. Sanchez-Heredia, J. Valenzuela-Valdes, A. Martinez-Gonzalez, and D. Sanchez-Hernandez, "Emulation of MIMO Rician-fading environments with mode-stirred reverberation chambers," *Antennas and Propagation, IEEE Transactions on*, vol. 59, no. 2, pp. 654–660, Feb. 2011.

[27] P. Kildal, A. Hussain, X. Chen, C. Orlenius, A. Skarbratt, J. Asberg, T. Svensson, and T. Eriksson, "Threshold receiver model for throughput of wireless devices with MIMO and frequency diversity measured in reverberation chamber," *Antennas and Wireless Propagation Letters, IEEE*, vol. 10, pp. 1201–1204, 2011.

[28] C. Orlenius, C. Patane, A. Skarbratt, J. Asberg, and M. Franzen, "Analysis of MIMO OTA measurements for LTE terminals performed in reverberation chamber," in *Antennas and Propagation (EUCAP), 2012 6th European Conference on*, Mar. 2012, pp. 1934–1938.

[29] K. Rosengren, P.-S. Kildal, C. Carlsson, and J. Carlsson, "Characterization of antennas for mobile and wireless terminals in reverberation chambers: improved accuracy by platform stirring," *Microwave and Optical Technology Letters*, vol. 30, pp. 391–397, Sep. 2001.

[30] A. Azoulay, T. Letertre, V. Monebhurrun, J. Bolomey, and B. Despres, "Characterization of spurious emissions of wireless devices in a reverberation chamber," in *Electromagnetic Compatibility, 2004. EMC 2004. 2004 International Symposium on*, vol. 1, Aug. 2004, pp. 128–132.

[31] P.-S. Kildal and C. Orlenius, "Characterization of mobile terminals in Rayleigh fading by using reverberation chamber," in *Applied Electromagnetics and Communications, 2005. ICECom 2005. 18th International Conference on*, Oct. 2005, pp. 1–4.

[32] J. Chen, A. McKernan, G. W. Irwin, and W. G. Scanlon, "Experimental characterisation and analysis of wireless network control systems," in *Signals and Systems Conference, 208. (ISSC 2008). IET Irish*, Jun. 2008, pp. 238–243.

[33] P. Kildal, X. Chen, C. Orlenius, M. Franzen, and C. Patane, "Characterization of reverberation chambers for OTA measurements of wireless devices: Physical formulations of channel matrix and new uncertainty formula," *Antennas and Propagation, IEEE Transactions on*, vol. 60, no. 8, pp. 3875–3891, Aug. 2012.

[34] G. Ferrara, M. Migliaccio, and A. Sorrentino, "Characterization of GSM non-line-of-sight propagation channels generated in a reverberating chamber by using bit error rates," *Electromagnetic Compatibility, IEEE Transactions on*, vol. 49, no. 3, pp. 467–473, Aug. 2007.

[35] S. Floris, K. Remley, and C. Holloway, "Bit error rate measurements in reverberation chambers using real-time vector receivers," *Antennas and Wireless Propagation Letters, IEEE*, vol. 9, pp. 619–622, 2010.

[36] E. Genender, C. Holloway, K. Remley, J. Ladbury, G. Koepke, and H. Garbe, "Simulating the multipath channel with a reverberation chamber: Application to bit error rate measurements," *Electromagnetic Compatibility, IEEE Transactions on*, vol. 52, no. 4, pp. 766–777, Nov. 2010.

[37] P. Hallbjorner and A. Rydberg, "Maximum doppler frequency in reverberation chamber with continuously moving stirrer," in *Antennas and Propagation Conference, 2007. LAPC 2007. Loughborough*, Apr. 2007, pp. 229–232.

[38] K. Karlsson, X. Chen, P.-S. Kildal, and J. Carlsson, "Doppler spread in reverberation chamber predicted from measurements during step-wise stationary stirring," *Antennas and Wireless Propagation Letters, IEEE*, vol. 9, pp. 497–500, 2010.

[39] J.-H. Choi, J.-H. Lee, and S.-O. Park, "Characterizing the impact of moving mode-stirrers on the doppler spread spectrum in a reverberation chamber," *Antennas and Wireless Propagation Letters, IEEE*, vol. 9, pp. 375–378, 2010.

[40] X. Chen, P.-S. Kildal, and J. Carlsson, "Determination of maximum doppler shift in reverberation chamber using level crossing rate," in *Antennas and Propagation (EUCAP), Proceedings of the 5th European Conference on*, Apr. 2011, pp. 62–65.

[41] X. Chen, P.-S. Kildal, and S.-H. Lai, "Estimation of average Rician K-factor and average mode bandwidth

in loaded reverberation chamber," *Antennas and Wireless Propagation Letters, IEEE*, vol. 10, pp. 1437–1440, 2011.

[42] C. Lemoine, E. Amador, and P. Besnier, "On the K-factor estimation for Rician channel simulated in reverberation chamber," *Antennas and Propagation, IEEE Transactions on*, vol. 59, no. 3, pp. 1003–1012, Mar. 2011.

[43] C. Lemoine, E. Amador, P. Besnier, J. Sol, J.-M. Floc'h, and A. Laisne, "Statistical estimation of antenna gain from measurements carried out in a mode-stirred reverberation chamber," in *General Assembly and Scientific Symposium, 2011 XXXth URSI*, Aug. 2011, pp. 1–4.

[44] X. Chen and P.-S. Kildal, "Comparison of RMS delay spread and decay time measured in reverberation chamber," in *Antennas and Propagation (EuCAP), 2010 Proceedings of the Fourth European Conference on*, Apr. 2010, pp. 1–3.

[45] C. Holloway, H. Shah, R. Pirkl, K. Remley, D. Hill, and J. Ladbury, "Early time behavior in reverberation chambers and its effect on the relationships between coherence bandwidth, chamber decay time, RMS delay spread, and the chamber buildup time," *Electromagnetic Compatibility, IEEE Transactions on*, vol. 54, no. 4, pp. 714–725, Aug. 2012.

[46] A. Coates, A. Duffy, K. Hodge, and A. Willis, "Investigating electromagnetic exposure of communication cables in reverberant chambers," in *Electromagnetic Compatibility, 2002. EMC 2002. IEEE International Symposium on*, vol. 1, Aug. 2002, pp. 233–237.

[47] R. De Leo, V. Primiani, F. Moglie, and A. Pastore, "SAR numerical analysis of the whole human body exposed to a random field," in *Electromagnetic Compatibility, 2009. EMC 2009. IEEE International Symposium on*, Aug. 2009, pp. 81–86.

[48] K. Harima, "Estimation of power absorbed by human body using reverberation chamber," in *Electromagnetic Compatibility (EMC), 2012 IEEE International Symposium on*, Aug. 2012, pp. 39–43.

[49] E. Genender, C. Holloway, K. Remley, J. Ladbury, G. Koepke, and H. Garbe, "Use of reverberation chamber to simulate the power delay profile of a wireless environment," in *Electromagnetic Compatibility-EMC Europe, 2008 International Symposium on*, Sep. 2008, pp. 1–6.

[50] C. Wright and S. Basuki, "Utilizing a channel emulator with a reverberation chamber to create the optimal MIMO OTA test methodology," in *Mobile Congress (GMC), 2010 Global*, Oct. 2010, pp. 1–5.

[51] A. Skarbratt, J. Asberg, and C. Orlenius, "Over-the-air performance testing of wireless terminals by data throughput measurements in reverberation chamber," in *Antennas and Propagation (EUCAP), Proceedings of the 5th European Conference on*, Apr. 2011, pp. 615–619.

[52] C. Lemoine, P. Besnier, and M. Drissi, "Investigation of reverberation chamber measurements through high-power goodness-of-fit tests," *Electromagnetic Compatibility, IEEE Transactions on*, vol. 49, no. 4, pp. 745–755, Nov. 2007.

[53] D. A. Hill, "Plane wave integral representation for fields in reverberation chambers," *IEEE Transactions on Electromagnetic Compatibility*, vol. 40, no. 3, pp. 209–217, 1998.

CHAPTER 2

Overview of propagation channels inside the mode-stirred reverberation chamber

An antenna of a wireless system may receive an amount of direct, reflected and scattered waves corresponding to transmitted signal. These scattered waves are created by vehicular motion, wind-blown foliage, etc. and because of the varying path lengths it results a random complex Gaussian process with various magnitudes, phases and angles of arrival, having zero mean and variance $2\sigma^2$.
When there is relative motion between the transmitter and the receiver, one must also include the Doppler effects on frequency and phase shifts. Considering that the ith reflected wave, whose amplitude is α_i and phase θ_i, arrives at the receiver from an angle φ_i relative to the direction of motion of the antenna. The Doppler pulsation of the ith reflected wave caused by the movement of the transmitter or receiver is then given with [1]:

$$\omega_{d_i} = \omega_c \frac{v}{c} \cos \varphi_i, \tag{2.1}$$

where

- ω_c represents the pulsation of the transmitted signal (frequency f_c),
- v is the velocity of the mobile,
- c is the speed of light, $3 \cdot 10^8$ m/s,
- φ_i represents the angles-of-arrival (AoA) of the ith path, $i = 1, \cdots, S$. These angles are independent and identically distributed (i.i.d.) over $[0, 2\pi)$,
- S is the number of scattered paths,
- $\omega_c = 2\pi f_c$ and f_c is the carrier frequency.

Considering the propagation channel as a linear filter between the input $x(t)$ and the output $y(t)$, a global description of this situation may be defined by the Bello's diagram [2] as in Fig. 2.1. In this context the parameters,

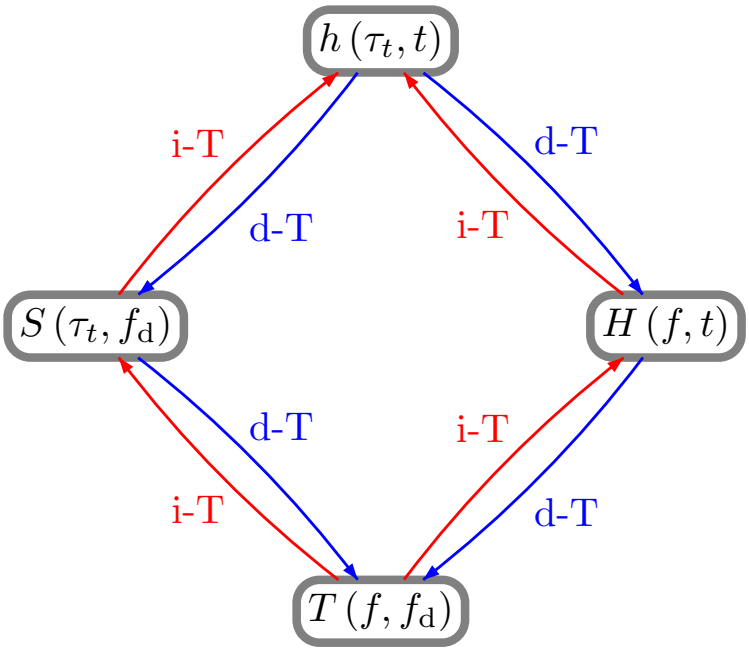

Figure 2.1: Bello's diagram (i-T: inverse transform, d-T: direct transform).

- $h(\tau_t, t)$ represents the delay spread function:

$$y(t) = h(\tau_t, t) \star x(t) = \int_{-\infty}^{\infty} h(\tau_t, t) x(t - \tau_t)\, \mathrm{d}\,\tau_t, \tag{2.2}$$

  and τ_t is the delay parameter;

- $H(f, t)$ is the time variant transfer function:

$$\begin{aligned} y(t) &= \int_{-\infty}^{\infty} x(t - \tau_t) h(\tau_t, t)\, \mathrm{d}\,\tau_t = \int_{-\infty}^{\infty} X(f) H(f, t) e^{j2\pi t f}\, \mathrm{d}\, f \\ &= \int_{-\infty}^{\infty} X(f) \int_{-\infty}^{\infty} h(\tau_t, t) e^{-j2\pi\tau_t f}\, \mathrm{d}\,\tau_t e^{j2\pi t f_\mathrm{d}}\, \mathrm{d}\, f, \end{aligned} \tag{2.3}$$

- $T(f, v)$ characterizes the Doppler spread function of the channel:

$$\begin{aligned} y(t) &= T(f, f_\mathrm{d}) \star X(f) = \int_{-\infty}^{\infty} T(f, f_\mathrm{d}) X(f - f_\mathrm{d})\, \mathrm{d}\, f_\mathrm{d} \\ &= \int_{-\infty}^{\infty} \int_{-\infty}^{\infty} \int_{-\infty}^{\infty} h(\tau_t, t) e^{-j2\pi t f_\mathrm{d}}\, \mathrm{d}\, t\ e^{-j2\pi\tau_t f}\ \mathrm{d}\,\tau_t X(f - f_\mathrm{d})\, \mathrm{d}\, f_\mathrm{d}, \end{aligned} \tag{2.4}$$

  where f_d is the Doppler shift;

- $S(f_\mathrm{d}, \tau_t)$ is the delay Doppler spread function:

$$\begin{aligned} y(t) &= \int_{-\infty}^{\infty} x(t-\tau_t) \int_{-\infty}^{\infty} S(\tau_t, f_\mathrm{d}) e^{j2\pi t f_\mathrm{d}} \,\mathrm{d}\, v \,\mathrm{d}\, \tau_t \\ &= \int_{-\infty}^{\infty} x(t-\tau_t) \int_{-\infty}^{\infty} \int_{-\infty}^{\infty} T(f, f_\mathrm{d}) e^{j2\pi f \tau_t} \,\mathrm{d}\, f \; e^{j2\pi t f_\mathrm{d}} \,\mathrm{d}\, f_\mathrm{d} \,\mathrm{d}\, \tau_t; \end{aligned} \tag{2.5}$$

2.1 Friis propagation model

In the absence of scattered components when the power of transmitted antenna is P_T, the spatial power density $\mathcal{S}$ is given by:

$$\mathcal{S} = \frac{EIRP}{4\pi d^2} = \frac{P_\mathrm{T} G_\mathrm{Tx} \left(1 - |\Gamma_\mathrm{Tx}|^2\right)}{4\pi d^2} e^{-\alpha d}, \tag{2.6}$$

where

- $EIRP$ is the equivalent isotropically radiated power,
- G_Tx is the gain of transmitting antenna,
- d is the distance from the source,
- $|\Gamma_\mathrm{Tx}|$ is the mismatch of the transmitting antenna,
- $e^{-\alpha d}$ corresponds to losses due to propagation environment.

The received power at a distance d by an antenna whose gain is G_Rx and mismatch $|\Gamma_\mathrm{Rx}|$ is written then as:

$$P_\mathrm{R} = \mathcal{S} \frac{\lambda^2}{4\pi} G_\mathrm{Rx} \left(1 - |\Gamma_\mathrm{Rx}|^2\right) \mathcal{P} e^{-\alpha d} = \frac{P_\mathrm{T} G_\mathrm{Tx} G_\mathrm{Rx} \left(1 - |\Gamma_\mathrm{Tx}|^2\right) \left(1 - |\Gamma_\mathrm{Rx}|^2\right)}{4\pi d^2} \frac{\lambda^2}{4\pi} \mathcal{P} e^{-\alpha d} \tag{2.7}$$

The factor $\mathcal{P}$ represents the polarization loss factor when the antennas are not polarization matched. The above model is for the situation when there are no scattered components and when the distance d is in the far field region of the transmission antenna. With the emergence of supplementary specular components more complex models have been derived depending on the transmission area (urban, suburban or open area) [3]. When in addition to specular components there are also scattered components (e.g., due to people movement, cars, leaves, etc.) many statistical models have been developed [4–7]. There are different types of fading. The most usual two fading models are presented in the following section.

2.2 Two fading models

2.2.1 Representation of a signal with Rayleigh fading

The complex fading channel envelope $R(p)$ is seen as the Fourier transform $\mathcal{F}\{\square\}$ of the varying channel impulse response $h(p)$ at the moment p in the frequency band of the received signal $y(p)$. When making measurements in reverberation chamber the moment p may correspond

to a stirrer position, an antenna position, a measurement frequency etc. For a sinusoidal transmitted signal with unit amplitude and frequency f_c:

$$x(p) = \cos(2\pi f_c p), \tag{2.8}$$

The received signal $y(p)$ and its inphase/quadrature expression, considering the Doppler over scattered components, can be written as:

$$\begin{aligned} y(p) = h(p) \star x(p) &= |\mathcal{F}\{h(p)\}||_{\omega=\omega_c} e^{j\left(\omega_c p + \angle \mathcal{F}\{h(p)\}|_{\omega=\omega_c}\right)} \\ &\overset{\text{noted}}{=} r(p) e^{j(\omega_c p + \Theta(p))} \overset{\text{noted}}{=} R(p) e^{j\omega_c p}. \end{aligned} \tag{2.9}$$

The $r(p)$ (noted r for simplicity) is the fading envelope Rayleigh distributed described by the pdf given by:

$$f(r/\sigma) = \frac{r}{\sigma^2} \exp\left(-\frac{r^2}{2\sigma^2}\right). \tag{2.10}$$

2.2.2 Representation of a Rician fading signal

When in addition to the scattered components a specular path between the transmitter and the receiver exists, the complex fading envelope $R(p)$ is defined as the sum of a specular components $R_{\text{sp}}(p)$ (constant or time-varying whose magnitude is A) and an equivalent scattered component $R_{\text{sc}}(p)$ (which is equal with $R(p)$ presented in (2.9)) [1]. The pdf of the Rician fading is defined as:

$$\begin{aligned} f(r/A,\sigma) &= \frac{r}{\sigma^2} \exp\left(-\frac{r^2 + A^2}{2\sigma^2}\right) I_0\left(\frac{rA}{\sigma^2}\right) \\ &= \frac{2r(K+1)}{\Omega} e^{-K - \frac{(K+1)r^2}{\Omega}} I_0\left(2r\sqrt{\frac{K(K+1)}{\Omega}}\right), \end{aligned} \tag{2.11}$$

where

- the parameter K is defined as the ratio of the local average power of the specular components to the local average power of the scattering components, $A^2/(2\sigma^2)$, and
- Ω is the second order moment of the Rician fading ($\Omega = A^2 + 2\sigma^2$).

This pdf characterizes the statistics of the signal in a limited frequency bandwidth (narrower than the correlation bandwidth of the channel, usually $\Delta f/f_c < 10\%$) and a limited time segment (long compared to the correlation time of the short-term fluctuations) in order to exclude the longer term changes in the fading process (e.g., diurnal effects for fixed terminals or locale changes for mobile terminals) [8]. It results that the complex fading envelope $R(p)$ becomes as [9]:

$$\begin{aligned} R(p) &= r(p) e^{j\Theta(p)} = R_{\text{I}}(p) + jR_{\text{Q}}(p) = R_{\text{sp}}(p) + R_{\text{sc}}(p) \\ &= Ae^{j(\theta_0 + \omega_{\text{d}} p)} + \sqrt{2}\sigma \lim_{S\to\infty} \frac{1}{\sqrt{S}} \sum_{i=1}^{S} \alpha_i(p) e^{j\left(\theta_i(p) + \omega_{d_i} p\right)}, \end{aligned} \tag{2.12}$$

where

- $R_{\mathrm{I}}(p)$ is the in-phase component, non-central Gaussian distributed,
- $R_{\mathrm{Q}}(p)$ is the quadrature component, non-central Gaussian distributed,
- A is the level of the specular components,
- θ_0 is the phase of specular components,
- $\alpha_i(p)$ represents the amplitude weights for each scattered path i,
- $\theta_i(p)$, corresponds to the phase of the scattered component coming from the ith direction at the moment p and depends on the propagation distance,
- $\Theta(p)$ is the fading phase of the complex fading envelope, $\Theta(p) = \angle R(p)$. When the Doppler effect is missing, for a Rayleigh fading this phase becomes uniform distributed in $[-\pi, \pi)$, otherwise the phase will be given by the phase distribution of the dominant component,
- ω_{d} is the Doppler pulsation of the specular component.

Properties of the Rician signal envelope

The reverberation chamber used in this thesis as measurement environment has a large mechanical stirrer, Fig. 2.2. Each paddle position of the stirrer corresponds to a measurement of the pth channel in the pth propagation environment. When using the mode-stirring paddle in continuous mode, the propagation channels become dynamic time varying. For our chamber, the minimum time duration for a complete rotation of the stirrer (corresponding to the maximum speed of the stirrer) is 30 s. It results that the Doppler effect becomes almost insignificant for the envelope fading and it will not be considered. Moreover, in almost all the following analyses the stirrer is used in stepped mode (mode-tuned) for which the propagation channels are static, time invariant. The complex envelope of the scattered components

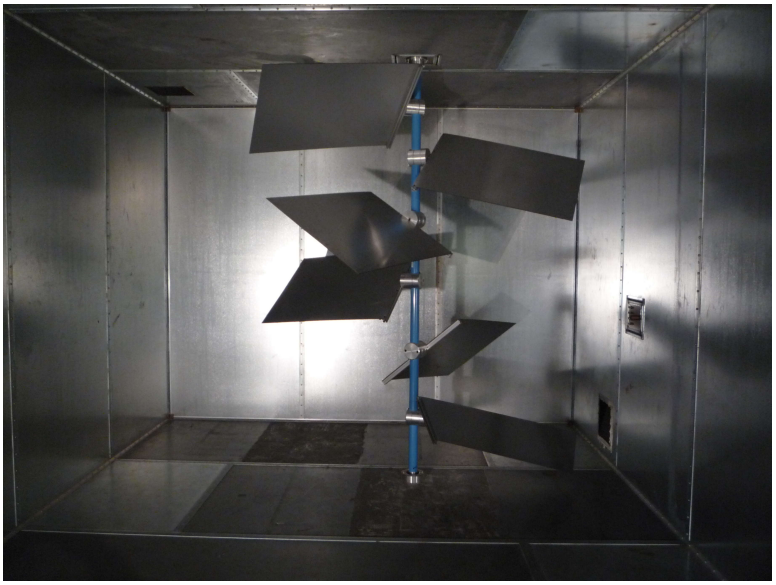

Figure 2.2: Reverberation chamber stirrer.

R_{sc} is zero mean Gaussian distributed, its magnitude is Rayleigh distributed and its phase is uniformly distributed in the range $[-\pi, \pi)$. It results that for a signal with Rician fading, the expected value $E[\square]$ of the complex fading amplitude over a set of realizations is given by the specular component, R_{sp}:

$$E[R] = E[R_{sp}] + E[R_{sc}] = E[R_{sp}] = A, \tag{2.13}$$

The power of the scattered components is computed as the variance, denoted $\mathrm{Var}[\square]$, of the complex fading envelope:

$$\begin{aligned} \mathrm{Var}[R] &= E\left[(R_{sc} + R_{sp})^2\right] - E^2[(R_{sc} + R_{sp})] = E\left[R_{sp}^2\right] + 2\underbrace{E[R_{sc}]}_{=0} E[R_{sp}] - \underbrace{E^2[R_{sc}]}_{=0} \\ &= E\left[R_{sc}^2\right] = 2\sigma^2, \end{aligned} \tag{2.14}$$

while the total fading power is given by the second order moment of the Rician distribution as:

$$\begin{aligned} E\left[|R|^2\right] &= E\left[r^2\right] = E\left[(R_{sp,I})^2 + (R_{sp,Q})^2\right] + E\left[(R_{sc,I})^2 + (R_{sc,Q})^2\right] \\ &\quad + \underbrace{E\left[2R_{sp,I}R_{sp,Q} + 2R_{sc,I}R_{sc,Q}\right]}_{=0} \\ &= E\left[(R_{sp,I})^2 + E\left[(R_{sc,I})^2 + (R_{sc,Q})^2\right] + (R_{sp,Q})^2\right] \\ &= E\left[|R_{sp}|^2\right] + E\left[|R_{sc}|^2\right] = A^2 + 2\sigma^2, \end{aligned} \tag{2.15}$$

with

- $R_{sp} = R_{sp,I} + jR_{sp,Q}$, and
- $R_{sc} = R_{sc,I} + jR_{sc,Q}$.

Additional details about these distributions and several other distributions used in this thesis are provided in annex A.

2.3 Overview on channel measurements in reverberation chamber

A first step in the characterization of a wireless communication link is to quantify the power of scattered and specular components and to identify how these signals fade in time. In this section we analyze the effect of the fading on the transmitted signal by making several measurements in reverberation chamber. Different works have shown that this environment can be properly used to recreate a propagation channel affected by strong fading. There are several dimensions which can be changed in order to modify the properties of the channel: changing the working frequency, the type of antennas and the distance between them, loading or not the chamber with absorbing objects, adding scattering objects.
The measurements are performed in both time and frequency domains using an arbitrary waveform generator (AWG Tektronix 7052), a digitally storage oscilloscope (DSO Tektronix TDS6124C), a spectrum analyzer (Aeroflex IFR 2395) and a vector network analyzer (VNA

Agilent N5230A). At emission and reception horn antennas (ETS Lindgren, model 3115), discone antennas (ARA, model CMA 118/A), and log-periodic antennas (ETS Lindgren, model 3148) are used. In order to modify the quality factor of the chamber we use several parallelepiped absorbers (Hyfral P150) whose dimensions are $0.6 \times 0.6 \times 0.6\,\mathrm{m}^3$ and canisters with salty water (SLAAM195BA). The fading is created by using a mechanical stirrer. The electronic stirring and the antennas movement in different positions are used to increase the number of realizations. The reverberation chamber is a propagation environment in which the wireless channel is characterized by both specular and scattered components. We identify three type of components, which are highlighted in Fig. 2.3:

- specular direct components, Fig. 2.3 trace (a), and specular secondary components, Fig. 2.3 trace (b), reflected by the chamber walls but not by the stirrer. These components are invariant with the time. In this thesis they are named "unstirred components";
- scattered components, Fig. 2.3 trace (c), which are components reflected by the stirrer and which are statistically distributed over the time. These components are named "stirred components".

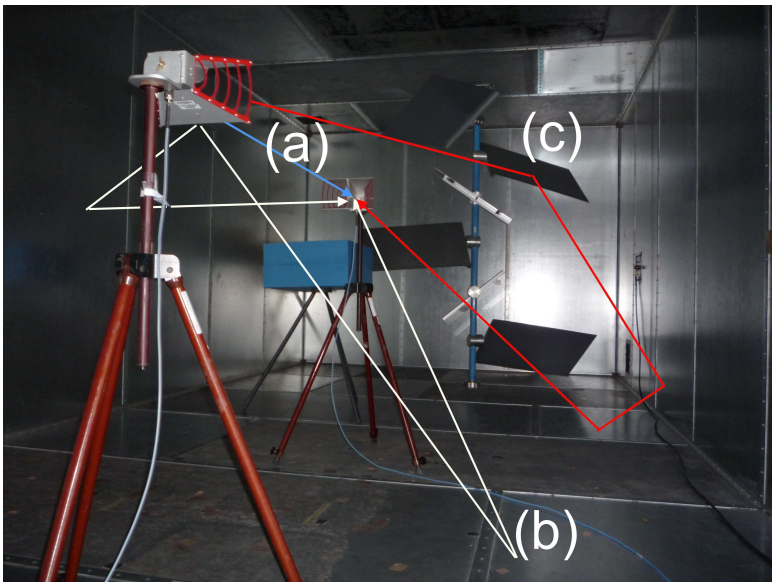

Figure 2.3: Reverberation chamber components: (a) unstirred components, (b) unstirred secondary components, (c) stirred components.

Some measurements are made in order to have independent individual realizations while for others we want to have correlated experiments. All the measurements are conducted by the use of Matlab software.

Characterizing propagation channels by using amplitude parameters

A first analysis of the received signal is proposed in time domain. The two horn antennas are placed back to back and in a cross polarized arrangement. The sent signal is a continuous sinusoidal wave with a frequency of 1.5 GHz generated by the AWG whose sampling rate is 5 GS/s. At the DSO the signal is saved for a time of 2 µs with a sampling frequency of 10GS/s

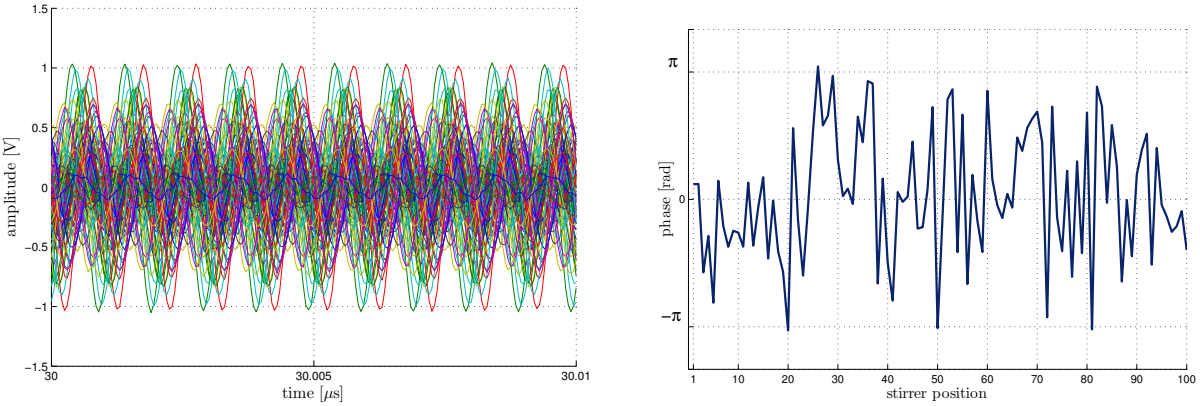

(a) (b)

Figure 2.4: The received signal amplitude r in steady state (a) and its phase Θ (b) for 100 stirrer positions.

(which corresponds to 40 000 sampling points). To reduce the level of the noise of the signal, for every stirrer position, an average over 50 consecutive acquisitions of the signal on the DSO is performed. We perform 100 independent measurements of the signal [10] for each stirrer position in order to detect the signal distribution. The received signal, affected by the fading, is plotted in Fig. 2.4. As we can observe, both the amplitude 2.4(a) and the phase 2.4(b) change strongly with the stirrer position. A better representation of the variation of the signal level with the stirrer position is done in Fig. 2.5. This figure presents the normalized amplitude of the signal with the stirrer position to the lower neighbour: $(r(p) - r(p-1))/r(p-1)$. It results that the variation of the envelope from one stirrer position to another stirrer position can be very strong. For example, in these measurements (which are made for a non-line-of-sight configuration at 1.5 GHz without changing the chamber with absorbing materials) the maximum detected variation is around 250% while the minimum variation is 1%.

Placing the antennas in a non-line-of-sight configuration implies that the unstirred energy is very low. It results that the envelope fading at reception becomes Rayleigh distributed. This is illustrated in Fig. 2.6(a). Changing the amount of unstirred energy (i.e., by changing the position of antennas to have a direct path between them, or by changing the ratio between the unstirred and stirred energy by adding absorbers) this distribution will change into a Rician one, Fig. 2.6(b).

If we analyze the transient part of the signal we can clearly see the influence, constructive or destructive, of the waves arriving at antenna reception as a function of time, Fig. 2.7. It results that it is possible to have an amplitude which is higher in transient regime than the amplitude found in steady state. The time necessary for the signal to arrive in steady state depends on the quality factor of the chamber (e.g., the losses in the chamber) as well as on the dimensions of the chamber. This time represents the decay constant of the environment. Comparing with the signal measured for single frequency, Fig. 2.8 presents the impulse response of the channel in the bandwidth 0–2.5 GHz. To shorten this signal, the chamber is loaded with several absorbing materials (15 canisters with salty liquid and 5 parallelepiped foam absorbers). These absorbers are placed in the reverberation chamber, but not between the two antennas, affecting especially the stirred components and less the unstirred components. The transmitted signal

in the chamber is generated with the AWG. It is not a perfect Dirac impulse since the AWG has a limited bandwidth (i.e., 2.5 GHz) and is influenced by the transfer functions of the cables and also by the transmitting and receiving antennas. Thus, each measurement is influenced not only by the propagation channel but also by the devices which are used in these experiments. Analyzing the signals in Fig. 2.8 we can identify two areas. In the first part of the impulse response all the 100 signals (corresponding to 100 stirrer positions) match perfectly. This part of the signal corresponds to the shortest propagation distance between antennas and to reflections with the metallic walls which are not affected by the stirrer (remaining invariant with the stirrer rotation). In the second area the signals are mixed due to multiple reflections with the blades of the stirrer which modify the overall amplitude and phase of the received signal.

Rather than working in a time domain, we can use a VNA which has its own advantages. A direct improvement of this type of measurement is a higher sensitivity and in consequence a lower noise floor compared with a DSO. Otherwise, the additive white Gaussian noise introduced in measurements of a signal via the receiver has a great influence when the amplitude level of the signal is small. The effects of the receiver noise are additive, these influences are present in both static and dynamic channels [11]. The only disadvantage of this device is that it can only be used to measure the complex transfer function of the propagation channel. In order to carry out an analysis in time domain we have to use a frequency-to-time domain transform. The channel response at different transmitted signals can be estimated from the product of the input signal in frequency domain and the transfer function of the channel. An example of the measured transfer functions of the channel for 100 stirrer positions is presented in Fig. 2.9. From this results we can see that, as observed in time domain, the magnitude of the signal may have strong fluctuations with frequency (e.g., $30 - 40\,\mathrm{dB}$).
The attenuation of both unstirred and stirred received signals can be evaluated measuring the insertion loss. This parameter defines the loss of signal power between the transmitted P_{Tx} and received power P_{Rx} due to absorption in antennas, cables, metallic walls, etc. For N realizations (e.g., stirrer positions) and M trials (e.g., antenna positions, independent frequencies,

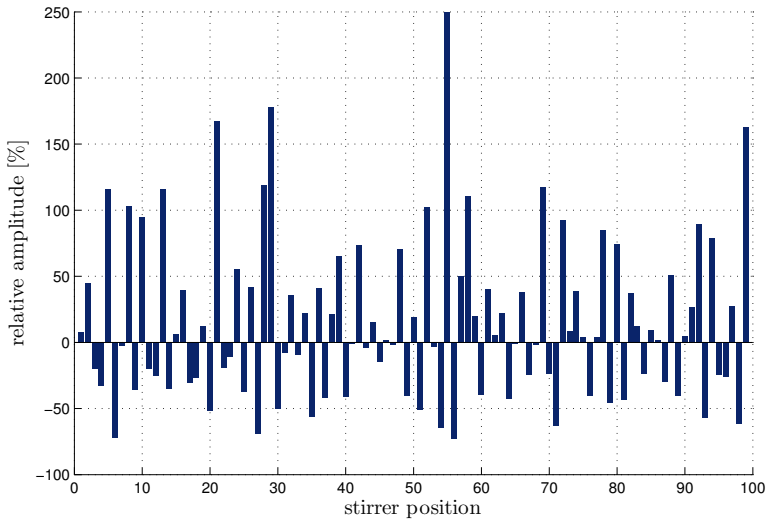

Figure 2.5: Relative fluctuation of the amplitude for a complete stirrer rotation (i.e., 100 stirrer positions).

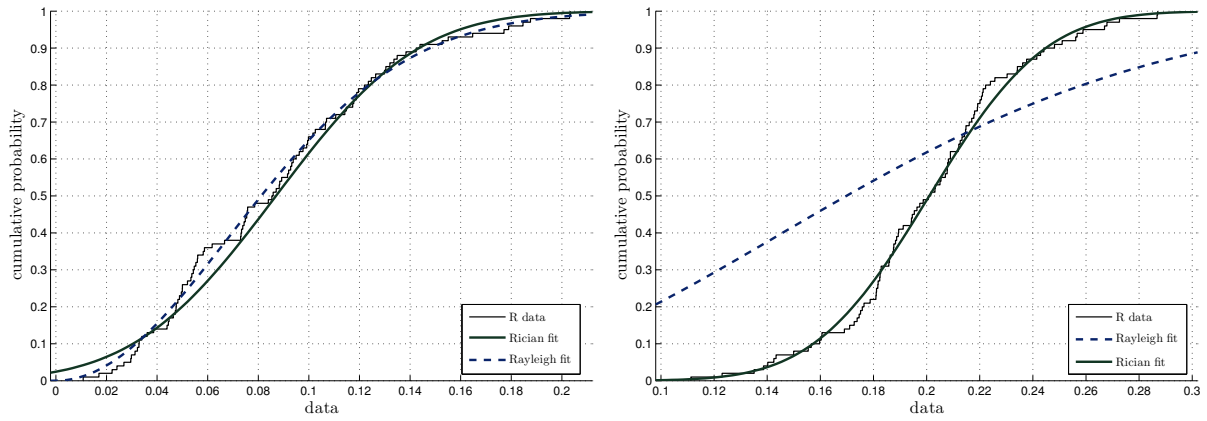

(a) (b)

Figure 2.6: The fitting distribution for a non-line-of-sight configuration (a), and for a line-of-sight configuration (b). The number of realizations is 100.

etc.) the insertion loss is defined as the expected value over the number of trials with:

$$IL = E\left[\frac{E\left[P_{\mathrm{Rx}}\right]_N}{P_{\mathrm{Tx}}}\right]_M \tag{2.16}$$

Characterizing propagation channels by using time parameters

Another simple way to characterize a propagation channel is to estimate different time parameters. These parameters depend on the emergence of the multiple paths between emission and reception, on the respective positions of transmitter and receiver, on the degree of absorption of the propagation environment and on the objects illuminated by electromagnetic waves. The decay constant of the signal can be quickly extracted from the measured signal. It is estimated

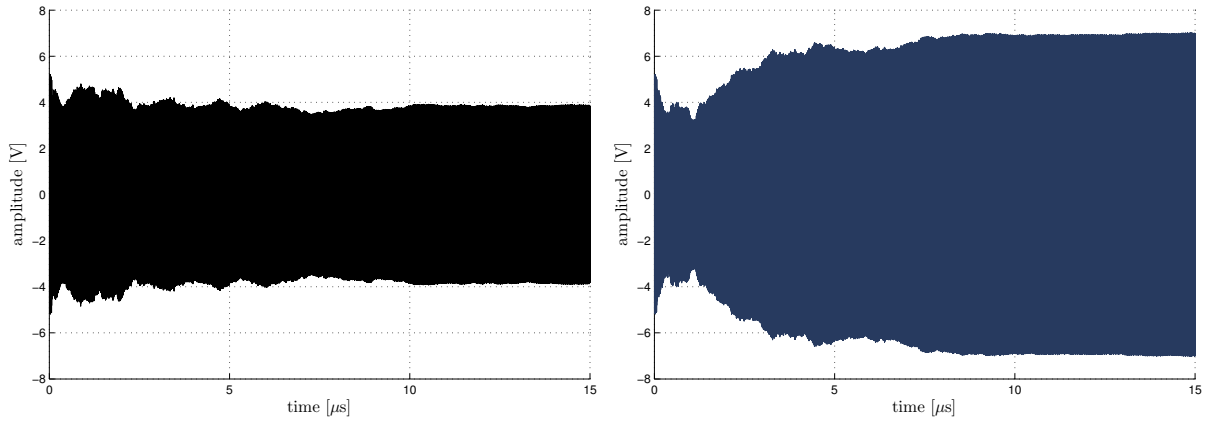

(a) (b)

Figure 2.7: Examples of the transient and steady state regimes of the signal for two different stirrer positions.

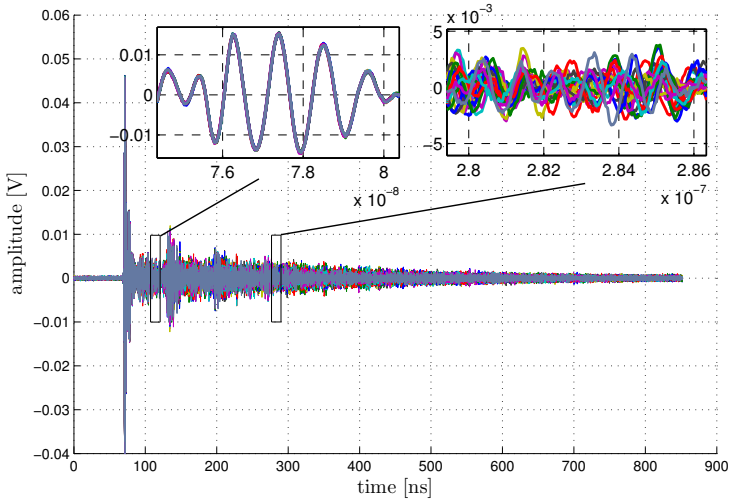

Figure 2.8: 100 impulse responses of the reverberation chamber when measuring the signal using the DSO.

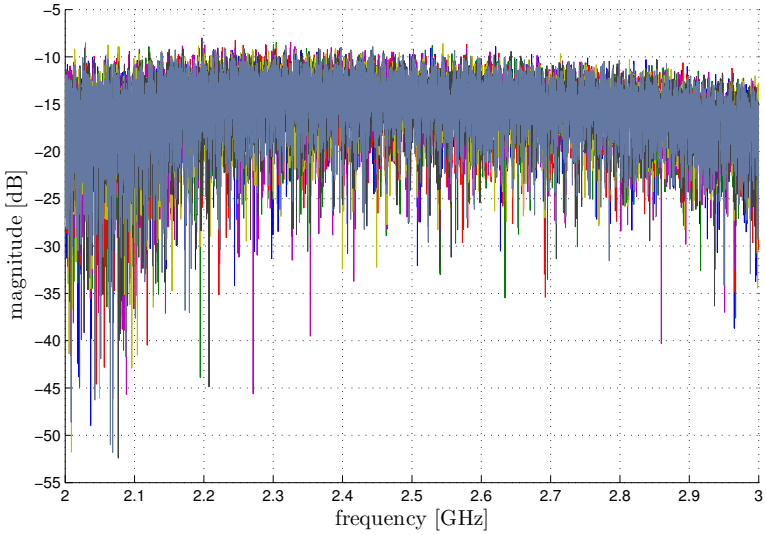

Figure 2.9: Transfer functions of the propagation channel for 100 stirrer positions.

from the average of instantaneous normalized power delay profiles (PDPs), as in the example presented in Fig. 2.10. This parameter uses the impulse response of the channel $h(t)$ and is

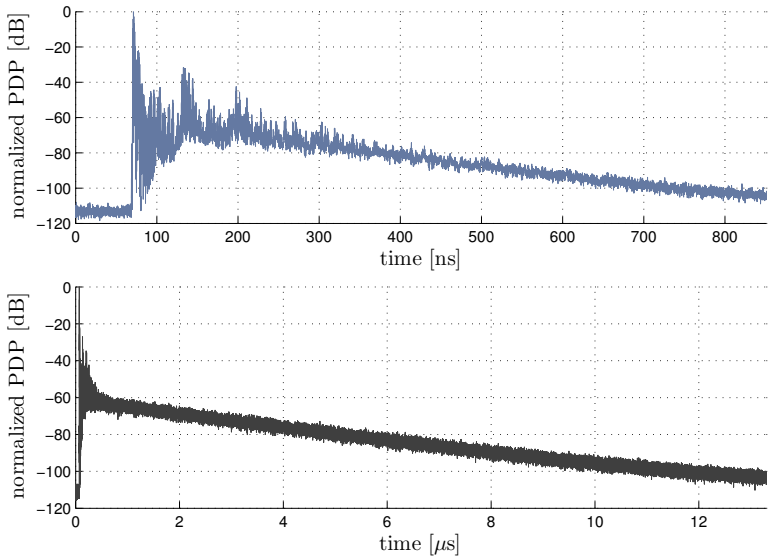

Figure 2.10: Example of the measured normalized power delay profile for a loaded (top) and an empty chamber (bottom) in the same line-of-sight configuration.

defined as:

$$P^{\text{norm}}(t) = \frac{|h(t)|^2}{\int_0^\infty |h(t)|^2 \, \mathrm{d}\, t}. \tag{2.17}$$

When extracting the time delays it is mandatory to define a noise level of the signal which depends on the sensitivity of the measuring equipment. The noise level for the DSO used in our experiments changes from 670 µV for a full scale of 100 mV to 50 mV for a full scale of 10 V. The detection of a noise threshold may be done during the triggering period.
For example, in Fig. 2.11(a) shows the decay constant τ of the chamber with several quantities of absorbers, 2.11(b). This parameter characterizes the stored energy in the chamber having an exponential variation with time $e^{-t/\tau}$ [12]. In this example, it is computed for a frequency bandwidth of 1 GHz (between 1 and 2 GHz) and varies from 2.7 µs to 100 ns. This method to control the propagation channels in reverberation chamber with absorbing materials will be frequently used in this thesis. Beside the decay constant of the chamber we can define other time parameters, Fig. 2.12. Among them are the mean delay τ_μ and the root mean square (RMS) delay spread τ_{rms} [1]:

$$\tau_\mu = \frac{\int_0^\infty (t - \tau_a) P^{\text{norm}}(t) \, \mathrm{d}\, t}{\int_0^\infty P^{\text{norm}}(t) \, \mathrm{d}\, t}, \tag{2.18}$$

and

$$\tau_{\text{rms}} = \sqrt{\frac{\int_0^\infty (t - \tau_a - \tau_\mu)^2 P^{\text{norm}}(t) \, \mathrm{d}\, t}{\int_0^\infty P^{\text{norm}}(t) \, \mathrm{d}\, t}}. \tag{2.19}$$

In these equations, the parameter τ_a is the arrival time of the signal at receiver corresponding to the shortest path between antennas. We can also define a maximum delay $\tau_{\max}$ which

represents the time for which the level of PDP is under a defined limit (e.g., −30 dB) compared with the maximal value of the signal. An example of the instantaneous values of the mean delay τ_μ and the RMS delay spread τ_{rms} for each stirring position and those obtained from the averaged PDPs over all 100 stirrer positions are presented respectively in Table 2.1(a) and in Table 2.1(b). These values are evaluated from measurements made by using the DSO for two situations: when the chamber is empty and when it is loaded with 15 canisters with salty water and 5 parallelepiped absorbers. The results in Table 2.1(a) describe the variation of the channel with the stirrer position from which we can evaluate the effects of short term fading whereas the results in Table 2.1(b) gives a global image of the channel. Modifying the degree of absorption, the delay parameters changes too.

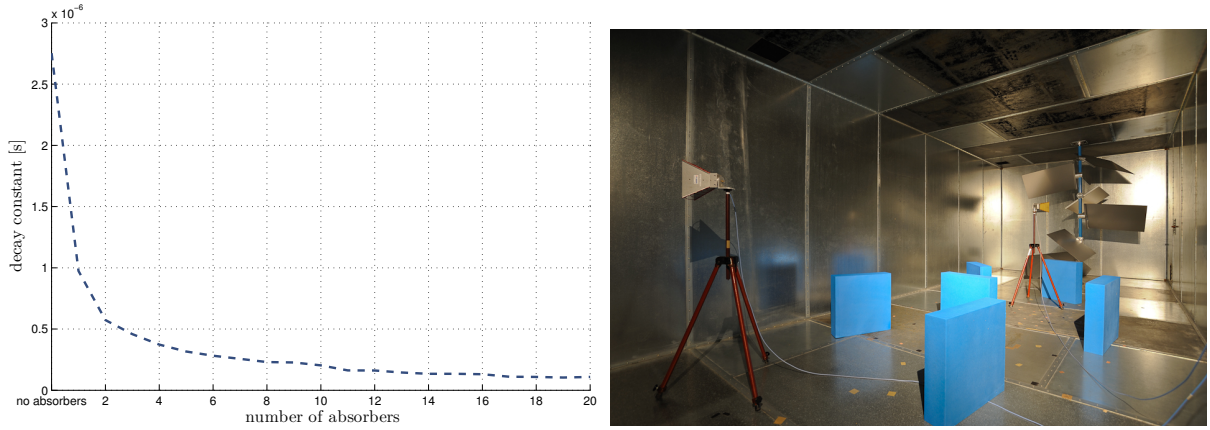

(a) (b)

Figure 2.11: Decay constant of the chamber τ with the quantity of absorbers (a). Reverberation chamber configuration when using absorbers (b).

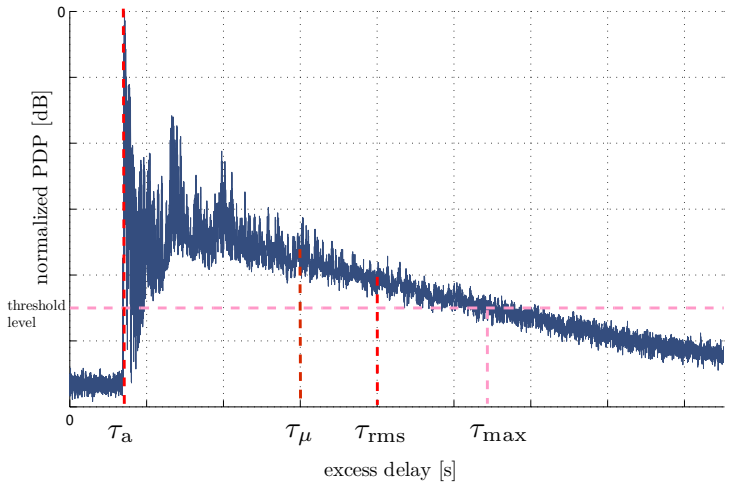

Figure 2.12: Definitions of excess delays extracted from normalized power delay profile (estimated from measurements in reverberation chamber).

Table 2.1: Excess delays when the PDP is evaluated for each stirrer position (a), and excess delays when the PDP is evaluated as an average over all 100 stirrer positions when the chamber is loaded with 15 canisters with salty water and 5 foam absorbers (b).

(a)

	with absorbers		without absorbers	
	τ_μ [ns]	τ_{rms} [ns]	τ_μ [µs]	τ_{rms} [µs]
min	45.3	92.5	2.14	2.54
max	53.8	102	2.30	2.65
Δ = max − min	8.5	9.5	0.16	0.11
averaged excess delays	49.5	98.1	2.21	2.60
standard deviation of excess delays	1.78	2	0.032	0.021

(b)

	with absorbers		without absorbers	
	τ_μ [ns]	τ_{rms} [ns]	τ_μ [µs]	τ_{rms} [µs]
excess delays evaluated from an averaged PDP	43.4	80.3	2.11	2.40

In Table 2.2 are presented τ_{a}, τ_μ, τ_{rms} and τ_{max} when the chamber is successively loaded with different quantities of absorbers and these delay spreads are evaluated from averaged PDPs over 100 stirrer positions. The parameter τ_{a} is invariant with the degree of absorption as it depends only on the distance between antennas. The small variation of τ_{a} is only due to the measurement noise. The other parameters τ_μ, τ_{rms} and τ_{max} change with the quantity of absorbing materials as they depend on the duration of the impulse response.

2.4 Conclusions

In this chapter we have presented a quick overview on the measurements in reverberation chamber for both time and frequency domains, as well on the type of the signals that can be evaluated. In the following chapters we insist on a detailed evaluation and control of both amplitude and time parameters. We chose to make the measurements in frequency domain in order to have a lower noise level and a faster measurement speed. Moreover, we use several offline post-processing techniques to obtain the signals in time domain.

Table 2.2: Excess delays with the absorbing quantity.

	τ_a [ns]	τ_μ [ns]	τ_{rms} [ns]	τ_{max} [µs]
15 canisters and 5 foam absorbers	69.4	43.4	80.3	0.57
6 canisters absorbers	69.8	386.4	578	3.16
5 canisters absorbers	69.3	463.7	667.5	3.51
4 canisters absorbers	69.8	552.1	768.6	3.97
No absorbers	69.1	2111	2406.1	11.48

Bibliography

[1] G. L. Stüber, *Principles of Mobile Communication (2nd Edition)*. Boston: Kluwer Academic, 2001.

[2] I. I. S. on Personal Indoor and M. R. Communications, *Conference Proceedings*. IEEE Service Center, 2004, no. 1 to 4. [Online]. Available: http://books.google.fr/books?id=BatVAAAAMAAJ

[3] A. Goldsmith, *Wireless Communications*. Cambridge University Press, Aug. 2005.

[4] T. Aulin, "A modified model for the fading signal at a mobile radio channel," *IEEE Transactions on Vehicular Technology*, vol. 28, no. 3, pp. 182–203, 1979.

[5] A. Saleh and R. Valenzuela, "A statistical model for indoor multipath propagation," *Selected Areas in Communications, IEEE Journal on*, vol. 5, no. 2, pp. 128–137, Feb. 1987.

[6] T. Kurner, D. Cichon, and W. Wiesbeck, "Concepts and results for 3D digital terrain-based wave propagation models: an overview," *Selected Areas in Communications, IEEE Journal on*, vol. 11, no. 7, pp. 1002–1012, Sep. 1993.

[7] G. Messier and J. Hartwell, "An empirical model for nonstationary Ricean fading," *Vehicular Technology, IEEE Transactions on*, vol. 58, no. 1, pp. 14–20, Jan. 2009.

[8] L. Greenstein, S. Ghassemzadeh, V. Erceg, and D. Michelson, "Ricean K-factors in narrow-band fixed wireless channels: Theory, experiments, and statistical models," *Vehicular Technology, IEEE Transactions on*, vol. 58, no. 8, pp. 4000–4012, Oct. 2009.

[9] C. Tepedelenlioglu and G. B. Giannakis, "On velocity estimation and correlation properties of narrow-band mobile communication channels," *IEEE Transactions on Vehicular Technology*, vol. 50, no. 4, pp. 1039–1052, 2001.

[10] C. Lemoine, P. Besnier, and M. Drissi, "Advanced method for estimating number of independent samples available with stirrer in reverberation chamber," *Electronics Letters*, vol. 43, no. 16, pp. 861–862, Aug. 2007.

[11] K. Remley, S. Floris, H. Shah, and C. Holloway, "Static and dynamic propagation-channel impairments in reverberation chambers," *Electromagnetic Compatibility, IEEE Transactions on*, vol. 53, no. 3, pp. 589–599, Aug. 2011.

[12] D. A. Hill, *Electromagnetic Fields in Cavities: Deterministic and Statistical Theories*, I. Press, Ed. Wiley/IEEE Press, Piscataway, NJ, 2009.

Part II

Estimating channel parameters

In this part of the thesis we analyze several channel parameters. Their evaluation and measurements are done in reverberation chamber. First we test different K-factor estimators and their capabilities. We present the useful limits in which several complex, phase and envelope K-factor estimators can be used. Due to the fact that the envelope estimators are more affected by statistical uncertainties compared with those which use the complex fading signal, we propose two new envelope-based estimators. These two new estimators improve the useful range of detectable values of K-factor in a propagation channel when the level of unstirred power is low and the measured signal is the fading envelope. The first estimator has the advantage of a very simple mathematical expression while offering good results compared with other envelope-based estimators. The second estimator has a slight more complicated mathematical expression and is based on an approximation of the pdf of the Rician fading to which a correction factor is added. It gives improved results in the testing conditions becoming the best envelope based estimator between the estimators selected for test.

Having established a good method to distinguish the unstirred and stirred powers with the use of K-factor, we focus on one of the possibilities to control a propagation channel inside reverberation chamber using absorbing materials. In these conditions we present a method to predict and measure the average absorbing cross section by using only one antenna. This technique consists in measuring the complex reflection coefficient of this antenna, from which we isolate the stirred energy modified by the presence of absorbers. As the Q factor of the chamber changes with the degree of absorption, it results a connection between the degree of absorption and the coherence bandwidth of the propagation channel as measured by the antenna (which plays the role of both the transmitter and receiver). Then, we extend our analysis to predict the average absorbing cross section when we know the physical dimensions of the absorber as well its electromagnetic properties. We can easily obtain an approximation of the average absorbing cross section if the absorber is parallelepiped (or any other shape for which any face of the absorber does not partially masks other faces). Our results show a good agreement between simulated and measured values of the average absorbing cross section. Moreover, the estimation of the average absorbing cross section is affected by random fluctuations of much lower amplitude than the classical method.

The next step presented in this part of the thesis is to create a model of the propagation channel for both transient regime and steady state. We use an ideal approximation of the envelope of the signal measured in time domain. With this model, depending on the available information, we can extract the K-factor, the average absorbing cross section and different time spreads parameters (i.e., mean delay spread and the root mean square delay spread). We also discuss the effects of secondary unstirred components which, depending on the propagation environment, can spread over tens/hundreds of nanoseconds. We compare the simulated and the measured values and we show that this model can be used with good results.

CHAPTER 3

Rician K-factor estimators

3.1 Introduction

An important parameter to characterize the severity of the small-scale fading on the signal reception is the Rician K-factor. Beside many other parameters (i.e., signal to noise ratio, power delay profile, etc.), a reliable estimation of the Rician K-factor is necessary in many applications. It is defined as the ratio of the local average power of the specular components (invariant components during large time intervals) to the local average power of the scattering components (random components depending on the statistics of the channel) [1–5]. K-factor is used in channel characterization in order to measure the relative strength of the specular component, in channel-aware resource allocation algorithms, in transmitting diversity schemes and adaptive transmission systems [6–8], to estimate the Nakagami m parameter [9], for link budget calculations [10], etc. The distribution of K-factor depends on various parameters of the communication link, e.g., heights and distance between antennas, beamwidths and gains of the antennas, nature of the intervening terrain, distribution of scattering, etc. For many applications, the use of an accurate and efficient K-factor estimator is critical as the channel quality assessment must take place over short observation windows for which the fading statistics remain unchanged. Our analysis has revealed that there are many concurrent methods for evaluating K, most of them cannot successfully estimate the K-factor over the whole range of interest. Depending on the transmission environment, K-factor may evolve typically over an important range and some estimators become unusable beyond a limit [11]. The estimation of K may be unstable and the quality of this estimation depends on the selected method.

In the first part of this chapter we enumerate the most common methods to compute the K-factors found in literature, briefly describing each estimator. Then, based on statistical analyses, we evaluate the performances of the chosen estimators in terms of rejection rate, confidence interval (CI) and bias. With these analyses and depending on the kind of available data we define a useful interval for each K-factor estimator. Also, we discuss the fluctuations of K-factor with frequency and causes are identified. The consequences of these fluctuations could lead to false or heavily biased values of K-factor. The methods to compute K-factor

must have an accessible mathematical expression while providing satisfactory results by using simple measured signals (e.g., amplitude or instantaneous power of the signal). Later, we propose two alternatives to estimate K-factor. Both alternatives use fading envelope signals. The purpose of our estimators is to extend the useful range of values and to reduce the uncertainties of estimation, while using a small sample size for estimation. The first estimator is based on a approximation of the power of unstirred components. For the second estimator the maximum-likelihood estimation (MLE) (see annex B.8) of the probability density function (pdf) of the fading envelope is computed by using an approximation of the modified Bessel function of the first kind (see annex C.1). The performances of both proposed estimators are compared with other envelope based estimators, including analyses with regards to the measured sample size and signal to noise ratio (SNR).

3.2 Methods to estimate K-factor

3.2.1 Classification of methods

In general, based on the estimation technique, we can organize the K-factor estimations in two categories: maximum-likelihood methods and moment-based methods. For each of these techniques the fading signal can be complex or real. Some estimators consider independent and noiseless channel realizations, while others include the channel noise in estimation and the realizations can be correlated. Also, there are estimators for which the specular components are considered as time invariant, while others include the Doppler variation of specular components.

The maximum likelihood methods result in efficient estimates for the unknown parameters of a given pdf (e.g., Rician fading pdf when estimating K-factor). The disadvantage of this method is the complexity of implementation, which is a time-consuming and computationally extensive procedure. In these conditions, not being suited for real-time implementation, this approach is more useful for testing whether the measured envelope is Rician distributed rather than estimating K-factor. Various approaches have been done to find the K-factor using maximum-likelihood methods. Using realizations of the phase and envelope of the fading signal two methods to extract K-factor from independent and identically distributed (i.i.d.) complex Rician fading channel, incorporating the specular Doppler shift, are presented in [9, 12]. In [13] the maximum-likelihood estimate is obtained using an expectation maximization algorithm [14]. This method reduces the computational complexity but it is not easy to use in a communication scenario. In [15] is derived a maximum-likelihood estimator using complex realizations which is later improved in [16, 17].

Simpler than the alternatives mentioned above are the moment-based methods. These have received more attention because of their simplicity and computational efficiency. As for the maximum-likelihood methods, some techniques use measurements of the received fading envelope or complex realizations. The envelope base moment methods are not optimal in coherent wireless systems because they do not take into account the additional phase information of the complex fading realizations. The estimation is done by equating a function of K-factor to a ratio of the measured moments. For example, in [18, 19] the first and second order moments of the fading envelope are used. In general, using the first two moments, the K-factor is extracted through the research of the roots of a nonlinear equation. Another way is to compute the distribution of the fading envelope and then to compare it with a set of distributions using a suitable goodness-of-fit test. A simpler solution is presented in [4]

in which two simple K-factor estimations are obtained by approximating the moments ratio with a linear and quadratic function. In [3, 20] the estimated K-factor is extracted from the ratio of the second and the 4th moments of the fading envelope. Compared with the envelope-based estimators, the use of complex fading realization can improve the performances of the K-factor estimate. For example in [5] is proposed an estimator using complex realizations suitable for the situation when the specular component is time-variant and/or the realizations are correlated. In [17] a similar estimator includes a correction factor which improves its performances. In [21, 22], the second-order fading statistics of the channel are used to derive K-factor estimators which work with independent and noisy correlated realizations.

Beside the above presented methods, there are other techniques which can be used to estimate K-factor. For example in [23] the K-factor is estimated based on the fading of the instantaneous frequency (which is the time derivative of the fading phase).

3.2.2 Selection of different methods to compute K-factor

From the multiple methods to estimate K-factor, we choose the methods which provide a quick result (i.e., these methods do not need an iterative algorithm to give a final result) and which can be applied in reverberation chamber. For each of them a short description is presented in the following lines and later we analyze the performances of the chosen estimators based on statistical analyses. Compared with the previous classification, in this section we have reorganized the chosen methods depending on the type of the measured fading signal (complex or real), and considering both maximum-likelihood and moment-based estimators.

The first set of estimators use complex fading realizations. Compared with the methods which use only the fading envelope or the fading phase, these methods are more robust with channels perturbations, as they have access on two information: the phase and the amplitude of the fading. A first chosen method, among these, uses the fading envelope and the fading phase [12]. From the joint pdf of envelope and phase, and considering N i.i.d. fading channel realizations of envelope $r = \{r(1), r(2), \ldots, r(N)\}$ and phase $\Theta = \{\Theta(1), \Theta(2), \ldots, \Theta(N)\}$ by applying log-likelihood function it results the following K estimator:

$$\widehat{K}_{\mathrm{a}} = \frac{\frac{1}{N}\sum_{p=1}^{N} r(p)\cos\left(\Theta(p) - \widehat{\theta}_0\right)}{\frac{1}{N}\sum_{p=1}^{N} r(p)^2 - \widehat{A}^2} \tag{3.1}$$

with

$$\widehat{\theta}_0 = \arctan\left[\frac{\sum_{p=1}^{N} r(p)\sin\Theta(p)}{\sum_{p=1}^{N} r(p)\cos\Theta(p)}\right] \tag{3.2}$$

and

$$\widehat{A} = \frac{1}{N}\sum_{i=1}^{N} r(p)\cos\left(\Theta(p) - \widehat{\theta}_0\right). \tag{3.3}$$

Another option to estimate the K-factor is the use of the real and imaginary part of complex fading signals $H = H_{\mathrm{I}} + H_{\mathrm{Q}}$ as it is presented in [2]. The method uses the estimated mean and

variance of the complex fading signals (e.g., the measured S_{21} parameters in reverberation chamber) over the N realizations (e.g., stirrer positions) and is computed as:

$$\widehat{K}_* = \frac{|E_N[H]|^2}{\mathrm{Var}[H_\mathrm{I}] + \mathrm{Var}[H_\mathrm{Q}]}, \tag{3.4}$$

where

- $E_N[\square]$ is the expected value over N realizations, and
- $\mathrm{Var}[\square]$ represents the variance over the same number of realizations as above.

A supplementary stirring process increases the number of realizations at a value of MN, and the new estimator becomes as [16, 17]:

$$\widehat{K}_\mathrm{b} = \frac{N-2}{N-1} E_M\left[\widehat{K}_*\right] - \frac{1}{N} \tag{3.5}$$

where

- $E_M[\square]$ is the expected value over M samples (which may correspond to several antenna positions, frequency stirring, etc.)

Other methods, simpler than those mentioned above, use only the received fading phase or the fading envelope. In [12] is presented a method which uses the maximum-likelihood applied on the realizations of the fading phase. This estimator cannot be used properly when the specular component becomes very low, but this approach is still useful for systems which use the phase for synchronization. The expression for K-factor is given by:

$$\widehat{K}_\mathrm{c} = \frac{N}{2\sum\limits_{p=1}^{N} \sin^2\left(\Theta(p) - \widehat{\theta}_0\right)} \tag{3.6}$$

Having measured the fading envelope with an oscilloscope (in time domain) or a spectrum analyzer (in frequency domain) several methods can be applied. Such methods are not solid in coherent wireless systems because they do not take into account the additional phase information provided by the complex baseband realizations. The main advantage of these estimators is represented by the optimal compromise between computational convenience and statistical efficiency, and it can be used for practical applications. The main disadvantage is the limited K-factor interval in which these methods can be used (i.e., approximately from values of K-factor bigger than 0 dB as it is presented later).

As presented in [4] K-factor can be extracted from the approximation of the moments ratio $P = \widehat{\mu}_1/\sqrt{\widehat{\mu}_2}$ between the first $\mu_1 = E_N[r]$, and the second order moments $\mu_2 = E_N\left[r^2\right]$, of the fading envelope. Using a fitting process, two estimators are obtained:

- a first degree estimator:

$$\widehat{K}_\mathrm{d} = \frac{P - p_0}{p_1 - P}, \tag{3.7}$$

with $a_0 = 0.9969$ and $a_1 = 0.7967$,

- and a second degree estimator given by:

$$\widehat{K}_{\mathrm{e}} = \frac{P - q_1 + \sqrt{(P - q_1)^2 + 4q_2 (P - q_0)}}{2q_2}, \tag{3.8}$$

  with $b_2 = 0.0005$, $b_1 = 0.9866$ and $b_0 = 0.8293$.

Another envelope estimator is presented in [3, 5]. It is extracted from the ratio between the second, μ_2, and the fourth order moments, $\mu_4 = E_N\left[r^4\right]$, of the received envelope, resulting a K-factor estimation, simple and easy to implement in practice:

$$\widehat{K}_{\mathrm{f}} = \frac{-2\widehat{\mu}_2^2 + \widehat{\mu}_4 - \widehat{\mu}_2\sqrt{2\widehat{\mu}_2^2 - \widehat{\mu}_4}}{\widehat{\mu}_2^2 - \widehat{\mu}_4}. \tag{3.9}$$

We obtain the same estimator as in (3.9) if using the recurrence identity between the first $L_1(x)$ and the second $L_2(x)$ Laguerre polynomials (see annex C.4) [24]:

$$\begin{aligned} &2L_2(-K) = (3 + K) L_1(-K) - 1, \\ &\text{and} \begin{cases} \mu_2 = 2\sigma^2 L_1(-K), \\ \mu_4 = 8\sigma^4 L_2(-K). \end{cases} \end{aligned} \tag{3.10}$$

3.2.3 Validation of the methods

In order to characterize the above selected estimators, we perform several Monte Carlo simulations and measurements in reverberation chamber.

Simulations

Simulations consist in generating a random set of values with a certain distribution (one single generating value is named a realization/experiment) and repeating this process several times to evaluate the quality of estimation (repetition which is called trial). The Rician envelope is obtained by calculating the absolute value of the Gaussian complex distribution whose average is given by the specular component and variance given by the scattered components [10].
The Monte Carlo simulations are performed by considering a number of 5000 realizations (e.g., 100 are equivalent to mechanical stirring while 50 are equivalent to frequency stirring), and 10 000 trials. To carry out the Monte Carlo simulations we use the following method: let X and Y be two independent normally-distributed random values with mean A (i.e., the amplitude of specular component) and standard deviation σ (i.e., the amplitude of scattered components). Because the measurements (presented later) are done in a frequency range in which the modal density is mainly influenced by chamber losses and less by antennas, the scattered energy is proportional with the quality factor of the chamber ($\approx 1/\sqrt{f}$ [25]), resulting that the variance of scattered components barely changes with frequency in a small bandwidth. In simulations $\sigma = 1$ as we evaluate the K-factor with the variation of A. For each value of $K \in [-30, 30]$ dB, A is deduced from $K = A^2/\left(2\sigma^2\right)$ [5]. Then we compute the signal envelope as $\sqrt{X^2 + Y^2}$. The analysis of these estimators is done using three measures of the K-factor estimation quality: the rejection rate, the bias between the expected and the true value of K-factor, and the confidence interval (CI) computed at a 95% level of confidence.

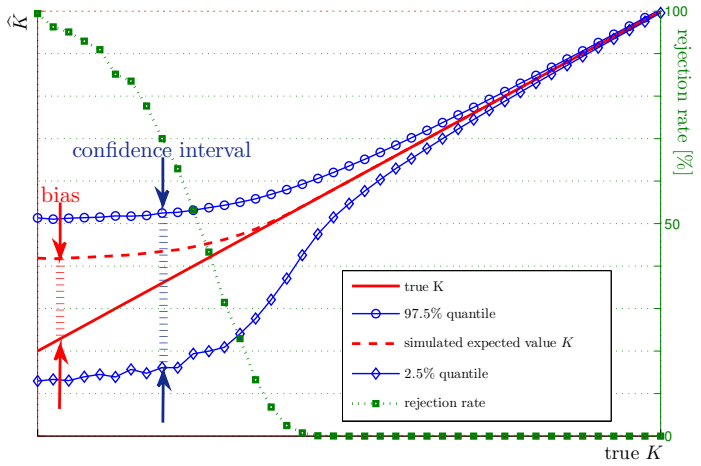

Figure 3.1: Rejection rate, bias and confidence interval to characterize K-factor.

In Fig. 3.1 is presented an example of these parameters as they are extracted from the simulations results. The results show that for some estimators and ranges of K-factor the effect of mathematical functions which depends on rather poorly estimated parameters and the limited number of realizations possibly yields undefined values which can be negative or complex. These erroneous values have to be discarded from the final analysis. The percentage of these absurd values, either complex or negative, represents the rejection rate. The distribution of these values with the level of K-factor is presented in Fig. 3.2. Identifying the two types of errors (i.e., negative or complex values) we can see that the estimators which use the complex samples and the estimators which use the envelope are affected by negative values. Moreover, the estimator which uses the second and the fourth moments is affected by the emergence of complex values. Depending on the accepted limit of the absurd values, due to this problem one can obtain a very short useful range of K.

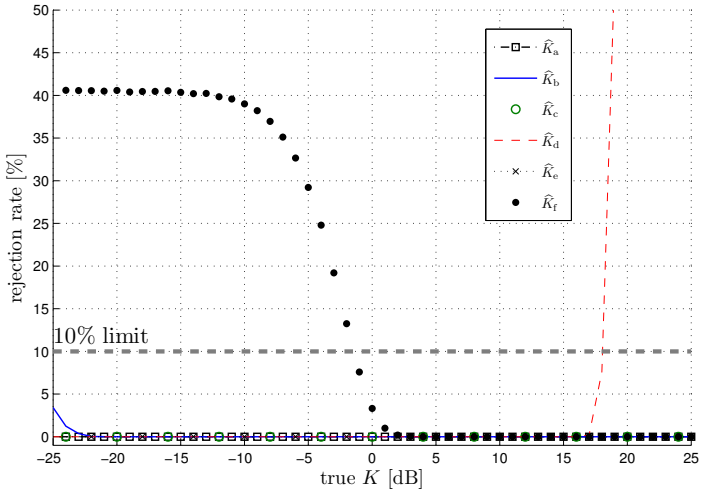

Figure 3.2: Rejection rate over the variation of K-factor using Monte Carlo simulations.

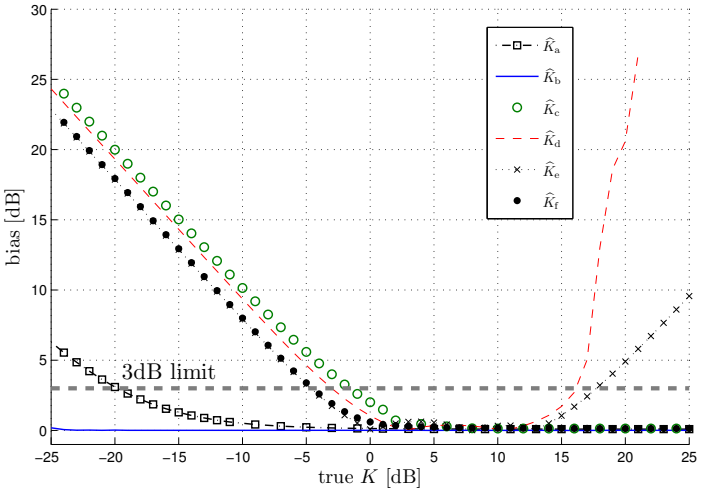

Figure 3.3: Comparison between the biases of different estimations of K-factor using Monte Carlo simulations.

From the Fig. 3.3, the analysis of biases indicates that the methods which use the complex envelope (i.e., amplitude and phase) or complex Gaussian variables offer good results starting with low values of K-factor (around $-32, -20\,\text{dB}$). The estimators which use the phase or the envelope are not optimized for small values of K-factor ($K < 0\,\text{dB}$), resulting in a strong bias. Having only information about the amplitude or phase makes these estimators more sensitive to uncertainty and therefore sample size. We conclude that we can use an envelope estimator from values of K-factor bigger than $-4, -3\,\text{dB}$ while a phase estimator can be used starting from $-2, -1\,\text{dB}$.
Regarding the confidence interval, from Fig. 3.4 one can see that complex envelope estimators and phase estimators have a short confidence interval for $K < 0\,\text{dB}$, while for envelope estimators the confidence interval increases strongly even for positive values of K. One possibility to reduce the confidence interval is to increase the sample size. In the case of measurements, the sample size is limited by the condition to have a low correlation factor between successive realizations.
Using the analysis presented above and accepting a rejection rate of 10% (absurd values), a maximum bias of 3 dB, and a maximum confidence interval of 6 dB we show that the choice of an estimator should be done according to the range of use in Table 3.1.

Measuring K-factor in reverberation chamber

In order to analyze the variation of K-factor in reverberation chamber from the results from Table 3.1, we select the estimator which gives the largest usable range, $\widehat{K}_b$. We evaluate this parameter in different measurement configurations. In order to change the value of this parameter we use [2]. In the hypothesis that all the reflected components interact with the paddle and there is only one unstirred component (as predicted by the Friis formula) the K-factor in reverberation chamber is defined with:

$$K = \frac{V}{\lambda Q}\frac{1}{d^2} D_1 \eta_1 D_2 \eta_2 \left(\rho_1 \rho_2\right)^2, \tag{3.11}$$

where:

- V is the chamber volume,
- Q is the total quality factor (i.e., in general it is influenced by the quality factor of the chamber),
- D_1 and D_2 are the directivities of the transmitting and receiving antennas,
- η_1 and η_2 are the total efficiencies

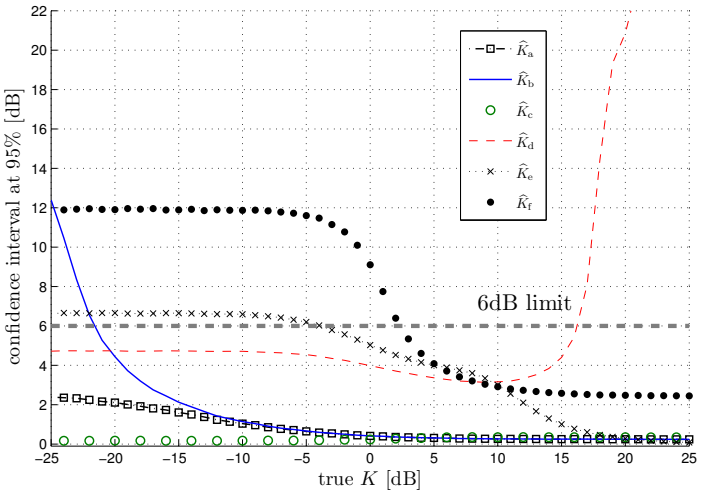

Figure 3.4: Comparison between the CI of different estimations of K-factor using Monte Carlo simulations.

Table 3.1: Useful K-factor intervals for 10% rejection rate, 3 dB bias, and 6 dB confidence interval.

Type of estimator	**Range of K[dB]**
$\widehat{K}_a$ [12]	> -20
$\widehat{K}_b$ [16, 17]	> -24.75
$\widehat{K}_c$ [12]	> -1.75
$\widehat{K}_d$ [4]	$[-2.75, 16.15]$
$\widehat{K}_e$ [4]	$[-3.90, 17.75]$
$\widehat{K}_f$ [3, 5]	≥ 2.40

- $(\rho_1\rho_2)$ is the polarization loss factor,
- d is the free-space propagation distance between antennas.

It results that the level of measured K-factor depends not only on transmission system (i.e., using different antennas will provide other results) but also on the propagation environment (i.e., the degree of absorption, the distance between the transmitter and receiver).
The experiments are made in the reverberation chamber of our laboratory. These measurements are performed using a vector network analyzer (VNA-Agilent N5230A) in a frequency bandwidth between $1-2\,\text{GHz}$ (which is well above the lowest usable frequency, 250 MHz, of the chamber [26]), with a frequency step of 200 kHz. The two horn antennas (ETS Lindgren-model 3115) are placed at distances varying from 1 to 4 m, and the chamber is loaded with different quantities of absorbing materials (having dimensions $0.6 \times 0.6 \times 0.15\,\text{m}^3$), Fig. 3.5. The mechanical stirrer is used to create a statistical distribution of modes while frequency stirring expands this distribution, increasing the number of trials. Depending on the type of parameter we want to estimate, we may want to measure the signal in transient or steady state regime. In this chapter, we measure a steady state parameter of the signal in frequency domain. When using the VNA sweep time has to be chosen appropriately so that the steady state is reached. Otherwise we may measure a transient signal instead of the desired steady state signal. For example in Fig. 3.6 is presented a comparison between the estimated K-factor from a signal measured after only 5 µs (for 20001 frequencies it represents a sweep time of 0.1 s) and the one estimated from a signal measured after 50 µs (for 20001 frequencies the sweep time is 1 s). With the time more secondary stirred components arrive at reception which will decrease the value of K-factor, the differences between the two estimation could be as high as 3 dB. Another way to make the measurements is to use a synchronized oscilloscope with the signal generator, and then to measure the signal in steady state. We avoid this method because of the high level of noise compared with its level on the VNA. Moreover, if we want to analyze the signal with the variation of frequency it will take more time using an oscilloscope than a

Figure 3.5: Reverberation chamber measurement configuration.

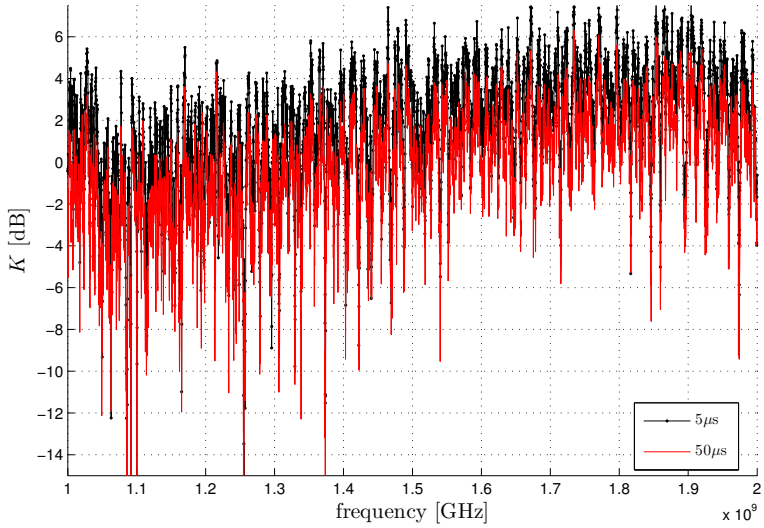

Figure 3.6: The effect of the frequency sweep duration on the estimated value of K-factor.

VNA. The measurements in frequency domain can be also made using a spectrum analyzer, but in these conditions we do not have any information about the phase. It results that this type of data can be used only to evaluate envelope-based estimators.
In Fig. 3.7 we present the results for the case when measurements are made for a distance of 1 and 4 m between antennas, and when the absorbers are not used. From this figure one can see that with the decrease of distance, but still avoiding the near field situations the K-factor increases, result which is expected as there is a stronger specular path. The small fluctuations in the result at 1 m are especially due to small estimation uncertainties which depends on the type of estimator and the number of observations. To reduce the estimator's uncertainties highlighted in Fig. 3.7 a supplementary stirring mechanism can be used. Enlarging the distance between antennas to 4 m the level of K-factor reduces and more fluctuations in the estimation of this parameter appear. The total specular component at reception can reach very small values and due to an increase of the level of uncertainty it can strongly influence the estimation of K-factor. These fluctuations could also be explained by the antenna's fast gain changes with frequency. However, antennas datasheets show that the rate of gain fluctuations with regard to frequency is much slower. Even if the variation of the gain is not flat with frequency, it does not change rapidly with frequency, (Fig. 3.8). A better explication is the fact that with the distance additional secondary specular components arrive at reception having a stronger influence in the final signal. These components do not reflect on the stirrer, characterizing its ineffectiveness. These fluctuations are generated by the phases combinations between specular paths which change with frequency. To diminish the effects of multiple additions of the specular components one solution is to make measurements at several antenna positions (keeping the same distance between antennas) or several polarizations (which are changed simultaneously for both antennas). For a better understanding of the K-factor fluctuations we analyze the specular phase, which is independent of the stirrer positions, Fig. 3.9. Also we compare the estimated phase from measurements with the theoretical specular phase (which depends only on the frequency and the distance between antennas). The ripples of the phase, whose density increases with the distance, are due to secondary specular components.

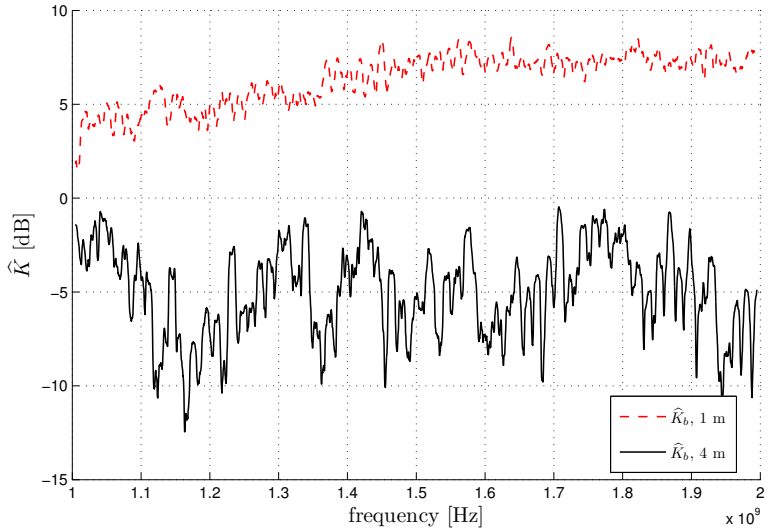

Figure 3.7: Experimental results for K-factor computed at a distance of 1 and 4 m; reverberation chamber is not loaded with absorbers.

We conduct one more measurement, this time loading the chamber with absorbers and measuring the K-factor as before for different distances between antennas and the phase of unstirred components. In general when absorbers are placed somewhere in the chamber, but not between the emission and reception antennas, they influence more the stirred energy and less the energy of secondary unstirred components. In this way, for the same distance between antennas, the value of K-factor should increase and the fluctuations in the measured values should be similar as for the case when no absorbers are used. The results are shown in Fig. 3.10. Even if the variations of the total specular phase are slightly reduced, the increased level of K at 1 and 4 m have the same pattern as when the reverberation chamber is not loaded. It

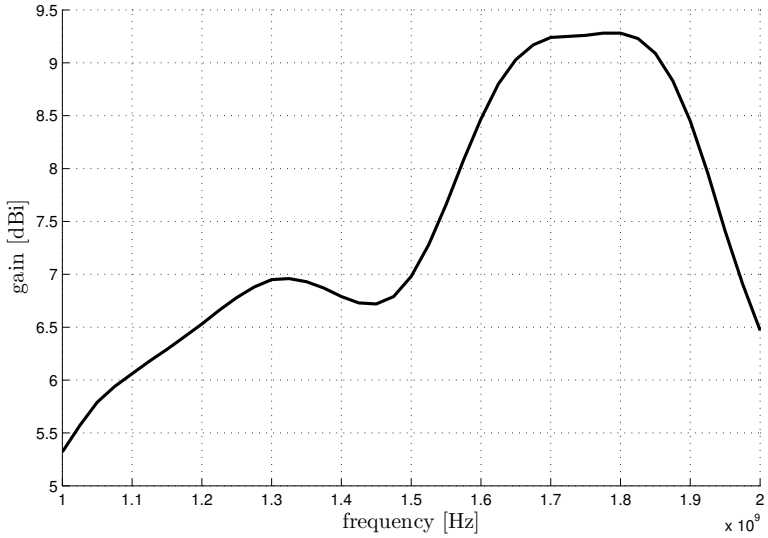

Figure 3.8: Measured horn antenna gain model 3115 in near-field-chamber.

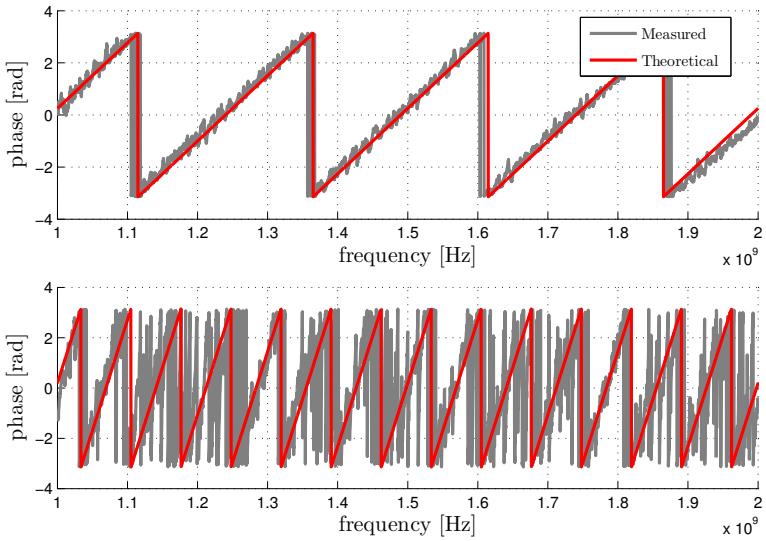

Figure 3.9: The specular phase, for distances between antennas of 1 m (top) and 4 m (bottom); reverberation chamber is not loaded with absorbers.

results that the hypothesis is verified. We also present the phase of unstirred components in the presence of absorbers, Fig. 3.11. Compared with the previous situation, Fig. 3.9, the fluctuations in the phase of unstirred components are slightly reduced. This is due to a small absorption of secondary unstirred components by the absorbers which is more visible when the distance between antennas increases to 4 m.

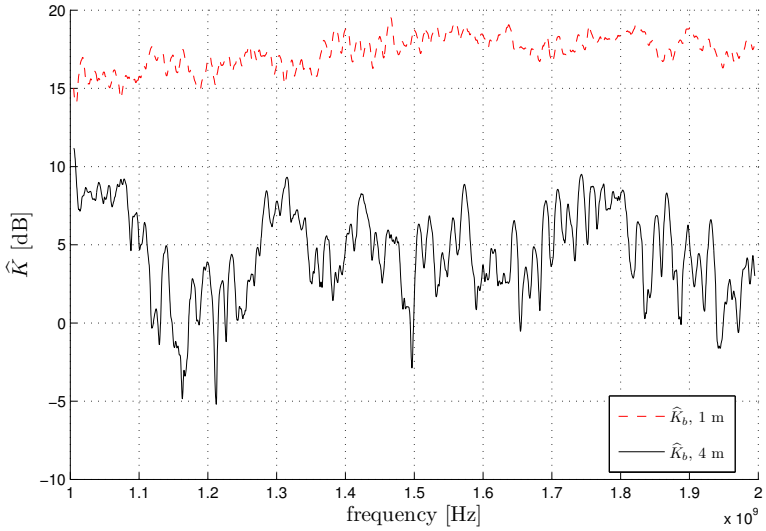

Figure 3.10: Experimental results for K-factor computed at a distance of 1 and 4 m; reverberation chamber is loaded with absorbers.

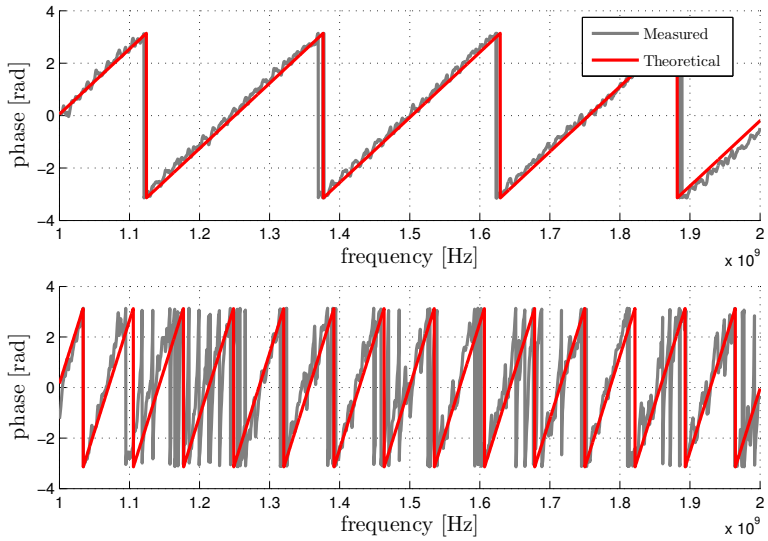

Figure 3.11: The specular phase, for distances between antennas of 1 m (a) and 4 m (b); reverberation chamber is loaded with absorbers.

3.2.4 The necessity of new estimators: two extreme situations

In a real environment the K-factor may fluctuate over high ranges of values. From table 3.1 we have seen that there are some estimators (i.e., envelope and phase based) which can provide acceptable results only in a limited range of values. We test different measurement configurations for which the above estimators may not work anymore. The two extremes values (very low and very high K-factors) are controlled by changing the distance between antennas and their relative orientation (line-of-sight or non-line-of-sight) and also adding/removing absorbing materials from reverberation chamber (practically changing the quality factor of the chamber). Two qualitative examples are presented in Fig. 3.12 ((a) and (b)). First, to obtain the results in Fig. 3.12(a) the antennas are placed at very small distances between them (0.5 m) in a line-of-sight configuration and the chamber is loaded with three parallelepiped absorbers. For the second example, Fig. 3.12(b), the antennas are placed as before but the distance between them is 6 m and the chamber is not loaded with absorbers. The frequency bandwidth is the same as before between 1 to 2 GHz. For the situation in Fig. 3.12(a), we can see that as the value of K increases beyond a limit, not all estimators give the same results. The same problem appears when the distance between antennas increases, the results given by different estimators become strongly dissimilar, Fig. 3.12(b). As discussed before the most biased estimators are those which use the envelope fading and in measurements in real environments it is more difficult to make use of the phase of the signal. Hence the need of a reliable method to compute K-factor in a large range of values when using only the fading envelope. To this end the next section presents two alternatives to estimate the K-factor using the fading envelope only which increase the useful range of values.

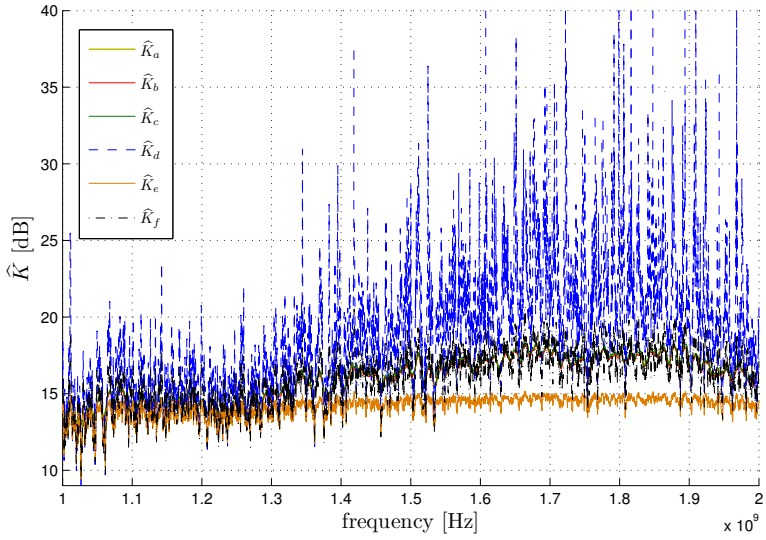

(a)

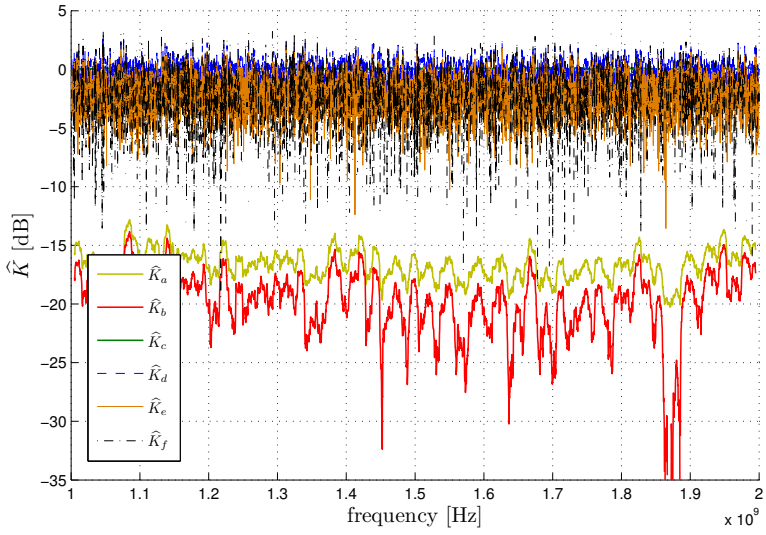

(b)

Figure 3.12: Measured K-factor in reverberation chamber for a distance between antennas of 0.5 m and loading the chamber (a) and for a distance between antennas of 6 m without loading the chamber (b).

3.3 Our proposal for new K-factor estimators

In this section two new improved envelope based estimators are presented. These estimators increase the useful range of K values while having a simple mathematical expression. First part of this section describes a simple and fast method to estimate K-factor while in the second part a more robust estimator which uses a maximum-likelihood method is presented. To prove the utility of the first new estimators, comparisons with other three common envelope based

estimators, with the variation of sample size and signal to noise ratio of realizations are made.

3.3.1 A simple approximation

A first proposed estimator is a fast and easy method to implement using the second moment of the envelope and the second moment of the difference between consecutive data. It is not influenced by erroneous values and gives acceptable results compared with other envelope based estimators. This property is especially useful for the measurements where the sample size is small (e.g., 100 stirrer positions as in reverberation chamber).

The second order moment $E\left[r^2\right]$ of the fading envelope r is defined as the sum of the power of specular, A^2, and scattered components, $2\sigma^2$:

$$E\left[r^2\right] = A^2 + 2\sigma^2, \tag{3.12}$$

where $E\left[\square\right]$ represents the expected value.
When $K = A^2/2\sigma^2$ is small ($K << 1$), the power of specular component becomes insignificant compared with the power of scattered components. One can therefore approximate:

$$E\left[r^2\right] \approx 2\sigma^2. \tag{3.13}$$

If K-factor is big ($K >> 1$) the power of specular components becomes predominant and the total mean power is approximated as:

$$E\left[r^2\right] \approx A^2. \tag{3.14}$$

We denote respectively $\widehat{A^2}$ and $\widehat{2\sigma^2}$ as the estimators of the power of specular and scattered components computed using the fading envelope.
As presented in [5], for $K << 1$ the asymptotic variance (see annex B.6) of the envelope estimators goes to infinity when K-factor goes to zero. It is associated with a non accurate estimation of $\widehat{A^2}$ which is overestimated while $\widehat{2\sigma^2}$ is underestimated. The analysis of these estimators shows that both estimators are in the same range of values:

$$\widehat{A^2} \approx \widehat{2\sigma^2}, \quad \text{for } K << 1. \tag{3.15}$$

Since $A^2 << 2\sigma^2$, it results that the estimation $\left\langle r^2 \right\rangle_N$ of the second order moment of the fading envelope for a N sample size is given by

$$2\sigma^2 \approx \left\langle r^2 \right\rangle_N \approx \widehat{A^2} + \widehat{2\sigma^2} \approx 2 \times \widehat{2\sigma^2}, \quad \text{for } K << 1, \tag{3.16}$$

where $\langle \cdot \rangle_N$ denotes the average over N realizations.
For $K >> 1$, the estimators of the power of the specular and scattered components are well defined:

$$A^2 \approx \left\langle r^2 \right\rangle_N \approx \widehat{A^2}, \text{and } 2\sigma^2 \approx \widehat{2\sigma^2}, \quad \text{for } K >> 1. \tag{3.17}$$

The variation of the power of true and estimated specular and scattered components and of the estimated second order moment of the envelope are presented in Fig. 3.13. Consequently, the impact of the correction factor must be significant only for small values of K-factor ($K << 1$). By using the (3.16) and (3.17) relationships we can approximate the correction factor as $\langle r^2 \rangle_N / \widehat{A^2}$. For big values of K-factor ($K >> 1$) this factor becomes insignificant (≈ 1), while

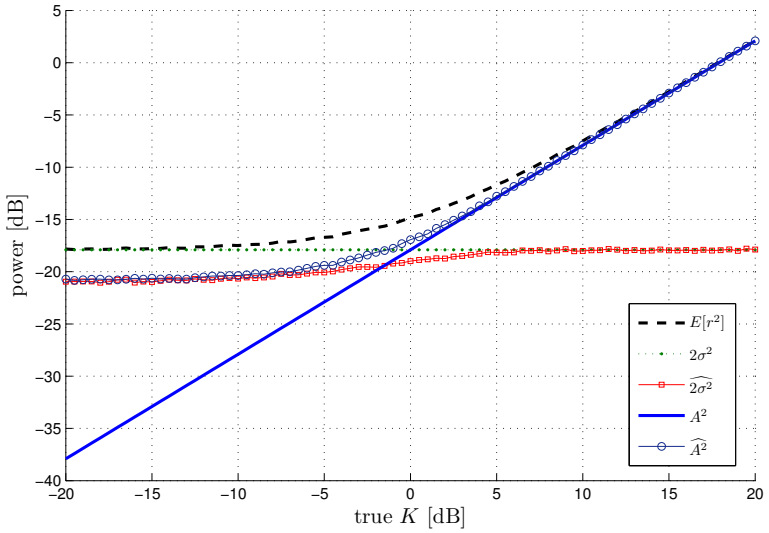

Figure 3.13: Variation of the true and the estimated power of specular and scattered components.

when K-factor is small ($K << 1$), this factor is around a value of 2. The power of the scattered components is approximated with the mean value of the power of the difference between two consecutive measurements of fading envelope:

$$\widehat{2\sigma^2} = \frac{1}{N-1}\sum_{i=1}^{N-1}\left(r_{i+1}-r_i\right)^2 \tag{3.18}$$

To reduce the bias, highlighted previously for $K << 1$, we apply the correction factor $\langle r^2\rangle_N/\widehat{A^2}$ to the estimator of power of stirred components, leading to the following expression:

$$\widehat{2\sigma^2}^* = \frac{\langle r^2\rangle_N}{\widehat{A^2}}\frac{1}{N-1}\sum_{i=1}^{N-1}\left(r_{i+1}-r_i\right)^2 \approx 2\sigma^2. \tag{3.19}$$

The K-factor estimator is defined as the ratio of the two powers, and is therefore given by

$$\widehat{K} = \frac{\widehat{A^2}}{\widehat{2\sigma^2}^*} = \frac{\left(\widehat{A^2}\right)^2}{\langle r^2\rangle_N \times \frac{1}{N-1}\sum_{i=1}^{N-1}\left(r_{i+1}-r_i\right)^2}, \tag{3.20}$$

In this equation the power of specular components $\widehat{A^2}$ is computed as:

$$\widehat{A^2} \approx \langle r^2\rangle_N - \frac{1}{N-1}\sum_{i=1}^{N-1}\left(r_{i+1}-r_i\right)^2. \tag{3.21}$$

Validation

The Monte Carlo simulations are performed by considering a number of 100 realizations (i.e., the number of independent stirrer positions in the frequency bandwidth 1 – 2 GHz), and 50 000 trials. As presented in the above section, in general an envelope estimator is

lower bounded due to an increase bias. Simulations presented in this section are only for a range of $K \in [-20, 20]$ dB. Comparisons with other envelope-based estimators presented above ($\widehat{K}_{\mathrm{d}}, \widehat{K}_{\mathrm{e}}, \widehat{K}_{\mathrm{f}}$) are done. The analysis of this estimator is done by using the three measures of the estimator quality, presented before: the rejection rate (characterizing erroneous values-negative or complex of K), the bias and the confidence interval.

From the Fig. 3.14, which provides the rejection rate, one can see that the first new estimator (3.20) is not affected by this issue. The other estimators are affected: $\widehat{K}_{\mathrm{f}}$ for small values of K-factor ($K < 0$ dB) and $\widehat{K}_{\mathrm{d}}$ for big values of K-factor ($K > 16$ dB). The estimator $\widehat{K}_{\mathrm{e}}$ is slightly affected for $N = 100$. However the rejection rate increases up to 6% for $N = 50$.

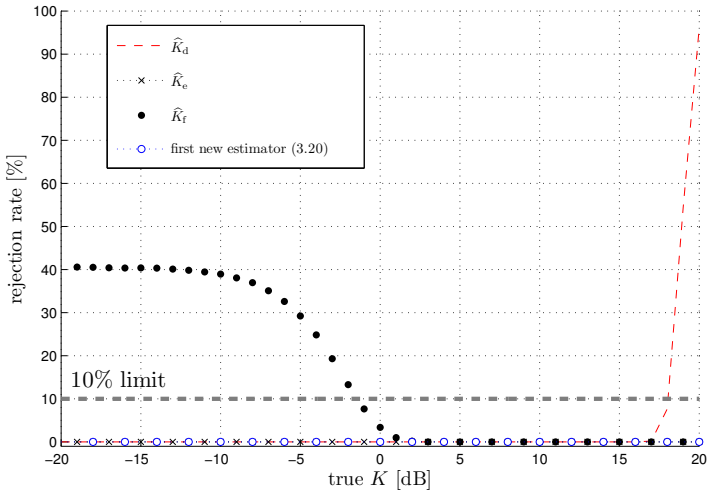

Figure 3.14: Comparison between different rejection rates of K-factor (Monte-Carlo simulation).

Fig. 3.15 shows the confidence interval results. The first new estimator (3.20), has a better confidence interval for small values of K-factor ($K < 3$ dB) compared with $\widehat{K}_{\mathrm{f}}$ while it gives results in the same range as $\widehat{K}_{\mathrm{d}}$. For values of $K > 3$ dB, the first new estimator (3.20) differs from $\widehat{K}_{\mathrm{f}}$ by only 0.5 dB. For $K > 10$ dB the CI of the first new estimator and $\widehat{K}_{\mathrm{f}}$ are in the same range of values, the CI of $\widehat{K}_{\mathrm{d}}$ decreases, and the CI of $\widehat{K}_{\mathrm{e}}$ increases greatly.

Fig. 3.16 presents the bias between the true and the estimated value of K. One can see that the bias for the first new estimator (3.20) is almost identical with the $\widehat{K}_{\mathrm{f}}$ for big values of K-factor and has a small deviation from these estimators, less than < 1 dB, for values of $K < 0$ dB. The estimators which are the most affected by the bias are the $\widehat{K}_{\mathrm{d}}$ and $\widehat{K}_{\mathrm{e}}$ estimators.

The estimator (3.20) is further tested with regards to the signal to noise ratio and some relevant results can be drawn. Simulations show that when $K < 0$ dB the impact of SNR on the bias remains negligible (< 1 dB) for small values of SNR (< 15 dB). The reason is that all envelope estimators have already a high bias for low values of K-factor so the influence of the noise is not relevant. When $K > 0$ dB, the bias decreases with SNR and increases with K-factor leading to significant values. For example, for $K = 10$ dB and SNR = 5 dB the bias is 6 dB using the estimator (3.20), a maximum of 6.3 dB using $\widehat{K}_{\mathrm{d}}$ and $\widehat{K}_{\mathrm{e}}$, and 7 dB using $\widehat{K}_{\mathrm{f}}$. As far as the confidence interval is concerned, in the simulation interval of SNR = $[0, 30]$ dB and $K \in [-20, 20]$ dB, we find a maximum fluctuation of 2.5 dB for the first new estimator (3.20),

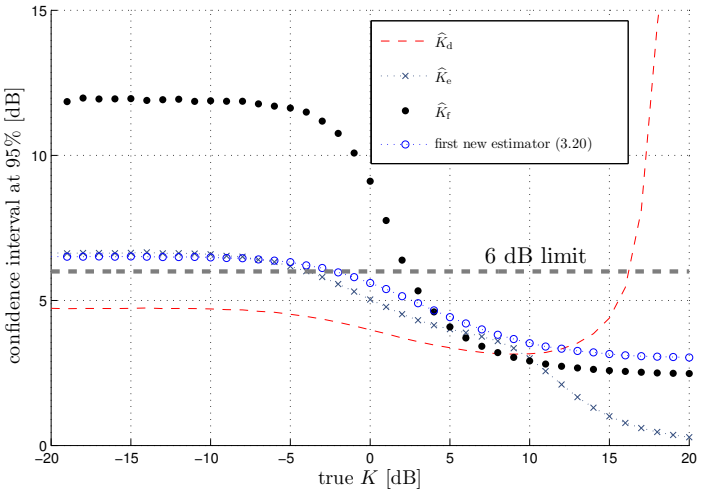

Figure 3.15: Comparison between different confidence intervals at 95% of K-factor (Monte-Carlo simulation).

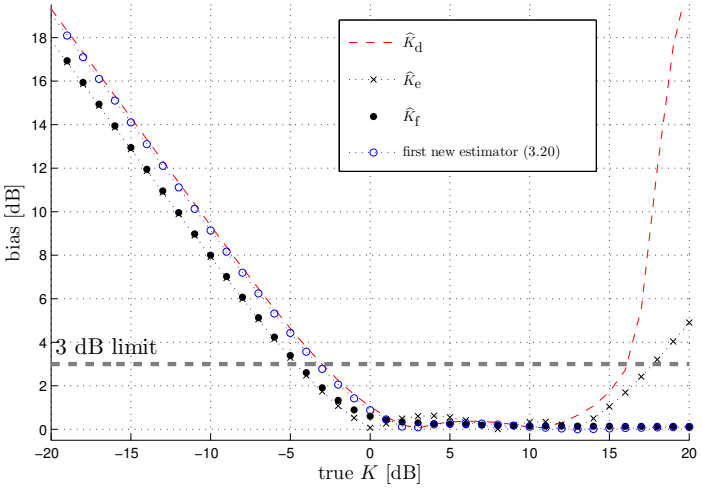

Figure 3.16: Comparison between different biases of K-factor (Monte-Carlo simulation).

1 dB for $\widehat{K}_{\mathrm{d}}$ and $\widehat{K}_{\mathrm{e}}$, and 9.5 dB for $\widehat{K}_{\mathrm{f}}$. While the rejection rate does not affect the first new estimator (3.20), the rejection rate slightly increases for $\widehat{K}_{\mathrm{f}}$ as SNR decreases under 10 dB. We have carried out an investigation about the stability of the estimators with respect to the sample size used. We find that the bias related to the first new estimator (3.20) does not decrease very much with the increasing of the sample size compared with the other estimators. The bias remains around 0.6 dB for a sample size of $N = 200$, while for $\widehat{K}_{\mathrm{d}}$, $\widehat{K}_{\mathrm{e}}$ and $\widehat{K}_{\mathrm{f}}$ the bias stabilizes around 0.06 dB for $N = 500$. If the sample size increases the confidence interval changes strongly, becoming much narrower, for all the estimators. The confidence interval of the first new estimator (3.20) is always smaller than for $\widehat{K}_{\mathrm{d}}$, $\widehat{K}_{\mathrm{e}}$ and $\widehat{K}_{\mathrm{f}}$. The rejection rate decreases with the sample sizes for $\widehat{K}_{\mathrm{d}}$, $\widehat{K}_{\mathrm{e}}$ and $\widehat{K}_{\mathrm{f}}$.

It results that the first new estimator (3.20), which is a simple approximation based on the analysis of the specular and scattered powers, gives good results compared with other envelope estimators and it can be used successfully in a large range of K-factor values.

3.3.2 A maximum-likelihood approximation

The second new estimator we suggest here is computed with a maximum-likelihood method based on an approximation of the modified Bessel function of first kind. We recall the pdf of the Rician fading envelope r as:

$$\begin{aligned} f(r|A,\sigma) &= \frac{r}{\sigma^2}\exp\left(-\frac{A^2+r^2}{2\sigma^2}\right) I_0\left(\frac{rA}{\sigma^2}\right) \\ &= \frac{2r\,(K+1)}{A^2+2\sigma^2}\exp\left(-K-\frac{(K+1)\,r^2}{A^2+2\sigma^2}\right) I_0\left(2r\sqrt{\frac{K\,(K+1)}{A^2+2\sigma^2}}\right), \end{aligned} \tag{3.22}$$

where $I_n\,(\square)$ is the modified Bessel function of first kind and nth order.
The second new estimator is extracted from an approximation of the series expansion at $z \to \infty$ of the modified Bessel function of first kind:

$$I_0\,(z) \approx \frac{e^z}{\sqrt{2\pi z}}. \tag{3.23}$$

Using (3.23), the natural logarithm of the zeroth order modified Bessel function of first kind, when $z = rA/\sigma^2$, becomes:

$$\ln\left(I_0\left(\frac{rA}{\sigma^2}\right)\right) \approx \frac{rA}{\sigma^2} - \frac{1}{2}\ln\left(2\pi\frac{rA}{\sigma^2}\right). \tag{3.24}$$

For a set of N realizations $r(1), r(2), r(3), \cdots r(N)$, the likelihood function of the pdf of the Rician fading envelope is defined with:

$$\mathcal{L}(A,\sigma|r(1),r(2),\ldots,r(N)) = f(r(1),r(2),\ldots,r(N)|A,\sigma) = \prod_{p=1}^{N} f(r(p)|A,\sigma). \tag{3.25}$$

Applying the logarithm to this function the log-likelihood is given by:

$$\ln\mathcal{L}(A,\sigma|r(1),r(2),\ldots,r(N)) = \sum_{p=1}^{N} \ln f(r(p)|A,\sigma). \tag{3.26}$$

Using the approximation in (3.24), the maximum log-likelihood of the Rician pdf becomes:

$$\ln\left(\prod_{p=1}^{N} f\left(r\left(p\right)|A,\sigma\right)\right) = \sum_{p=1}^{N} \ln r\left(p\right) - N\ln\sigma^2 - N\frac{A^2}{2\sigma^2} - \frac{\sum_{p=1}^{N} r\left(p\right)^2}{2\sigma^2} + \sum_{p=1}^{N}\left(\frac{r\left(p\right)A}{\sigma^2} - \frac{1}{2}\ln\left(2\pi\frac{r\left(p\right)A}{\sigma^2}\right)\right) \overset{\text{noted}}{=} \ln\mathcal{L}. \tag{3.27}$$

The power of the specular $\widehat{A}^2$ and scattered components $2\widehat{\sigma}^2$ are computed by maximizing the approximation of the log-likelihood of the Rician pdf (3.27):

$$\begin{cases} \dfrac{\partial \ln\mathcal{L}}{\partial A} = 0, \\ \dfrac{\partial \ln\mathcal{L}}{\partial \sigma} = 0. \end{cases} \tag{3.28}$$

from which it results the following equations system:

$$\begin{cases} 2NA^2 - 2A\sum\limits_{p=1}^{N} r(p) + N\sigma^2 = 0, \\ N\sigma^2 - \sum\limits_{p=1}^{N} r(p)^2 - NA^2 + 2A\sum\limits_{p=1}^{N} r(p) = 0. \end{cases} \tag{3.29}$$

For the estimation of $\widehat{A}$ it results two solutions. The first solution is given by:

$$\widehat{A} = \frac{2\widehat{\mu}_1 + \sqrt{4\widehat{\mu}_1^2 - 3\widehat{\mu}_2}}{3}, \tag{3.30}$$

while the other solution does not have any physical meaning. The parameter σ^2 is computed with:

$$\widehat{\sigma}^2 = 2\widehat{A}\left(\widehat{\mu}_1 - \widehat{A}\right). \tag{3.31}$$

The estimators $\widehat{\mu}_1$ and $\widehat{\mu}_2$ are respectively the first and the second non-central moments of the signal envelope. The above solutions are obtained using a series expansion of the modified Bessel function of first kind. With the decrease of z in (3.23), corresponding to a decrease of K-factor, the bias between the estimated and the true value of K increases. To lower this bias we define an error function of the estimation of scattered components. The input of this function corresponds to $2\widehat{\sigma}^2/\widehat{\mu}_2$ and changes between 0 and 0.5. The output, $\widehat{\sigma}^2/\sigma^2$, changes between 0.5 and 1 and represents the error between the estimated and the true value of scattered components.

$$\mathcal{E}\left(x\right) = -0.145e^{4.9x^2+1.95x} + 1.12, \tag{3.32}$$

where $x = 2\widehat{\sigma}^2/\widehat{\mu}_2$ and $\mathcal{E}\left(x\right) = \widehat{\sigma}^2/\sigma^2$. With this correction the following expression for the estimator of the power of the scattered components results:

$$2\widehat{\sigma}^{2*} = \frac{1}{\mathcal{E}\left(\dfrac{2\widehat{\sigma}^2}{\widehat{\mu}_2}\right)} 2\widehat{\sigma}^2 \approx 2\sigma^2. \tag{3.33}$$

From the definition of K-factor and using (3.30) and (3.33), the second new estimator becomes as follows:

$$\widehat{K} = \frac{\widehat{A}^2}{2\widehat{\sigma}^{2*}} = \frac{1}{4}\frac{\widehat{A}}{\widehat{\mu}_1 - \widehat{A}}\mathcal{E}\left(\frac{4\widehat{A}\left(\widehat{\mu}_1 - \widehat{A}\right)}{\widehat{\mu}_2}\right). \tag{3.34}$$

Simulations

Simulations with the sample size and the signal-to-noise ratio are performed in order to compare the properties of the second new estimator with other common envelope-based estimators $\widehat{K}_{\mathrm{d}}$, $\widehat{K}_{\mathrm{e}}$ and $\widehat{K}_{\mathrm{f}}$ presented in section 3.2.2. As in previous validations, Monte Carlo simulations are performed by using a number of 100 i.i.d. realizations (i.e., the number of independent stirrer positions), and a sample of size $M = 10\,000$. These values are high enough to test the performances of K estimators. The Rician fading envelope is obtained by considering the scattered power $2\sigma^2$ as constant and computing the specular component A^2 as a function of K. The analysis of all the estimators is done using three criteria of the estimation quality: the rejection rate (characterizing erroneous values of K, which can be negative or complex), the bias between the true and the expected value of K, and the confidence interval measured at a 95% level of significance.

Fig. 3.17 presents the variation of the bias as a function of the true value of K. When $K \leq 0\,\mathrm{dB}$ and $K \geq 5\,\mathrm{dB}$, the second new estimator has the smaller bias compared with other chosen estimators. For $K \in (0, 5)$ dB, the bias of the second new estimator increases slightly but it remains in the same range of values as for the other estimators.

The analysis for the 95% confidence interval is shown in Fig. 3.18. While the confidence intervals, for all tested estimators, become comparable when $K \in [5, 10]$ dB and there is a high offset between them when $K > 10\,\mathrm{dB}$. At values of $K < 5\,\mathrm{dB}$ the CI of the second new estimator has a maximum value of $\sim 5.7\,\mathrm{dB}$.

Fig. 3.19 displays the rejection rates which increase for $K < 2\,\mathrm{dB}$. For the second new estimator the maximum rejection rate is $\sim 6\%$. When $K > 2\,\mathrm{dB}$, the rejection rate for all tested estimators is negligible, and only $\widehat{K}_{\mathrm{d}}$ is affected by erroneous values for $K > 16\,\mathrm{dB}$. Using

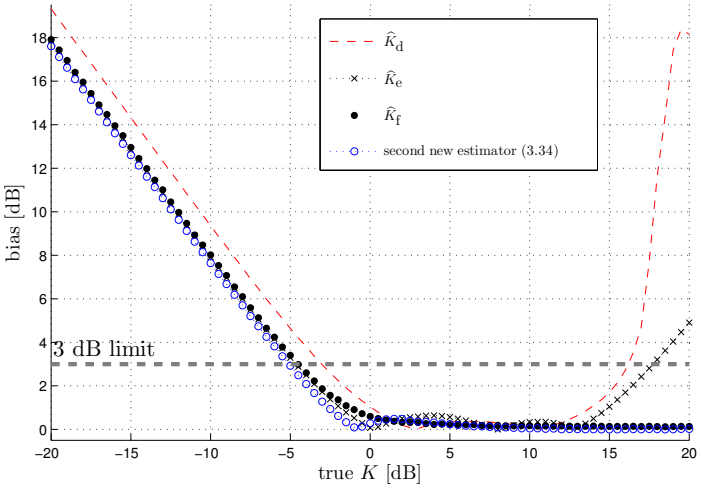

Figure 3.17: Comparisons of K-factors estimators in terms of bias.

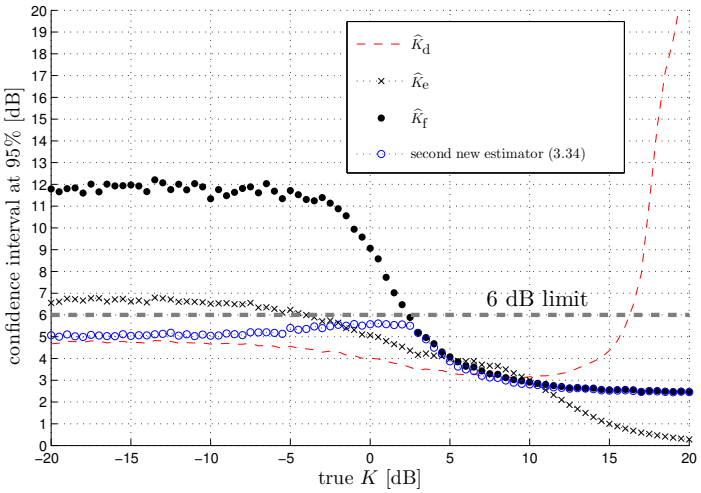

Figure 3.18: The 95% confidence intervals associated with K-factor estimators.

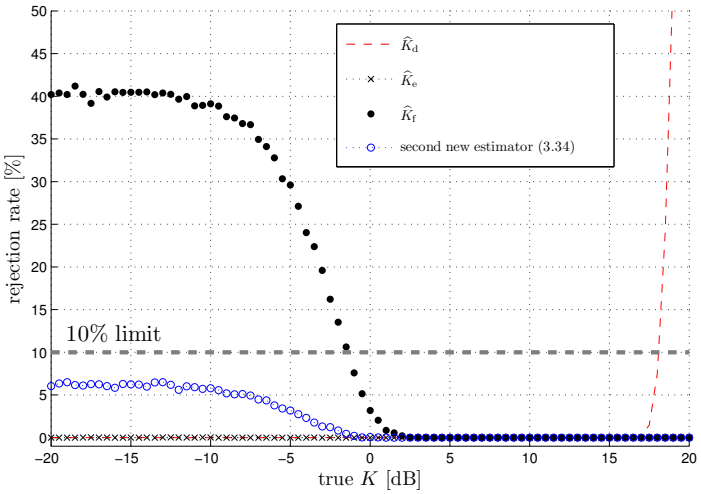

Figure 3.19: Comparisons of K-factor estimators in terms of rejection rates.

Table 3.2: Useful K intervals at 10% rejection rate, 3 dB bias, and 6 dB confidence interval.

Type of estimator	**Range of** K[dB]
$\widehat{K}_{\mathrm{d}}$, [4]	$[-2.75, 16.15]$
$\widehat{K}_{\mathrm{e}}$, [4]	$[-3.90, 17.75]$
$\widehat{K}_{\mathrm{f}}$, [3, 5]	≥ 2.40
first new estimator, (3.20)	≥ -2.20
second new estimator, (3.34)	≥ -5.10

the above analysis, Table 3.2 sums up the useful range of the new and selected K-factors at the same imposed limits as those used in section 3.2.3 (i.e., a bias of 3 dB, a 95% confidence interval of 6 dB, and a maximum rejection rate of 10%). We compare the results for both the first and the second proposed estimators with the three selected envelope-based estimators. It results that both the new envelope-based estimators have their utility. The first estimator has a very simple mathematical form, while the second have the largest useful interval.
Supplementary simulations concerning the root mean square error (RMSE) (see annex B.5) between the estimated and the true value of K-factor are presented in Fig. 3.20. These simulations confirm that the second new estimator provides good results and extends the useful range of K-factor compared with other estimators.

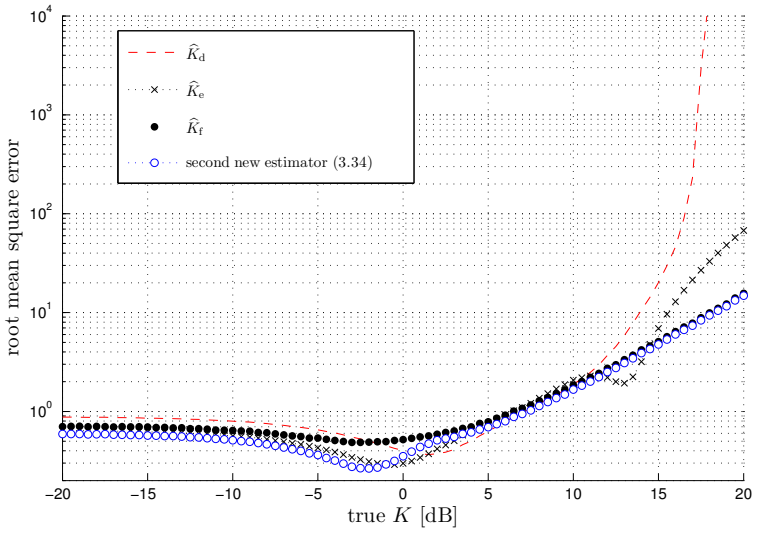

Figure 3.20: The RMSE associated with K-factor estimators.

Robustness to signal-to-noise ratio Depending on the characteristics of the propagation channel, the fading envelope can fluctuate widely. Moreover, due to phase combination between the direct paths, the total specular component can reach very small values becoming hidden by the noise and therefore influencing the estimation of K-factor. As the above analysis has shown that the value of $K = 10\,\text{dB}$ is in the valid range for all the selected estimators, the following simulations are done only at this value. Similar conclusions can be drawn for other values of K. In these simulations, the level of SNR changes from 0 to 50 dB by adding different levels of white Gaussian noise to the power of unstirred components.
Fig. 3.21 shows the bias with the variation of SNR. For all the estimators, the bias increases in the same way as SNR decreases. For SNR < 25 dB, the bias of $\widehat{K}_\text{f}$ is slightly lower than for the other estimators while for SNR > 25 dB the second new estimator has the lowest bias.

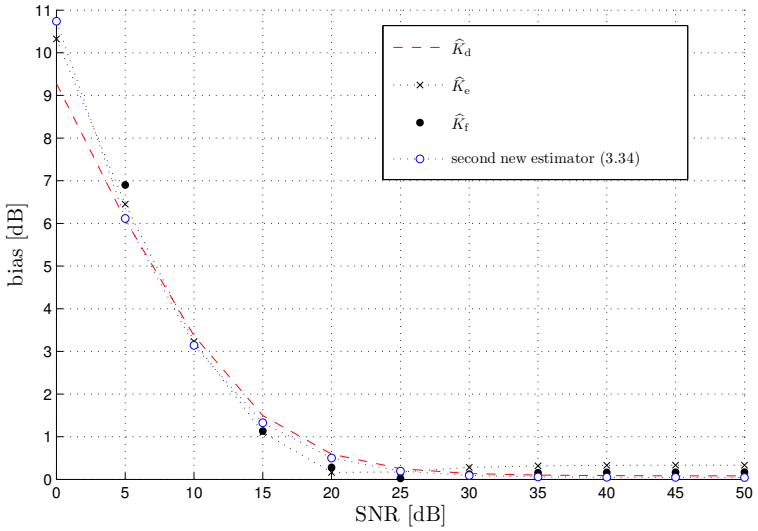

Figure 3.21: Comparison of biases with the variation of SNR (for $K = 10\,\text{dB}$).

The confidence interval is presented in Fig. 3.22. For SNR > 10 dB the second new estimator is the less influenced by the noise having the smaller CI. For values of SNR below 15 dB, the CI starts to increase when the SNR decreases.
In the absence of noise, when $K = 10\,\text{dB}$ the rejection rate for tested all estimators is 0%. When SNR < 6 dB, the rejection rate starts to increase. The most influenced estimator is $\widehat{K}_\text{f}$ for which the rejection rate at 0 dB becomes ~ 60% while for the second new estimator the rejection rate is ~ 3.5%. The estimators $\widehat{K}_\text{d}$ and $\widehat{K}_\text{e}$ are very little influenced by SNR. For SNR > 6 dB and $K = 10\,\text{dB}$ none of the tested estimators are influenced by noise.

Robustness to sample size One main requirement to compute K-factor with the methods presented above is to use N independent realizations. In a fast fading environment the measurements have to be done in a limited time window in order to avoid slow changes in the statistics of the channel. The properties of the new and the selected estimators as a function of the sample size are presented. The analysis is done for $K = 10\,\text{dB}$.
The bias, presented in Fig. 3.23, becomes almost constant for $N > 200$. Reducing the number of realizations, the bias starts to increase in the same way for all estimators. When $K > 0$, the biases of $\widehat{K}_\text{d}$ and $\widehat{K}_\text{e}$ are affected by oscillations. The positions of the minimum values of

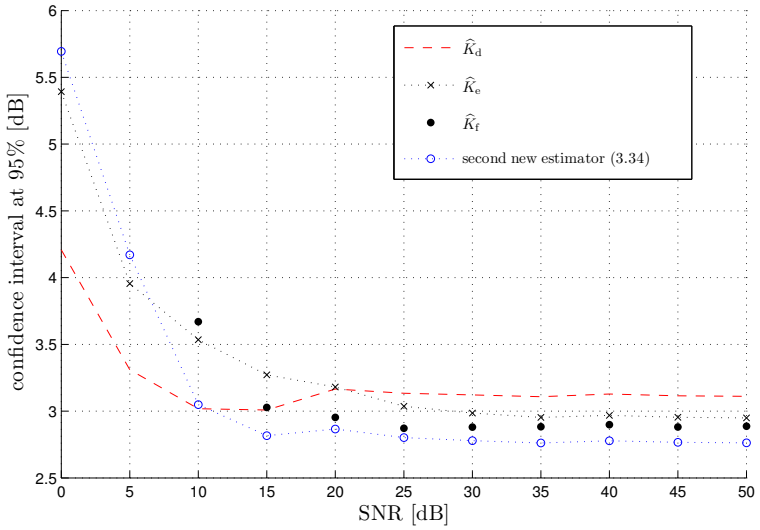

Figure 3.22: Comparison of 95% confidence intervals with the variation of SNR (for $K = 10\,\mathrm{dB}$).

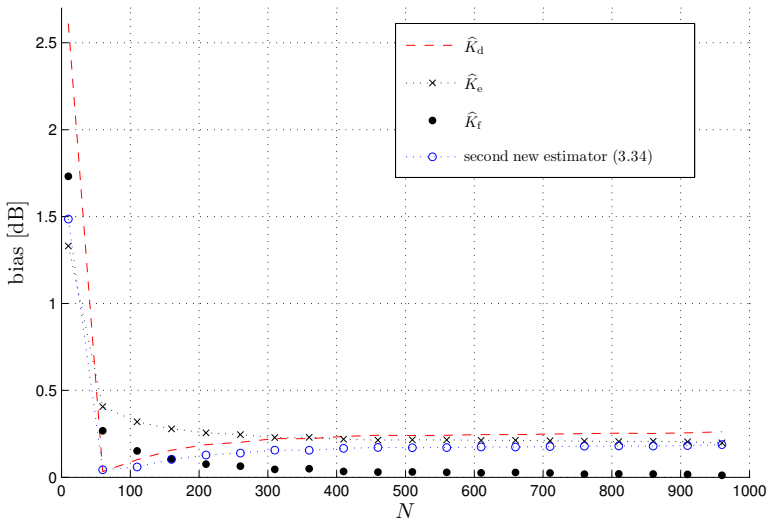

Figure 3.23: Comparison of biases with the variation of the sample size (for $K = 10\,\mathrm{dB}$).

these oscillations change as the number of realizations increases. When $K = 10\,\mathrm{dB}$, the value of the bias for $N = 100$ is smaller than the bias for $N = 1000$. This is a particular case and no general rule can be formulated for the all range of K.

Fig. 3.24 shows the variation of the 95% confidence interval with the sample size. When $N < 100$, the slope of CI is very abrupt. After $N > 100$, the CI reduces from 4 dB to 1 dB (for $N = 1000$). For a sample size bigger than 1000, the decrease of CI is insignificant. The differences between the CIs of presented estimators are very small.

For $K \geq 5\,\mathrm{dB}$, the rejection rate is very little influenced by N. For $K < 5\,\mathrm{dB}$, N has to be bigger than 50 to have a rejection rate less than 10%. The increase of rejection rate is faster for $\widehat{K}_{\mathrm{f}}$ than for the second new estimator. For $\widehat{K}_{\mathrm{d}}$ and $\widehat{K}_{\mathrm{e}}$ the rejection rate does not exceed 2%.

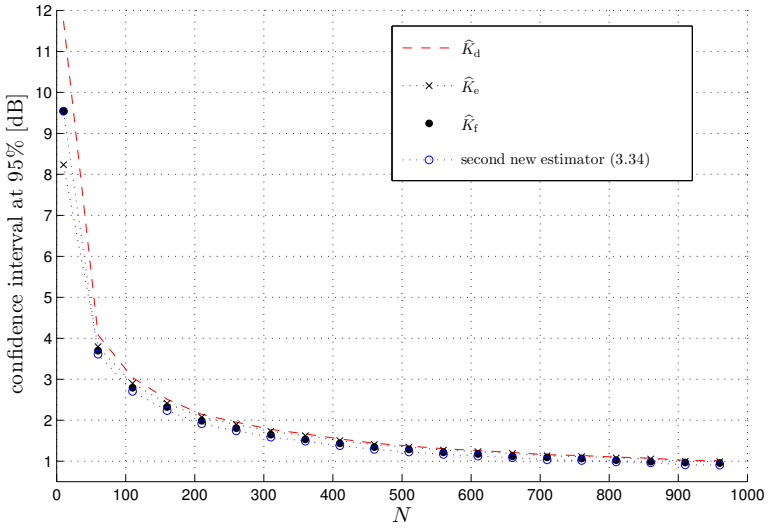

Figure 3.24: Comparison of 95% confidence intervals with the variation of sample size (for $K = 10\,\mathrm{dB}$).

Until now, the simulations corresponding to a strong Rician fading have shown that the second new estimator improves the useful range of K-factor estimation, giving good results compared with other estimators. Next section presents the experimental validation of this second new estimator.

Experimental validation

The validation of the second new estimator in real environments is done with measurements in our reverberation chamber. These experiments highlight the advantages of the second new estimator and the utility of an increased range of K-factor in a transmission environment. We use the same testing frequency range as before (i.e., $[1, 2]$ GHz). The horn antennas are placed successively at two distances: 1 and 4 m in line-of-sight, and the chamber is loaded with absorbing materials, Fig. 3.5. The result of changing frequency can be seen as a slow fading affecting the specular components. The statistical distribution of the electromagnetic field is created with a sample of 100 independent realizations corresponding to 100 positions of the mechanical mode stirrer. The hypothesis of having i.i.d. measured realizations is correct as the density of modes is high enough to provide uncorrelated experiments [27]. We have already shown in Fig. 3.23 and 3.24 that this value is high enough to acquire acceptable results for all tested estimators.

The first configuration aims to test the upper limit of the estimators. The antennas are placed in line-of-sight, at a distance of 1 m from each other. Fig. 3.25(a) presents a zoom over 40 MHz bandwidth of the measured K-factors. Beside a strong bias and a high confidence interval, some values of the estimator $\widehat{K}_{\mathrm{d}}$ have to be discarded as they are corrupted, i.e., negative or complex. The estimator $\widehat{K}_{\mathrm{e}}$ is strongly biased. The results for $\widehat{K}_{\mathrm{f}}$ and the second new estimator resemble.

In the second experiment, the line-of-sight component is reduced by increasing the distance between antennas to 4 m. The signal level fluctuates strongly with frequency which implies the need for an improved range of K-factor. As the level of K-factor decreases, $\widehat{K}_{\mathrm{d}}$ and $\widehat{K}_{\mathrm{e}}$

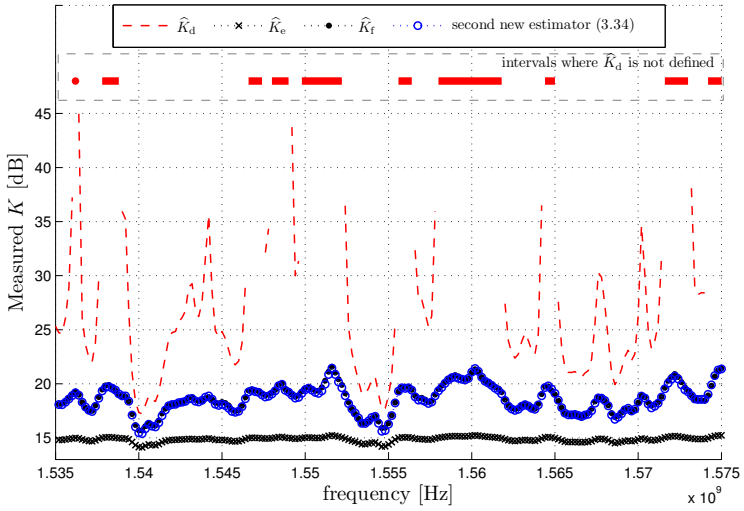

(a)

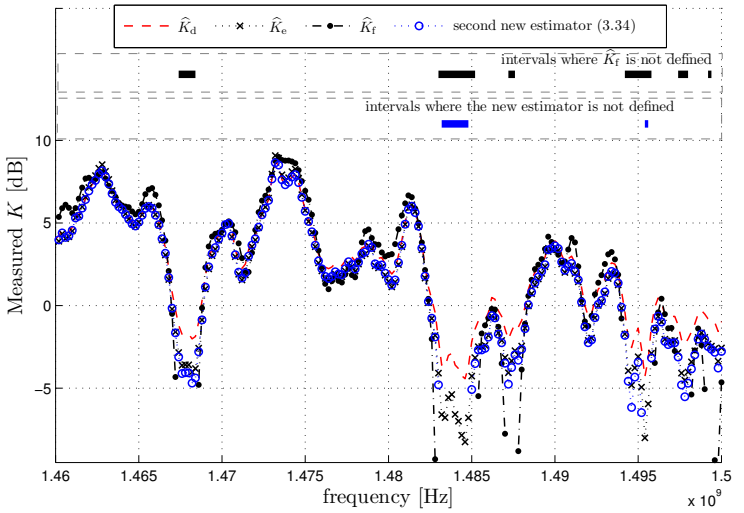

(b)

Figure 3.25: Measured K-factors in reverberation chamber using absorbers and horn antennas placed in line-of-sight at a distance of 1 m (a) and a distance of 4 m (b).

become biased. The second new estimator is slightly affected by erroneous values, while for the $\widehat{K}_{\mathrm{f}}$ the number of these erroneous values is five times higher. Also, in Table 3.2 it is shown that $\widehat{K}_{\mathrm{f}}$ becomes strongly biased for values under 2 dB. For the imposed limits, in both examples the second new estimator works correctly while other envelope-based estimators can favor erroneous or biased values.

3.3.3 Conclusion

This chapter analyzes the propagation channel with respect to K-factor. In the first part of this chapter, we present a detailed statistical analysis of the K-factor and the ways it can be estimated. It seems that K-factor may evolve typically over an important range. There are many concurrent methods for evaluating K-factor. Most of these methods cannot successfully estimate the K-factor over the whole range of interest. Moreover, the estimation of K-factor may be unstable and the quality of this estimation depends on the selected method. It results that depending on the equipment and configuration, there may be only some estimators, among all those available, that could be used. We identify three main criteria on which we evaluate the quality of multiple estimators. Based on these criteria we define a useful interval for each estimator of K-factor. This analysis enables to determine which estimator is to employ and what is the expected K-factor range.
For the same uncertainty levels, the simulations show that the estimators which use the envelope and the phase are less likely to be biased compared with the estimators which use only the envelope. These later estimators are much more affected by the errors introduced by the detection of small levels of K-factor, becoming biased. Increasing the number of realizations may improve the quality of estimation but may be very difficult to acquire. The methods which use complex data are more robust with the change in the sample size and are less sensitive to the uncertainty of small measurements values. The simplest methods are related to envelope-based estimators. The main limitation of these estimators is the narrow range of use, imposed by their properties.
In the second part we analyze the causes of fluctuations which appear if the K-factor is used in a large frequency bandwidth. The consequences of these fluctuations could lead to false or heavily biased values of K estimations. If the distance between antennas is small (i.e., in our experiments less than 2 m) with regards to frequency range the value of the estimation is only influenced by the uncertainties. This statistical uncertainty is bound to the sample size under analysis. For bigger distances, multiple specular components are likely to be present. Therefore the total specular received power is strongly affected by the variation of each subcomponent phase with frequency. In these conditions the choice of the estimator is critical since it may be affected by either absurd values, or big bias or large uncertainties. In reverberation chamber K-factor may reach values of less than −15 dB by using complex fading envelope. For these cases an envelope based estimator overestimates the true value of K-factor and therefore cannot be used properly.
In the third and fourth part of this chapter we propose two new envelope-based estimators which improve the useful range of K-factor. The first new estimator is defined as a fast and easy method using the second moment of the envelope and the second moment of the difference between two consecutive samples. The comparisons with other envelope estimators show that the new approximation gives good results and it can be used properly to estimate K-factor. One major improvement is that this estimator is not influenced by erroneous values. This property is especially useful for the measurements where the sample size is small (e.g. as in

reverberation chamber).
The second method which aims to improve envelope-based K-factor uses the maximum likelihood with an approximation of the modified Bessel function of the first kind. The simulations and comparisons with other envelope based estimators, [3–5], show a significant improvement of the valid range of K-factor in which it can be used. This new estimator is tested in reverberation chamber in two different configurations. For small specular components, the lower bound of any envelope-based estimator is a major disadvantage especially when the number of realizations is small. However, the second new estimator extends the detectable range of K-factor. This second new estimator has been tested in reverberation chamber in two different configurations in order to illustrate its utility in transmission environments. For both experiments, the second new estimator works properly while other estimators have some limitations.

Bibliography

[1] J. D. Parsons, *The Mobile Radio Propagation Channel, 2nd.* New York: John Wiley & Sons, 2000.

[2] C. Holloway, D. Hill, J. Ladbury, P. Wilson, G. Koepke, and J. Coder, "On the use of reverberation chambers to simulate a Rician radio environment for the testing of wireless devices," *Antennas and Propagation, IEEE Transactions on*, vol. 54, no. 11, pp. 3167–3177, Nov. 2006.

[3] L. Greenstein, D. Michelson, and V. Erceg, "Moment-method estimation of the Ricean K-factor," *Communications Letters, IEEE*, vol. 3, no. 6, pp. 175–176, Jun. 1999.

[4] G. Azemi, B. Senadji, and B. Boashash, "Estimating the Ricean K-factor for mobile communication applications," in *Signal Processing and Its Applications, 2003. Proceedings. Seventh International Symposium on*, vol. 2, Jul. 2003, pp. 311–314.

[5] C. Tepedelenlioglu, A. Abdi, and G. Giannakis, "The Ricean K factor: estimation and performance analysis," *Wireless Communications, IEEE Transactions on*, vol. 2, no. 4, pp. 799–810, Jul. 2003.

[6] S. Catreux, V. Erceg, D. Gesbert, and J. Heath, R. W., "Adaptive modulation and MIMO coding for broadband wireless data networks," *IEEE Communications Magazine*, vol. 40, no. 6, pp. 108–115, 2002.

[7] I.-M. Kim, Z. Yi, D. Kim, and W. Chung, "Improved opportunistic beamforming in Ricean channels," *IEEE Transactions on Communications*, vol. 54, no. 12, pp. 2199–2211, 2006.

[8] Y.-C. Ko and M.-S. Alouini, "Estimation of Nakagami-m fading channel parameters with application to optimized transmitter diversity systems," *IEEE Transactions on Wireless Communications*, vol. 2, no. 2, pp. 250–259, 2003.

[9] Y. Chen and N. C. Beaulieu, "Estimators using noisy channel samples for fading distribution parameters," *IEEE Transactions on Communications*, vol. 53, no. 8, pp. 1274–1277, 2005.

[10] G. L. Stüber, *Principles of Mobile Communication (2nd Edition).* Boston: Kluwer Academic, 2001.

[11] M. Andries, P. Besnier, and C. Lemoine, "Rician channels in a RC: Statistical uncertainty of K estimations versus K fluctuations due to unstirred paths," in *Antennas and Propagation (EUCAP), Proceedings of the 5th European Conference on*, Apr. 2011, pp. 1758–1762.

[12] Y. Chen and N. C. Beaulieu, "Maximum likelihood estimation of the K factor in Ricean fading channels," *IEEE Communications Letters*, vol. 9, no. 12, pp. 1040–1042, 2005.

[13] N. Shroff and K. Giridhar, "Biased estimation of Rician K factor," in *Information, Communications & Signal Processing, 2007 6th International Conference on*, Singapore, 2007, pp. 1–5.

[14] T. L. Marzetta, "EM algorithm for estimating the parameters of a multivariate complex Rician density for polarimetric SAR," in *Acoustics, Speech, and Signal Processing ICASSP-95, International Conference on*, vol. 5, Detroit, MI, 1995, pp. 3651–3654.

[15] K. Baddour and T. Willink, "Improved estimation of the Ricean K factor from I/Q samples," in *Vehicular Technology Conference, 2007. VTC-2007 Fall. 2007 IEEE 66th*, Baltimore, MD, 2007, pp. 1228–1232.

[16] ——, "Improved estimation of the Ricean K-factor from I/Q fading channel samples," *IEEE Transactions on Wireless Communications*, vol. 7, no. 12, pp. 5051–5057, 2008.

[17] C. Lemoine, E. Amador, and P. Besnier, "On the K-factor estimation for Rician channel simulated in reverberation chamber," *Antennas and Propagation, IEEE Transactions on*, vol. 59, no. 3, pp. 1003–1012, Mar. 2011.

[18] K. K. Talukdar and W. D. Lawing, "Estimation of the parameters of the Rice distribution," *Journal of the Acoustical Society of America*, vol. 89, no. 3, pp. 1193–1197, Mar. 1991.

[19] F. van der Wijk, A. Kegel, and R. Prasad, "Assessment of a pico-cellular system using propagation measurements at 1.9 GHz for indoor wireless communications," *IEEE Transactions on Vehicular Technology*, vol. 44, no. 1, pp. 155–162, 1995.

[20] C. Tepedelenlioglu and G. B. Giannakis, "On velocity estimation and correlation properties of narrowband mobile communication channels," *IEEE Transactions on Vehicular Technology*, vol. 50, no. 4, pp. 1039–1052, 2001.

[21] Y. Chen and N. C. Beaulieu, "Estimators for K factor and local average SNR using noisy correlated samples," in *Communications, 2006. ICC '06. IEEE International Conference on*, vol. 12, Istanbul, 2006, pp. 5590–5594.

[22] ——, "Estimation of Ricean K parameter and local average SNR from noisy correlated channel samples," *IEEE Transactions on Wireless Communications*, vol. 6, no. 2, pp. 640–648, 2007.

[23] G. Azemi, B. Senadji, and B. Boashash, "Ricean K-factor estimation in mobile communication systems," *Communications Letters, IEEE*, vol. 8, no. 10, pp. 617–619, Oct. 2004.

[24] R. HAMMING and R. Hamming, *Numerical Methods for Scientists and Engineers*, ser. Dover Books on Mathematics Series. Dover Publ., 1973. [Online]. Available: http://books.google.fr/books?id=

Y3YSCmWBVwoC

[25] D. A. Hill, M. T. Ma, A. R. Ondrejka, B. F. Riddle, M. Crawford, and R. T. Johnk, "Aperture excitation of electrically large, lossy cavities," *IEEE Transactions on Electromagnetic Compatibility*, vol. 36, no. 3, pp. 169–178, Aug. 1994.

[26] C. Lemoine, P. Besnier, and M. Drissi, "Investigation of reverberation chamber measurements through high-power goodness-of-fit tests," *Electromagnetic Compatibility, IEEE Transactions on*, vol. 49, no. 4, pp. 745–755, Nov. 2007.

[27] ——, "Advanced method for estimating number of independent samples available with stirrer in reverberation chamber," *Electronics Letters*, vol. 43, no. 16, pp. 861–862, Aug. 2007.

CHAPTER 4

Estimating the average absorbing cross section to control propagation channels

4.1 Introduction

When the analysis of the wireless propagation channels is done in frequency domain, one important parameter which characterizes the channel performances is the coherence bandwidth (CB). The coherence bandwidth is a statistical measure of the frequency range in which all the spectral components have approximately equal amplitude and linear phase. It results that two frequencies in this frequency range will have a strong amplitude correlation [1]. Comparing the modulation bandwidth of the signal with coherence bandwidth, the channel can be considered as flat (the channel transfer function acts as a filter with equal gain and linear phases) when the modulation bandwidth of a signal is smaller than the coherence bandwidth of a channel, Fig. 4.1 (a). Otherwise when the channel interferes constructively and destructively within the bandwidth of the modulated signal (the coherence bandwidth is comparable to or narrower than the signal bandwidth of the communication channel) the channel is considered frequency selective, Fig. 4.1 (b). In many EMC or wireless applications, the chambers are loaded with absorbing materials. Objects loading the chamber, beside antennas, walls, cables, connectors, etc., modify the propagation channels as they absorb and scatter the diffuse field modifying the quality factor of the cavity. Considering all the losses mechanisms in reverberation chamber, the total quality factor of the chamber is defined as:

$$\frac{1}{Q} = \frac{1}{Q_{\text{walls}}} + \frac{1}{Q_{\text{antennas}}} + \frac{1}{Q_{\text{absorbers}}} \tag{4.1}$$

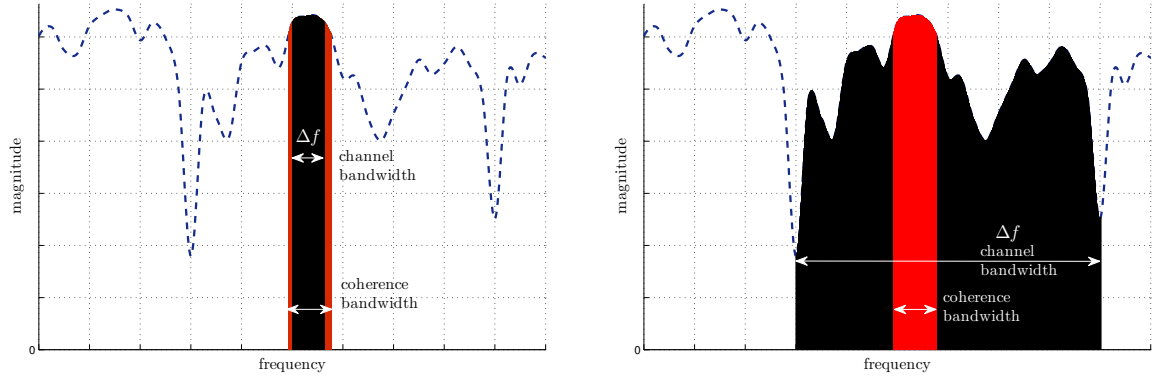

Figure 4.1: Frequency flat (a) and frequency selective (b) channel.

Depending on the origin of losses each quality factor from (4.1) may vary differently with frequency [2]:

$$\begin{cases} \dfrac{1}{Q_{\text{walls}}} & \approx \sqrt{f}, \\ \dfrac{1}{Q_{\text{antennas}}} & \approx f^3, \\ \dfrac{1}{Q_{\text{absorbers}}} & \approx f. \end{cases} \tag{4.2}$$

In our experiments, the reverberation chamber is used at frequencies for which $Q_{\text{walls}} << Q_{\text{antennas}}$, $Q_{\text{absorbers}} << Q_{\text{antennas}}$ and $Q_{\text{absorbers}} < Q_{\text{walls}}$. It results that the total quality factor Q is approximately given by the quality factor of the chamber when the cavity is empty or the combination between the quality factor of the chamber and the absorbers when the cavity is loaded with absorbers. The quality factor has a direct impact over the dissipated power in reverberation chamber, from [2] this power being written as:

$$P_{\text{D}} = \frac{2\pi}{\lambda}\frac{E_0^2}{\eta}\frac{V}{Q}. \tag{4.3}$$

In this equation λ is the wavelength, E_0 represents the mean square amplitude of the electric field and V is the chamber volume. Using the formulations in [2] the absorbing cross section of an object is defined as the power dissipated in the object under plane wave incidence over the power density of the incident wave. The average absorbing cross section (AACS) is obtained by averaging the absorbing cross sections for any plane wave directions and polarizations. This hypothesis stands for well oversized reverberation chambers. The coherence bandwidth of the wireless environment changes with the degree of absorption of the absorbers and it may affect the quality of the signal at reception.

In this chapter we compute in frequency domain the average absorbing cross section of a quantity of absorbers from the estimated coherence bandwidths of the empty and loaded chamber. The measured input data using a single antenna is S_{11} parameter from which the frequency response of the channel is extracted. The measurements are made in successive

bandwidths in the frequency range $2-3\,\mathrm{GHz}$ for different number of parallelepiped absorbers whose dimensions and electrical parameters are known. As the coherence bandwidth is inversely proportional to the quality factor, the average absorbing cross section is easily estimated. A theoretical approach for simulating the average absorbing cross section is presented in this chapter. This model uses the average projected surface and includes a correction associated with the absorber edges effect. Comparisons between simulations and measurements are done. We show that for a parallelepiped absorber the simulated and the measured average absorbing cross section are in the same range of values. Vice versa, it results that the changes in the wireless transmissions in the presence of absorption can be a priori approximated from the estimations of the average absorbing cross section if the geometrical and electromagnetic parameters of the absorbers are known.

4.2 Estimating the average absorbing cross section from measurements in reverberation chamber

4.2.1 Transfer function of the channel used as input data

The reflection coefficient $S_{11_{\mathrm{RC}}}$ measured in reverberation chamber with a VNA is a combination of a deterministic free-space component and a component specific to the propagation channels inside the cavity, and can be written as:

$$\begin{aligned} S_{11_{\mathrm{RC}}} &= S_{11_{\mathrm{FS}}} + \sqrt{\frac{\lambda^2}{8\pi}}\left(1-|S_{11_{\mathrm{FS}}}|^2\right)\eta\left(\frac{\sqrt{2}}{\sqrt{4\pi}}\sqrt{\frac{\mathcal{S}_{\mathrm{unSti}}}{P_{\mathrm{inj}}}}+\sqrt{2}\sqrt{\frac{\mathcal{S}_{\mathrm{Sti}}}{P_{\mathrm{inj}}}}\right) \\ &= S_{11_{\mathrm{FS}}} + \left(1-|S_{11_{\mathrm{FS}}}|^2\right)\eta\left(H_{\mathrm{unSti}}+H_{\mathrm{Sti}}\right), \end{aligned} \tag{4.4}$$

where $S_{11_{\mathrm{FS}}}$ represents the free-space reflection coefficient measured in anechoic chamber and η is the antenna radiation efficiency. The parameters H_{unSti} and H_{Sti} (respectively $\mathcal{S}_{\mathrm{unSti}}$ and $\mathcal{S}_{\mathrm{Sti}}$) are the voltage complex transfer functions (respectively the power spectrum densities) and represent therefore the contributions of the components reflected back to the emission antenna by chamber walls and the stirrer. H_{Sti} ($\mathcal{S}_{\mathrm{Sti}}$) depends on stirrer position whereas $S_{11_{\mathrm{FS}}}$ and H_{unSti} ($\mathcal{S}_{\mathrm{unSti}}$) are invariant with the stirrer position. The factor $\lambda^2/(8\pi)$ is the average effective surface area of the antenna in reverberation chamber. The value $\sqrt{2}$ in front of $\mathcal{S}_{\mathrm{unSti}}$ appears because these components are invariant with the stirring mechanism and the effective area of antenna for these components is the one of antenna in free space, $\lambda^2/(4\pi)$. The factor $\sqrt{2}$ of the $\mathcal{S}_{\mathrm{Sti}}$ is due to the fact that the same antenna is both transmitter and receiver [3]. The parameter P_{inj} represents the injected power in the chamber by the VNA. For a complete rotation of the stirrer, the rectangular components of the transfer function follow a non-centered Gaussian distribution whose average is given by the reflected unstirred components and variance by the stirred components. From 4.4 the transfer function of the propagation channel created only by the stirred components when using the same antenna for emission and reception becomes:

$$H_{\mathrm{Sti}} = \frac{S_{11_{\mathrm{RC}}} - S_{11_{\mathrm{FS}}}}{\eta\left(1-|S_{11_{\mathrm{FS}}}|^2\right)} - H_{\mathrm{unSti}}, \tag{4.5}$$

where H_{unSti} is equal to the average of the total transfer function over a complete stirrer rotation.

4.2.2 Average absorbing cross section in frequency domain from the coherence bandwidth

From the frequency response of the channel $H_{\mathrm{Sti}}(f;t)$, a general definition of the autocorrelation in frequency domain is [4]:

$$A_{\mathrm{H}}(f, f+\Delta f;\Delta t) = E\left[H_{\mathrm{Sti}}(f;t)H^{H}_{\mathrm{Sti}}(f+\Delta f;t+\Delta t)\right], \tag{4.6}$$

where $E[\square]$ represents the averaging operator over the number of realizations of the autocorrelation function and the operator ^{H} is the Hermitian transpose. For an established configuration in reverberation chamber (e.g., a stirrer or antenna position), the propagation channel becomes wide sense stationary and therefore we can write

$$A_{\mathrm{H}}(f, f+\Delta f;\Delta t) = A_{\mathrm{H}}(f, f+\Delta f). \tag{4.7}$$

The coherence bandwidth is defined as the frequency bandwidth of the autocorrelation of the frequency response measured at different levels of correlation, i.e., 0.5, 0.7, 0.9, of the envelope or complex frequency response. In this chapter the analysis of the frequency selectivity of the channel with the absorption degree is done computing the complex coherence bandwidth for each stirrer position at a correlation level of 0.7. The distribution of modes in reverberation chamber changes with the degree of absorption, influencing both the coherence bandwidth and the 3 dB bandwidth of the modes, we denote $\Delta f_{3\,\mathrm{dB}}$. Using [5], this last bandwidth can be approximated with the half of the coherence bandwidth computed from complex realizations at a correlation level of 0.5 which is proportional with the coherence bandwidth for the same level of correlation obtained from envelope realizations:

$$\Delta f_{3\,\mathrm{dB}} \approx \frac{1}{2} CB^{\mathrm{cpx},0.5} = \frac{\sqrt{3}}{2} CB^{\mathrm{env},0.5}. \tag{4.8}$$

Also from [5], the coherence bandwidth computed from envelope realizations at a correlation level of 0.5 is equal with the coherence bandwidth computed from complex realizations at a correlation level of 0.7:

$$CB^{\mathrm{env},0.5} = CB^{\mathrm{cpx},0.7}. \tag{4.9}$$

With (4.8) and (4.9) the quality factor computed from coherence bandwidths at a correlation level of 0.7 using complex realizations results as:

$$Q = \frac{f}{\Delta f_{3\,\mathrm{dB}}} \approx \frac{2}{\sqrt{3}} \frac{f}{CB^{\mathrm{cpx},0.7}}. \tag{4.10}$$

When a "target" is illuminated by a wave, it will scatter and absorb a percentage of the wave energy. The cross section represents an apparent area used to describe the amount of the radiation interacting with this target. The total cross section of an object $\overset{\blacktriangle}{\sigma}_{\mathrm{T}}$ is the sum of the cross-sections due to absorption and scattering:

$$\overset{\blacktriangle}{\sigma}_{\mathrm{T}} = \overset{\blacktriangle}{\sigma}_{\mathrm{A}} + \overset{\blacktriangle}{\sigma}_{\mathrm{S}}\,. \tag{4.11}$$

The absorbing cross section, denoted $\overset{\blacktriangle}{\sigma}_{\mathrm{A}}$, represents the area which multiplied by the power density of incident plane-wave radiation gives the power absorbed and dissipated by the object. The scattering cross section $\overset{\blacktriangle}{\sigma}_{\mathrm{S}}$ is the hypothetical area normal to the incident radiation that

would geometrically intercept the total amount of radiation actually scattered by a scattering object [6]. In this chapter we are interested by the average absorbing cross section.
From (4.3) [7], we write the Q factor as:

$$Q = \frac{2\pi f V E_{0,\mathrm{E}}^2}{\eta c P_{\mathrm{D}}}, \tag{4.12}$$

and using equation (4.10), the average scalar power density $\mathcal{S}_{\mathrm{E}}$ and the dissipated power $P_{\mathrm{D,E}}$ in an empty reverberating cavity of an average equivalent absorbing surface $\overset{\blacktriangle}{\sigma}_{\mathrm{RC}}$ (i.e., representing antennas, cables, walls, apertures, etc.) are:

$$\begin{aligned} \mathcal{S}_{\mathrm{E}} &= \frac{E_{0,\mathrm{E}}^2}{\eta} \approx \frac{1}{\pi\sqrt{3}} \frac{c P_{\mathrm{T}}}{CB_{\mathrm{E}}^{\mathrm{cpx},0.7} V}, \\ P_{\mathrm{D,E}} &= \frac{E_{0,\mathrm{E}}^2}{\eta} \overset{\blacktriangle}{\sigma}_{\mathrm{RC}} . \end{aligned} \tag{4.13}$$

In the presence of absorbers, whose average absorbing cross section is $\overset{\blacktriangle}{\sigma}_{\mathrm{A}}$, the power density $\mathcal{S}_{\mathrm{L}}$ and the dissipated power $P_{\mathrm{D,L}}$ become:

$$\begin{aligned} \mathcal{S}_{\mathrm{L}} &= \frac{E_{0,\mathrm{L}}^2}{\eta} \approx \frac{1}{\pi\sqrt{3}} \frac{c P_{\mathrm{T}}}{CB_{\mathrm{L}}^{\mathrm{cpx},0.7} V}, \\ P_{\mathrm{D,L}} &= \frac{E_{0,\mathrm{L}}^2}{\eta} \left(\overset{\blacktriangle}{\sigma}_{\mathrm{RC}} + \overset{\blacktriangle}{\sigma}_{\mathrm{A}} \right), \end{aligned} \tag{4.14}$$

where c is the speed of light, P_{T} is the total power transmitted in the chamber, V is the volume of the reverberation chamber (e.g., $93.351\,\mathrm{m}^3$ for the reverberation chamber used in this analysis), η is the free space impedance, E_0^2 is the mean square value of the electric field and is proportional to the variance of stirred components [7]. The indexes "E" and "L" correspond to respectively *"empty"* and *"loaded"* reverberating cavity. Since the transmitted power P_{T} is equal to the total absorbed power in both cases ($P_{\mathrm{T}} = P_{\mathrm{D,E}} = P_{\mathrm{D,L}}$), the average absorbing cross section is computed from (4.13) and (4.14) as:

$$\overset{\blacktriangle}{\sigma}_{\mathrm{A,mes}} \approx \frac{V\pi\sqrt{3}}{c} \left(CB_{\mathrm{L}}^{\mathrm{cpx},0.7} - CB_{\mathrm{E}}^{\mathrm{cpx},0.7} \right), \tag{4.15}$$

where $\overset{\blacktriangle}{\sigma}_{\mathrm{A,mes}}$ and $CB^{\mathrm{cpx},0.7}$ are averaged values calculated over a number of several realizations (i.e., stirrer rotation, several positions of antenna, etc.).

4.3 Prediction of the average absorbing cross section of the parallelepiped absorbers

In the above section we have presented a method to estimate the average absorbing cross section from a set of measured coherence bandwidths. In this section we provide an approximate theoretical evaluation of the average absorbing cross section. From [7], the dissipated power on a surface can be written as a function of the power density in the cavity and the absorbing cross section:

$$P_{\mathrm{D,abs}} = \mathcal{S}_{\mathrm{L}} \overset{\blacktriangle}{\sigma}_{\mathrm{A}} = \mathcal{S}_{\mathrm{L}} E\left[\overset{\blacktriangle}{\sigma}_{\mathrm{a}}(n) \right], \tag{4.16}$$

where $\overset{\blacktriangle}{\sigma}_{\mathrm{a}}(n)$ is the corresponding absorbing cross section at the nth experiment, and $E[\square]$ is the average operator over all realizations. With the hypothesis that over the stirring mechanism the electromagnetic (EM) waves in the cavity can be represented as plane waves (i.e., no unstirred components, working at frequencies higher than the LUF ensuring the uniformity of the field, having a high quality factor, etc.), then the average $E[\square]$ is equivalent with an average over all angles of incidence, θ and ϕ, and all polarizations. We assume that any face of an absorber is seen as an interface between air and an absorbing surface of infinite depth [8]. The dissipated power on one face of absorber can be written as a function of the projected surfaces on the azimuth plane $S_{\mathrm{proj}}(n)$ and the plane wave transmission coefficients $T(n)$, $(\overset{\blacktriangle}{\sigma}_{\mathrm{a}}(n) = S_{\mathrm{proj}}(n)\,T(n))$:

$$P_{\mathrm{D,abs}} = \mathcal{S}_{\mathrm{L}} E\left[S_{\mathrm{proj}}(n)\,T(n)\right]. \tag{4.17}$$

It results that the degree of absorption of an absorber depends on its electrical (i.e., permittivity $\epsilon_{r,\mathrm{abs}}$ and conductivity σ_{abs}) and its geometrical parameters. For a parallelepiped absorber in reverberation chamber, due to the fact that one face of the absorber does not partially mask another face, the total average absorbing cross section can be approximated by a sum of the individual average absorbing cross sections of each face:

$$\overset{\blacktriangle}{\sigma}_{\mathrm{A,theo}} \approx \sum_{i=1}^{6} \frac{\int_{\theta=0}^{\pi/2}\int_{\phi=0}^{2\pi} S_{\mathrm{proj},i}(\theta)T_i(\theta)\sin\theta d\theta d\phi}{\int_{\theta=0}^{\pi/2}\int_{\phi=0}^{2\pi}\sin\theta d\theta d\phi}, \tag{4.18}$$

where the spherical coordinate system is attached to the absorbing surface, θ and ϕ being respectively the elevation and the azimuth incidence angles of the plane wave. The projected surface depends only on the θ angle and not on ϕ, and $S_{\mathrm{proj},i}(\theta) = S_i\cos\theta$, S_i representing the surface of ith face, Fig. 4.2. Computing the average absorbing cross section for the ith face of the absorber and multiplying and dividing by a factor of 2, we obtain:

$$\overset{\blacktriangle}{\sigma}_{\mathrm{A,theo},i} \approx \frac{S_i}{2}\cdot 2\int_{\theta=0}^{\pi/2} T(\theta)\cos\theta\sin\theta d\theta. \tag{4.19}$$

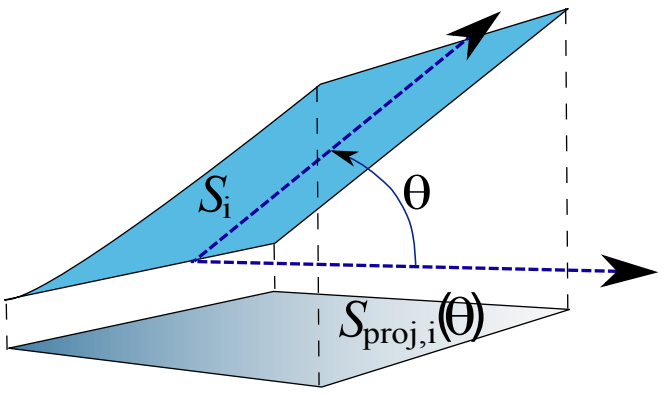

Figure 4.2: Projected Surface.

In this equation the first factor, $S_i/2$, represents the average projected surface (APS) of the ith face and is computed as the average surface projected over all angles θ and ϕ:

$$\frac{S_i}{2} = \frac{\int_{\phi=0}^{2\pi}\int_{\theta=0}^{\pi/2} S_i \cos\theta \sin\theta d\theta d\phi}{\int_{\phi=0}^{2\pi}\int_{\theta=0}^{\pi/2} \sin\theta d\theta d\phi}. \tag{4.20}$$

For a parallelepiped absorber the total average projected surface is:

$$S_{\text{APS}} = \sum_{i=1}^{6} \frac{S_i}{2} = \frac{S_{\text{Tot}}}{2}, \tag{4.21}$$

where S_{Tot} is the total surface of the absorber. The second factor in (4.19), corresponds to average plane wave transmission coefficient which depends on the incidence angle and the electrical parameters and is computed by averaging transmission coefficients over all angles of incidence θ, and polarizations H and V, [9]:

$$\overline{T} = 2\int_{\theta=0}^{\pi/2} T(\theta)\cos\theta\sin\theta d\theta = 2\int_{0}^{\pi/2}\left[1 - \frac{|\Gamma_{\text{TM}}(\theta)|^2 + |\Gamma_{\text{TE}}(\theta)|^2}{2}\right]\cos\theta\sin\theta d\theta, \tag{4.22}$$

where the parameters $\Gamma_{\text{TM}}(\theta)$ and $\Gamma_{\text{TE}}(\theta)$ are the transverse electric and transverse magnetic plane wave Fresnel reflection coefficients which depend on material properties, polarization of waves, angle of incidence and signal frequency:

$$\begin{aligned}
\Gamma_{\text{TM}}(\theta) &= \frac{\mu_{\text{abs}}\widetilde{k}_{\text{air}}\cos\theta - \mu_{\text{air}}\sqrt{\widetilde{k}_{\text{abs}}^2 - \widetilde{k}_{\text{air}}^2\sin^2\theta}}{\mu_{\text{abs}}\widetilde{k}_{\text{air}}\cos\theta + \mu_{\text{air}}\sqrt{\widetilde{k}_{\text{abs}}^2 - \widetilde{k}_{\text{air}}^2\sin^2\theta}}, \\
\Gamma_{\text{TE}}(\theta) &= \frac{\mu_{\text{air}}\widetilde{k}_{\text{abs}}^2\cos\theta - \mu_{\text{abs}}\widetilde{k}_{\text{air}}\sqrt{\widetilde{k}_{\text{abs}}^2 - \widetilde{k}_{\text{air}}^2\sin^2\theta}}{\mu_{\text{air}}\widetilde{k}_{\text{abs}}^2\cos\theta + \mu_{\text{abs}}\widetilde{k}_{\text{air}}\sqrt{\widetilde{k}_{\text{abs}}^2 - \widetilde{k}_{\text{air}}^2\sin^2\theta}}.
\end{aligned} \tag{4.23}$$

In these equations $\widetilde{k}_{\text{abs}} = \omega\sqrt{\mu_{\text{abs}}\left(\epsilon'_{\text{abs}} - j\sigma_{\text{abs}}/\omega\right)}$ and $\widetilde{k}_{\text{air}} \approx \omega/c$ are respectively the complex wave number of the absorber and the air, and $\mu_{\text{abs}} = \mu_0\mu_{r,\text{abs}}$ and $\epsilon'_{\text{abs}} = \epsilon_0\epsilon_{r,\text{abs}}$ are respectively the permeability and the permittivity of the absorbing material. The parameter σ_{abs} is the conductivity of the absorbing material. It results that the average reflection coefficient over all angles and polarizations of the absorber is: $\overline{R} = 1 - \overline{T}$. If the distributions of angles θ and ϕ are uniform for all surfaces i.e., if we assume a uniform illumination of the absorber, with (4.19), (4.21) and (4.22), the total average absorbing cross section of a parallelepiped absorber may be approximated with:

$$\overset{\blacktriangle}{\sigma}_{\text{A,theo}} \approx \overline{T} S_{\text{APS}}. \tag{4.24}$$

This equation is easily validated with simulations in which the parallelepiped absorber is modeled as a 3D object using Matlab, Fig. 4.3 (see annex E). For each pair of angles (θ, ϕ) an image of the object is taken and the pixels of this image are converted to an equivalent area $S_{\text{sim\_area}}$ which is then multiplied with the corresponding transmission coefficient:

$$\overset{\blacktriangle}{\sigma}_{\text{A,3Dsim}} = \frac{1}{2\pi}\int_{\theta=0}^{\pi}\int_{\phi=0}^{2\pi}\left[1 - \frac{|\Gamma_{\text{TM}}(\theta)|^2 + |\Gamma_{\text{TE}}(\theta)|^2}{2}\right] S_{\text{sim\_area}}(\theta,\phi)\sin(\theta)d\theta d\phi. \tag{4.25}$$

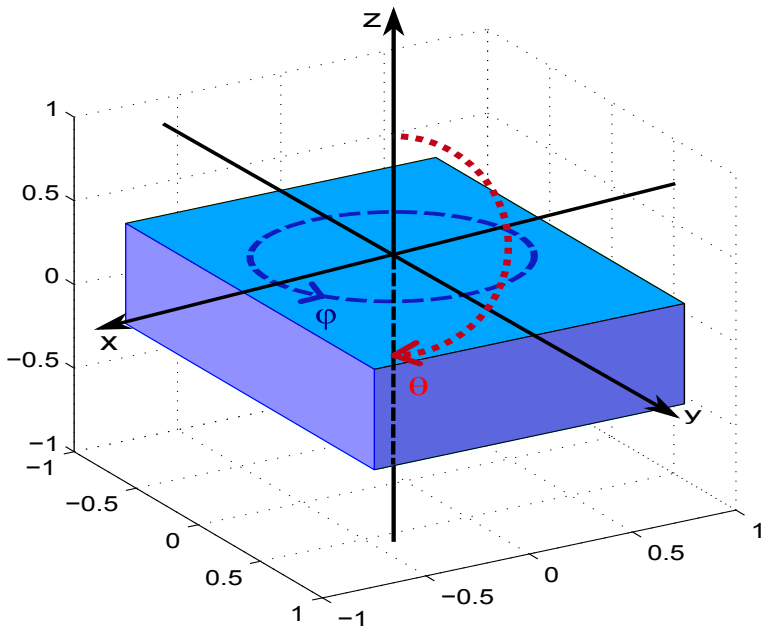

Figure 4.3: Matlab 3D simulation of the parallelepiped absorber.

The parameter $S_{\text{sim\_area}}$ is the visible simulated surface obtained by counting the number of colored pixels for pair of angles (θ, ϕ).
In equation (4.24) we assume that the absorber has a skin depth equal to zero which does not correspond to a real absorber. In other words we consider that the depth of the absorber is high enough to entirely dissipate the incoming waves whatever their angles of incidence. Without including the effects of the re-radiation of the electromagnetic waves after they passed through the absorber, the simulated average absorbing cross section is overestimated. To overcome this problem we make the assumption that if the traveled distance of a wave through an absorber is bigger than the skin depth δ of the absorber, then this wave is entirely dissipated in the absorber. With the hypotheses that the geometrical dimensions of the absorber (width, length and height) are all bigger than the skin depth (Fig. 4.4) and the waves arrive with equal probability from different directions on the surface of the absorber the corrected average projected surface of the ith face of the absorber becomes:

$$\begin{aligned}\frac{S_{\text{corr},i}}{2} &= \frac{\int_{\phi=0}^{2\pi}\int_{\theta=0}^{\pi/2} S(\theta,\phi)\sin\theta d\theta d\phi}{\int_{\phi=0}^{2\pi}\int_{\theta=0}^{\pi/2}\sin\theta d\theta d\phi} = \frac{4\int_{\phi=0}^{\pi/2}\int_{\theta=0}^{\pi/2}(l-\delta\sin\phi)(L-\delta\cos\phi)\cos\theta\sin\theta d\phi}{\int_{\phi=0}^{2\pi}\int_{\theta=0}^{\pi/2}\sin\theta d\theta d\phi} \\ &= \frac{\pi lL - 2\delta(l+L)+\delta^2}{2\pi} = \frac{S_i}{2} - \left[\frac{\delta(l+L)}{\pi} - \frac{\delta^2}{2\pi}\right].\end{aligned} \tag{4.26}$$

With (4.26) the corrected average projected surface becomes:

$$S_{\text{APS,corr}} = S_{\text{APS}} - \frac{6\delta(l+L)-3\delta^2}{\pi}, \tag{4.27}$$

from which the average absorbing cross section of a parallelepiped absorber may be approximated with:

$$\sigma_{\text{A,theo}} \approx \overline{T} S_{\text{APS,corr}}. \tag{4.28}$$

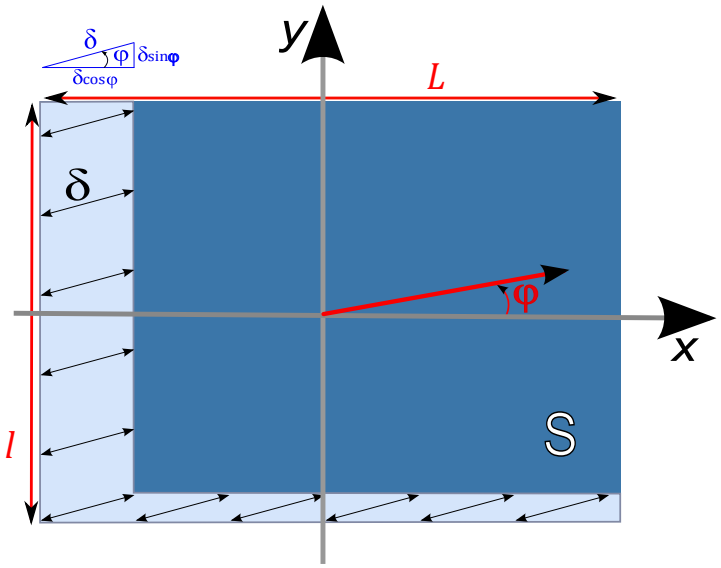

Figure 4.4: Absorbing surface approximation (top side view).

4.4 Validation of the method

4.4.1 Experimental setup

Experiments are made in our reverberation chamber. The transfer function of the channel is measured in the test bandwidth $2-3\,\mathrm{GHz}$ with a bin resolution of $50\,\mathrm{kHz}$ using a VNA and then the data is saved using Matlab. We use the stirrer in stepped mode, resulting a time of around 35 min to make all measurements. A faster approach is the use of the stirrer in continuous mode. This will reduce the measurement time but it will require an adequate synchronization between the measurement and the stirrer rotation. Without needing the synchronization a solution consists in using two or mores stirrers to reduce the correlation time between positions. To extend the number of realizations we use two identical horn antennas (model Lindgren 3115) at two positions. The powers received at both antennas are measured simultaneously. These antennas are placed in a cross polarized configuration at a distance of $1.5\,\mathrm{m}$ from the stirrer and $1\,\mathrm{m}$ from the absorbers, and directed to the opposite wall to reduce the amount of unstirred components, (Fig. 4.5). In order to test the influence of the absorbers on the coherence bandwidth and to extract the average absorbing cross section, 1 up to 4 identical parallelepiped absorbers, type Hyfral P150 ($0.6\times0.6\times0.15\,\mathrm{m}^3$), are used. The absorbers are placed vertically on a polystyrene cube to fulfill the conditions of a uniform illumination as assumed in the previous section. They are also joined together to remove the shadowing effect between them. For each quantity of absorbers and each of the 100 stirrer positions, rotated in mode-tuned, the parameter $S_{11_{\mathrm{RC}}}$ is measured. To remove the influence of the antenna mismatch, as requested by (4.5), the parameter $S_{11_{\mathrm{FS}}}$ is measured in anechoic chamber in the same frequency bandwidth and with the same frequency step. However, if the unstirred components in the measured signal are very small ($K < -15\,\mathrm{dB}$), we can also use directly the S_{11} parameters measured in the reverberation chamber, since $S_{11_{\mathrm{FS}}} \approx E\left[S_{11_{\mathrm{RC}}}\right]$ (i.e., average over a stirrer rotation, antenna positions, etc.).
We identify different problems which may affect the estimations and thus explain that the

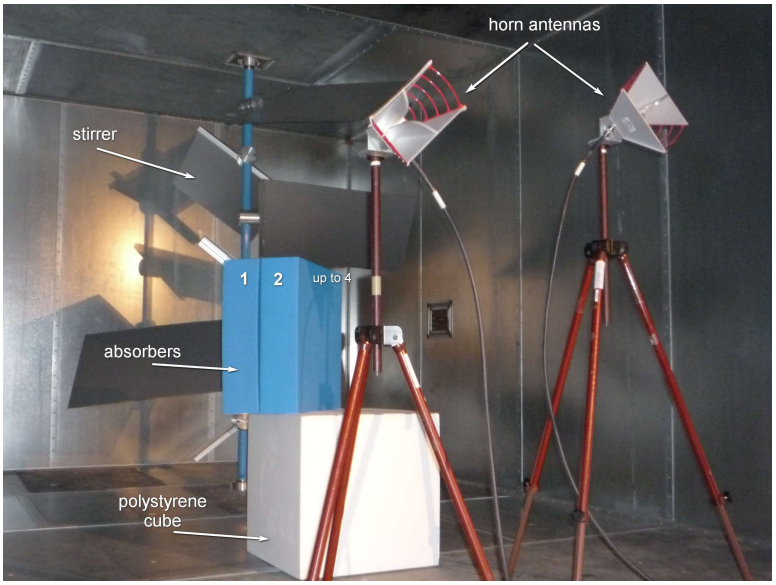

Figure 4.5: RC measurement configuration.

measured values may differ from the simulations. To reduce these effects, some precautions must be taken during the measurements:

- the direct coupling between the antenna and the absorbers has to be avoided otherwise the absorbers will block some energy before arriving to the walls and/or the stirrer of the chamber, and the measured value of the absorption will be therefore overestimated compared to the situation when the absorbers are uniformly illuminated. In these experiments we use directive antennas with a change in polarization of 45° and the absorbers are placed behind them;

- when the absorbers are placed directly on the chamber's floor, it is not possible to have an evenly illuminated absorber. Because the hypothesis of plane wave spectrum of the field is not respected the measured average absorbing cross section will be underestimated with respect to the situation in which the absorbers are uniformly illuminated. The results presented in this chapter are for the situation when the absorbers are placed on a polystyrene cube (at 0.6 m from the floor);

- an increasing number of realizations in the evaluation of the coherence bandwidth reduces the variance of the estimation of this parameter, but it increases the time to make the measurement as the frequency step becomes smaller;

- when the unstirred components exist, they should be removed otherwise they will overestimate the coherence bandwidth. Therefore, we can use (4.5) to estimate H_{Sti}, from which coherence bandwidths is evaluated.

4.4.2 Data processing and results

The coherence bandwidths are computed in sub-bandwidths of 10 MHz each with an arbitrary step between two consecutive estimations of 1 MHz. When computing the coherence bandwidth, the number of frequencies included in the operation has to be high enough otherwise

the coherence bandwidth may be wrongly estimated and also its variance may increase. A higher number of frequencies in the evaluation bandwidth improves the estimation of coherence bandwidth, but requests measurements with a higher frequency resolution. Increasing the width of the evaluation bandwidth has also some limitations since the electromagnetic field may not have the same statistics in the whole bandwidth under test. In this analysis, a frequency resolution of 50 kHz over an evaluation bandwidth of 10 MHz (representing 200 frequencies per sub-bandwidth) ensures to have correlated realizations described by the same statistic [10].

During the correlation evaluation process, the average component over the analysis bandwidth is subtracted from the frequency response. A supplementary interpolation refines the frequency step of the average autocorrelation function to 1 kHz. The complex correlation functions are computed for each stirrer position and the coherence bandwidth is extracted as an average over all stirrer positions of the corresponding coherence bandwidths. The variation of the measured coherence bandwidths with frequency for different number of absorbers is plotted in Fig. 4.6. As it was expected, the level of the coherence bandwidth increases with the number of absorbers in the chamber. Since the coherence bandwidth is extracted from the same number of stirrer positions, these provide less independent realizations with the number of absorbers as the quality factor decreases. This may explain the higher uncertainty levels in the estimations. Also, statistical fluctuations of the coherence bandwidth may hide the small variations of the electromagnetic parameters of the tested absorbers. The complex relative permittivity of P150 absorbers, $\epsilon'_{\text{abs}} - j\sigma_{\text{abs}}/\omega$, used in these measurements as provided by the manufacturer changes from $1.90 + 3j$ at 2 GHz to $1.79 + 2.16j$ at 3 GHz. Fig. 4.7 shows the attenuation of a plane wave propagating through an absorber of infinite dimensions which has the same electrical properties as the P150 absorbers.

In [11] are presented two minimum thresholds of the quality factor. Compared with the situation of an infinite Q factor which would cause discrete resonances frequencies, an excess of losses would degrade the spatial uniformity and decrease the field level under a desired level.

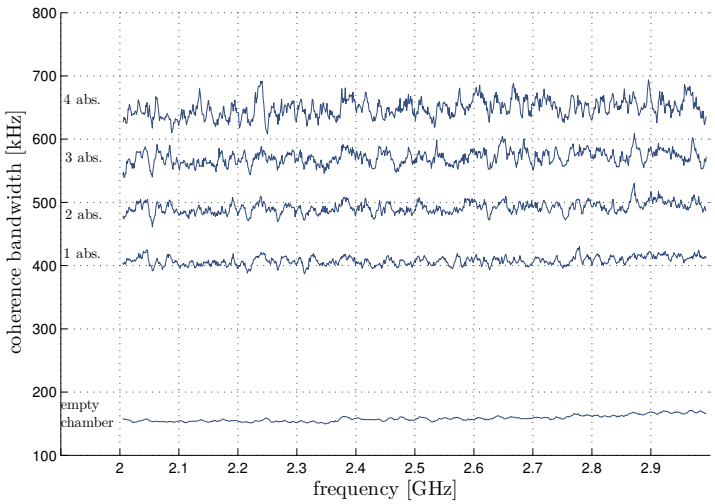

Figure 4.6: Coherence Bandwidths computed between 2 – 3 GHz in sub-bandwidths of 10 MHz each with a step between two consecutive sub-bandwidths of 1 MHz.

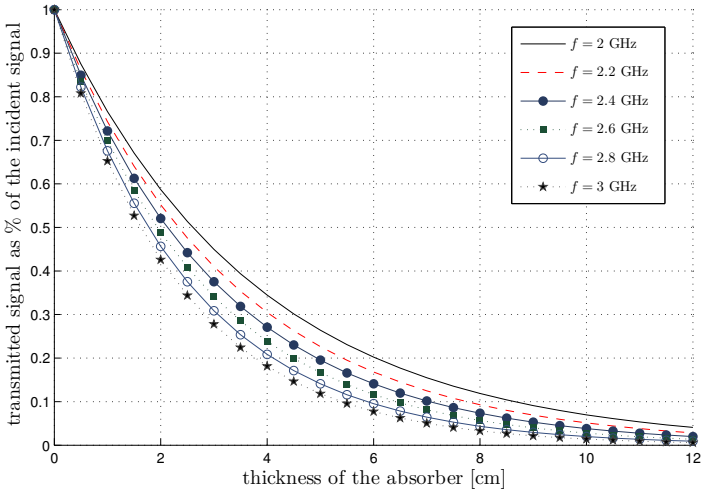

Figure 4.7: Transmitted signal as percentage of the incidence signal for the absorber P150.

The direct effect is seen in standard deviation of the electric field: a high standard deviation of the average total squared field indicating a reduction of the spatial field uniformity and a degradation of the performances of the chamber [11]. In the hypothesis that the stirred energy exceeds the unstirred energy, the threshold level of the quality factor of the chamber may be evaluated from the power density of the stirred components with:

$$Q_{\text{threshold}} => \left(\frac{4\pi}{3}\right)^{2/3} \frac{1}{2} \frac{V^{1/3}}{\lambda}. \tag{4.29}$$

The second threshold level of the quality factor results from the hypothesis that the electric field is Rayleigh distributed:

$$Q_{\text{threshold}} => \left(\frac{4\pi}{3}\right)^{2/3} \frac{3}{2} \frac{V^{1/3}}{\lambda}. \tag{4.30}$$

Note that in all our experiments we take into account the inferior limit of the quality factor avoiding to load the chamber with too many absorbers.

Using the measured values of the coherence bandwidths for different quantities of absorbers, we use (4.15) to estimate the average absorbing cross section while with (4.28) and the approximated average projected surface in (4.27) we simulate this parameter. The measured average absorbing cross sections correspond to a weighted average of absorbing cross sections by the mode densities of the chamber in the evaluation bandwidth of 10 MHz. From the electrical properties of the absorber it results an average skin depth δ of 3 cm in the bandwidth $2-3$ GHz estimated with [12]:

$$\delta = \sqrt{\frac{2}{2\pi f \mu_0 \sigma_{\text{abs}}}} \sqrt{\sqrt{1 + \left(2\pi f \frac{\epsilon'_{\text{abs}}}{\sigma_{\text{abs}}}\right)^2} + 2\pi f \frac{\epsilon'_{\text{abs}}}{\sigma_{\text{abs}}}}. \tag{4.31}$$

Fig. 4.8 presents the variations of the measured and simulated average absorbing cross sections for up to 4 identical absorbers. Fig. 4.8 (a) presents the simulation results of the average

absorbing cross section calculated from (4.24). Using the corrected average projected surface (4.27), Fig. 4.8 (b) presents the results when the simulated average absorbing cross section is computed with (4.28). Increasing the number of absorbers, the visible surface changes from $1.08\,\mathrm{m}^2$ for one absorber to $2.16\,\mathrm{m}^2$ for 4 absorbers while average absorbing cross section changes from values around $0.42\,\mathrm{m}^2$ to $0.83\,\mathrm{m}^2$. The uncertainties of the estimation increase with the quantity of absorbers, effect which has been seen previously on coherence bandwidths, (Fig. 4.6). Also, for comparison, we present the average absorbing cross section for 1 absorber when using the experimental method in [2].

The simulated values of average absorbing cross section are obtained based on the geometrical and the electrical parameters of absorbers. Comparing the simulated and the measured results we find a good accordance between them, even if some differences may appear as the simulations may not model some characteristics which occur in measurements:

- in experiments, depending on the thickness of the absorber and its electrical parameters some electromagnetic waves can pass through it, situation which is not completely modeled in simulations. This shortcoming is manifested by an increase of the simulated average absorbing cross section. A more sophisticated model than (4.26) would be required, if necessary;
- the complex relative permittivity included in simulations has some uncertainty in reality and it may affect the simulations (e.g., the absorbing cross section increases with the increase of conductivity σ and the decrease of relative permittivity ϵ_r).

In a lesser extent, other problems may increase the discrepancies between simulations and measurements:

- while in simulations all the directions have the same weight, in measurements some direction may be slightly favored over the others and the absorbers may not be evenly illuminated by the electromagnetic waves. These preferential directions may depend on the position of the absorbers in the chamber and on the relative position of the absorbers from the antenna;
- the measurements are made placing the absorbers on a polystyrene cube whose height is 0.6 m. This cube is not perfectly transparent for the electromagnetic waves, so the surfaces which are in contact with the polystyrene cube may have a reduced influence in the total average absorbing cross section.

All these imperfections of the simulations and the measurements may influence the comparisons of the measured values with those estimated.

If the average absorbing cross sections of the absorbers are known, from (4.15) it results an estimation on how the coherence bandwidth changes with the number of absorbers:

$$CB_{\mathrm{L}}^{\mathrm{cpx},0.7} \approx CB_{\mathrm{E}}^{\mathrm{cpx},0.7} + \frac{c\,\overset{\blacktriangle}{\sigma}_{\mathrm{A}}}{\sqrt{3}\pi V}, \tag{4.32}$$

where $CB_{\mathrm{E}}^{\mathrm{cpx},0.7}$ depends on the empty reverberation chamber. Fig. 4.9 is an example of the measured variation of average absorbing cross section at a central frequency of 2.5 GHz for the parallelepiped P150 absorbers in the tested reverberation chamber which may be used as an abacus to obtain any coherence bandwidths for an established value of average absorbing cross section.

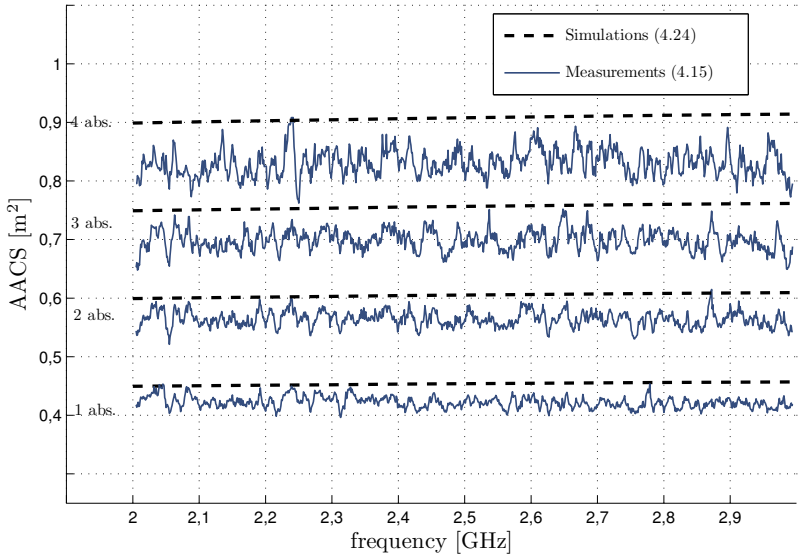

(a)

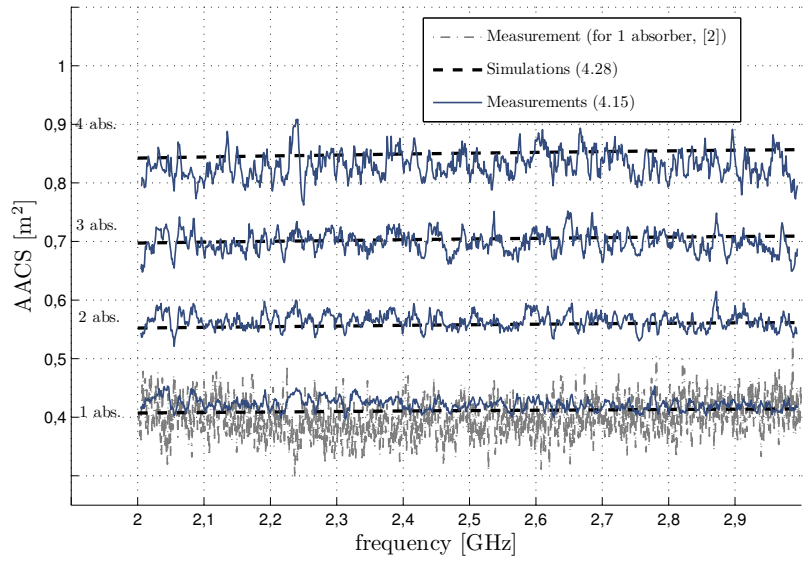

(b)

Figure 4.8: Measured and simulated average absorbing cross section as a function of the number of absorbers in the frequency bandwidth $2-3\,\mathrm{GHz}$ for P150 absorbers:
(a) when using (4.24) and (b) when using (4.28) to simulate the average absorbing cross section.

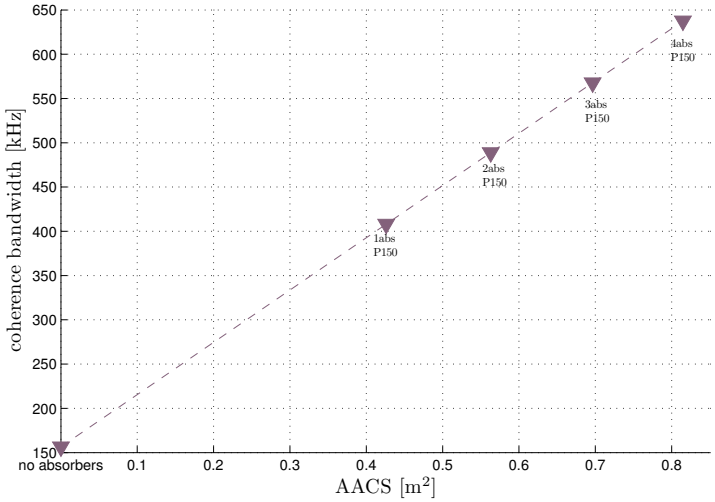

Figure 4.9: Coherence Bandwidth as function of the Average Absorbing Cross Section for P150 absorbers, at a central frequency of 2.5 GHz.

4.5 Conclusions

In this chapter we have obtained the average absorbing cross sections for several quantities of absorbing materials from the coherence bandwidths measured for the empty and loaded cavity. We use only one antenna and the S_{11} parameters measured in reverberation and if necessary in anechoic chambers. From the relationship between the coherence bandwidths and the average absorbing cross section we can determine how the wireless signal is affected when some absorbers are placed or removed from the reverberation chamber. Using this approach the other way round, it is possible to estimate what is the necessary load in order to obtain a desired coherence bandwidth of the channel which would be requested for a specified wireless transmission system.

If the parallelepiped absorbers are evenly illuminated and the electromagnetic radiation in the chamber is well represented as plane waves, the average absorbing cross section may be predicted from the average projected surface (which requests the knowledge of the dimensions of the absorbing surface) and the average transmission coefficient (for which the complex permittivity of the material has to be known).

Bibliography

[1] T. S. Rappaport, *Wireless Communications: Principles and Practice (2nd Edition)*, 2nd ed. Prentice Hall, Jan. 2002.

[2] D. A. Hill, M. T. Ma, A. R. Ondrejka, B. F. Riddle, M. Crawford, and R. T. Johnk, "Aperture excitation of electrically large, lossy cavities," *IEEE Transactions on Electromagnetic Compatibility*, vol. 36, no. 3, pp. 169–178, Aug. 1994.

[3] I. Junqua, P. Degauque, M. Lienard, and F. Issac, "On the power dissipated by an antenna in transmit mode or in receivemode in a reverberation chamber," *Electromagnetic Compatibility, IEEE Transactions on*, vol. PP, no. 99, pp. 1–7, 2011.

[4] A. Goldsmith, *Wireless Communications*. Cambridge University Press, Aug. 2005.

[5] X. Chen and P.-S. Kildal, "Theoretical derivation and measurements of the relationship between coherence bandwidth and RMS delay spread in reverberation chamber," in *Antennas and Propagation, 2009. EuCAP 2009. 3rd European Conference on*, Mar. 2009, pp. 2687–2690.

[6] N. SP-7, "Nasa thesaurus," Tech. Rep., 1965.

[7] D. A. Hill, "Plane wave integral representation for fields in reverberation chambers," *IEEE Transactions on Electromagnetic Compatibility*, vol. 40, no. 3, pp. 209–217, 1998.

[8] ——, "A reflection coefficient derivation for the Q of a reverberation chamber," *IEEE Transactions on Electromagnetic Compatibility*, vol. 38, no. 4, pp. 591–592, Nov. 1996.

[9] J. A. Stratton, *Electromagnetic Theory*. McGraw-Hill, 2006, vol. 51, no. 1312. [Online]. Available: http://usir.salford.ac.uk/3420/

[10] C. Lemoine, P. Besnier, and M. Drissi, "Advanced method for estimating number of independent samples available with stirrer in reverberation chamber," *Electronics Letters*, vol. 43, no. 16, pp. 861–862, Aug. 2007.

[11] C. Holloway, D. Hill, J. Ladbury, and G. Koepke, "Requirements for an effective reverberation chamber: unloaded or loaded," *Electromagnetic Compatibility, IEEE Transactions on*, vol. 48, no. 1, pp. 187–194, Feb. 2006.

[12] K. Zhang and D. Li, *Electromagnetic Theory for Microwaves and Optoelectronics*. Springer London, Limited, 2008. [Online]. Available: http://books.google.fr/books?id=3Da7MvRZTlAC

CHAPTER 5

Simultaneous control of emulated propagation channel parameters

5.1 Introduction

MANY authors have proposed different approaches to quantify and control different parameters in reverberation chamber. The relation between the coherence bandwidth and root mean square (RMS) delay spread is analyzed in [1]. In [2] Rician wireless environments are controlled by modifying the chamber and antennas characteristics while in [3] the RMS delay spread is analyzed with the quantity of loading. Generally, the parameters measured in reverberation chamber are investigated separately. However, in order to make reverberation chamber a relevant test facility and a repeatable environment, the parameters which affect the emulated multipath wireless channel have to be simultaneously controlled.

In this chapter a fast way to control simultaneously the propagation channel inside reverberation chamber in terms of K-factor, time parameters and the degree of absorption is proposed. Using a simple statistical model of the power delay profile (PDP) of the channel response to a pulse modulated sine wave, analytical equations for different channel parameters are extracted. K-factor is described as a function of time moments and the normalized power level of the signal envelope. Analytical relations for the mean delay spread τ_{μ} and the root mean square delay spread τ_{rms} are computed as functions of K-factor and other time constants. Assuming that the absorption of energy in reverberation chamber affects only the stirred components, the average absorbing cross section (AACS) of the loading materials is also estimated with regard to K-factor. An iterative relation to estimate K with regard to the quantity of absorbers is presented. Simulations and measurements, for arbitrary distances between antennas and degrees of absorption, validate and show the utility of this approach.

5.2 Signal model

5.2.1 Hypothesis

The following time constants are used to describe the functionality of reverberation chamber in transient regime:

- τ is the decay constant of the chamber associated to the stored energy in the reverberation chamber which evolves with time as $e^{-t/\tau}$ [4]. It is related to the composite quality factor (i.e., the losses in the chamber and the distribution of modes at the measurement frequency), $Q = 2\pi f\tau$;

- t_{unSti} is the delay time of the unstirred signal, traveling from transmitting to receiving antenna. The transmission starts at $t = 0$;

- t_{Sti} is defined as the moment at which the reverberation process begins to take place. Therefore the storage or release of energy mentioned above starts at $t = t_{\text{Sti}}$.

Let first consider the situation when, at reception, the envelope of the electric field in steady state, a_{Sti}, contains only stirred components. The complex rectangular components of the electric field are zero-mean Gaussian distributed while their phases are uniformly distributed. Therefore, the envelope of the electric field follows a Rayleigh distribution [5]. It results that: $E\left[a_{\text{Sti},i}^2\right] = 2\sigma^2$, the parameter σ^2 representing the variance of the rectangular components, [6]. The average of the power of the signal envelope for the transient regime may be modeled as an exponential function [4], with a decay constant τ:

$$P_{\text{Sti}}(t) = E\left[p_{\text{Sti},i}(t)\right] = E\left[a_{\text{Sti},i}^2\right]\left[1 - e^{-(t-t_{\text{Sti}})/\tau}\right]u(t - t_{\text{Sti}}), \tag{5.1}$$

where

- "Sti" defines the stirred components;

- $E\left[\square\right]$ is the expected value over a set of realizations;

- i represents the ith realization generated by changing the mechanical stirrer position, antenna position, measurement frequency, etc. Each realization is taken into account in the artificially created fading, whose duration is longer than the transient regime;

- $p_{\text{Sti},i}(t)$ is the power profile of the envelope for the ith realization of the stirred components which has in steady state an exponential distribution;

- $a_{\text{Sti},i}$ represents the ith realization of the envelope of the electric field of stirred components, and is Rayleigh distributed;

- $u(t-t_{\text{Sti}})$ is the step function, defining the moment t_{Sti} from which the reverberation process has begun.

When the received signal also contains unstirred components, the envelope of the electric field in steady state becomes Rician distributed. The power profile of the total signal for the ith realization can approximately be given by [7]:

$$\begin{aligned} p_{\text{total},i}(t) =& A_{\text{unSti}}^2 u(t - t_{\text{unSti}}) + a_{\text{Sti},i}^2\left[1 - e^{-(t-t_{\text{Sti}})/\tau}\right]u(t - t_{\text{Sti}}) \\ &+ 2A_{\text{unSti}}a_{\text{Sti},i}\sqrt{1 - e^{-(t-t_{\text{Sti}})/\tau}}\cos\left(\theta_{\text{Sti},i}\right)u(t - t_{\text{Sti}}). \end{aligned} \tag{5.2}$$

In the above equations,

- "unSti" defines the unstirred components;

- "total" defines the combination of unstirred and stirred components;
- A_{unSti} is the maximum level of the envelope of the electric field of unstirred components, remaining constant with the stirring mechanism;
- $u(t-t_{\text{unSti}})$ is the step function defining the moment t_{unSti} starting from which the unstirred components arrive at reception;
- $\theta_{\text{Sti},i}$ is the equivalent phase in steady state for the ith realization, obtained from the combination of several scattered components arriving with different angles of arrival; it has a uniform distribution over the number of realizations.

In steady state the parameter $p_{\text{total},i}(t)$ has a noncentral chi-squared distribution. The mean over a number of realizations is then modeled with:

$$P_{\text{total}}(t) = E\left[p_{\text{total},i}(t)\right] \approx A_{\text{unSti}}^2 u(t-t_{\text{unSti}}) + 2\sigma^2\left[1-e^{-(t-t_{\text{Sti}})/\tau}\right]u(t-t_{\text{Sti}}), \tag{5.3}$$

From the central limit theorem (see annex B.2) [6] and considering (5.2), the estimate of $P_{\text{total}}(t)$ (denoted $\widehat{P}_{\text{total}}(t)$) follows a Gaussian distribution, having the mean given by (5.3) and the standard deviation by:

$$\widetilde{\sigma} = \frac{2\sigma}{\sqrt{N}}\sqrt{A_{\text{unSti}}^2\left[1-e^{-(t-t_{\text{Sti}})/\tau}\right] + \sigma^2\left[1-e^{-(t-t_{\text{Sti}})/\tau}\right]^2}. \tag{5.4}$$

It results that the confidence interval of $\widehat{P}_{\text{total}}(t)$ depends on the number N of realizations, and respectively the level of unstirred and stirred components, A_{unSti} and σ.

Two Monte Carlo simulations of the average power profiles of the electric field and their corresponding limits of a 99.7% confidence interval are presented in Fig. 5.2. This confidence interval is obtained by considering three standard deviations ($\pm 3\widetilde{\sigma}$) from the mean of the Gaussian distribution of the $\widehat{P}_{\text{total}}(t)$. The decay constant of a reverberating chamber, Fig. 5.1, is computed with the equation presented in [8]:

$$\tau = -\frac{L}{2c\ln(1-\overline{T})}. \tag{5.5}$$

The parameter L is the characteristic distance and represents the mean distance between two consecutive reflections in the chamber [9]:

$$L = 4\frac{V}{S}. \tag{5.6}$$

If the dimensions of the reverberation chamber are: $8.7\times3.7\times2.9\,\text{m}^3$ (i.e., as the reverberation chamber of our laboratory), this value is $L = 2.74\,\text{m}$. Considering an arbitrary value of the average absorption coefficient $\overline{T} = 0.0019$, it results $\tau \approx 2.4\,\mu\text{s}$ (as the measured decay constant of the chamber in our laboratory). We consider the antennas as directive and perfectly matched. In the direction of propagation they have a gain of 7 dBi and are placed in line-of-sight at 0.5 m of each other. The equivalent unstirred component is estimated with the Friis equation. At this distance between antennas, we have $t_{\text{unSti}} = 1.67\,\text{ns}$. If the parameter t_{Sti} equals to five times the characteristic time of the chamber as in [10] then $t_{\text{Sti}} = 91.4\,\text{ns}$. The characteristic

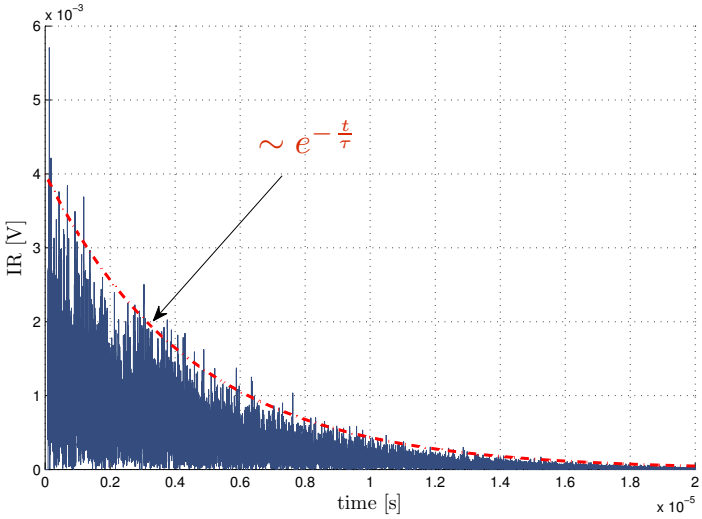

Figure 5.1: Decay constant of a impulse response sent in reverberation chamber.

time corresponds to the average time of two consecutive reflections and is evaluated from the characteristic distance as:

$$t_c = \frac{2L}{c}. \tag{5.7}$$

The sample is constituted from $N = 100$ independent realizations [11], and the signal, whose frequency is 2.5 GHz, is analyzed for 10 µs with a time resolution of ≈ 53 ps. In Fig. 5.2 we can see two types of curves: power profiles whose power in steady state is bigger than the power of unstirred components (a), and power profiles whose power in steady state is smaller than the power of unstirred components (b). This is due to the Gaussian distribution of the total power profile in steady state, whose standard deviation is computed in (5.4). It results that the estimated power of the signal in steady state may be equal with/or smaller than

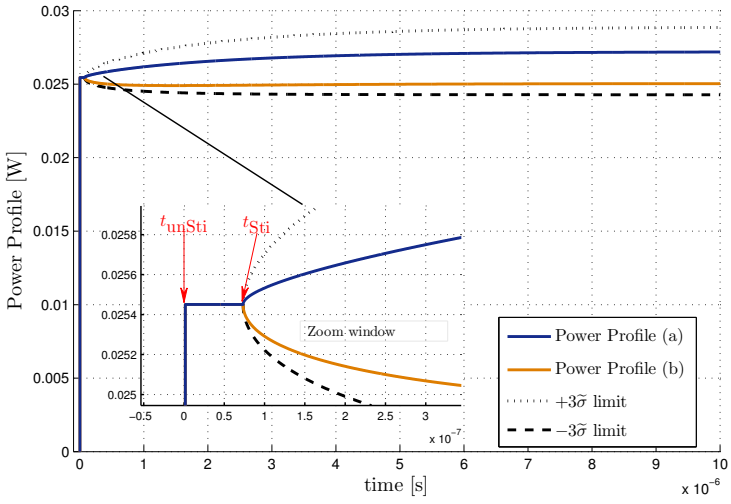

Figure 5.2: The power profile of the total envelope.

the power of the signal corresponding to unstirred components, (Fig. 5.2-profile (b)). This situation can be avoided by increasing the number N of realizations, decreasing the power of unstirred components or increasing the power of stirred components.

5.2.2 Defining the "steady state time"

The parameter t_{Ss} represents the time for which the steady state is reached. More precisely, t_{Ss} is defined as the necessary time for the signal at reception to reach a level of $\alpha\%$ of the averaged power of the signal envelope. At $t = t_{\mathrm{Ss}}$ most of the energy of the pulse modulated sine wave has already arrived at reception, and the steady state begins, the envelope of the electric field having a Rician distribution. Using (5.3), the normalized power profile to the total power at $t = t_{\mathrm{Ss}}$ is written as:

$$C + (1 - C)\left[1 - e^{-(t_{\mathrm{Ss}} - t_{\mathrm{Sti}})/\tau}\right] = \alpha, \quad t_{\mathrm{Sti}} > t_{\mathrm{unSti}}, \tag{5.8}$$

where $C = A_{\mathrm{unSti}}^2/(A_{\mathrm{unSti}}^2 + 2\sigma^2)$ represents the ratio between the power of the unstirred components and the second order raw moment of the envelope of the signal, i.e., representing the summation between the power of the unstirred and the stirred components. With (5.8), the steady state time results:

$$t_{\mathrm{Ss}} = -\tau \ln \frac{1}{1 - C} + \tau \ln \frac{1}{1 - \alpha} + t_{\mathrm{Sti}}. \tag{5.9}$$

In (5.9), two terms can be identified:

- the first is $\tau \ln \dfrac{1}{1 - \alpha} + t_{\mathrm{Sti}}$ which also appears when only stirred components exist;
- the second $-\tau \ln \dfrac{1}{1 - C}$ corresponds to the emergence of unstirred components.

The absolute steady state time results from (5.9) as:

$$\Delta t = t_{\mathrm{Ss}} - t_{\mathrm{unSti}} = t_{\mathrm{Sti}} - t_{\mathrm{unSti}} + \tau \ln \frac{1}{1 - \alpha} - \tau \ln\left(\frac{1}{1 - C}\right). \tag{5.10}$$

From section 5.2.1 we have observed that not all the power profiles over the confidence interval can be used, some of them in steady state being less or comparable with the power of the unstirred signal. These situations must be excluded from the calculus as they do not provide realistic results. Here, we compute the percentage of erroneous values as a function of K-factor, limit parameter α and the sample size N. This percentage is linked to the probability that $P_{\mathrm{total,Ss}} < A_{\mathrm{unSti}}^2/\alpha$ and is equal to:

$$\Pr\left(P_{\mathrm{total,Ss}} < \frac{A_{\mathrm{unSti}}^2}{\alpha}\right) = \frac{1}{2}\operatorname{erfc}\left(\sqrt{N}\frac{K\dfrac{\alpha - 1}{\alpha} + 1}{\sqrt{2K + 1}}\right), \tag{5.11}$$

where erfc is the complementary error function. In Fig. 5.3 is presented the percentage of erroneous values when $\alpha = 0.95$, the sample size N changes from 10 to 5000 and the K-factor changes from 0 to 15 dB. For a percentage of errors less than 1%, when the number of samples N is 5000, the maximum detectable value of K-factor is less than 12.15 dB. In practice the choice of the parameter α depends on the smoothness of the measured power profile while the number of samples depends on the measurement conditions (e.g., efficiency of the mode stirrer for instance).

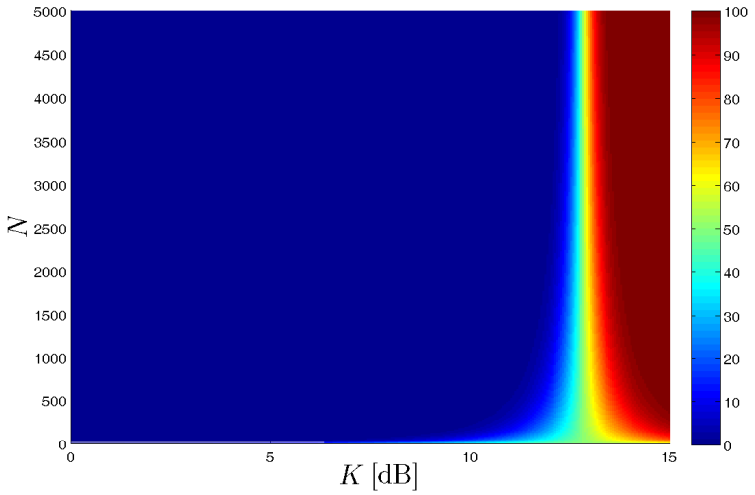

Figure 5.3: The percentage of erroneous values of K-factor as a function of N for $\alpha = 0.95$.

5.3 Relating K-factor with various time parameters

5.3.1 K-factor as a function of time parameters

K-factor is defined as the ratio between the powers of the specular and the scattered components of the received signal at the reception antenna [12] (see chapter 3):

$$K = \frac{A_{\text{unSti}}^2}{2\sigma^2} \tag{5.12}$$

From (5.9) and (5.12), K-factor can be easily extracted with:

$$K = \frac{1}{1-\alpha} e^{-(t_{\text{Ss}} - t_{\text{Sti}})/\tau} - 1. \tag{5.13}$$

In (5.13), the parameter K is computed using time parameters t_{unSti}-linked to specular paths, t_{Sti}-linked to scattered paths, t_{Ss}-corresponding to the moment from which the steady state of the power of the signal envelope is considered to begin, τ-which is the decay constant of the chamber, and the limit parameter α-corresponding to the level of the power of the signal envelope at $t = t_{\text{Ss}}$. If the estimation errors of t_{Ss} and t_{Sti} are respectively $\pm\chi\%$ and $\pm\delta\%$ (e.g., due to the limited time resolution of the measuring instrument), the absolute relative error of the estimation of K-factor becomes:

$$K_{\text{error}}^{\text{relative}} = 1 - e^{\mp(|\chi| t_{\text{Ss}} - |\delta| t_{\text{Sti}})/\tau}. \tag{5.14}$$

It results that overestimating t_{Ss} will overestimate the parameter K, whereas overestimating t_{Sti} the parameter K is underestimated.

5.3.2 Time parameters: τ_μ and τ_{rms} as functions of K-factor

For a wideband signal, the mean delay and the RMS delay spread are defined as, [13]:

$$\tau_\mu = \frac{\int_0^\infty (t - t_{\text{unSti}}) P_{\text{total}}^{\text{norm}}(t)\, \mathrm{d}\, t}{\int_0^\infty P_{\text{total}}^{\text{norm}}(t)\, \mathrm{d}\, t}, \tag{5.15}$$

and

$$\tau_{\mathrm{rms}} = \sqrt{\frac{\int_0^\infty (t - t_{\mathrm{unSti}} - \tau_\mu)^2 P_{\mathrm{total}}^{\mathrm{norm}}(t)\,\mathrm{d}\,t}{\int_0^\infty P_{\mathrm{total}}^{\mathrm{norm}}(t)\,\mathrm{d}\,t}}. \tag{5.16}$$

The parameter $P_{\mathrm{total}}^{\mathrm{norm}}(t)$ represents the normalization of the mean total power $P_{\mathrm{total}}(t)$ in (5.3) to the total power $A_{\mathrm{unSti}}^2 + 2\sigma^2$ in order to describe time spread parameters as function of K-factor. By using equations (5.15) and (5.16), we provide analytical expressions of the mean delay and the RMS delay spread for the transient regime of the sinusoidal pulse. First, the mean delay spread (as a function of K-factor, limit parameter α, decay constant of the chamber τ, and time constants t_{Sti} and t_{unSti}). The denominator of the parameter in (5.15) and (5.16) is computed as:

$$\begin{aligned}\int_0^\infty P_{\mathrm{total}}^{\mathrm{norm}}(t)\,\mathrm{d}\,t &= \int_{t_{\mathrm{unSti}}}^{t_{\mathrm{Ss}}} P_{\mathrm{total}}^{\mathrm{norm}}(t)\,\mathrm{d}\,t = \frac{K}{K+1} t\big|_{t_{\mathrm{unSti}}}^{t_{\mathrm{Ss}}} + \frac{1}{K+1}\left(t\big|_{t_{\mathrm{Sti}}}^{t_{\mathrm{Ss}}} + \tau e^{t_{\mathrm{Sti}}/\tau} e^{-t/\tau}\big|_{t_{\mathrm{Sti}}}^{t_{\mathrm{Ss}}}\right) \\ &= -\tau \ln\left[(1+K)(1-\alpha)\right] + \frac{K}{1+K}\beta - \alpha\tau,\end{aligned} \tag{5.17}$$

while the numerator of (5.15) is given by:

$$\begin{aligned}\int_0^\infty P_{\mathrm{total}}^{\mathrm{norm}}(t)(t - t_{\mathrm{unSti}})\,\mathrm{d}\,t = \int_{t_{\mathrm{unSti}}}^{t_{\mathrm{Ss}}} P_{\mathrm{total}}^{\mathrm{norm}}(t)(t - t_{\mathrm{unSti}})\,\mathrm{d}\,t &= \frac{K}{K+1}\frac{t^2}{2}\big|_{t_{\mathrm{unSti}}}^{t_{\mathrm{Ss}}} - \frac{K}{K+1} t_{\mathrm{unSti}} t\big|_{t_{\mathrm{unSti}}}^{t_{\mathrm{Ss}}} \\ &+ \frac{1}{K+1}\frac{t^2}{2}\big|_{t_{\mathrm{Sti}}}^{t_{\mathrm{Ss}}} - t_{\mathrm{unSti}}\frac{1}{K+1} t\big|_{t_{\mathrm{Sti}}}^{t_{\mathrm{Ss}}} - \tau\frac{1}{K+1} t_{\mathrm{unSti}} e^{t_{\mathrm{Ss}}/\tau} e^{t_{\mathrm{Sti}}/\tau} \\ &+ \tau\frac{1}{K+1} t_{\mathrm{unSti}} + \tau\frac{1}{K+1} e^{t_{\mathrm{Sti}}/\tau}\left(t e^{-t/\tau}\big|_{t_{\mathrm{Sti}}}^{t_{\mathrm{Ss}}} + \tau e^{-t/\tau}\big|_{t_{\mathrm{Sti}}}^{t_{\mathrm{Ss}}}\right).\end{aligned} \tag{5.18}$$

With (5.15), (5.17) and (5.18) and the description of the parameter t_{Ss} in (5.9), the mean delay spread τ_μ becomes:

$$\begin{aligned}\tau_\mu = &\frac{\frac{K}{1+K}\frac{\beta^2+\tau^2}{2} - \tau\alpha\beta}{\beta\frac{K}{K+1} - \tau\ln\left[(1+K)(1-\alpha)\right] - \alpha\tau} - \frac{(\beta\tau - \alpha\tau^2)\ln\left[(1+K)(1-\alpha)\right]}{\beta\frac{K}{K+1} - \tau\ln\left[(1+K)(1-\alpha)\right] - \alpha\tau} \\ &+ \frac{\frac{\tau^2}{2}\ln^2\left[(1+K)(1-\alpha)\right]}{\beta\frac{K}{K+1} - \tau\ln\left[(1+K)(1-\alpha)\right] - \alpha\tau},\end{aligned} \tag{5.19}$$

where $\beta = t_{\mathrm{Sti}} + t_{\mathrm{unSti}} + \tau$.
Moreover, the RMS delay spread (5.16), depending on the above presented parameters and the mean delay spread), is given by:

$$\tau_{\mathrm{rms}} = \sqrt{\frac{\int_{t_{\mathrm{unSti}}}^{t_{\mathrm{Ss}}} t^2 P_{\mathrm{total}}^{\mathrm{norm}}(t)\,\mathrm{d}\,t}{\int_{t_{\mathrm{unSti}}}^{t_{\mathrm{Ss}}} P_{\mathrm{total}}^{\mathrm{norm}}(t)\,\mathrm{d}\,t} - 2\gamma\frac{\int_{t_{\mathrm{unSti}}}^{t_{\mathrm{Ss}}} t P_{\mathrm{total}}^{\mathrm{norm}}(t)\,\mathrm{d}\,t}{\int_{t_{\mathrm{unSti}}}^{t_{\mathrm{Ss}}} P_{\mathrm{total}}^{\mathrm{norm}}(t)\,\mathrm{d}\,t} + \gamma^2}, \tag{5.20}$$

where $\gamma = t_{\mathrm{unSti}} + \tau_\mu$ and the different integrals are calculated as:

$$\begin{aligned}\int_{t_{\mathrm{unSti}}}^{t_{\mathrm{Ss}}} t^2 P_{\mathrm{total}}^{\mathrm{norm}}(t)\,\mathrm{d}\,t &= \frac{K}{K+1}\frac{t^3}{3}\Big|_{t_{\mathrm{Sti}}}^{t_{\mathrm{Ss}}} + \frac{t^3}{3}\Big|_{\mathrm{Sti}}^{t_{\mathrm{Ss}}} - \frac{K}{K+1}\frac{t^3}{3}\Big|_{t_{\mathrm{unSti}}}^{t_{\mathrm{Ss}}} - \frac{1}{K+1}e^{t_{\mathrm{Sti}}/\tau} \\ &\quad \cdot \left(-\tau t^2 e^{-t/\tau} - \tau^2 2te^{-t/\tau} - 2\tau^3 e^{-t/\tau}\right)\Big|_{t_{\mathrm{Sti}}}^{t_{\mathrm{Ss}}} \\ &= -\frac{\tau^3}{3}\ln^3\left[(1+K)(1-\alpha)\right] + \tau^2\left[t_{\mathrm{Sti}} + \tau(1-\alpha)\right]\ln^2\left[(1+K)(1-\alpha)\right] \\ &\quad - \tau\left[t_{\mathrm{Sti}}^2 + 2\tau(t_{\mathrm{Sti}}+\tau)(1-\alpha)\right]\ln\left[(1+K)(1-\alpha)\right] \\ &\quad + \frac{K}{1+K}\left[\tau(t_{\mathrm{Sti}}+\tau)^2 + \tau^3 + \frac{t_{\mathrm{Sti}}^3}{3} - \frac{t_{\mathrm{unSti}}^3}{3}\right] - \alpha\tau\left[(t_{\mathrm{Sti}}+\tau)^2 + \tau^2\right],\end{aligned}$$

$$\begin{aligned}\int_{t_{\mathrm{unSti}}}^{t_{\mathrm{Ss}}} tP_{\mathrm{total}}^{\mathrm{norm}}(t)\,\mathrm{d}\,t &= \frac{K}{K+1}\frac{t^2}{2}\Big|_{\mathrm{unSti}}^{t_{\mathrm{Ss}}} + \frac{1}{K+1}\frac{t^2}{2}\Big|_{\mathrm{Sti}}^{t_{\mathrm{Ss}}} - \frac{1}{K+1}e^{t_{\mathrm{Sti}}/\tau}\left(-\tau te^{-t/\tau} - \tau^2 e^{-t/\tau}\right)\Big|_{t_{\mathrm{Sti}}}^{t_{\mathrm{Ss}}} \\ &= \frac{\tau^2}{2}\ln^2\left[(1+K)(1-\alpha)\right] - \tau\left[t_{\mathrm{Sti}} + \tau(1-\alpha)\right]\ln\left[(1+K)(1-\alpha)\right] \\ &\quad + \frac{K}{1+K}\left[\tau(t_{\mathrm{Sti}}+\tau) + \frac{t_{\mathrm{Sti}}^2}{2} - \frac{t_{\mathrm{unSti}}^2}{2}\right] - \alpha\tau(t_{\mathrm{Sti}}+\tau).\end{aligned}$$

The mean delay and the RMS delay spread in (5.19) and (5.20) depend on several parameters:

- the K-factor which is influenced by the volume of the chamber and its quality factor, the frequency of the signal, the distance between antennas, and the directivity of the transmitting antenna [2];
- the decay constant τ which in turn depends on the characteristic distance L and the average absorption coefficient $\overline{T}$;
- the parameter t_{unSti} which is directly linked to the distance between antennas while t_{Sti} is related to the characteristic time of the chamber;
- the limit parameter α selected to take into account the maximum of energy in order to assure that the distribution in steady state is well determined.

5.3.3 Parameters for a loaded chamber

Most of the above parameters depend on the chamber quality factor. This factor can be controlled by using absorbers. This section deals with the relationships between the average absorbing cross section of the loads, the decay constant of the chamber, and the K-factor. One considers absorbers placed in reverberation chamber, but not between antennas, in order to influence only the scattered components. Assuming that the received signals consist only of scattered components, the average scalar power density $\mathcal{S}_{\mathrm{E}}$ (proportional to the mean energy density) and the dissipated power $P_{\mathrm{D,E}}$ in an empty chamber of equivalent absorbing surface $\overset{\blacktriangle}{\sigma}_{\mathrm{RC}}$ (corresponding to antennas, cables, metallic walls, apertures, etc.) are given by [2]:

$$\begin{aligned}\mathcal{S}_{\mathrm{E}} &= \frac{E_{0,\mathrm{E}}^2}{\eta} = 3\frac{2\sigma_{\mathrm{E}}^2}{\eta} = \frac{Q_{\mathrm{E}}P_{\mathrm{T}}}{\epsilon\eta\omega V}, \\ P_{\mathrm{D,E}} &= \frac{E_{0,\mathrm{E}}^2}{\eta}\,\overset{\blacktriangle}{\sigma}_{\mathrm{RC}}\,.\end{aligned} \tag{5.21}$$

In these equations:

- $E_{0,\mathrm{E}}^2$ is the mean square value of the total electric field and is proportional to the variance of stirred components [5],
- Q_{E} is the quality factor of the empty chamber ($Q_{\mathrm{E}} = 2\pi f \tau_{\mathrm{E}}$). It indicates the degree of energy stored in the chamber with regard to dissipated energy. In the presence of unstirred components, the quality factor does not change very much since the energy contained in the stirred components is much higher than the one contained in unstirred components [4];
- P_{T} is the total power transmitted to the chamber;
- ϵ is the permittivity of free space;
- η is the free space impedance;
- $\omega = 2\pi f$;
- V is the volume of the chamber.

When a quantity of absorbers, whose average absorbing cross section is $\overset{\blacktriangle}{\sigma}_{\mathrm{A}}$, is placed in reverberation chamber then (5.21) becomes:

$$\begin{aligned} \mathcal{S}_{\mathrm{L}} &= \frac{E_{0,\mathrm{L}}^2}{\eta} = 3\frac{2\sigma_{\mathrm{L}}^2}{\eta} = \frac{Q_{\mathrm{L}} P_{\mathrm{T}}}{\epsilon\eta\omega V}, \\ P_{\mathrm{D,L}} &= \frac{E_{0,\mathrm{L}}^2}{\eta}\left(\overset{\blacktriangle}{\sigma}_{\mathrm{RC}} + \overset{\blacktriangle}{\sigma}_{\mathrm{A}}\right), \end{aligned} \tag{5.22}$$

where $Q_{\mathrm{L}} = 2\pi f \tau_{\mathrm{L}}$ and $E_{0,\mathrm{L}}$ represent respectively the quality factor of the chamber and the mean square value of the electric field in the presence of absorbers. In the above equations the indexes "E" and "L" correspond to *"empty"* and *"loaded"* reverberating chamber.

Two general situations are analyzed:
1) In the first situation, the decay constants of the chamber without and with absorbers: τ_{E} and τ_{L} are considered known. The corresponding powers of the stirred components, $2\sigma_{\mathrm{E}}^2$ and $2\sigma_{\mathrm{L}}^2$ are also a priori known.

As the dissipated powers for the two situations (i.e., empty and loaded chamber) are equal with the transmitted power in the chamber ($P_{\mathrm{T}} = P_{\mathrm{D,E}} = P_{\mathrm{D,L}}$), from (5.21) and (5.22) it results:

$$P_{\mathrm{T}}\left(1 - \frac{\sigma_{\mathrm{L}}^2}{\sigma_{\mathrm{E}}^2}\right) = 3\frac{2\sigma_{\mathrm{L}}^2\,\overset{\blacktriangle}{\sigma}_{\mathrm{A}}}{\eta} \tag{5.23}$$

for which the transmitted power P_{T} can be evaluated from:

$$P_{\mathrm{T}} = 2\sigma_{\mathrm{E}}^2 \frac{\omega\epsilon V}{Q_{\mathrm{E}}}, \tag{5.24a}$$

or

$$P_{\mathrm{T}} = 2\sigma_{\mathrm{L}}^2 \frac{\omega\epsilon V}{Q_{\mathrm{L}}}. \tag{5.24b}$$

If in a Rician fading environment only the stirred energy is absorbed, identifying (5.23) with (5.24a) or (5.23) with (5.24b), the equivalent average absorbing cross section $\overset{\blacktriangle}{\sigma}_{\mathrm{A}}$ may be computed with:

$$\overset{\blacktriangle}{\sigma}_{\mathrm{A}} = \frac{V}{c\tau_{\mathrm{L}}}\left(1 - \frac{K_{\mathrm{E}}}{K_{\mathrm{L}}}\right), \tag{5.25a}$$

or

$$\overset{\blacktriangle}{\sigma}_{\mathrm{A}} = \frac{V}{c\tau_{\mathrm{E}}}\left(\frac{K_{\mathrm{L}}}{K_{\mathrm{E}}} - 1\right), \tag{5.25b}$$

for which

- $K_{\mathrm{E}} = A^2_{\mathrm{unSti,E}}/(2\sigma^2_{\mathrm{E}})$;
- $K_{\mathrm{L}} = A^2_{\mathrm{unSti,L}}/(2\sigma^2_{\mathrm{L}})$;
- c is the speed of light.

In practice, these equations allow us to control the chamber behavior with the degree of absorption. The differences between (5.25b) and (5.25a) consist in the use of the decay constant τ_{E} or τ_{L}, and consequently in the level of uncertainty of the results as discussed below. In these equations unstirred components are assumed to be not affected by the absorption of energy. When this hypothesis is not verified both equations in (5.25) are affected by estimation errors. Considering that $A_{\mathrm{unSti,E}}$ is different from $A_{\mathrm{unSti,L}}$ with $\pm\delta\%$ ($A_{\mathrm{unSti,E}}/A_{\mathrm{unSti,L}} = 1 \pm \delta$), the estimations of $\overset{\blacktriangle}{\sigma}_{\mathrm{A}}$ in (5.25b) and (5.25a), denoted $\overset{\blacktriangle}{\sigma}{}'_{\mathrm{A}}$, become respectively:

$$\overset{\blacktriangle}{\sigma}{}'_{\mathrm{A}} = \frac{V}{c\tau_{\mathrm{L}}}\left(\frac{\sigma^2_{\mathrm{E}}}{\sigma^2_{\mathrm{L}}} - 1\right) - \underbrace{\pm\delta\frac{V}{c\tau_{\mathrm{L}}}}_{\text{estimation error}}, \tag{5.26a}$$

and

$$\overset{\blacktriangle}{\sigma}{}'_{\mathrm{A}} = \frac{V}{c\tau_{\mathrm{E}}}\left(\frac{\sigma^2_{\mathrm{E}}}{\sigma^2_{\mathrm{L}}} - 1\right) - \underbrace{\frac{\pm\delta}{1 \pm \delta}\frac{V}{c\tau_{\mathrm{E}}}\frac{\sigma^2_{\mathrm{E}}}{\sigma^2_{\mathrm{L}}}}_{\text{estimation error}}. \tag{5.26b}$$

If in the above equations: τ_{E}, τ_{L}, σ^2_{E} and σ^2_{L} are perfectly estimated, then the bias of $\overset{\blacktriangle}{\sigma}{}'_{\mathrm{A}}$ depends only on δ. An error of $+\delta\%$ may correspond to the situation when the energy of the specular components is partially absorbed or when $A_{\mathrm{unSti,L}}$ is underestimated, while an error of $-\delta\%$ characterizes the case when $A_{\mathrm{unSti,L}}$ is overestimated. If we suspect an overestimation of the level of unstirred components (e.g., due to estimation uncertainties) then it is more appropriate to use (5.26a) while if the level of unstirred components is underestimated (e.g., due to absorption of some specular energy) equation (5.26b) provides the smallest error. When the initial decay constant τ_{E}, the K_{E}-factor for the empty chamber, and the average absorbing cross section $\overset{\blacktriangle}{\sigma}_{\mathrm{A}}$ are known, then from (5.26b) it results a fast way to estimate K-factor when chamber is loaded:

$$K_{\mathrm{L}} = K_{\mathrm{E}}\underbrace{\left(\frac{c\tau_{\mathrm{E}}\,\overset{\blacktriangle}{\sigma}_{\mathrm{A}}}{V} + 1\right)}_{\text{absorption factor}}. \tag{5.27}$$

The estimator K_{E} in (5.27) can be computed with (5.13) or with other envelope-based methods presented in [14–17], etc.

There are other ways to compute the average absorbing cross section in a reverberating chamber. In [18], this is done by using the decay constants of the chamber with and without absorbers:

$$\overset{\blacktriangle}{\sigma}_{\mathrm{A}} = \frac{V}{c}\left(\frac{1}{\tau_{\mathrm{L}}} - \frac{1}{\tau_{\mathrm{E}}}\right). \tag{5.28}$$

2) For the second situation, knowing the average absorbing cross section $\overset{\blacktriangle}{\sigma}_{\mathrm{A}}$ and the initial conditions (i.e., the power of the stirred components σ_{E}^2, and the decay constant of the empty chamber τ_{E}), one computes the magnitude of stirred components σ_{L} and the decay constant τ_{L} when the chamber is loaded. This allows to determine a priori the time characteristics of a loaded chamber once the empty chamber properties and the equivalent surface of absorption materials are known:

$$\sigma_{\mathrm{L}} = \sigma_{\mathrm{E}} \sqrt{\frac{1}{c\tau_{\mathrm{E}}\dfrac{\overset{\blacktriangle}{\sigma}_{\mathrm{A}}}{V} + 1}}, \tag{5.29}$$

and

$$\tau_{\mathrm{L}} = \frac{1}{c\dfrac{\overset{\blacktriangle}{\sigma}_{\mathrm{A}}}{V} + \dfrac{1}{\tau_{\mathrm{E}}}}. \tag{5.30}$$

Separating the influences of the chamber and the absorbers, (5.30) is reorganized as:

$$\frac{1}{\tau_{\mathrm{L}}} = \frac{c\,\overset{\blacktriangle}{\sigma}_{\mathrm{A}}}{V} + \frac{1}{\tau_{\mathrm{E}}}. \tag{5.31}$$

Using (5.21) and (5.22) a simple relation between the powers of the stirred components and the decay constants of the chamber with and without absorbers is described by:

$$\tau_{\mathrm{E}}\sigma_{\mathrm{L}}^2 = \tau_{\mathrm{L}}\sigma_{\mathrm{E}}^2. \tag{5.32}$$

5.4 Validation

5.4.1 Measurements and Simulations scenario

This section presents some validation measurements in reverberation chamber, Fig. 5.4, and the simulations carried out in order to obtain the various parameters computed with the methods presented in section 5.3. The measurements are made in frequency domain as it also provides the necessary parameters of reference for the simulations. However, measurements may be carried out directly in time domain by using an oscilloscope, at the cost of an increasing noise level of the measured signal. The transfer function of the channel is measured in the bandwidth $2 - 3\,\mathrm{GHz}$ with a bin resolution of $50\,\mathrm{kHz}$, resulting a number of 20001 measured frequencies. We measure 100 transfer functions of this kind from 100 independent stirrer positions [11], Fig. 5.5(a). Then, after removing the mismatches of antennas we compute the equivalent impulse response of the channel by using the inverse-CZT transform and using a Kaiser filter (parameter β is set to 13 in order to have low amplitude side-lobes even though the main lobe is wider) in order to reduce the influence of the limited bandwidth, Fig. 5.5(b)

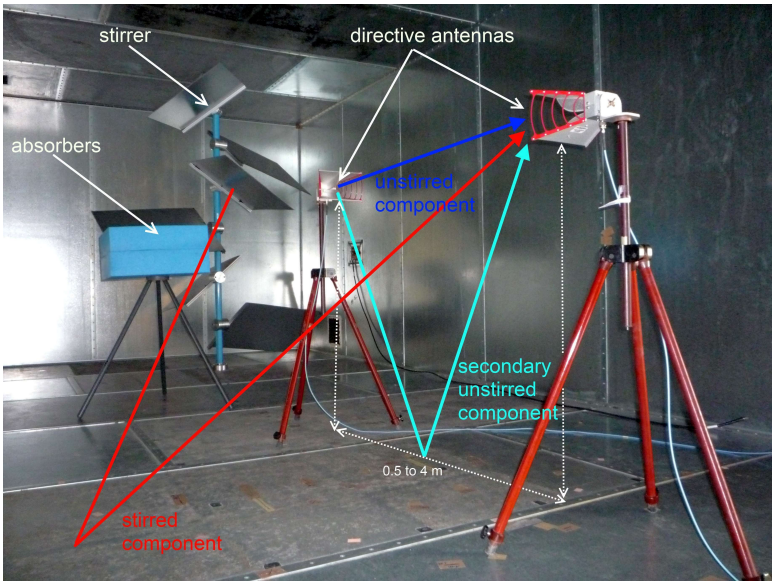

Figure 5.4: Simulation and measurement scenario (example).

(see annex D). The width of the pulse in time domain linked to the chosen β factor of the Kaiser filter is around 2.8 ns which much smaller than the characteristic time t_c = 18.3 ns of this chamber. The duration of the obtained impulse response is 20 µs with a time resolution of about 53 ps (meaning a sampling frequency of 19 GHz). We need this resolution as this impulse response is later convolved with 50 sinusoidal signals whose frequency changes from 2.495 GHz to 2.5048 GHz representing 10 MHz around a central frequency of 2.5 GHz, Fig. 5.5(c). This will form the electronic stirring process. The duration of the sine wave is 25 µs. After these 5000 convolutions (100×50) are computed, we rescale the resulting signal by the corresponding factors due to use of Kaiser filter and a higher sampling frequency in time domain, then we extract the envelopes of the signals, Fig. 5.5(d). Averaging the power of the envelopes over the 5000 realizations we obtain finally the average power profile, Fig. 5.5(e).

Estimating t_{unSti}

First step in analyzing this envelope is to find the parameter t_{unSti}. This value is found by considering the distance between two antennas plus the delay generated by the phase shift of the two antennas.

$$t_{\mathrm{unSti}} = \frac{d}{c} + 2t_{\mathrm{delays}}^{\mathrm{ant.}}. \tag{5.33}$$

The parameter $2t_{\mathrm{delays}}^{\mathrm{ant.}}$ is obtained from the measured phase of antennas by using 3 measurements which correspond to 3 different distances between antennas: 0.5, 1 and 1.5 m. Considering that the two antennas have phases ($\Delta\varphi_{\mathrm{ant.}}$) changing linearly in the bandwidth 2–3 GHz and that the phases of the channel ($\Delta\varphi_{\mathrm{channel}}$) also change linearly with the distance,

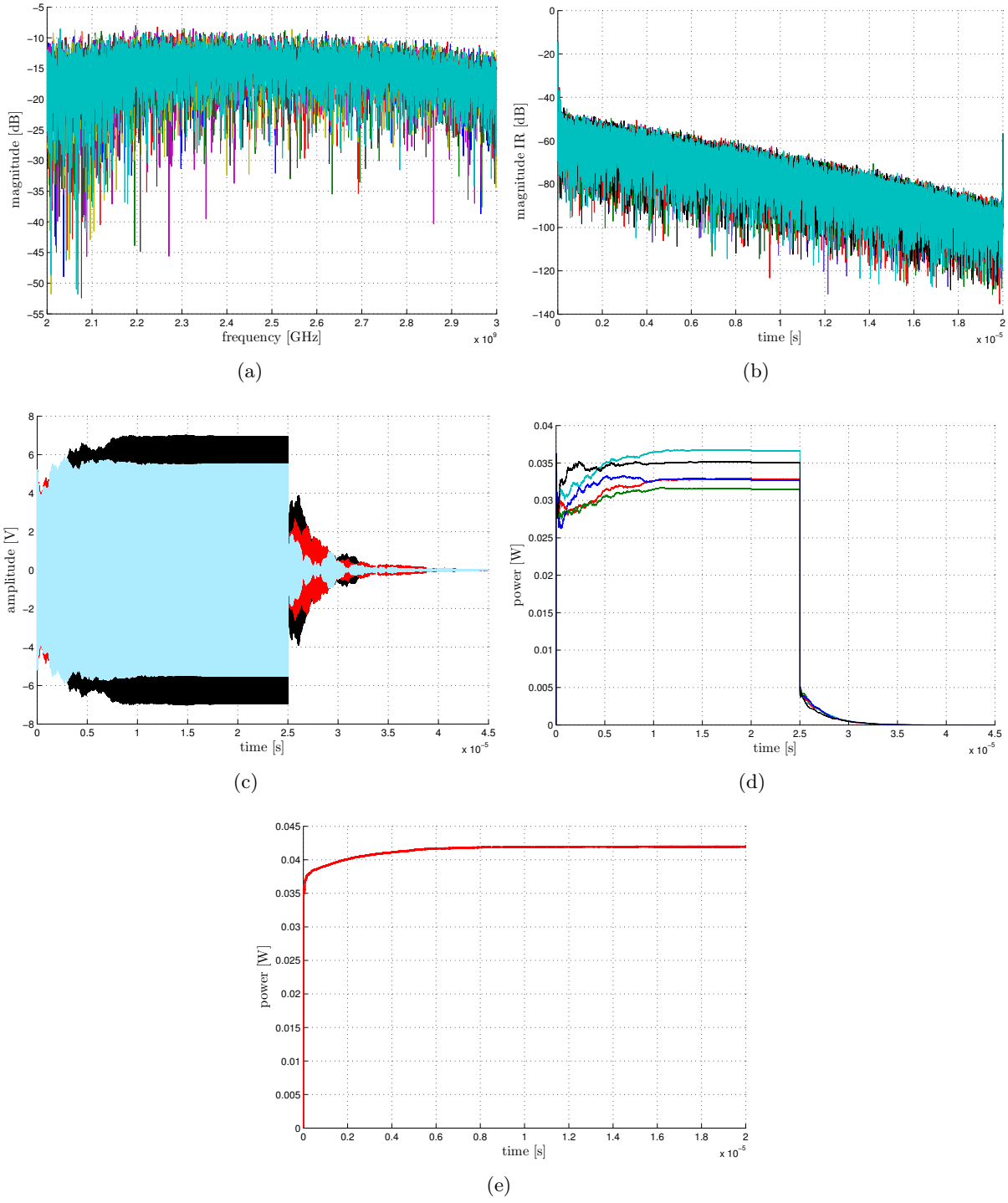

Figure 5.5: Schematic Description of inverse transform and envelope extraction:
(a) examples of transfer functions of the channel, (b) examples of impulse responses of the channel, (c) examples of resulted convolved signals, (d) examples of extracted power delays profiles, (e) averaged power delay profile.

then the phase shifts for the 3 measurements are written as:

$$\begin{cases} \Delta\varphi_{0.5\,\mathrm{m}} &= \Delta\varphi^1_{\mathrm{ant.}} + \Delta\varphi^2_{\mathrm{ant.}} + \Delta\varphi_{\mathrm{channel}}, \\ \Delta\varphi_{1\,\mathrm{m}} &= \Delta\varphi^1_{\mathrm{ant.}} + \Delta\varphi^2_{\mathrm{ant.}} + 2\Delta\varphi_{\mathrm{channel}}, \\ \Delta\varphi_{1.5\,\mathrm{m}} &= \Delta\varphi^1_{\mathrm{ant.}} + \Delta\varphi^2_{\mathrm{ant.}} + 3\Delta\varphi_{\mathrm{channel}}. \end{cases} \tag{5.34}$$

From the above equations system, the phase shifts of antennas are extracted. Assuming $\Delta\varphi^1_{\mathrm{ant.}} = \Delta\varphi^2_{\mathrm{ant.}}$, then the time delay due to one antenna is computed with:

$$t^{\mathrm{ant.}}_{\mathrm{delays}} = \frac{c}{2\pi}\frac{\Delta\varphi_{\mathrm{ant.}}}{\Delta f} \tag{5.35}$$

In this equation $\Delta f = 1\,\mathrm{GHz}$, and the time delay due to phase shift of antenna is 0.9 ns for one antenna (or 1.8 ns for both antennas). As an example of the importance to consider this parameter, we remind that the time for an electromagnetic wave to travel a distance of 0.5 m is 1.67 ns.

Estimating t_{Sti}

Referring to the discussion in section 5.2.1, this parameter represents the moment when the reverberation process begins to take place and the moment at which the power of unstirred components is evaluated. Extracting the power of unstirred components from the averaged power profile (in the transient regime) with a small error level is a more complicated task. This is due to the fact that in measurements there are also secondary unstirred components which are created by reflections on walls or other scatterers but not by the stirrer. Depending on how the measurement is configured, this secondary energy may represent an important percentage from the total unstirred energy. It results that the power of the unstirred components may converge at the power found in frequency domain after several hundreds of nanoseconds. An example of the normalized power of unstirred components to the power estimated in steady state (i.e., after 18 – 19 µs) for a duration of 500 ns is presented in Fig. 5.6. We can see that with time, depending on the measurement configuration, there are unstirred components which are added constructively and destructively to the received signal. In order to identify the level of unstirred components directly from the averaged power profile, we need a time limit at which we can evaluate the power of unstirred components. Presented in [7, 10] and validated later with measurements at a moment $t_{\mathrm{Sti}} = 5t_{\mathrm{c}} + 2t^{\mathrm{ant.}}_{\mathrm{delays}}$, depending on the directivity of antennas and the distances between them, most of the unstirred energy (75 – 90%) arrives at reception. In our reverberation chamber, this parameter is 93.2 ns (corresponding to a traveled distance of propagating waves of 27.95 m). As seen in Fig. 5.6 we can have a relative difference of the power of unstirred components measured at $t_{\mathrm{Sti}} = 93.2\,\mathrm{ns}$ to the one measured in steady state of 1.35% when the distance is 1 m and almost 20% when the distance becomes 3.5 m. In order to have a low detection error of the total power of unstirred components we suggest:

- the use of a heavily loaded chamber with absorbing materials (which will also change the quality factor of the chamber),
- the use of antennas with a high directivity or a reverberation chamber with a better stirring process (i.e., using multiple mechanical stirrers);

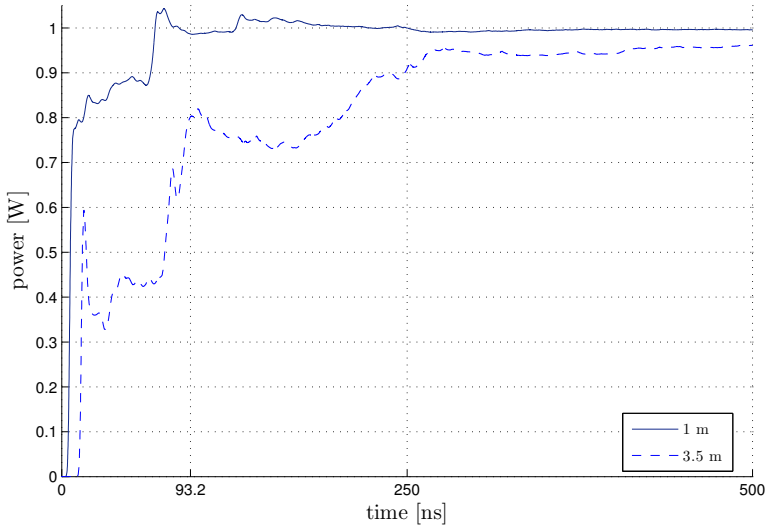

Figure 5.6: Example of the measured unstirred power delay profile for two different separation distances between antennas (1 m and 3.5 m).

- to work at high frequencies, in order to improve the detection of the level of unstirred components due to a higher degree of absorption. Also, working at higher frequencies may improve the directivity of antennas. For example, the antennas used to make the experiments presented in this chapter have a half power beamwidth varying from 60 to 42 ° for both polarizations E and H in the bandwidth 2 – 3 GHz, while in the bandwidth 9 – 10 GHz, the beamwidth is reduced to 30 – 40 °, also for both polarizations.

As we do not necessarily want to change the quality factor of the chamber, and since we have to use the available antennas in our laboratory, we try another solution in order to estimate the power of unstirred components with a low error. Because we cannot remove the secondary unstirred components after t_{unSti}, we try to increase the percentage of the energy of the impulse response contained in the interval $[0 - t_{\mathrm{unSti}}]$ compared with the total energy of the impulse response. We do that by slightly turning one antenna (less than $3 - 5\,^{\circ}$) in both planes H and V, but without modifying significantly the magnitude of the direct unstirred component. In this way the secondary paths are weighted with different antenna gains and the signal at reception changes. Even if this method needs several adaptations of the antenna until the maximum total power is found, from experiments we have found that the level of unstirred components could be approximated at $t = t_{\mathrm{unSti}}$ with an absolute relative errors less than 5 % compared with the values estimated in frequency domain. We validate the estimation of t_{Sti} by comparing the power identified in time domain with the one found in frequency domain.

Input parameters for simulations

The purpose of these simulations is to analyze the errors introduced by measurements in time domain compared with an expected value. Even though the measured values in frequency domain are also affected by uncertainties, due to a high number of realizations these are reduced. The input parameters for the simulations L and t_{c} are respectively computed with (5.6) and (5.7). The parameters t_{unSti} and t_{Sti} are estimated as presented in above paragraphs. The parameters A_{unSti}, σ and τ are estimated in frequency domain from 5000 realizations. The

first two parameters (i.e., A_{unSti} and σ) are estimated by computing the average and the variance of the measured sample, while the parameter τ is computed with [4]:

$$\tau = 2\sigma_{\text{norm}}^2 \frac{8\pi V f^2}{c^3} \tag{5.36}$$

In the above equation, the parameter $2\sigma_{\text{norm}}^2$ corresponds to the ratio of the stirred components over the injected power in the chamber and evolves as the quality factor of the chamber Q [5]. We choose the parameter limit $\alpha = 0.95$, for which from Fig. 5.3 the maximum detectable K-factor is 12.15 dB for an error less than 1%. This limit is acceptable as the highest detectable value of K-factor in these measurements is less than 10 dB. In these simulations, at emission, the sinusoidal signal is considered to have a frequency of 2.5 GHz and amplitude 1 V. At reception, the total duration of the recorded signal (i.e., the transient regime and the steady state) is 19 µs. The time resolution is around 53 ps. The total signal is created in two stages. First, the envelope of the stirred components in steady state is obtained by generating the Gaussian distributed rectangular components of the electric field having their phases uniformly distributed. Then, the unstirred envelope is added to create a signal whose variation with time follows (5.3). Simulations are done based on Monte Carlo method. The number of realizations is 5000 (as described above) and the number of Monte Carlo simulations is also 5000. Even though the sample sizes in measurements and simulations are equal, the corresponding distributions are not perfectly identical. For each stirrer position, the realizations of the electric field in measurements are the resulted superposition of plane waves arriving at reception from different directions while in simulations we generate directly this superposition. As a direct consequence, the confidence interval of the power profile computed in simulations may be higher than the true confidence interval found in measurements.

5.4.2 Results

We make two types of measurements (see section 5.4.1). For the first type of measurements we change the distance between antennas from 0.5 to 4 m with a step of 0.5 m. Even though at 0.5 m the receiving antenna is placed at the limit of the far field region of the transmitting antenna, this will not influence the results of our experiment. This is because by changing the distance between antennas we just want to modify the unstirred direct energy level at reception without necessarily considering a plane wave representation for this component. For the second type we place the antennas at two different distances (1.5 m and 2.5 m) and the chamber is loaded gradually with 4 identically parallelepiped absorbers placed in air at a distance of 1 m from the floor and behind one antenna so unstirred components will be less influenced by the absorption of energy. The absorbers are joined together to remove the shadowing effect between them. The dimensions of one absorber are: $0.6 \times 0.6 \times 0.15\,\text{m}^3$ resulting a total visible surface of one absorber of $1.08\,\text{m}^2$, while for 4 absorbers this surface is $2.16\,\text{m}^2$.

5.4.2.1 Variation with the distance

Fig. 5.7 presents the simulated (5.36) and the estimated decay constant of the chamber from the normalized averaged power profile. The differences between the results found in simulations and in measurements may be due to irregularities of the envelope or because of the estimation error of unstirred components. To discard the first hypothesis, we extract the decay

constant searching a level of 86.5% from the normalized averaged power profile corresponding to 2 decay constants of an exponential function. We choose this level as the power profile is smoother and the slope is stepper. It results that the error of the estimation of unstirred components may have enough influence to bias the decay constant even though the energy of unstirred components is much smaller than the energy of stirred components.

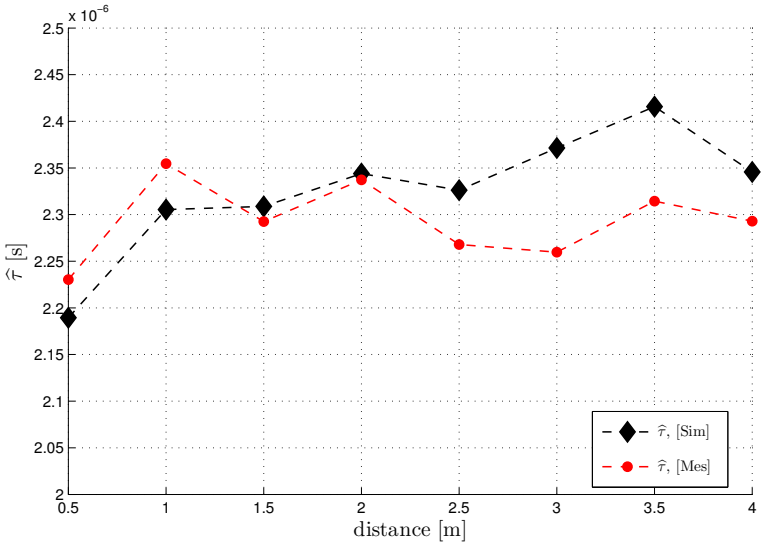

Figure 5.7: Variation of the estimated decay constant τ of the chamber. The distance between antennas changes from 0.5 to 4 m (empty chamber).

Using (5.13) to compute the K-factor, Fig. 5.8 shows the variation of the measured, and expectation of simulated K-factor as a function of the distance. For $d \leq 2$ m the results obtained from measurements are in agreement with the simulation. After this distance some differences between the measured and simulated values appear. This happens because with the increase of the distance the percentage of the energy at reception created by the secondary unstirred components increases and it is much difficult to control it, (see section 5.4.1). The maximum difference between the two results presented in this example is 1.5 dB for $d = 3.5$ m.

The parameters τ_μ and τ_{rms} are estimated with (5.19) and (5.20) in which the K-factor is computed with (5.13), whereas t_{Ss} is found as the time where the power of the signal envelope reaches α=99.5% of its maximum value. The results are presented in Fig. 5.9. For $d > 2$ m, the quality of the estimation is slightly reduced due to secondary unstirred components which may affect the estimation of K-factor. The estimator $\widehat{\tau}_\mu$ is much more influenced than $\widehat{\tau}_{\text{rms}}$.

5.4.2.2 Variation with the number of absorbers

The second set of measurements allows the analysis of the influence of the average absorption cross section on different parameters.

Fig. 5.10 presents the variation of the decay constant of the chamber with the increase of the number of absorbers. When the energy of stirred components is reduced, the response of the chamber becomes shorter, resulting a decrease of τ. There are some small differences between curves due to the disparities between the simulated and measured power delay profiles: Knowing the K-factors for the empty and loaded chambers, respectively their decay

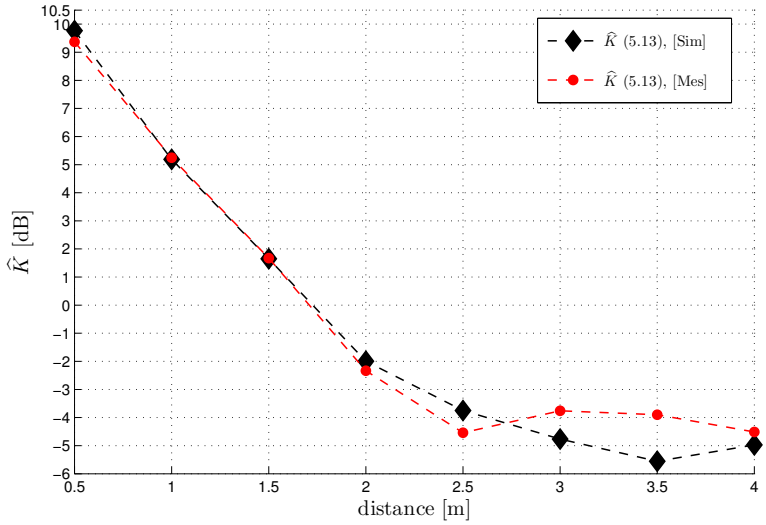

Figure 5.8: Variation of K-factor obtained from time parameters. The distance between antennas changes from 0.5 to 4 m (empty chamber).

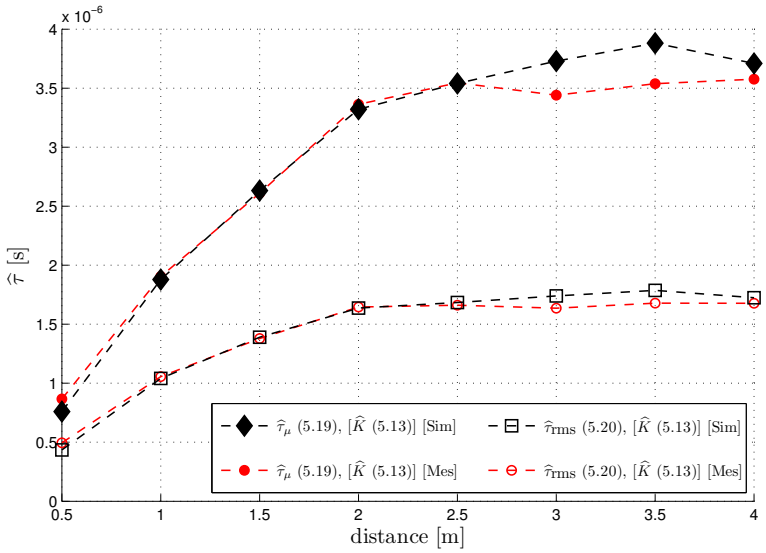

Figure 5.9: Variation of τ_μ and τ_{rms}. The distance between antennas changes from 0.5 to 4 m (empty chamber).

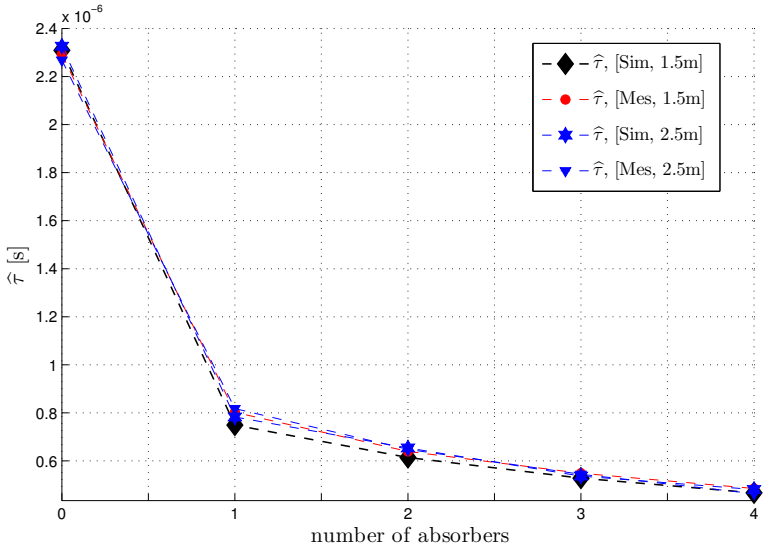

Figure 5.10: Variation of the estimated decay constant of the chamber with the number of absorbers; $d = 1.5$ and $2.5\,\mathrm{m}$.

constants τ_E and τ_L and the volume of the chamber, the average absorbing cross section can be computed with either (5.25b) or (5.25a). The K-factors are estimated with (5.13). The estimations of the average absorbing cross sections with the number of absorbers are presented in Fig. 5.11. For comparison, the average absorbing cross section given by (5.28) is also presented. The estimations of unstirred components, for the empty and loaded chamber, should be identical in order to reduce the estimation error in (5.26). As presented in section 5.4.1, the time at which we measure the unstirred power corresponds to a traveled distance of $27.95\,\mathrm{m}$. Analyzing the results for short distances between antennas (e.g., $d = 1.5\,\mathrm{m}$), the relative error ratio $\delta \to 0$. This is because a small part of the unstirred energy is absorbed. It results in this case that both (5.25a) and (5.25b) can be used to estimate the average absorbing cross section. When the distance between antennas increases (e.g., $2.5\,\mathrm{m}$), due to emergence of supplementary unstirred components the difference between the energy estimations of the unstirred components are more visible and the relative error ratio $\delta > 0$. For this situation the method (5.25b) provides results with smaller uncertainties. It results that the choice of the method also depends on the distance between antennas, because it influences the uncertainties associated with the estimation of the unstirred components level. A comparison between the K-factors estimated with (5.13) and (5.27) as function of the number of absorbers is shown in Fig. 5.12. The average absorbing surface for the estimator in (5.27) is computed with (5.28). The uncertainties of the method in (5.27) depend on the uncertainties of the initial K-factor (i.e., K_E when the chamber is empty) but also on the estimation errors of the average absorbing cross section. If the initial estimator is affected by a high degree of uncertainties, the later estimators may be affected by a higher degree of errors. We also present the measurement results when the antennas are placed at a distance of $2.5\,\mathrm{m}$. For this situation, there is a higher bias between the two measured values. This is probably because, at this distance, due to the appearance of supplementary unstirred components the value of K_E when using the method in (5.27) was slightly underestimated.

The evolutions of τ_μ (5.19) and τ_rms (5.20) with the variation of the number of absorbers are

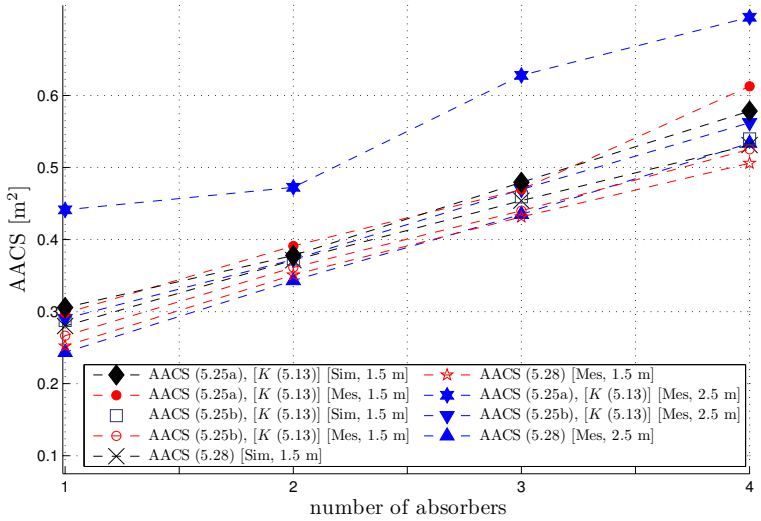

Figure 5.11: Variation of detectable average absorbing cross section, $\overset{\blacktriangle}{\sigma}_{\mathrm{A}}$, with the number of absorbers; $d = 1.5$ and $2.5\,\mathrm{m}$.

shown in Fig. 5.13. For these estimations, K-factors are estimated with (5.13) and with (5.27) for which the average absorbing cross section is estimated using (5.28). Even if between the two measured K-factors there is a small bias which changes with the quantity of absorbers (see Fig. 5.12), the effects on $\widehat{\tau}_{\mu}$ and $\widehat{\tau}_{\mathrm{rms}}$ are very small, the estimation of τ_{μ} (5.19) and τ_{rms} (5.20) being less influenced by uncertainties. The results obtained when the distance between antennas is $2.5\,\mathrm{m}$ are not presented as they are very close to those in Fig. 5.13 when the distance is $1.5\,\mathrm{m}$.

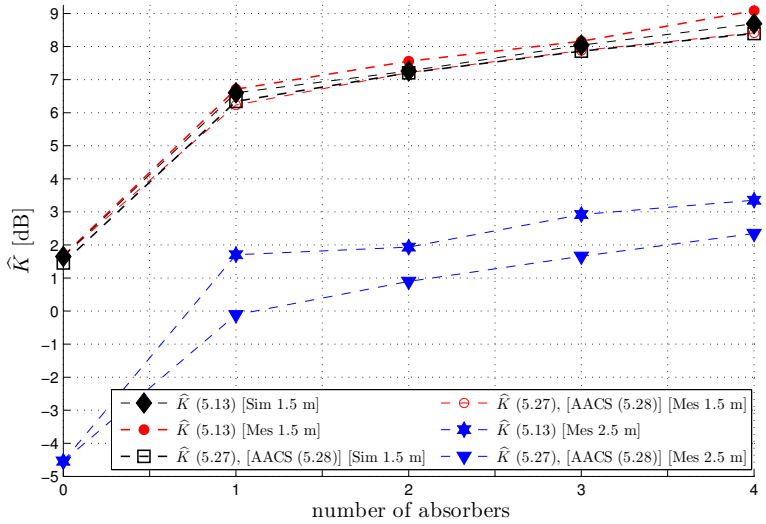

Figure 5.12: Variation of K-factor obtained from time parameters with the number of absorbers; $d = 1.5$ and $2.5\,\mathrm{m}$.

5.5 Conclusions

For a sinusoidal pulse modulated signal, the transient regime can be used to determine different parameters such as K-factor, τ, τ_{μ}, τ_{rms}, average absorbing cross section $\overset{\blacktriangle}{\sigma}_{\mathrm{A}}$, etc. The K-factor is obtained based on several time parameters (i.e., τ, steady state time t_{Ss}, t_{Sti}) and a limit parameter α which corresponds to the level of the normalized power of the signal at reception. Analytical relations for τ_{μ}, and τ_{rms} depending on τ, t_{Sti}, t_{Ss} and K-factor are computed. In the hypothesis that only the stirred energy is absorbed, the absorbing cross section is computed by using the respective K-factors of the empty and the loaded chamber. Knowing the average absorbing cross section a method to compute K-factor in the presence of absorbers is presented. Simulations and measurements with the variation of the distance between antennas and with the number of absorbers show the utility of this method to control different parameters.

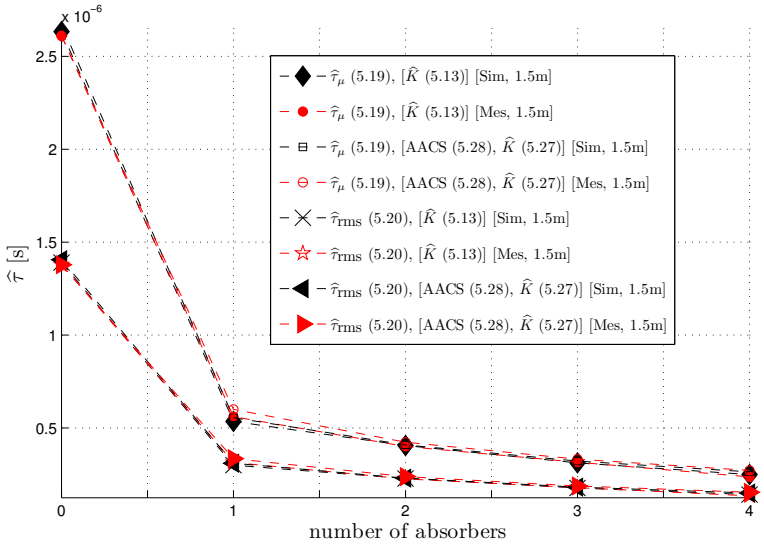

Figure 5.13: Variation of τ_{μ} and τ_{rms} with the number of absorbers; $d = 1.5\,\mathrm{m}$.

Bibliography

[1] X. Chen, P.-S. Kildal, C. Orlenius, and J. Carlsson, "Channel sounding of loaded reverberation chamber for over-the-air testing of wireless devices: Coherence bandwidth versus average mode bandwidth and delay spread," *Antennas and Wireless Propagation Letters, IEEE*, vol. 8, pp. 678–681, 2009.

[2] C. Holloway, D. Hill, J. Ladbury, P. Wilson, G. Koepke, and J. Coder, "On the use of reverberation chambers to simulate a Rician radio environment for the testing of wireless devices," *Antennas and Propagation, IEEE Transactions on*, vol. 54, no. 11, pp. 3167–3177, Nov. 2006.

[3] E. Genender, C. Holloway, K. Remley, J. Ladbury, G. Koepke, and H. Garbe, "Simulating the multipath channel with a reverberation chamber: Application to bit error rate measurements," *Electromagnetic Compatibility, IEEE Transactions on*, vol. 52, no. 4, pp. 766–777, Nov. 2010.

[4] D. A. Hill, *Electromagnetic Fields in Cavities: Deterministic and Statistical Theories*, I. Press, Ed. Wiley/IEEE Press, Piscataway, NJ, 2009.

[5] ——, "Plane wave integral representation for fields in reverberation chambers," *IEEE Transactions on Electromagnetic Compatibility*, vol. 40, no. 3, pp. 209–217, 1998.

[6] A. Papoulis and S. Pillai, *Probability, random variables, and stochastic processes*, ser. McGraw-Hill electrical and electronic engineering series. McGraw-Hill, 2002. [Online]. Available: http://books.google.fr/books?id=YYwQAQAAIAAJ

[7] M. I. Andries, P. Besnier, and C. Lemoine, "Estimating K-factor and time spread parameters from a transient response of a pulse modulated sine wave in reverberation chamber," *Antennas and Propagation, IEEE Transactions on*, vol. 61, no. 1, pp. 380–389, Jan. 2013.

[8] C. F. Eyring, "Reverberation time in "dead" rooms," *The Journal of the Acoustical Society of America*, vol. 1, no. 2A, pp. 217–241, 1930. [Online]. Available: http://dx.doi.org/10.1121/1.1915175

[9] T. Rossing and N. Fletcher, *Principles of vibration and sound*, Springer-Verlag, Ed. New York, 2004, vol. ch. 11.

[10] E. K. Dunens and R. F. Lambert, "Impulsive sound-level response statistics in a reverberant enclosure," *The Journal of the Acoustical Society of America*, vol. 61, no. 6, pp. 1524–1532, 1977. [Online]. Available: http://link.aip.org/link/?JAS/61/1524/1

[11] C. Lemoine, P. Besnier, and M. Drissi, "Advanced method for estimating number of independent samples available with stirrer in reverberation chamber," *Electronics Letters*, vol. 43, no. 16, pp. 861–862, Aug. 2007.

[12] C. Lemoine, E. Amador, and P. Besnier, "On the K-factor estimation for Rician channel simulated in reverberation chamber," *Antennas and Propagation, IEEE Transactions on*, vol. 59, no. 3, pp. 1003–1012, Mar. 2011.

[13] G. L. Stüber, *Principles of Mobile Communication (2nd Edition)*. Boston: Kluwer Academic, 2001.

[14] M. Andries, P. Besnier, and C. Lemoine, "Simple approximation for envelope based K estimator," *Electronics Letters*, vol. 47, no. 3, pp. 222–223, Mar. 2011.

[15] G. Azemi, B. Senadji, and B. Boashash, "Estimating the Ricean K-factor for mobile communication applications," in *Signal Processing and Its Applications, 2003. Proceedings. Seventh International Symposium on*, vol. 2, Jul. 2003, pp. 311–314.

[16] C. Tepedelenlioglu, A. Abdi, and G. Giannakis, "The Ricean K factor: estimation and performance analysis," *Wireless Communications, IEEE Transactions on*, vol. 2, no. 4, pp. 799–810, Jul. 2003.

[17] L. Greenstein, D. Michelson, and V. Erceg, "Moment-method estimation of the Ricean K-factor," *Communications Letters, IEEE*, vol. 3, no. 6, pp. 175–176, Jun. 1999.

[18] G. Lerosey and J. de Rosny, "Scattering cross section measurement in reverberation chamber," *Electromagnetic Compatibility, IEEE Transactions on*, vol. 49, no. 2, pp. 280–284, May 2007.

Part III

Applications

This part of the thesis deals with two possible applications of the reverberation chamber. First, we evaluate the pattern of an antenna from only the measurements of the reflection coefficient of an antenna. Even though this method to extract the gain of an antenna is not new, we extend the analysis to the evaluation of antenna pattern and its estimation errors. We also present results for antenna mismatch and half power beamwidth. We discuss the evaluation of the free space propagation distance taking into account the equivalent propagation distance inside antenna.

The next application evaluates the use of the reverberation chamber to characterize the diversity gain. First, we isolate the effects on the diversity gain due to different antenna efficiencies (in the antenna array), different stirred power levels and different K-factors, all these representing the composite power imbalance. Then, we present a simple relation of the power correlation (also discussing the envelope correlation) as a function of the complex correlation when the K-factors on different channels are not identical. The envelope/power correlation may decrease even though the complex correlation can be very high. It results that using an envelope/power correlation as a criterion to characterize the diversity (without taking into account other parameters) may bias the conclusions. By using Monte Carlo simulations we present results for different configurations (i.e., different levels of K-factor, power imbalance, complex correlation) which can be used as abacuses. We also show the effects over power level when averaging unstirred components in frequency domain as it is necessary in the measurements. We test the diversity gain when changing the separation distance between antennas (in an antenna array) and when the unstirred power at reception changes. Using statistical simulations we compare the measured diversity gain with the simulated values and the results are in accordance.

CHAPTER 6

Evaluation of antenna parameters in reverberation chamber

6.1 Introduction

An antenna is a device which transforms guided electromagnetic signals (e.g., on cables or waveguide) into free space electromagnetic waves [1]. It can be characterized on either a near-field or far-field range. One of these two options will be used depending on several criteria which can be: the budget, the size of antenna and its complexity, the requirements of measurement accuracy, the test frequency, the type of parameters we want to measure, etc. When measuring antenna in a near field chamber (NFC), the gain of the antenna under test (AUT) is obtained from a near field to far field transform. One or several probes scan the electromagnetic field over a surface at a near distance from the AUT. Dealing with a multiple probe system this method is very fast [2]. For the far-field techniques, an example of an antenna test facility is the anechoic chamber. Excepting the AUT, depending on the method used in anechoic chamber, one or two other antennas can be used [3]. There are several parameters which characterize an antenna: polarization, input impedance, directivity, gain, efficiency, effective isotropically radiated power, radiation pattern, antenna noise temperature, etc. [1]. These parameters have a direct impact on the wireless communication transmission [4, 5]. Many different methods are used to extract antenna parameters in near-field [6, 7] or in far-field [8, 9] for evaluating antenna pattern [10, 11], directivity [12, 13], efficiency [14, 15], etc. Beside the environments designed for antenna measurements, a cheaper alternative to characterize different antenna parameters is the use of a reverberation chamber (RC). For example several methods to extract antenna radiation efficiency in reverberation chamber are discussed in [16, 17], the antenna gain in [18], the power transmitted and received by an antenna in [19] and the evaluation of antenna arrays of MIMO systems in [20, 21]. These methods take advantage of the statistical properties of a conventional reverberation chamber. On the other hand, a method to compute the gain of an antenna when it is placed in front of a large metallic wall was introduced in [22]. This method consists in analyzing the resulting reflection coefficient. Years later, this method has been improved for different measurement conditions. For example, in [23] the mismatch of antenna and the bouncing back reflections from the antenna are discussed. In [24], the authors estimate the maximum gain of antenna

using a generator and spectrum analyzer while in [25] the phase of the free-space electric field is also estimated.

In this chapter we develop an appropriate signal processing inspired from these earlier works within the frame of a diffuse media of a reverberation chamber. Based on time filtering of the measured S_{11} parameter several antenna parameters are computed. A first estimated parameter is the antenna mismatch. Then, we examine the question of the propagation distance estimation to further determine the antenna gain for a given position/orientation with respect to the chamber wall to which the antenna is directed. An uncertainty analysis of the free-space propagation distance shows the conditions in which this parameter is estimated. Results show that providing a careful estimation of time gatings and of the free-space distance, antenna pattern and half-power beamwidth are measured in good agreement with reference results.

6.2 The Method

6.2.1 Gain estimation from a single transmitting-receiving antenna

A simple and cheap solution is the use of only the test antenna to measure its own pattern. For that, a large metallic reflector is placed in its far field. Then, antenna is rotated (as in an anechoic chamber) and for each pair of angles (θ, φ) a voltage transfer function derived from Friis equation is defined as:

$$|H_{\mathrm{FS}}(\theta,\varphi)|^2 = \left(\frac{1}{4\pi} \times \frac{\lambda}{2d}\right)^2 \mathcal{D}^2(\theta,\varphi), \tag{6.1}$$

where

- $H_{\mathrm{FS}}(\theta,\ \varphi)$ is the complex voltage transfer function, in the direction $(\theta,\ \varphi)$, measured between a transmitter and a receiver. It is equivalent to the complex voltage transfer function measured in free-space (i.e., anechoic chamber), while in reverberation chamber it corresponds to the complex voltage transfer function of unstirred direct component; the angles θ and φ are taken with respect to the metallic reflector;
- $\mathcal{D}(\theta,\varphi)$ is the directivity of the AUT;
- d is the free-space propagation distance between the transmitter and the metallic reflector;
- λ is the wavelength.

The gain of antenna is thus obtained with:

$$G(\theta,\varphi) = \left(1 - |S_{11_{\mathrm{FS}}}|^2\right)\eta\mathcal{D}(\theta,\varphi) = \left(1 - |S_{11_{\mathrm{FS}}}|^2\right)\eta|H_{\mathrm{FS}}(\theta,\varphi)|\left(\frac{8\pi d}{\lambda}\right). \tag{6.2}$$

In order to compute (6.2) in the context of a reverberation chamber, a first step is to extract the voltage transfer function. To do this, we measure the reflection coefficient $S_{11_{\mathrm{RC}}}$ in reverberation chamber, in frequency domain using a vector network analyzer (VNA). This signal is a combination of a deterministic free-space component and components specific to propagation channels inside the cavity and the mismatch of antenna:

$$S_{11_{\mathrm{RC}}}(\theta,\varphi) = S_{11_{\mathrm{FS}}} + \left(1 - |S_{11_{\mathrm{FS}}}|^2\right)\eta \cdot \left(H_{\mathrm{FS}}(\theta,\varphi) + H^{\mathrm{sec}}_{\mathrm{unSti}}(\theta,\varphi) + H_{\mathrm{Sti}}(\theta,\varphi)\right), \tag{6.3}$$

where

- $S_{11_{\mathrm{FS}}}$ represents the free-space mismatch coefficient;
- η is the antenna radiation efficiency;
- $H^{\mathrm{sec}}_{\mathrm{unSti}}$ and H_{Sti} are the complex voltage transfer functions and represent secondary electromagnetic waves reflected back to the transmitting antenna by chamber walls, the stirrer, etc. Subscript "*sec*" denotes the secondary unstirred components.

To extract only the free-space transfer function H_{FS} from (6.3), the antenna is placed in the far-field area from one wall. We use this configuration to reach a maximum amplitude of the signal coming from the first reflection on the wall and lower amplitudes from other reflections associated with other walls. Moreover, all other reflections have to arrive at reception later than the first reflection. Eventually we can add some absorbers if some undesired reflections may appear. We do not use the stirrer even though it may reduce the fluctuations created by stirred components in frequency domain. Next, the impulse response is obtained by applying to the measured reflection coefficient $S_{11_{\mathrm{RC}}}$ an inverse-CZT transform function (see annex D). Eventually a Kaiser filter may be used to reduce the influence of the limited bandwidth of the signal. By filtering the signal in time domain and then applying a direct CZT transform to switch to frequency domain we keep only the components associated with the complex free-space transfer function H_{FS}.

Far field zone

Before starting the measurements we need to make sure the AUT is placed in the far-field zone. When the dimensions of the AUT are comparable with half of the wavelength of the transmitted signal, then the free-space propagation distance has to be bigger than the Fraunhofer distance. This distance corresponds to the limit between the near-field and far-field zone. It results the following constraints for the free-space propagation distance d:

$$d = \frac{2D^2}{\lambda}, \tag{6.4}$$

with two other conditions:

$$\begin{cases} d >> D, \\ d >> \lambda. \end{cases}$$

where

- D is the largest physical dimension of antenna;
- λ is the wavelength of the signal.

6.2.2 Estimating propagation distance

Estimating free-space propagation distance d

Extracting antenna gain as presented in (6.2), requires the knowledge of the free-space propagation distance d. The estimation quality of this parameter has a direct impact over the estimation of the antenna gain, as the estimation error of antenna gain is identical with the estimation error of free-space propagation distance. With the decrease of the distance between antennas this error increases. We can easily measure the physical distance between the chamber wall and antenna support but the true propagation distance differs from this value.

A residual unknown length d_x representing the distance between antenna mounting support and the border from which antenna starts to radiate in free space may bias the estimation of this propagation distance (Fig. 6.1). Moreover, this free-space propagation distance changes

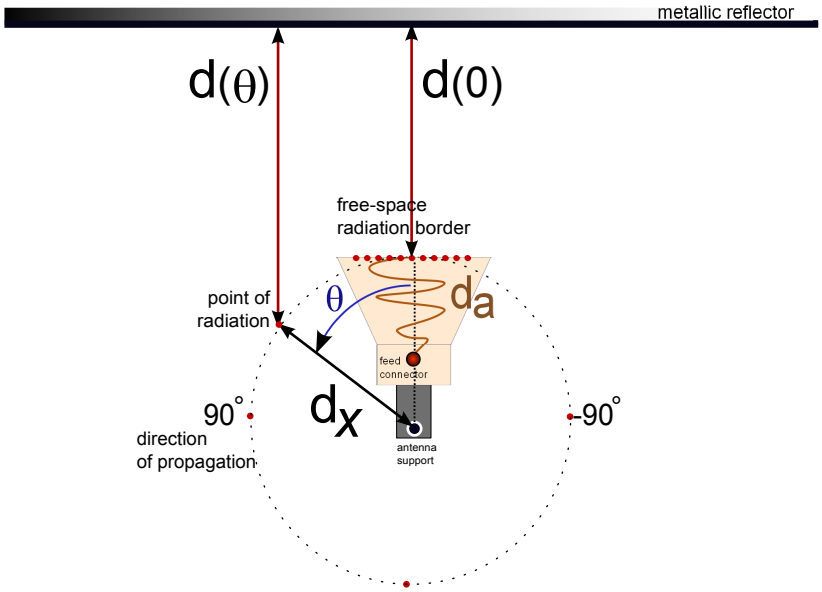

Figure 6.1: Free-space propagation distances when antenna turns for $\theta \in [0, 2\pi)$.

with the rotation of antenna (i.e., with the angle θ) and it is difficult to physically measure it for each antenna angle. To find the free-space propagation distance one solution is to extract the time corresponding to the maximum of amplitude of the impulse response, corresponding to the propagation distance of the first reflection, d_{IR}. This moment represents two times the total propagation distance: a free-space propagation distance d and a guided propagation distance d_{a} in AUT which in general has the same order of magnitude as the highest physical dimension of the test antenna in the direction of propagation.

$$d_{\mathrm{IR}}(\theta) = 2(d(\theta) + d_{\mathrm{a}}), \tag{6.5}$$

Using the scheme presented in Fig. 6.1, this parameter becomes:

$$d_{\mathrm{IR}}(\theta) = \underbrace{2\left[d(0) + (1 - \cos\theta)d_{\mathrm{x}}\right]}_{\substack{\text{free space} \\ \text{propagation distance}=2d(\theta)}} + 2d_{\mathrm{a}}, \tag{6.6}$$

from which we can extract the free-space distance $d(\theta)$. The factor "2" is due to the fact that the same antenna is used as transmitter and receiver. It results that extracting the free-space propagation distance d from measurements of impulse response, the propagation distance inside antenna d_{a} has to be known.

Estimating antenna propagation distance d_{a}

For estimating the propagation distance inside antenna we search for the maximum of signal. According to section 6.2.1, we remove the part of the signal corresponding to reflections of

antenna mismatch. Making two measurements, further denoted "1" and "2", at two different distances from the chosen wall for an angle $\theta = 0$, the extracted distances corresponding to the maximum of the amplitude of the impulse response of the signal are:

$$\begin{cases} d_{\mathrm{IR},1}(0) = 2d_1(0) + 2d_{\mathrm{a}}, & \text{(6.7a)} \\ d_{\mathrm{IR},2}(0) = 2d_2(0) + 2d_{\mathrm{a}}. & \text{(6.7b)} \end{cases}$$

Both d_1, d_2 and d_{a} in (6.7) are unknown variables. From (6.1), the corresponding complex voltage transfer functions (for any pair of angles θ, and φ) are:

$$\begin{cases} |H_{\mathrm{FS},1}| = G\dfrac{1}{(1-|S_{11_{\mathrm{FS}}}|^2)\,\eta}\dfrac{\lambda}{8\pi d_1(0)}, & \text{(6.8a)} \\ |H_{\mathrm{FS},2}| = G\dfrac{1}{(1-|S_{11_{\mathrm{FS}}}|^2)\,\eta}\dfrac{\lambda}{8\pi d_2(0)}. & \text{(6.8b)} \end{cases}$$

Using (6.7) and (6.8), the equivalent guided antenna propagation distance is found with:

$$d_{\mathrm{a}} = \frac{1}{2}\frac{d_{\mathrm{IR},1}(0)|H_{\mathrm{FS},1}| - d_{\mathrm{IR},2}(0)|H_{\mathrm{FS},2}|}{|H_{\mathrm{FS},1}| - |H_{\mathrm{FS},2}|}. \tag{6.9}$$

By using only the time evaluations of the measured signal in time domain it is actually not necessary to measure the distance between the antenna support and the metallic wall. The evaluation of this distance is done only to verify the far-field condition before starting the measurements.

Estimation errors of antenna propagation distance

The estimation of the distance d_{a} is influenced by errors. First, the transfer functions in (6.9) correspond only to the first reflection with the wall at two different distances. Due to limited resolution and frequency bandwidth of the transfer function, windowing effects might arise, the energy of a pulse in time domain (i.e., the energy of a reflection) being scattered over the side pulses. Multiplying the signal in frequency domain with different types of filters (i.e., Kaiser, Hamming, Han) will reduce the side lobes but it will also change the width of the main pulse (fact which later might influence the results). Then, the impulse response is truncated in time domain and transformed again in frequency domain. Therefore the magnitude of the signal in frequency domain may be affected by fluctuations which also may have negative influences over the result in (6.9). One solution which provides a biased but stable result with frequency, which is used in this chapter, is to compute the energy contained in the pulse corresponding to the first reflection with the wall and so, one finds the equivalent amplitude which provides the same level of energy. Applying a time-to-frequency domain transform, it results a constant signal with frequency (not affected by the spectral leakage) whose energy is smaller than the energy of the true signal due to filtering process, Fig. 6.2.

Two other problems might influence the estimation distance when using (6.9). First, the extraction of the distances $d_{\mathrm{IR},1}(0)$ and $d_{\mathrm{IR},2}(0)$ are influenced by errors linked to sampling frequency in time domain, f_{s}. Considering the true antenna distance d_{a} as in (6.9):

$$d_{\mathrm{a}} = \frac{1}{2}\frac{d_{\mathrm{IR},1}(0)|H_{\mathrm{FS},1}| - d_{\mathrm{IR},2}(0)|H_{\mathrm{FS},2}|}{|H_{\mathrm{FS},1}| - |H_{\mathrm{FS},2}|} = \frac{1}{2}\frac{c\,t_{\mathrm{IR},1}|H_{\mathrm{FS},1}| - c\,t_{\mathrm{IR},2}|H_{\mathrm{FS},2}|}{|H_{\mathrm{FS},1}| - |H_{\mathrm{FS},2}|}, \tag{6.10}$$

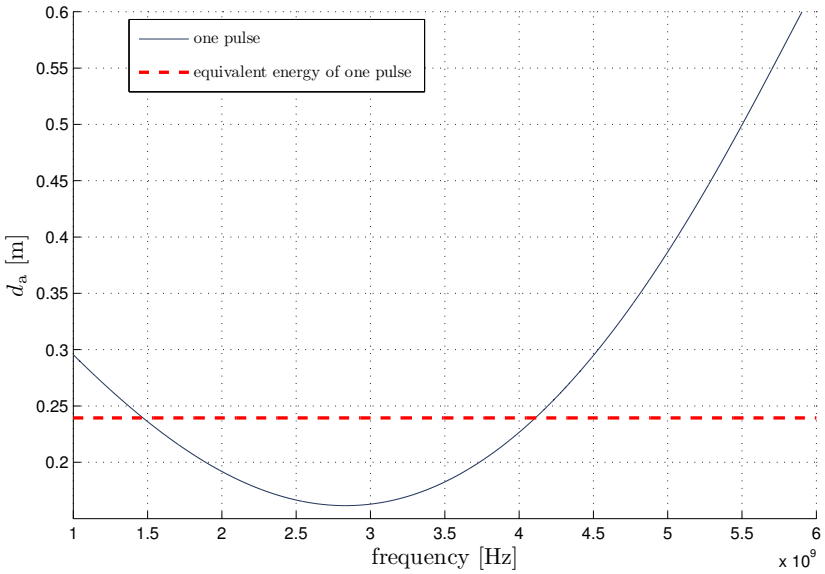

Figure 6.2: Comparison between the estimation of the antenna distance d_a when applying the inverse CZT to one filtered pulse and when applying the inverse CZT to a renormalized pulse whose energy is equal to the energy of the filtered pulse.

and the biased antenna distance due to sampling frequency for the same transfer functions as above:

$$\widehat{d}_a = \frac{1}{2}\frac{\widehat{d}_{IR,1}(0)|H_{FS,1}| - \widehat{d}_{IR,2}(0)|H_{FS,2}|}{|H_{FS,1}| - |H_{FS,2}|} = \frac{1}{2}\frac{c(t_{IR,1} \pm 1/f_s)|H_{FS,1}| - c(t_{IR,2} \pm 1/f_s)|H_{FS,2}|}{|H_{FS,1}| - |H_{FS,2}|}, \tag{6.11}$$

the estimation of the relative error of antenna distance due to sampling frequency of the signal in time domain results:

$$\xi_{d_a,f_s} = \frac{\widehat{d}_a - d_a}{d_a} = \pm\frac{c}{f_s}\frac{1}{d_a}. \tag{6.12}$$

Second, (6.9) considers that the equivalent gains of antenna for both measurements are equal. When we make an error over the gain estimation for two successive measurements, then we can write the true antenna distance as (6.9) while the biased antenna distance is:

$$\begin{aligned}\widehat{d}_a &= \frac{1}{2}\frac{d_{IR,1}(0)|\widehat{H}_{FS,1}| - d_{IR,2}(0)|\widehat{H}_{FS,2}|}{|\widehat{H}_{FS,1}| - |\widehat{H}_{FS,2}|} = \frac{1}{2}\frac{d_{IR,1}(0)\gamma\, d_2(0)/d_1(0) - d_{IR,2}(0)}{\gamma\, d_2(0)/d_1(0) - 1} \\ &= \frac{1}{2}\frac{d_{IR,1}(0)\gamma(d_{IR,2}(0) - d_a) - d_{IR,2}(0)(d_{IR,1}(0) - d_a)}{\gamma(d_{IR,2}(0) - d_a) - (d_{IR,1}(0) - d_a)}.\end{aligned} \tag{6.13}$$

In this equation, the parameter $\gamma = \widehat{G_1}/\widehat{G_2}$ corresponds to bias between estimated gains in the two consecutive measurements, and $\delta = d_{IR,1}(0)/d_{IR,2}(0)$ ($\delta < 1$) is the ratio between the two measurement distances. Reorganizing (6.13) as a function of γ, the true antenna distance d_a, and the measured distances $d_{IR,1}(0)$ and $d_{IR,2}(0)$, the relative error due to gain estimation

results as:

$$\xi_{d_a,G} = \frac{\widehat{d_a} - d_a}{d_a} = \frac{d_a(1-\gamma\,\delta) + d_{IR,2}(0)\delta(\gamma-1)}{d_{IR,2}(0)(\gamma-\delta) + d_a(1-\gamma)} \frac{d_{IR,2}(0)}{d_a} - 1. \tag{6.14}$$

6.3 Data processing and Results

The details of a measurement configuration are presented in Fig. 6.3(a). In the tested measurement bandwidth, the AUT is considered to be in far field when the distance to the metallic walls is bigger than 1 m. With this condition, antenna is placed at 1.25 m from the nearest wall. Using a reverberation chamber whose height is 2.9 m, the support of the antenna is placed at 1.15 m from the floor and 1.75 m from the ceiling. To remove all possible influences of the floor due to early secondary reflections, 3 absorbers are added. A chamber with a higher height may improve measurement conditions. The antenna is manually turned around its vertical axis (angle θ) and rotated around its horizontal axis (angle φ), as illustrated in Fig. 6.3(b). Fig. 6.4 shows the impulse response of S_{11} parameter over the first 100 ns, measured in reverberation chamber using a VNA. This response is obtained from a measured signal in the frequency bandwidth 1 – 9 GHz, with a bin frequency of 400 kHz resulting an impulse response of 2.5 µs long. The transformation in time domain was done applying a Kaiser filter (with $\beta = 6$). Analyzing this impulse, a first part corresponds to reflections due to antenna mismatch, a second part provides the free-space voltage transfer function and a third part corresponds to reflections with the other walls, including the stirrer.

6.3.1 Extracting antenna mismatch $S_{11_{FS}}$

As presented in (6.3), the parameter $S_{11_{RC}}$ measured in reverberation chamber includes the antenna mismatch and the channel transfer functions of the propagation channel. To extract only the antenna mismatch we filter the time response of $S_{11_{RC}}$ for the first 7 ns and then we transform this signal back to frequency domain. The time limit of 7 ns is estimated from the time response of the measured $S_{11_{RC}}$, see Fig. 6.4, and it is smaller than the necessary time for a wave to be reflected back to emission by chamber walls. Considering a measurement configuration as in Fig. 6.3(a), the antenna mismatch is computed using one measurement of $S_{11_{RC}}$ parameter. Fig. 6.5, shows the antenna mismatch in the frequency bandwidth 2 – 6 GHz for a horn type antenna, model ETS 3115 when filtering the signal in time domain. The measurements were done in a frequency bandwidth larger than this one, but due to time filtering we had to remove the frequency ranges below and above this bandwidth for which the results are biased. For comparisons, two other results are added: one is the antenna mismatch measured in near-field chamber, while the other is the result obtained by averaging the several measurements of $S_{11_{RC}}$ parameter while rotating antenna around its axis (i.e., variation of θ angle in the range $[0, 2\pi]$, with an angle step of 15 °). We chose to present this later result due to the fact that the tested antenna is directive. It results that when rotating the antenna, we may consider that the complex rectangular components of the electric field received by this antenna are zero-mean Gaussian distributed.

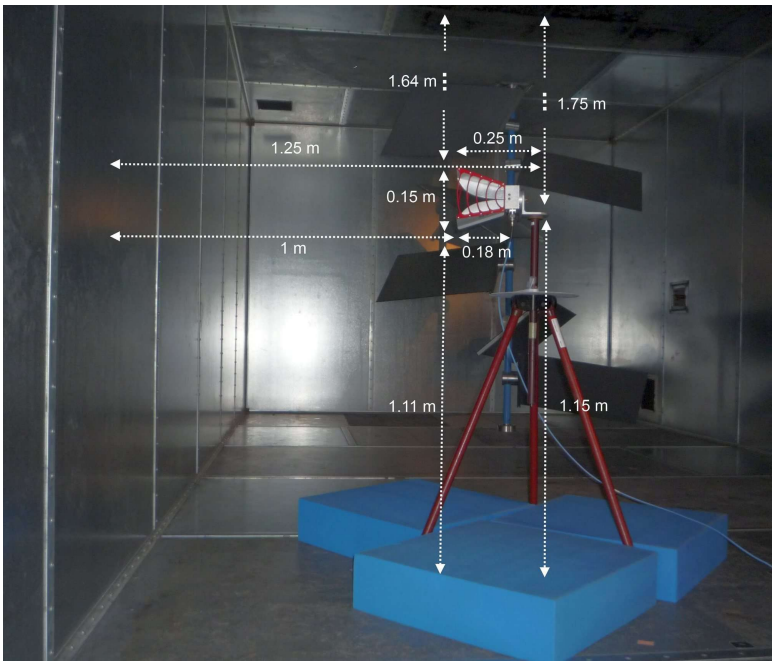

(a)

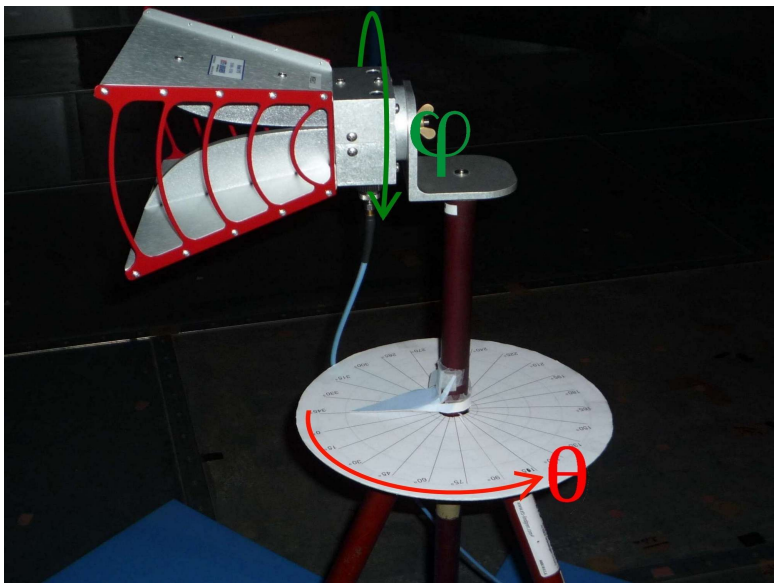

(b)

Figure 6.3: Antenna measurement configuration in reverberation chamber (a), and antenna polar coordinate system-θ and φ (b).

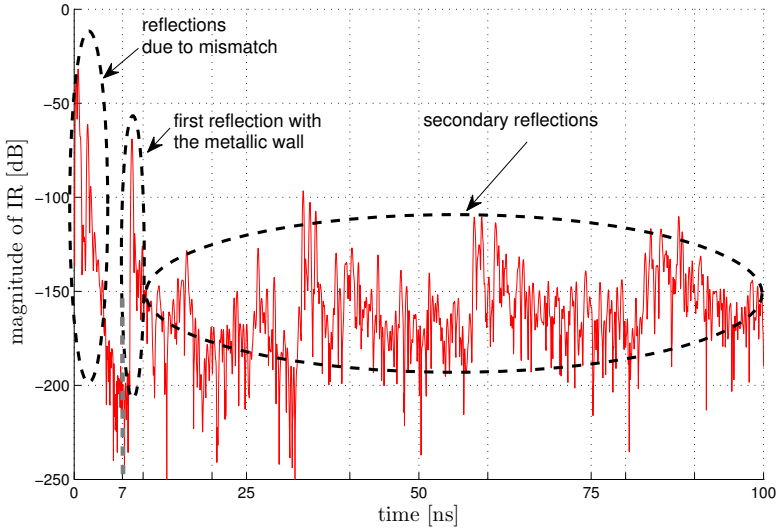

Figure 6.4: Example of the time response of the channel obtained from S_{11} measurement. Antenna mismatch is not removed.

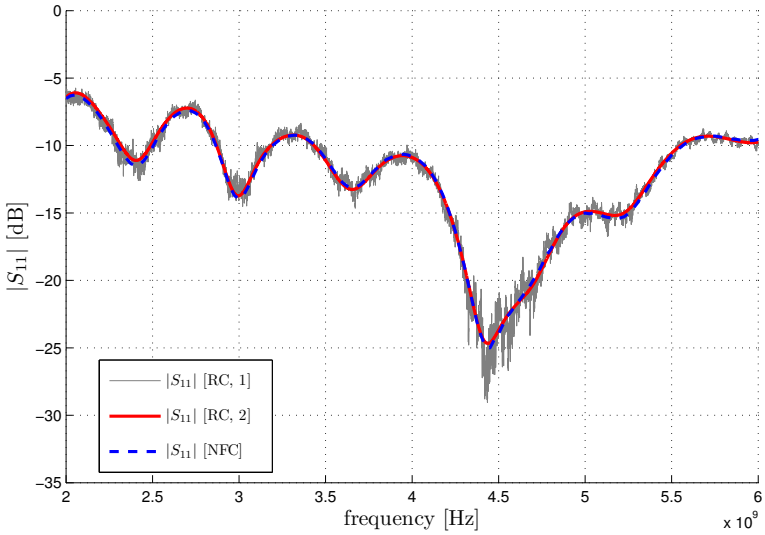

Figure 6.5: Antenna mismatches: [RC, 1] - using average over several measurements, [RC, 2] - using time filtering, [NFC] - measurement made in NFC.

6.3.2 Estimating the free-space transfer function of the channel $H_{\mathrm{FS}}(0,0)$

Considering the same experimental configuration as in Fig. 6.3(a), and the relation (6.3), we then extract the transfer function of the channel. We use the method presented in section 6.2.1. We measure, for the direction $\theta = 0$ and $\varphi = 0$, the parameter $S_{11_{\mathrm{RC}}}$ and we apply an inverse-CZT transform ($\beta = 6$) resulting a time response whose duration is 2.5 µs and true sampling frequency of 27 GHz. In order to extract the transfer function corresponding to first reflection with the metallic wall, the signal has to be truncated in time domain to extract the corresponding energy and to remove the reflections due to antenna mismatch and the secondary reflections with the other walls (Fig. 6.4). The initial time of 7 ns to remove the reflections due to antenna mismatch is the same as for the extraction of S_{11} parameter used before. The final moment of this truncation depends on the total propagation time (inside antenna and in free-space) but also on the dispersion of energy of the main tap corresponding to first reflection with the metallic wall over side taps. Fig. 6.6 presents a comparison between the magnitude of the free-space voltage transfer function estimated using the antenna gain measured in near-field chamber and those measured in reverberation chamber, in the bandwidth 2 – 6 GHz, for several durations of the truncation interval. In these results, we consider for the Friis transfer function the true propagation distance, 2 m. In this figure the parameter

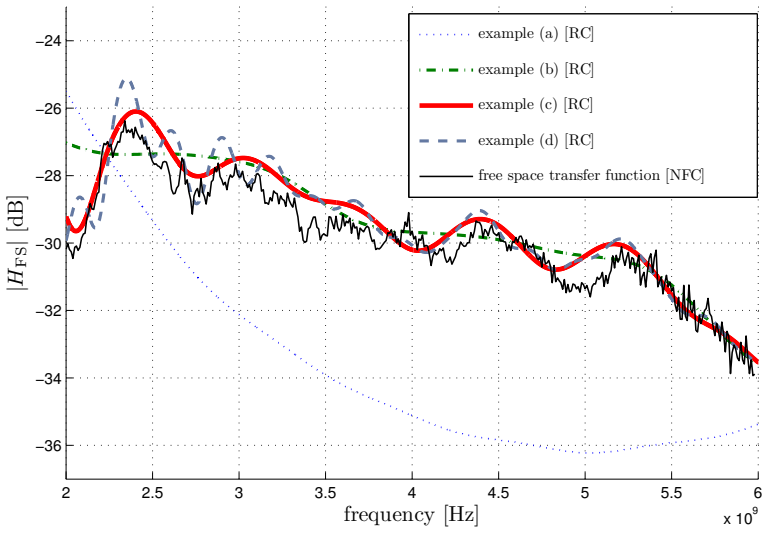

Figure 6.6: Comparison between measured transfer functions in direction ($\theta = 0$, $\varphi = 0$) in near-field chamber and in reverberation chamber. For reverberation chamber the free space transfer function is computed for different truncation intervals: (a) $[7\,\mathrm{ns}, t_{\max}]$, (b) $[7\,\mathrm{ns}, t_{\max} + 1\,\mathrm{ns}]$, (c) $[7\,\mathrm{ns}, t_{\max} + 2\,\mathrm{ns}]$, (d) $[7\,\mathrm{ns}, t_{\max} + 4\,\mathrm{ns}]$.

$t_{\max}$ corresponds to the time where the maximum of the first reflection is found. When the signal is strongly truncated (example "a" in Fig. 6.6), the energy of the first reflection is underestimated. On the opposite side, if the truncation interval is too large, the signal in frequency domain may fluctuate widely because it may contain energy from other reflections (example "d" in Fig. 6.6). We chose a truncation time interval from 7 ns to $t_{\max}+2$ ns to include the most of the energy of the searched signal with a small influence due to secondary reflections. This duration depends only on the signal in time domain and not on the chamber characteristics.

6.3.3 Estimating antenna gain G

Next step in our study is to extract antenna gain for the direction $\theta = 0$ and $\varphi = 0$. This can be done by using relation (6.2). From this relation, it results that we need the knowledge of the free-space propagation distance, d.

Measuring the free-space distance, and antenna propagation distance and its estimation errors

Due to the significant antenna propagation distance d_a compared with the free-space propagation distance d using only the measured distance between the metallic wall and the antenna support will generate significant errors on the estimation of antenna gain. To reduce the estimation error of free-space distance, we use the following method. First we extract the distance $d_{IR}(\theta)$ corresponding to maximum of the signal amplitude in time domain for each azimuthal angle θ. Then, in order to apply (6.6) we estimate the guided antenna propagation distance d_a from two measurements at two different distances from the metallic wall: $d_{IR,1}(0)$ and $d_{IR,2}(0)$ in direction ($\theta = 0$, $\varphi = 0$) and using (6.9) (see section 6.2.2). As discussed in section 6.2.2, the estimation of the distance d_a is affected by errors, computed in (6.12) and (6.14). Fig. 6.7 shows the error computed in (6.12) due to sampling frequency f_s for the case when $f_s \in [20, 100]$ GHz and $d_a \in [1, 60]$ cm. The only parameter we can control in the

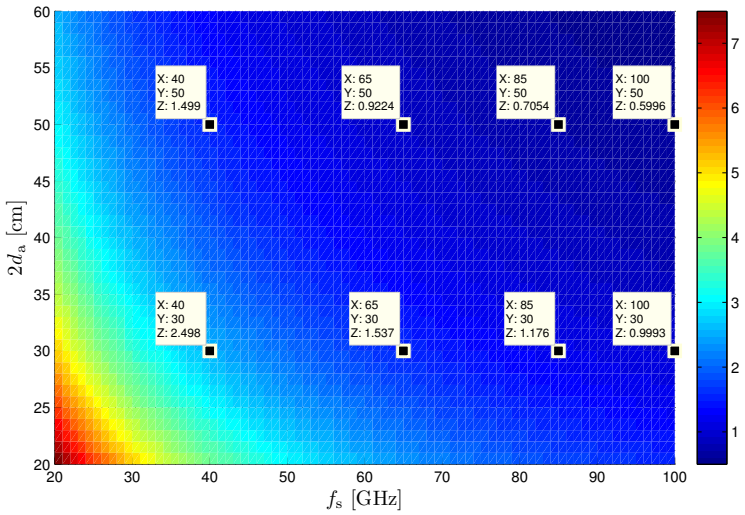

Figure 6.7: Relative error of the guided antenna propagation distance d_a; (X) - f_s sampling frequency, (Y) - $2d_a$ two times propagation distance in antenna, (Z) - percentage of the propagation distance relative error.

above error is the sampling frequency in time domain, f_s. To reduce as possible this error we use a high sampling frequency (e.g., $> 75 - 100$ GHz). In this analysis the sampling frequency in time domain is 85 GHz.

Fig. 6.8 presents the analysis of the second relative error, presented in (6.14), when $\gamma \in [0.98, 1.02]$ and $d_a \in [20, 60]$ cm. In our experiments, the parameter δ is 0.625 and it corresponds to the distances estimated from the maximum of the signal with: $d_{IR,1} = 2.5$ m and $d_{IR,2} = 4$ m. A lower δ will reduce estimation errors of d_a, but due to chamber dimensions

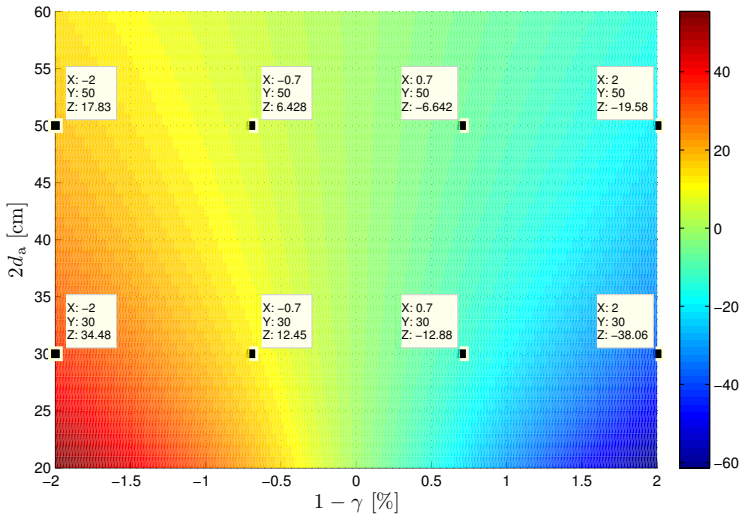

Figure 6.8: Relative error of the guided antenna propagation distance d_a; (X) - 1-γ ratio between antenna gains of two consecutive measurements, (Y) - $2d_a$ is two times propagation distance in antenna, (Z) - percentage of the propagation distance relative error.

and far field conditions for $d_{IR,1}$ this cannot be achieved. From this analysis, it results that the estimation of the propagation distance inside antenna is quite sensitive to the estimation of antenna gain much more than the sampling frequency in time domain. This may be the case if the successive measurements are done in different conditions (e.g., at the inferior limit of the far field for which a slight modification of the distance still influences the level of the estimated gain, which may be different from the true gain of antenna if we are not in far-field conditions) or when during the movement of the antenna from one position to another position, the antenna slightly turns and the gain in the measurement direction may change. The first problem is reduced if we perform the measurements at the greatest distance possible by the measurement system. The second problem is removed if the antenna is controlled by an accurate positioning system. Also, the last error depends on the antenna pattern. For example, Fig. 6.9 illustrates the relative error over the gain in direction ($\theta = 0,\ \varphi = 0$) for the antenna used in our experiments at a frequency of 2.5 GHz and $\theta \in [-6°, 6°]$, as measured in near field chamber. Because of the limited angle step, we also present an interpolated approximation of this relative error. For this particular case, it results from Fig. 6.8 and 6.9 that even a misalignment of at least 4°, corresponding to $1-\gamma \approx 2\%$, would create an error of around ±19% over the estimation of the guided antenna propagation distance d_a when this distance is 2×24 cm (value which was found for the antenna used in our experiments, (6.14)).

In conclusion, the propagation distance inside antenna is a parameter whose detection without errors may be difficult to implement. This parameter has the same order of magnitude as the highest physical dimension of antenna under test in the direction of propagation. For small antennas (e.g., patch antennas), the estimation of d_a using the above method may be even more difficult to implement, but in this case its detection has less impact on the antenna gain error as this distance is much smaller than the free-space propagation distance.

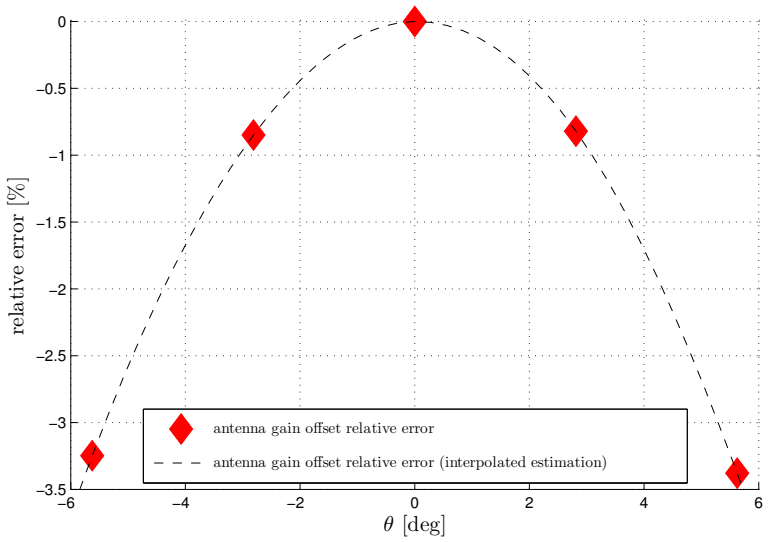

Figure 6.9: Antenna gain offset relative error with the variation of azimuthal angle θ at a frequency of 2.5 GHz; here, this *relative error* represents $1-\gamma$ from the previous figure.

Antenna gain and its uncertainties of measurement

Estimation of maximum gain By using (6.2), and the propagation distance computed using (6.6) and (6.9), the resulted antenna gain (corresponding to direction: $\theta = 0$, $\varphi = 0$) is presented in Fig. 6.10. Differences between the measured value of the gain in near-field chamber and in reverberation chamber (limited to around 0.5 dB) are due to several uncertainties. One factor is the error of estimation of the free-space propagation distance. The uncertainties increase even more when the antenna gain is smaller, because in this situation the signal amplitude is much lower and it is more difficult to extract the maximum of the signal. In this analysis all measurements have been done using a manual positioning of the AUT. This inevitably causes uncertainties both in azimuthal and elevation planes of the AUT. Nonetheless, the measurements in near-field chamber are also affected by uncertainties. All in all, we can be reasonably satisfied by the results in reverberation chamber in comparison with measurements in near field chamber.

Gain estimation for a limited θ range For a more detailed analysis we estimate the gain for a variation of the angle $\theta \in [-30\,^\circ, 30\,^\circ]$. The measurements in reverberation chamber are made rotating the antenna manually around its vertical axis for both polarizations H and V with a step of 5 °. Then, we compare the normalized gain measured in reverberation chamber with the one measured in near-field chamber in the frequency bandwidth $2-6$ GHz for the same range of θ angle. In near-field chamber measurements, the angle step is around 2.8 ° (i.e., $\pi/64$). In order to compare the results we interpolate both measurements using a

spline interpolation to have a better frequency and angle resolution. We compute the relative difference of the measured value in reverberation chamber over the value measured in near field chamber. The results are presented in Fig. 6.11(a) for the horizontal polarization of antenna and in Fig. 6.11(b) for the vertical polarization. From these results, we show in Table 6.1 a synthetic analyses of errors for the horizontal and vertical polarizations. Other

Table 6.1: Gain relative differences (see Fig. 6.11(a) and 6.11(b)).

Relative differences	**Percentage of data**	
less than	**for H Polarization**	**for V Polarization**
10%	76.15%	81.10%
15%	87.85%	87.70%
20%	94.40%	93.36%

source of uncertainties, that may bias the results, are the uniformity of the metallic wall and the inclination of the tripod on which antenna is placed. A last possible factor that may influence the results is the extraction method: the frequency-to time transformations and back to frequency domain may influence the shape of the signal especially when it has low energy.

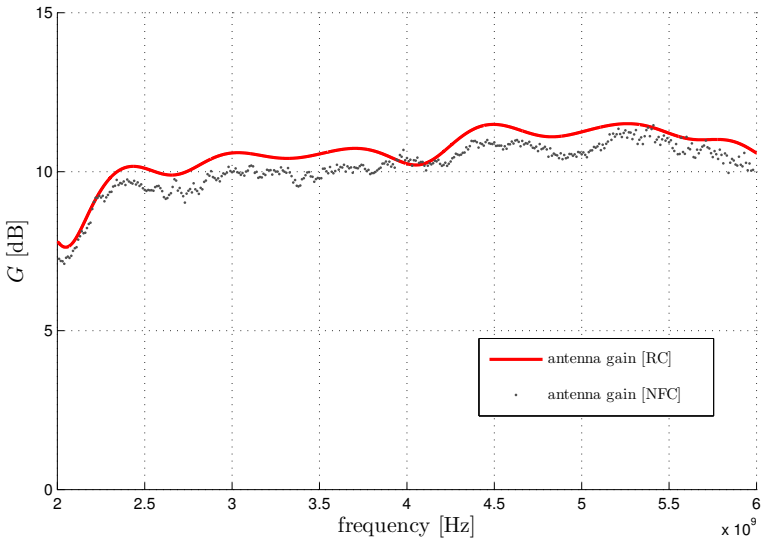

Figure 6.10: Comparison between measured gain in direction (θ = 0, φ = 0) in NFC and in RC.

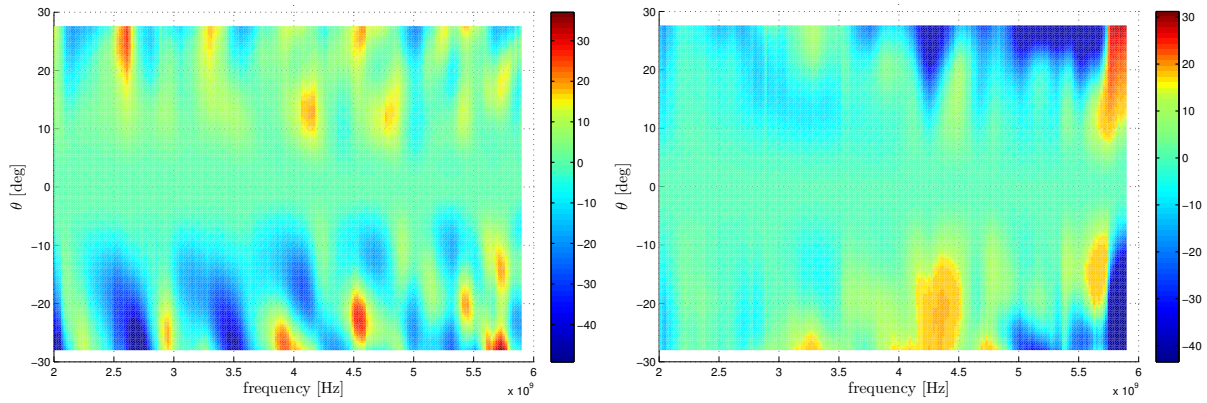

(a) (b)

Figure 6.11: Relative difference (%) of normalized gain for H plane (a), and for V plane (b) of the values measured in reverberation chamber over the values measured in NFC.

6.3.4 Evaluation of antenna pattern

The previous analyses show that, compared with the measured values in near field chamber, the gain estimated in reverberation chamber is affected by uncertainties due to several factors. Extending our analysis of antenna gain for the all range of $\theta \in [0, 2\pi)$, we compare the polar gain measured in near-field chamber and in reverberation chamber. As the measurements are made manually in reverberation chamber we use an angle step of 15 °, all the other parameters and measurement conditions remaining as presented before.

In certain conditions it is not possible to use the method to extract the free space propagation distance from the total propagation distance d_{IR} estimated from the maximum of the signal. This may be the case when antenna is directive, for which at low levels of antenna gain this maximum may be difficult to identify as the level of the signal may be very low. From Fig. 6.1, it results that we can extract this distance using the previous estimated distances d_{IR} (e.g., for $\theta = 0$ and another angle $\widetilde{\theta}$ for which antenna gain is high). The free-space propagation distance results as:

$$2d(\theta) = \frac{\cos\theta - \cos\widetilde{\theta}}{1 - \cos\widetilde{\theta}}\, d_{\mathrm{IR}}(0) + \frac{1 - \cos\theta}{1 - \cos\widetilde{\theta}} d_{\mathrm{IR}}(\widetilde{\theta}) - 2d_{\mathrm{a}}. \tag{6.15}$$

We present four antenna patterns measurements, two for each polarization at two different frequencies, 3 and 5 GHz. Antenna patterns are shown for horizontal polarization in Fig. 6.12(a) and Fig. 6.12(b) and vertical polarization in Fig. 6.13(a) andk Fig. 6.13(b).
From these figures, it results that for high gain antenna the measured antenna patterns in reverberation chamber and near field chamber are similar. Patterns with lower gains and multiple secondary lobes are hardly detected (Fig. 6.13(b)). The possible sources of errors have been previously discussed.

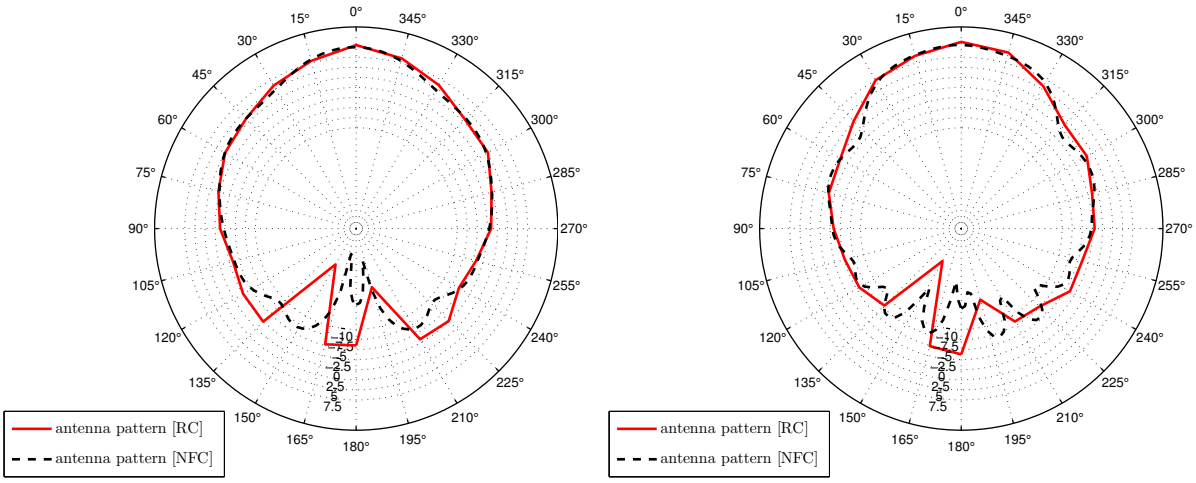

(a) (b)

Figure 6.12: Comparison between H plane antenna patterns, in dB, measured in near-field chamber and in reverberation chamber for $f = 3\,\mathrm{GHz}$ (a), and for $f = 5\,\mathrm{GHz}$ (b).

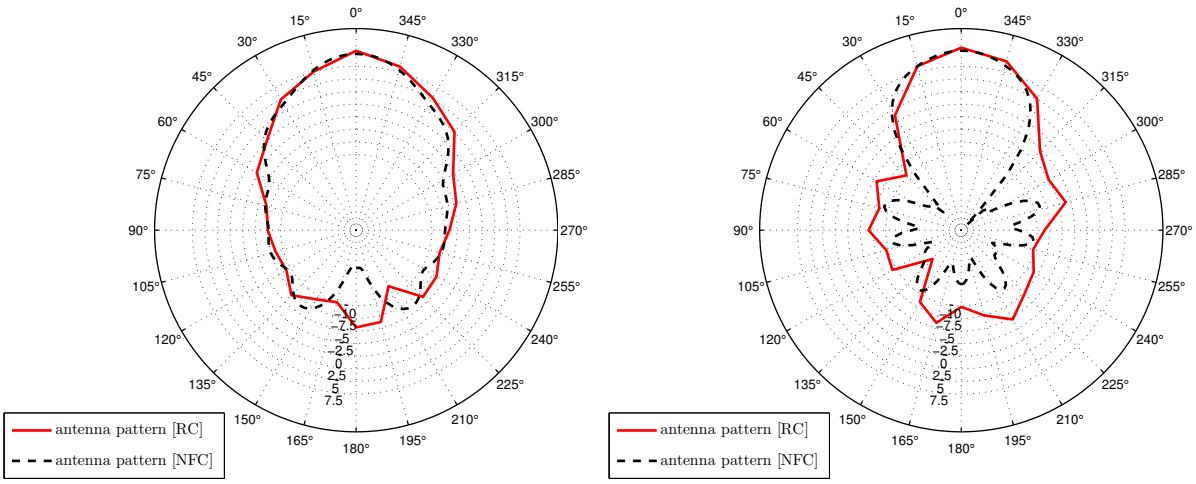

(a) (b)

Figure 6.13: Comparison between V plane antenna patterns, in dB, measured in near-field chamber and in reverberation chamber for $f = 3\,\mathrm{GHz}$ (a), and for $f = 5\,\mathrm{GHz}$ (b).

Evaluation of antenna half power beamwidth $\Theta_{3\,\mathbf{dB}}$

Previously, we have discussed the possibility to extract the antenna pattern. In this section, we reduce the interval of analysis for the range where the antenna gain is high, in order to extract the half power beamwidth. To do this, we use the measurements made in reverberation chamber for an angle $\theta \in [-30\,^\circ, 30\,^\circ]$ with a step of $5\,^\circ$. For the type of antenna used in our measurements, an angle range of only $60\,^\circ$ is enough since the antenna datasheet shows a lower half power beamwidth value. As in section 6.3.3, we use for both measurements a spline interpolation in order to have a finer mesh of the angle θ. In Fig. 6.14(a) and Fig. 6.14(b) we present the half power beamwidth for the horizontal polarization and the vertical polarization. We can see that the half power beamwidth measured in reverberation chamber follows the one measured in near-field chamber with however some differences. These results are analyzed in Fig. 6.15(a) for the horizontal polarization and in Fig. 6.15(b) for the vertical polarization, by computing the relative difference of the half power beamwidth measured in reverberation chamber over the one measured in near field chamber. With some exceptions, the relative difference stands in the $[-10\%, 10\%]$ range for the horizontal polarization and in the $[-6\%, 6\%]$ range for the vertical polarization. The same problems which affect the gain of antenna, discussed in section 6.3.3 also affect the half power beamwidth.

6.4 Conclusions

In this chapter we have presented a method to estimate several parameters linked to antenna gain from $S_{11_{\mathrm{FS}}}$ parameter measured in reverberation chamber. Extracting the path distance corresponding to the maximum of the signal and subtracting the guided antenna propagation distance we can estimate the free-space propagation distance. By rotating antenna around its vertical axis we estimate $S_{11_{\mathrm{FS}}}$ from the collection of several mismatch parameters in reverberation chamber. Filtering the time response of the measured signal, we then extract antenna mismatch parameter S_{11} and the free-space transfer function H_{FS}. Using the free-space propagation distance we can estimate the gain of antenna, and therefore obtain an approximation of antenna pattern. Reducing the interval of analysis we compute the half power beamwidth. Comparisons with the values measured in a near field chamber are made in addition to several error analysis. The methods presented in this chapter can provide good results and are easy to implement providing simple ways to characterize several antenna parameters.

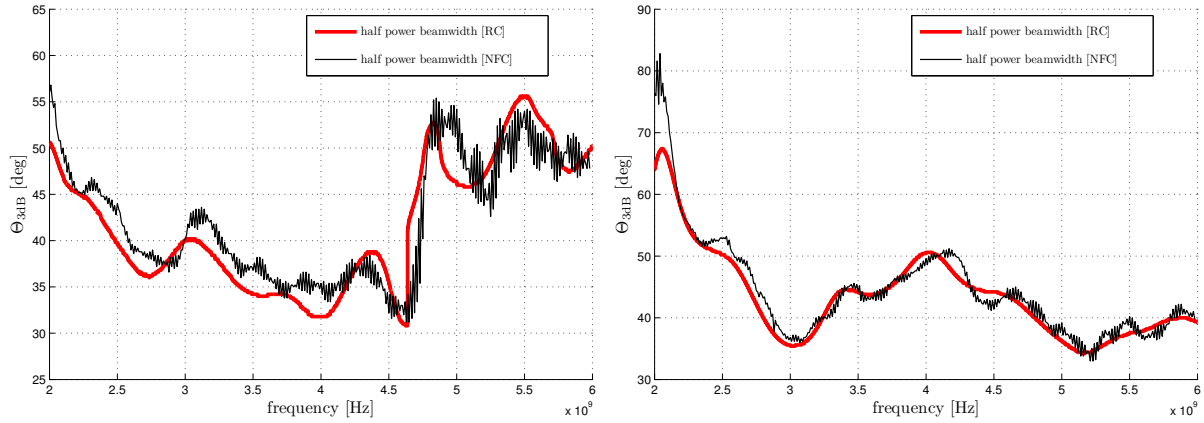

(a) (b)

Figure 6.14: Antenna half power beamwidth for H plane (a), and V plane (b) estimated in near-field chamber and RC.

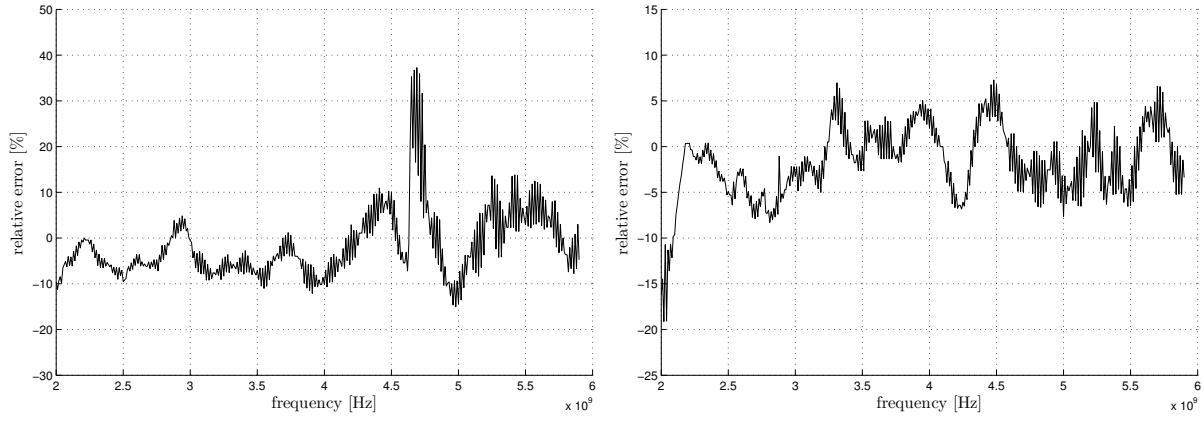

(a) (b)

Figure 6.15: Relative difference of antenna half power beamwidth measured in reverberation chamber over value measured in near-field chamber for H plane (a), and for V plane (b).

Bibliography

[1] C. Balanis, *Antenna theory-analysis and design (2nd Edition).* New York, USA: John Wiley and Sons Inc., 1997.

[2] J. Hansen, *Spherical near-field antenna measurements.* P. Peregrinus on behalf of the Institution of Electrical Engineers, London, U.K., 1988.

[3] G. Bryant, *Principles of Microwave Measurements.* Institution of Electrical Engineers, 1993.

[4] H. Arai, *Measurement of Mobile Antenna Systems*, A. House, Ed. Artech House, 2001.

[5] S. R. Saunders and A. Aragon-Zavala, *Antennas and Propagation for Wireless Communication Systems.* John Wiley and Sons, 2007.

[6] T. Brockett and Y. Rahmat-Samii, "A novel portable bipolar near-field measurement system for millimeter-wave antennas: construction, development, and verification," *Antennas and Propagation Magazine, IEEE*, vol. 50, no. 5, pp. 121–130, Oct. 2008.

[7] M. Serhir, P. Besnier, and M. Drissi, "An accurate equivalent behavioral model of antenna radiation using a mode-matching technique based on spherical near field measurements," *Antennas and Propagation, IEEE Transactions on*, vol. 56, no. 1, pp. 48–57, Jan. 2008.

[8] M. Migliore, "Fi LTE ring environmental reflections in far-field antenna measurement in semi-anechoic chambers by an adaptive pattern strategy," *Antennas and Propagation, IEEE Transactions on*, vol. 52, no. 4, pp. 1112–1115, Apr. 2004.

[9] R. Yamaguchi, Y. Kimura, K. Komiya, and K. Cho, "A far-field measurement method for large size antenna by using synthetic aperture antenna," in *Antennas and Propagation, 2009. EuCAP 2009. 3rd European Conference on*, Mar. 2009, pp. 1730–1733.

[10] V. Viikari, V.-M. Kolmonen, J. Salo, and A. Raisanen, "Antenna pattern correction technique based on an adaptive array algorithm," *Antennas and Propagation, IEEE Transactions on*, vol. 55, no. 8, pp. 2194–2199, Aug. 2007.

[11] S. Farzaneh, A. Ozturk, A. Sebak, and R. Paknys, "Antenna-pattern measurement using spectrum analyzer for systems with frequency translation [measurements corner]," *Antennas and Propagation Magazine, IEEE*, vol. 51, no. 3, pp. 126–131, Jun. 2009.

[12] C. Gennarelli, G. Riccio, and C. Savarese, "Fast and accurate evaluation of the antenna directivity via sampling expansion," in *Antennas and Propagation Society International Symposium, 2001. IEEE*, vol. 1, 2001, pp. 288–291.

[13] S. Ullah, J. Flint, and R. Seager, "Patch antenna directivity analysis using an equi-area method," in *Antennas and Propagation Conference, 2008. LAPC 2008. Loughborough*, Mar. 2008, pp. 349–352.

[14] S. Rogers, J. Aberle, and D. Auckland, "Two-port model of an antenna for use in characterizing wireless communications systems, obtained using efficiency measurements," *Antennas and Propagation Magazine, IEEE*, vol. 45, no. 3, pp. 115–118, Jun. 2003.

[15] I. Naqvi, G. Le Fur, J. Sol, P. Besnier, and A. Sharaiha, "Sub-band time reversal efficiency measurement: An enhanced method for efficiency characterization of UWB antennas," *Antennas and Propagation, IEEE Transactions on*, vol. 60, no. 3, pp. 1657–1660, Mar. 2012.

[16] C. Lee and A. Duffy, "Antenna efficiency measurements in a reverberation chamber without the need for a reference antenna," *Antennas and Wireless Propagation Letters, IEEE*, vol. 7, pp. 448–450, 2008.

[17] C. Holloway, H. Shah, R. Pirkl, W. Young, D. Hill, and J. Ladbury, "Reverberation chamber techniques for determining the radiation and total efficiency of antennas," *Antennas and Propagation, IEEE Transactions on*, vol. 60, no. 4, pp. 1758–1770, Apr. 2012.

[18] C. Lemoine, E. Amador, P. Besnier, J. Sol, J.-M. Floc'h, and A. Laisne, "Statistical estimation of antenna gain from measurements carried out in a mode-stirred reverberation chamber," in *General Assembly and Scientific Symposium, 2011 XXXth URSI*, Aug. 2011, pp. 1–4.

[19] I. Junqua, P. Degauque, M. Lié andnard, and F. Issac, "On the power dissipated by an antenna in transmit mode or in receive mode in a reverberation chamber," *Electromagnetic Compatibility, IEEE Transactions on*, vol. 54, no. 1, pp. 174–180, Feb. 2012.

[20] K. Rosengren and P.-S. Kildal, "Radiation efficiency, correlation, diversity gain and capacity of a six-monopole antenna array for a MIMO system: theory, simulation and measurement in reverberation chamber," *Microwaves, Antennas and Propagation, IEE Proceedings*, vol. 152, no. 1, pp. 7–16, Feb. 2005.

[21] B. Lindmark, L. Garcia-Garcia, N. Jalden, and C. Orlenius, "Evaluation of MIMO arrays using antenna patterns, reverberation chamber, and channel measurements," in *Antennas and Propagation, 2006. EuCAP 2006. First European Conference on*, Nov. 2006, pp. 1–6.

[22] E. M. Purcell, "A method for measuring the absolute gain of microwave antennas," Radiation Laboratory,

Massachusetts Institute of Technology, Tech. Rep. 41-9, 1943.

[23] Z. Wu, "Effect of mismatch on antenna gain measurement by purcell's method," *Electronics Letters*, vol. 22, no. 10, pp. 522–524, Aug. 1986.

[24] J. Glimm, R. Harms, K. Munter, M. Spitzer, and R. Pape, "A single-antenna method for traceable antenna gain measurement," *Electromagnetic Compatibility, IEEE Transactions on*, vol. 41, no. 4, pp. 436–439, Nov. 1999.

[25] J. Krieger, E. Newman, and I. Gupta, "The single antenna method for the measurement of antenna gain and phase," *Antennas and Propagation, IEEE Transactions on*, vol. 54, no. 11, pp. 3562–3565, Nov. 2006.

CHAPTER 7

Diversity gain for Rician and Rayleigh environments in reverberation chamber

7.1 Introduction

MOBILE and wireless communications are influenced by the fading due to multipath propagation, which may result in severe performance degradation. In these conditions the amplitude of the received signal may have minima of signal under a detectable signal-to-noise ratio (SNR). To face with these deleterious effects, several techniques are available. One of these techniques is the use of diversity [1, 2] which can significantly improve the performance of wireless terminals. This technique uses two or more received uncorrelated fading signals which are combined in order to reduce the probability of fading dip in the resulted signal. Due to different channel conditions, when the signal on one antenna is in a deep fade, the other has a significant probability to experience a higher level of the signal. In this way the signal-to-noise ratio increases and the fading margins in the system link budget can be reduced. Depending on the diversity techniques and on several factors of the communication system and propagation environment, the improvement in the fading margin can be as large as $10-12\,\mathrm{dB}$ for the worst 1% of cases [3]. Beside the role of diversity to increase the received signal power when transmitting the same signal on different channels, another application is the improvement of transmission capacity. In this case, channels that provide fading maxima are used to send different data in parallel. Generally, the signal is distributed among the channels and recombined after reception in such a way that the overall channel capacity is maximized [4]. It results that using diversity techniques improves the reliability of the wireless channels, thus increasing the efficiency of the radio link. Moreover, the diversity systems permit the use of lower transmit power for the same level of reliability, reducing the interferences between devices and the power consumption which is crucial for mobile systems.

There are many researches on diversity techniques. For example, [5] presents a statistical analysis of the combined signal for the case of the maximal-ratio combiner. In [6], based on several measurements an empirical relationship among diversity gain, branch envelope correlation, and power balance is obtained. Also, the outage probability and average error probability for a selective-diversity scheme in a Rayleigh environment is presented in [7]. Moreover, the impact of fading correlation and power imbalance on diversity gain is analyzed

in [8]. In [9], is discussed the performance of equal-gain diversity-scheme using a frequency-domain method to estimate the pdf of equal-gain diversity-scheme for Rayleigh, Rician and Nakagami fading. The performance of the maximum-ratio combining method for the Rician fading channels are analyzed in [10]. Some simulation results of diversity gain with the number of antennas and its influence over the capacity of transmission for Rician fading are discussed in [11].

Until now, in this thesis, we have analyzed several parameters of the propagation channels and different methods to evaluate and control these parameters. In this chapter we discuss the diversity in an emulated wireless channel in reverberation chamber (RC). The purpose is to analyze and obtain the same improvements on the propagation channel in the presence of the fading as in a real environment. In practice the measured signal can be a voltage or a power with or without measuring the signal phase depending on the type of instrumentation: VNA, oscilloscope, spectrum analyzer, etc. First we identify the factors which may influence the results. From the knowledge of these factors we determine what are the ranges in which the measured diversity gains should be expected. In many real environments, the received signal may not be anymore Rayleigh distributed. We extend the analysis of diversity gain to Rician channels, and we examine the case when the unstirred powers at reception are different. This is done using Monte Carlo simulations while the measurements in reverberation chamber validate our theoretical results. We show that in Rician environments, the diversity is influenced not only by the presence of unstirred components but also by the power imbalance due to these components. In these environments, the use of envelope or power correlation as a parameter to characterize the quality of the diversity techniques is not recommended as it may bias the conclusions.

7.2 Computing the diversity gain

Diversity gain quantifies the improvement in SNR of a signal obtained by combining several received signals. It corresponds to a reduction in fading depth and hence the required fading margin for system planning. It is evaluated using the envelope or the power of the signal. For example, for a system with two receiving antennas (i.e., two branches), the two received levels are combined according to a certain diversity combination rule. The resulting cumulative distribution function (CDF) for the combined signal is located to the right of the CDF of signals received by the two branches. In a CDF plot versus power levels in decibels, the diversity gain is defined as the difference along the abscissa axis between the power of the branch with the highest mean power amplitude and the one obtained at the output of the diversity combiner for a given probability or signal reliability, Fig 7.1. In general the level of reliability can be 99%, 95% or 90%, commonly chosen 99%:

$$\begin{aligned} G_{\mathrm{div},\alpha} &= \frac{P_{\mathrm{div},\alpha}}{P_{\mathrm{branch},\alpha}}, \\ G_{\mathrm{div},\alpha}\,[\mathrm{dB}] &= P_{\mathrm{div},\alpha}[\mathrm{dB}] - P_{\mathrm{branch},\alpha}[\mathrm{dB}], \end{aligned} \tag{7.1}$$

where

- $P_{\mathrm{div},\alpha}$ is the power level after diversity combining (see 7.5) measured at α% level of reliability;
- $P_{\mathrm{branch},\alpha}$ is the power level of the reference branch measured at α% level of reliability.

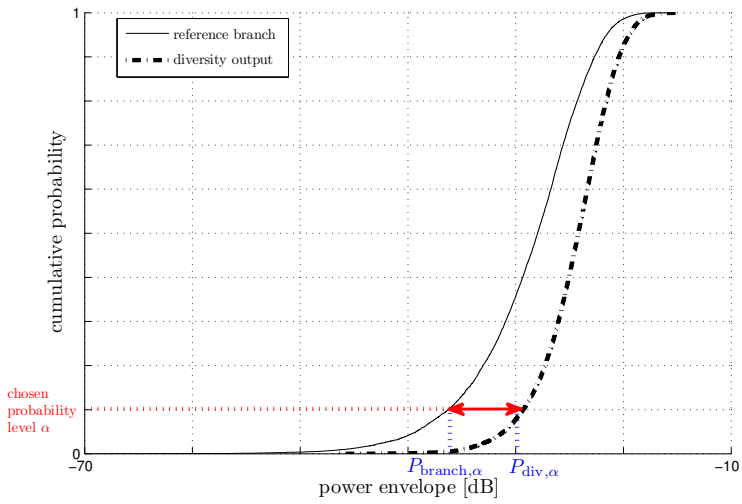

Figure 7.1: Computing the diversity gain from the CDF of the signals.

7.3 Linear diversity combining techniques

There are several mechanisms to achieve the diversity combining [5]. A first mechanism uses the properties of antenna arrays. These techniques are more effective in flat fading channels which affect the signal the same way over its bandwidth. Flat fading occurs in outdoor narrow-band systems and in indoor wide-band systems channels with small delay spreads. There are several antenna parameters which can be exploited in order to obtain low uncorrelated signals for a diversity scheme. Among these diversities, one identifies:

- Spatial diversity. This kind of diversity requires multiple antennas at reception or transmission, sufficiently spaced to have uncorrelated samples. Depending on the kind of the system and propagation environment, this diversity technique may require wide antenna spacing distances for proper operation [12]. In portable systems, the maximum separation distance between antennas is limited by the maximum dimensions of the terminal.

- Polarization diversity. It uses an antenna array with two or more different polarizations. It is based on the depolarization in the propagation medium and the resulting signals do not fade in a correlated manner. This is useful especially in systems affected by polarization imbalance due to random handset orientation [13]. The polarization imbalance can also be found in small reverberation chambers and may be removed by polarization stirring [14].

- Pattern or Angle(-of-Arrival) diversity. This diversity uses multiple directional antennas to discriminate signals over angle space. It requires narrow antenna beamwidths compared with the angular scatterer [5].

Another mechanism to achieve the diversity combining uses the properties of the system (or the signal):

- Frequency diversity. For this diversity technique, the transmission of the same signal is done at sufficiently spaced carrier frequencies providing independent fading versions of the signal.

- Time diversity and Multipath diversity. For this diversity, the same bit of information is repetitively transmitted at different time intervals, which are well separated compared with the delay spread of the environment.

In this chapter our analysis investigate only the configurations for spatial, polarization and pattern diversities.

7.4 Definitions of the diversity gain

As presented in section 7.2, the diversity gain is estimated as the difference between the levels of the CDFs of a reference signal and the one at the output of the diversity combiner. As the level of the signal received by one antenna in the presence of other antennas may be different compared with the situation when this antenna is alone, there are different definitions of the diversity gain. This is because the performances of an antenna in an antenna array change in the presence of the other antennas. A quantitative parameter which describe the performances of an antenna is the total efficiency which includes the impedance mismatch, losses in the antenna itself, and losses in the near environment [15]. The mutual coupling between antennas reduces the total efficiency because of modifications of impedance mismatch and absorption in other antennas [3]. As a result, the changes of antenna radiation efficiency will shift to the left the CDF of the power received by antenna, Fig. 7.2. Therefore estimating the diversity gain without taking into account the modification in the antenna efficiency is not relevant because different environments will give different results. Even though the efficiency of an antenna in an array decreases, the combination technique will compensates this reduction. It results that depending on the signal we use as the reference, one has different definitions of the diversity gain [16]:

- apparent diversity gain. The reference is one of the branches of the antenna array (antenna under test) which has the biggest average power;
- effective diversity gain. The reference is an ideal single antenna, which has a total efficiency of 100% (it is impedance-matched to the transmission line feeding it and has no dissipative losses). Compared with the diversity gain in (7.1), this diversity gain becomes:

$$G_{\text{eff\_div},\alpha} = \frac{P_{\text{div},\alpha}}{P_{\text{branch},\alpha}}\eta_{\text{rad}} = \frac{P_{\text{div},\alpha}}{P_{\text{ideal},\alpha}}, \tag{7.2}$$

  where η_{rad} is the radiation efficiency of the reference branch, and $P_{\text{ideal},\alpha}$ is the received power level of a single antenna with unit radiation efficiency estimated at $\alpha\%$ level of reliability. The apparent diversity gain is bigger than the effective diversity gain.

- actual diversity gain: The reference is an existing practical antenna which is replaced by the antenna array.

For a better explanation of the above description, a qualitative example is presented in Fig. 7.2. This figure illustrates the CDF curves of two references branches (i.e., with and without removing antenna radiation efficiency) as well as the one at the combiner output. Each of these CDFs are generated from measurements using a number of 10 000 realizations. Removing the radiation efficiency shifts the CDF of the reference branch to the right. Diversity gain associated with the reference branch whose power CDF includes antenna radiation efficiency represents the apparent diversity gain (a) while the other is the effective diversity gain (b).

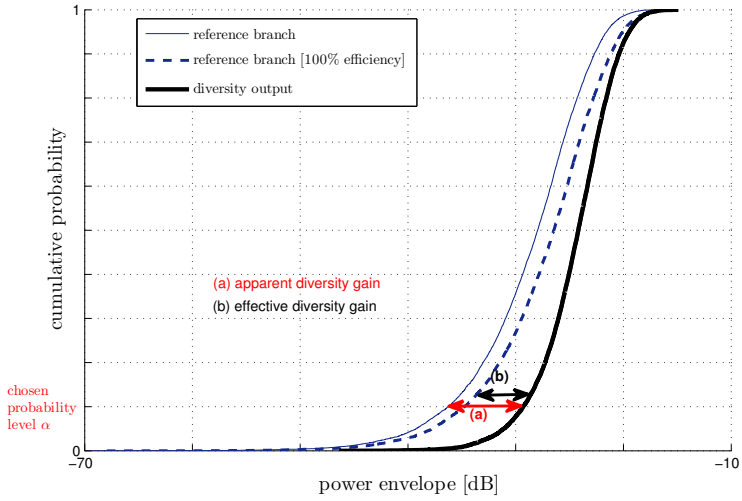

Figure 7.2: Example of the CDF of the reference received signal and the combined signal.

7.5 Methods to combine the signals for diversity gain

Assuming equal noise levels for a system which has M antenna branches and considering that the envelopes of the M diversity branches are given by r_1, r_2, $\cdots$, r_M. Depending on the combination technique, the resulting signal envelope r at the output of the combiner can be computed in many ways [17]:

7.5.1 For maximal-ratio combining

In a general case, the signals from all branches are weighted by their respective SNRs, cophased, and added:

$$r = \sqrt{\sum_{k=1}^{M} \gamma_k r_k^2}. \tag{7.3}$$

The parameters γ_k are weighting factors which depend on the level of fading on branches and evolve with time due to mobility of transmitter/receiver or surrounding objects. The optimum weight for each branch depend on the signal magnitude and the branch-noise power level. The signal at the output of the combiner varies more gradually with signal fading compared with other techniques, but the practical implementation to achieve the correct weighting factors is more complicated [5].

7.5.2 For selection combining

In this technique, the signal with the highest SNR is selected:

$$r = \sqrt{\max(\gamma_1 r_1^2, \gamma_2 r_2^2, \cdots, \gamma_M r_M^2)} \tag{7.4}$$

Selection combining can be seen as a particular case of the maximal-ratio combining where at any instant, all the γ_k are zero except for the branch with the largest SNR, which is an

arbitrary constant [5]. Compared with previous technique, selection combining combining involves transients in the output signal due to switching.

7.5.3 For equal-gain combining

The signals from the two branches are added together. The SNR at the output of the combiner is the sum of the instantaneous SNR's of each branch. When this technique is used, the risk is that the branch with the larger noise level dominates the output SNR even if the branch itself is weak in signal level:

$$r = \frac{\sum_{k=1}^{M} \gamma_k r_k}{\sqrt{M}}. \tag{7.5}$$

Therefore, if the noises on different branches are unequal, the parameters γ_k have the role to equalize the signals. For a Rayleigh environment, considering a two branch diversity combiner, receiving uncorrelated signals (i.e., $\rho \approx 0$), the theoretical maximum diversity gains estimated from Monte Carlo simulations are less than: 11.5 dB for maximal-ratio combining, 10 dB for selection combining, and 8 dB for equal-gain combining.

7.5.4 Other algorithms

Adaptive beamforming algorithms can also provide diversity gain, in addition to rejecting interfering signals [1, 18].

7.6 Parameters which may influence diversity gain

Diversity gain is considered as a function of signal correlation between branches, mutual coupling between antennas (i.e., radiation efficiency and mismatch), power imbalance and unstirred components. Each of these factors may have a more or less influence in the final result. We chose to discuss these factors separately to provide a better insight of the influence over diversity gain.

7.6.1 Mutual coupling between antennas: radiation efficiency and mismatch

The performances of an antenna can be described in terms of realized gain (i.e., gain containing antenna total efficiency) and radiation pattern. The realized gain equals the directivity times the total efficiency. While the directivity depends on the geometry of the antenna, the total efficiency depends on the absorption in lossy material in the antenna and its environment, and mismatches at the antenna port [4]. Compared with the case of a single antenna, a radiating element in an antenna array will induce currents on the neighboring elements which partially turn into losses implying a modification of the radiation efficiency. Also, due to reflections from the neighboring elements back to emission antenna, the mismatch will be also modified. The highest influence on the diversity gain is due to the radiation efficiency rather than to mismatch. Even though using an antenna array will reduce the efficiency of each element (compared with the case when it is single), the diversity compensates this drawback. The

diversity may be also seen as a method to compensate the fact that an antenna efficiency is not 100% when antennas are close to each other.

The radiation efficiency, mismatch and directivity of an antenna in an antenna array is modified not only by its presence in the array, but also by the neighboring objects (e.g., human hand, head, etc.). It means that the diversity gain of a mobile device during utilization may be smaller than the one predicted in the absence of the user.

7.6.2 The Ricean parameter K

K-factor represents the ratio between the power of unstirred components to power of stirred components. It depends on the distance between transmitting and receiving antennas, antenna characteristics and quality factor of the environment.

$$K = \frac{A^2}{2\sigma^2} \tag{7.6}$$

where

- A^2 is the power of unstirred components;
- $2\sigma^2$ is the power of stirred components.

In general, most of the papers discuss the diversity gain in Rayleigh channels. When direct paths between the transmitter and the receiver exist, the fading is less severe and the diversity gain is lower than for channels with Rayleigh fading. Even though this situation affects less the improvement of diversity over the received power at the output of combiner, it may however influence transmission capacity.

7.6.3 Power Imbalance

When the above presented parameters (i.e., total efficiency and K-factor) are not identical on all branches, the signal at the output of the combiner can be affected by a power imbalance. This appears because the average power received by one branch is different from the average power received by other branches and they are characterized by distributions which have different CDFs. For a Rician fading distribution and a two branches diversity combiner, the power imbalance (PI) becomes:

$$PI = \frac{\eta_1}{\eta_2} \frac{A_1^2 + 2\sigma_1^2}{A_2^2 + 2\sigma_2^2}, \tag{7.7}$$

where the subscript "1" denotes the first branch and "2" the second one. Re-organizing (7.7) using (7.6) it results:

$$PI = \frac{\eta_1}{\eta_2} \times \frac{2\sigma_1^2}{2\sigma_2^2} \times \frac{K_1 + 1}{K_2 + 1} = PI_\eta \times PI_{\mathrm{Sti}} \times PI_K \tag{7.8}$$

It means that the power imbalance may be due to:

- different antenna total efficiencies, PI_η (i.e., because antennas have different efficiencies, or when the efficiencies in antenna array change differently when they are close to some objects);

- different stirred components, PI_{Sti} (e.g., due to a polarization imbalance);
- different unstirred components, PI_K (e.g., due to a tilt of one antenna). This may be the case when there is a line-of-sight between the transmitter and receiver and a polarization diversity is used (see 7.3). Moreover, due to side lobes some secondary directions may be favored compared with others, and one antenna may receive the signal by a secondary lobe and not by the main lobe. The same result may happen when one antenna in the antenna array is more directive. Even though in reverberation chamber we consider that the angles of arrival is uniformly distributed over 4π steradians, in common environments (i.e., outdoor) there is a high probability that waves come from specific directions.

In all situations the diversity gain decreases as power imbalance between diversity branches increases because a branch that has a weak signal has only a small contribution to the combined signal [19].

7.6.4 Branch correlation

The correlation (see annex B.1) is primarily caused by mutual coupling between the elements of the antenna arrays at emission and reception [3]. When antenna patterns are different, the correlation between the signals received by these antennas is even smaller as the combined signals for each antenna are different. This may happen even if the antennas are identical but close one to each other, as the patterns may become distorted due to mutual coupling [20]. Diversity gain increases with decreasing signal correlation between branch antennas.
Considering two variables R_1 and R_2, representing the measured signal over a time window for a two branch system, the correlation (normalized covariance) between these two variables is given by:

$$\rho = \frac{E\left[(R_1 - \mu_{R_1})(R_2 - \mu_{R_2})^H\right]}{\sqrt{\mathrm{Var}(R_1)\,\mathrm{Var}(R_2)}}, \tag{7.9}$$

where

- ^{H} is the Hermitian transpose operation;
- $E[\square]$ represents the average over the time window;
- the parameters μ_{R_1} and μ_{R_2} are the averages of the two variables over time windows;
- the operator "Var" is the variance.

When the average is not subtracted, the correlation becomes:

$$\widetilde{\rho} = \frac{E\left[(R_1)(R_2)^H\right]}{\sqrt{\mathrm{Var}(R_1)\,\mathrm{Var}(R_2)}}. \tag{7.10}$$

In literature both expressions are used. In this study the correlation is further computed as in (7.9).

Modifying one parameter between antennas we can identify: spatial correlation, polarization correlation, antenna pattern correlation, etc. Also, the measured signals at the output of the two branches can be complex envelopes, voltage envelopes or power envelopes, and different types of correlation between branches can be computed: complex correlation, envelope correlation and power correlation. Depending on the type of the signal, the correlation changes accordingly.

Complex Envelope Correlation Considering that in a Rician environment there is no correlation between the unstirred and stirred components, the relation between the complex correlations ρ_{cpx} and $\widetilde{\rho}_{\text{cpx}}$ computed as in (7.9) and respectively in (7.10), and using [21] when the two branches receive signals having different K-factors, K_1 and K_2, is given by:

$$|\widetilde{\rho}_{\text{cpx}}| = \sqrt{\frac{1}{(K_1+1)(K_2+1)}}|\rho_{\text{cpx}}| + \sqrt{\frac{K_1K_2}{(K_1+1)(K_2+1)}}. \tag{7.11}$$

In spatial diversity systems, the complex correlation between antenna branches is a function of the spacing distance between the dipole antennas. Depending on the antenna pattern, several analytical expressions are computed as:

- For a uniform distribution in azimuth of angles of arrival and identically polarized omnidirectional receiving antennas, the complex correlation with the distance is a function of zeroth order Bessel function of the first kind [22]. This corresponds to a 2D model of antenna and propagation channel.

$$\rho_{\text{cpx, omni}} = J_0\left(kd\right). \tag{7.12}$$

- For an isotropic distribution of angles of incidences over 4π steradians [23], which corresponds to a 3D model of antenna and propagation channel:

$$\rho_{\text{cpx, iso}} = \frac{\sin(kd)}{kd}. \tag{7.13}$$

  - Using only longitudinal electric field (z-axis) [23]:

$$\rho_{\text{cpx, E}_\text{Z}} = \frac{3}{(kd)^2}\left[\frac{\sin(kd)}{kd} - \cos(kd)\right]. \tag{7.14}$$

  - Using only transversal electric field (x-axis or y-axis) [23]:

$$\rho_{\text{cpx, E}_\text{XY}} = \frac{3}{2}\frac{\sin(kd)}{kd} - \frac{1}{(kd)^2}\left[\frac{\sin(kd)}{kd} - \cos(kd)\right]. \tag{7.15}$$

In the above equations d represents antenna spacing distance, λ is the wavelength and $k = 2\pi d/\lambda$ is the wavenumber.

Power Correlation Using the general definition of correlation (7.9) the power correlation between the two measured power signals, r_1^2 and r_2^2, on the two branches becomes:

$$\rho_{\text{pwr}} = \frac{E\left[(r_1^2 - \mu_{r_1^2})(r_2^2 - \mu_{r_2^2})^H\right]}{\sqrt{\text{Var}(r_1^2)\,\text{Var}(r_2^2)}} = \frac{E\left[r_1^2(r_2^2)^H\right] - E\left[r_1^2\right]E\left[(r_2^2)^H\right]}{\sqrt{\left(E\left[r_1^4\right] - \left(E\left[r_1^2\right]\right)^2\right)\left(E\left[r_2^4\right] - \left(E\left[r_2^2\right]\right)^2\right)}}. \tag{7.16}$$

We extend the calculus of the power correlation in [24], which is computed when the K-factors are identical for all signals, to the general situation when the K-factors are different. In these

conditions we obtain:

$$\begin{cases} E\left[r_1^2 r_2^2\right] = A_1^2 A_2^2 + 2A_1^2\sigma_2^2 + 2A_2^2\sigma_1^2 + 4\sigma_1^2\sigma_2^2 + 4A_1^2A_2^2\sigma_1\sigma_2\Re(\rho_{\text{cpx}}) + 4A_1^2A_2^2\sigma_1^2\sigma_2^2|\rho_{\text{cpx}}|^2, \\ E\left[r_1^2\right] = A_1^2 + 2\sigma_1^2, \\ E\left[r_2^2\right] = A_2^2 + 2\sigma_2^2, \\ E\left[r_1^4\right] = A_1^4 + 8A_1^2\sigma_1^2 + 8\sigma_1^4, \\ E\left[r_2^4\right] = A_2^4 + 8A_2^2\sigma_2^2 + 8\sigma_2^4. \end{cases} \tag{7.17}$$

where A_1^2, A_2^2 and $2\sigma_1^2$, $2\sigma_2^2$ are respectively the power of unstirred and stirred components on the two branches, (see 2.2.2). With (7.16) and (7.17) the power correlation ρ_{pwr} as a function of the complex correlation and the K-factors on the two branches is given by:

$$\rho_{\text{pwr}} = \frac{\Re(\rho_{\text{cpx}})2\sqrt{K_1K_2} + |\rho_{\text{cpx}}|^2}{\sqrt{(2K_1+1)(2K_2+1)}}, \tag{7.18}$$

where $K_1 = A_1^2/\left(2\sigma_1^2\right)$ and $K_2 = A_2^2/\left(2\sigma_2^2\right)$ (see chapter 3).
For a Rayleigh environment ($K_1 \text{and} K_2 << 1$), this correlation becomes:

$$\rho_{\text{pwr}} \approx |\rho_{\text{cpx}}|^2, \tag{7.19}$$

while for a strong Rician fading ($K_1 \text{and} K_2 >> 1$), this correlation can be approximated with:

$$\rho_{\text{pwr}} \approx \Re(\rho_{\text{cpx}})\frac{2\sqrt{K_1K_2}}{\sqrt{(2K_1+1)(2K_2+1)}}. \tag{7.20}$$

It results that the power correlation depends not only on the complex correlation but also on the K-factors of the two branches.

In Fig. 7.3 is presented the maximum power correlation when using the expression in (7.18). The minimum K-factor on a branch ($\min\{K_1, K_2\}$) is changed between −20 and 15 dB while the K-factor for the other branch is estimated from the power imbalance PI_K and changes between −20 and 20 dB. The complex correlation is 1, meaning that the signals on the two branches are perfectly correlated. It results that the power correlation is upper bounded (i.e., $\rho_{\text{pwr}} \leq \rho_{\text{cpx}}$), and decreases as the power imbalance due to K-factors increases.

Voltage Envelope correlation An analytical expression for the voltage envelope correlation as a function of complex correlation and K-factors is more complicated. In general one finds that the envelope correlation coefficient and power correlation coefficient are approximately equal [25]:

$$\rho_{\text{env}} \approx \rho_{\text{pwr}}. \tag{7.21}$$

This relation holds for the situation when the K-factors on the two branches are equal. With this hypothesis, the envelope correlation for two extreme cases become:

$$\rho_{\text{env}} \approx |\rho_{\text{cpx}}|^2, \tag{7.22}$$

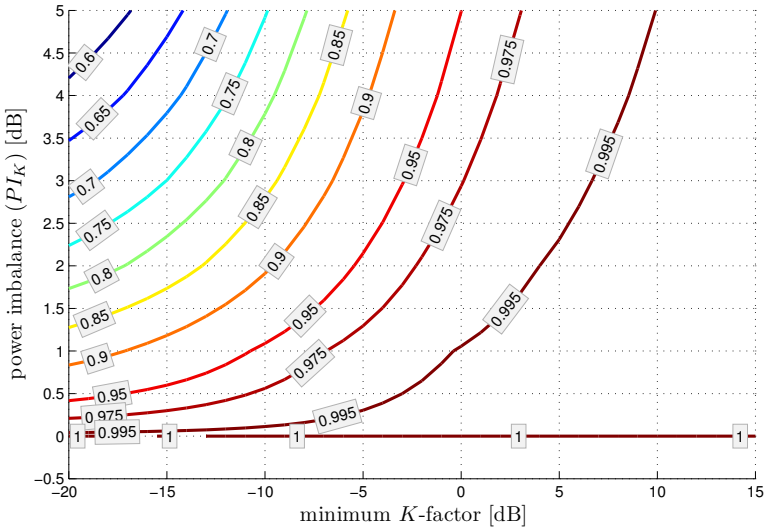

Figure 7.3: Maximum Power Correlation, ρ_{pwr}.

for a Rayleigh environment ($K_1 \text{and} K_2 << 1$), and:

$$\rho_{\text{env}} \approx \Re(\rho_{\text{cpx}}), \tag{7.23}$$

for an environment with a strong Rician fading ($K_1 \text{and} K_2 >> 1$). We do not have an analytical expression for the situation when the K-factors on the two branches are not identical, but the simulations have shown that, as for the power correlation, the envelope correlation is a function of complex correlation and K-factors on the two branches. Moreover the level of envelope correlation could be lower even by 50% than the power correlation for the same complex correlation and K-factors ($\rho_{\text{env}} \leq \rho_{\text{pwr}}$).

7.7 Results

In this section we present several Monte Carlo simulations and measurements in reverberation chamber in order to test different scenarios, and comparisons between them are performed.

7.7.1 Simulations

The simulations can be done varying several parameters: K-factors, complex correlations, antenna efficiencies. From section 7.6, the power imbalance may depend on antenna efficiencies, stirred powers and K-factors. As we want to analyze the influences of the different unstirred powers received by antenna branches for different separation distances between them so we chose to vary only the K-factor of a branch, the power imbalance due to K-factors (PI_K) and the complex correlation between the signals received by the two antennas. To test the influence of these parameters we make several Monte Carlo simulations for which the sample size is 10 000 and the number of trials is 50. The minimum K-factor of an antenna branch changes between −20 and 15 dB and the power imbalance PI_K changes between 0 and 5 dB (which corresponds to a variation of the K-factor on the second branch between −20 and 20 dB). The complex correlation changes between 0 and 1, Fig. 7.4. Several algorithms which enable

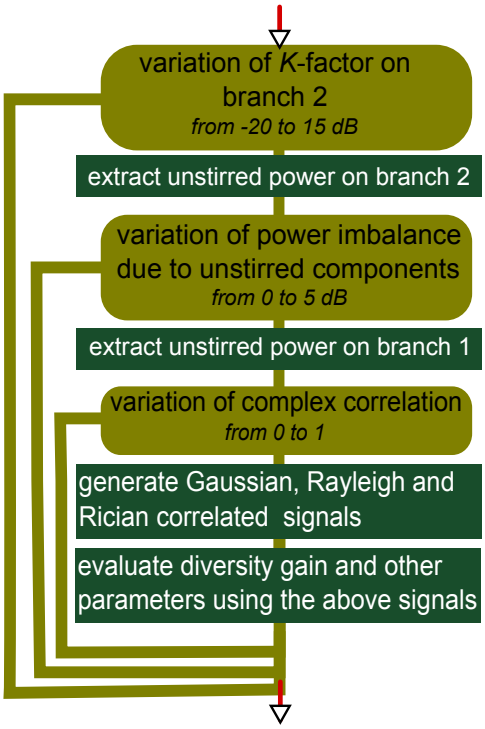

Figure 7.4: Stages of simulation algorithm.

to generate Gaussian and Rayleigh correlated realizations are found in literature [26–30]. We have tested two methods [26, 29]. Both methods generate Rayleigh correlated realizations with a desired correlation between them. The method in [26] is simple but then it requests a complicated mathematical inversion of a function in order to obtain the corresponding Rayleigh distributions. The method presented in [29], even though it is more difficult to implement, once implemented easily provides the requested distributions. Moreover, compared with the method in [26] the desired distributions in the latter method can be requested not only for the cross-correlation at zeroth lag but also for any other lag (delay between realizations). Both tested methods [26, 29] cannot be used to generate output correlated samples with a desired Rician envelope or power correlation in the presence of unstirred components. To generate two correlated signals, r_1 and r_2, whose sample size is N, the algorithm in [29] has the following steps:

- choosing the maximum correlation lag L $(0 \leq L \leq N-1)$;
- creating cross-correlation ρ_{r_1,r_2} and autocorrelation ρ_{r_1,r_1}, ρ_{r_2,r_2} vectors between the two channels until a lag L;
- constructing the covariance matrix at lag l:

$$\rho[l] = \begin{bmatrix} \rho_{r_1,r_1}[l] & \rho_{r_1,r_2}[l] \\ \rho_{r_2,r_1}[l] & \rho_{r_2,r_2}[l] \end{bmatrix}. \tag{7.24}$$

- constructing the covariance matrix $\boldsymbol{R}$ for any lag and adding a small bias ϵ so all the

eigenvalues are positive:

$$\boldsymbol{R} = \begin{bmatrix} \rho[0] & \rho[-1] & \cdots & \rho[-L+1] \\ \rho[1] & \rho[0] & \cdots & \rho[-L+2] \\ \cdots & \cdots & \cdots & \cdots \\ \rho[L-1] & \rho[L-2] & \cdots & \rho[0] \end{bmatrix} + \epsilon \boldsymbol{I}_{L\times L}; \tag{7.25}$$

- constructing $\boldsymbol{V}$ matrix:

$$\boldsymbol{V} = \begin{bmatrix} \rho[1] \\ \rho[2] \\ \cdots \\ \rho[L] \end{bmatrix}; \tag{7.26}$$

- computing AR coefficients:

$$\boldsymbol{A} = -\boldsymbol{R}^{-1}\boldsymbol{V}, \tag{7.27}$$

where matrix $\boldsymbol{A}$ is described as:

$$\boldsymbol{A} = \begin{bmatrix} \alpha[1] \\ \alpha[2] \\ \cdots \\ \alpha[L] \end{bmatrix}, \tag{7.28}$$

and

$$\alpha[k] = \begin{bmatrix} a_{11}[k] & a_{12}[k] \\ a_{21}[k] & a_{22}[k] \end{bmatrix}, \quad k = 1, 2, 3, \cdots L; \tag{7.29}$$

- generating the covariance matrix of the driving noise:

$$\boldsymbol{Q} = \rho[0] + \epsilon \boldsymbol{I}_{2\times 2} + \boldsymbol{V}\boldsymbol{A}; \tag{7.30}$$

- extracting the standard deviation matrix $\boldsymbol{G}$ from the product $\boldsymbol{G}\boldsymbol{G}^H = \boldsymbol{Q}$ using a Cholesky decomposition;

- generating the driving noise $\boldsymbol{w}$ based on a complex Gaussian random vector $\boldsymbol{Z}$ having mean 0 and variance 1:

$$\boldsymbol{w} = \boldsymbol{G}\boldsymbol{Z}; \tag{7.31}$$

- extracting the correlated complex random signals (denoted with $\widetilde{r}_1$ and $\widetilde{r}_2$) from the filter:

$$\begin{bmatrix} \widetilde{r}_1[N] \\ \widetilde{r}_2[N] \end{bmatrix} = -\sum_{l=1}^{L} \alpha[l] \begin{bmatrix} \widetilde{r}_1[N-l] \\ \widetilde{r}_2[N-l] \end{bmatrix} + w, \tag{7.32}$$

- modifying the variances and expected values of the $\widetilde{r}_1$ and $\widetilde{r}_2$, and including antennas efficiencies and then extracting their absolute values r_1 and r_2.

To apply the above algorithm we use an auto-regressive filter (AR) whose size is 80. For these first simulations both antennas are considered to have 100% efficiency. These simulations can be also done changing the efficiencies independently (and so the power imbalance due to antenna efficiency) or the power due to stirred components (and so the power imbalance due to these components). It results that we generate 8316 configurations (i.e., different K-factors, power imbalances and complex correlations) each one having 10 000 realizations and 50 trials. The time duration to simulate all the configurations is around $6-7$ h. From these simulations we obtain a theoretical estimated expected value of the effective diversity gain when using different techniques to combine the signals. We recall that the diversity gain using "equal gain" is smaller than the one using "selection combining" which in turn is smaller than the levels given by the technique using "maximal-ratio".

A first result for a particular case is the maximal ratio diversity gain when the complex correlation between the signals on antenna branches is 0, and both, the minimum K-factor and power imbalance, change, Fig. 7.5. This situation may correspond to the case when antennas have different polarizations and located far away from each other. When the minimum K-factor is less than a limit value ($K < -5$ dB) the diversity gain depends more on the power imbalance between branches due to unstirred components. With the increase of the minimum K-factor, diversity gain depends both on the power imbalance and the value of K-factor. This tendency is the same for all three techniques. A particular result is for the equal-gain diversity, Fig. 7.5(c), when for values of $K > 2.5$ dB, depending on the power imbalance, due to uncertainties (even though we have used a number of 10 000 realizations) the estimated diversity gain becomes negative.

Another selected example is for the case when there is no power imbalance due to K-factors, $PI_K = 0$ dB. In a real environment, this may be happen when both antennas receive the same unstirred power. The correlation may change when modifying the separation distance between antennas while the K-factor by favoring unstirred components between the transmitter and receiver. In this simulation K-factors change in the same manner for both antennas, Fig. 7.6 ((a), (b) and (c)). From this analysis it results that, depending on the level of diversity gain, as the K-factors remain low ($K < 0$ dB) the complex correlation has a higher impact than the K-factor (which corresponds to the emergence of unstirred components at reception antennas). With the increase of K-factor ($K > 0$ dB), the complex correlation between branches has a lower influence compared with the level of K-factor.

A third selected example is presented in Fig. 7.7. It is for the situation when the K-factor of one antenna is very low (-20 dB) while for the other antenna the K increases. As a result, the power imbalance PI_K increases too. This may be the case when the two antennas (in antenna array) are in a cross polarized configuration and only one antenna has the same polarization as the transmitter. In this situation the unstirred energy arriving at one antenna may be much higher than the one arriving on the other antenna even in the presence of depolarization. Practically one antenna sees a Rayleigh channel while the other a Rician channel. For this particular example (i.e., a K-factor on a branch of -20 dB and another which changes from -20 and 3.5 dB), for values of complex correlation lower than 0.75 the power imbalance PI_K has a higher influence on the diversity gain compared with the complex correlation. It may have a higher impact on the result only when the correlation becomes higher.

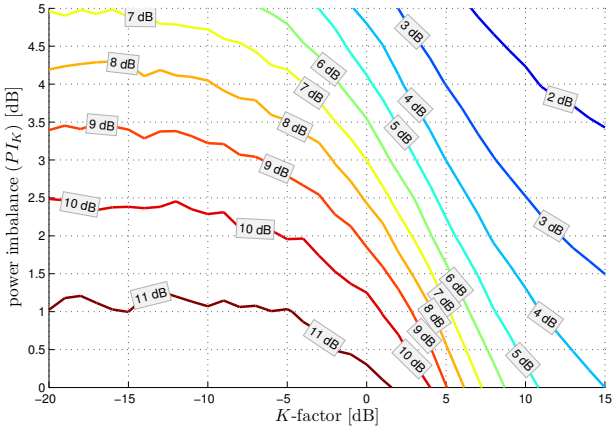

(a)

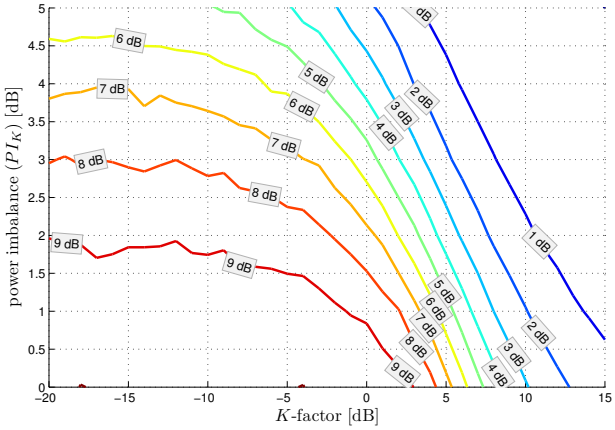

(b)

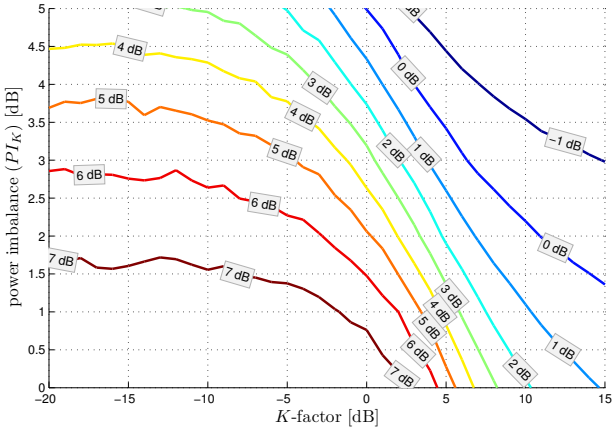

(c)

Figure 7.5: Diversity gain when $\rho_{\text{cpx}} = 0$:
(a) Maximal-Ratio method, (b) Selection-Combining method, (c) Equal-Gain method.

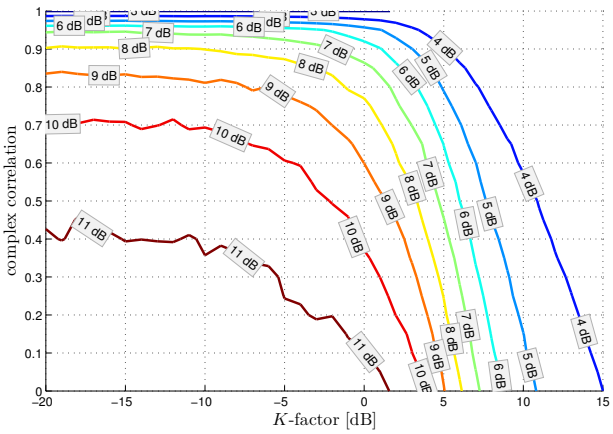

(a)

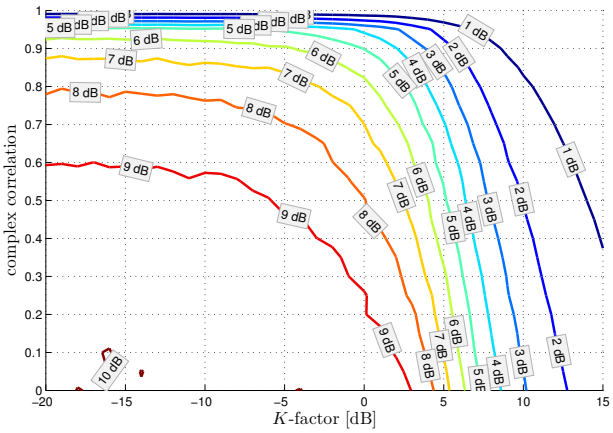

(b)

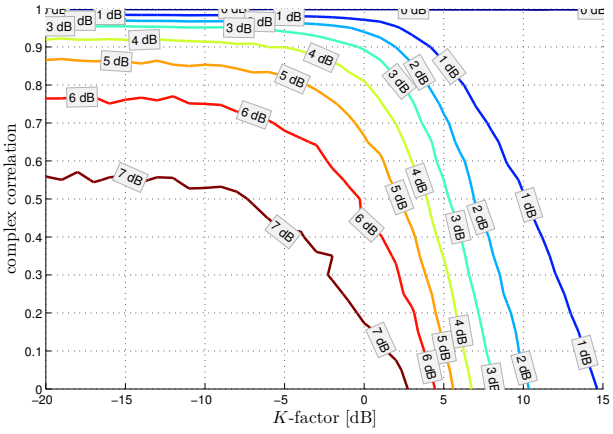

(c)

Figure 7.6: Diversity gain for $PI_K = 0\,\mathrm{dB}$:
(a) Maximal-Ratio method, (b) Selection-Combining method, (c) Equal-Gain method.

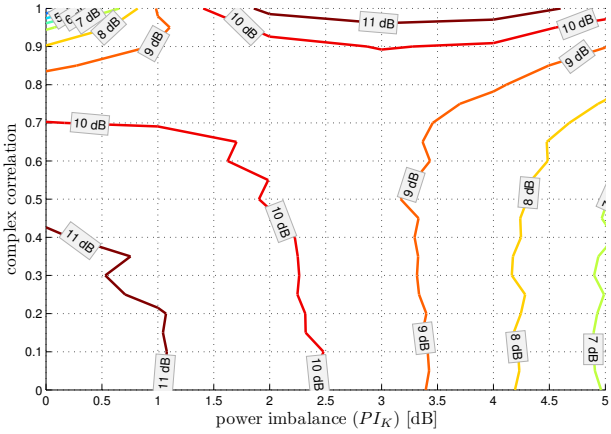

(a)

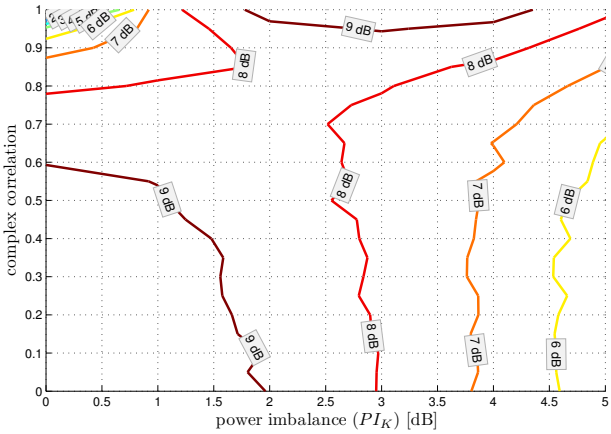

(b)

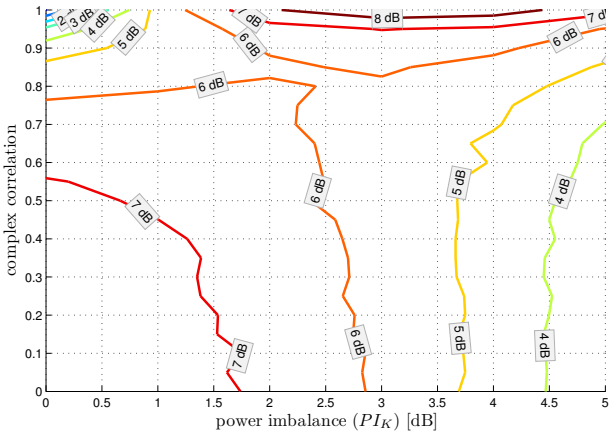

(c)

Figure 7.7: Diversity gain when the minimum K-factor of one antenna is −20 dB: (a) Maximal-Ratio method, (b) Selection-Combining method, (c) Equal-Gain method.

7.7.2 Measurements

To validate the above theory we make several measurements in reverberation chamber and in near field chamber (NFC). One horn antenna (Lindgren, Model 3115) is used as a transmitter while two directive printed dipole antennas with reflectors [31] are used as receivers. Both the dipoles and the horn antennas have directive patterns. The horn antenna is an ultra broadband antenna whose frequency range is between 750 MHz and 18 GHz while for dipole antennas the frequency bandwidth is much smaller, Fig. 7.11. The frequency is changed between 2.7 – 3.1 GHz. In order to have independent frequencies we use a frequency step of 200 kHz, which for the measurement bandwidth it results a number of 2000 discrete frequencies. The stirrer is used in stepped-mode and 100 independent measurements are performed [32]. For a supplementary control of the energy in the chamber 4 identical absorbers were used. The transmitter and receiver heights are approximately 1.5 m above the floor. We consider the noise levels as identical for both receiving dipole antennas.
The transmitting and receiving antennas are placed in a non-line-of-sight and later in a line-of sight configuration, Fig. 7.8. For the non-line-of-sight situation, Fig. 7.8(a), the horn antenna

(a) (b)

Figure 7.8: Non-Line-of-Sight (a), and Line-of-Sight (b) configuration.

has a 45 ° polarization while the dipole antennas have a vertical polarization and are directed to the stirrer. In order to evaluate different diversity techniques: spatial, pattern, polarization and mixed pattern and polarization we install dipole antennas on the test bench in four different configurations. The spatial diversity configuration is presented in Fig. 7.9(a). The distance d between dipole antennas varies with a non linear step (8, 10, 15, 20, 25, 30, 40, 60, 80 and 100 mm) which for a frequency of 2.9 GHz (i.e., the central frequency of dipole antennas) it corresponds to a variation of wavelength between 0.08λ and 1λ. Three other configurations are tested only when the dipole antennas are separated by 10 cm (i.e., 1λ at 2.9 GHz), Fig. 7.9 ((b), (c), (d)). In the line-of-sight configuration, Fig. 7.8(b), all antennas have the same vertical polarization and the distance between antenna array and horn antenna changes with a step of 15 cm (i.e., 50, 75, 100, 115, 125, 150, 175 and 200 cm).
The complex voltage transfer functions of the propagation channel are measured with a 4-port VNA. It means that during measurements all the antennas are connected on a matched load (i.e., the 50 Ω of the VNA ports), and all the measurements are made sequentially. The

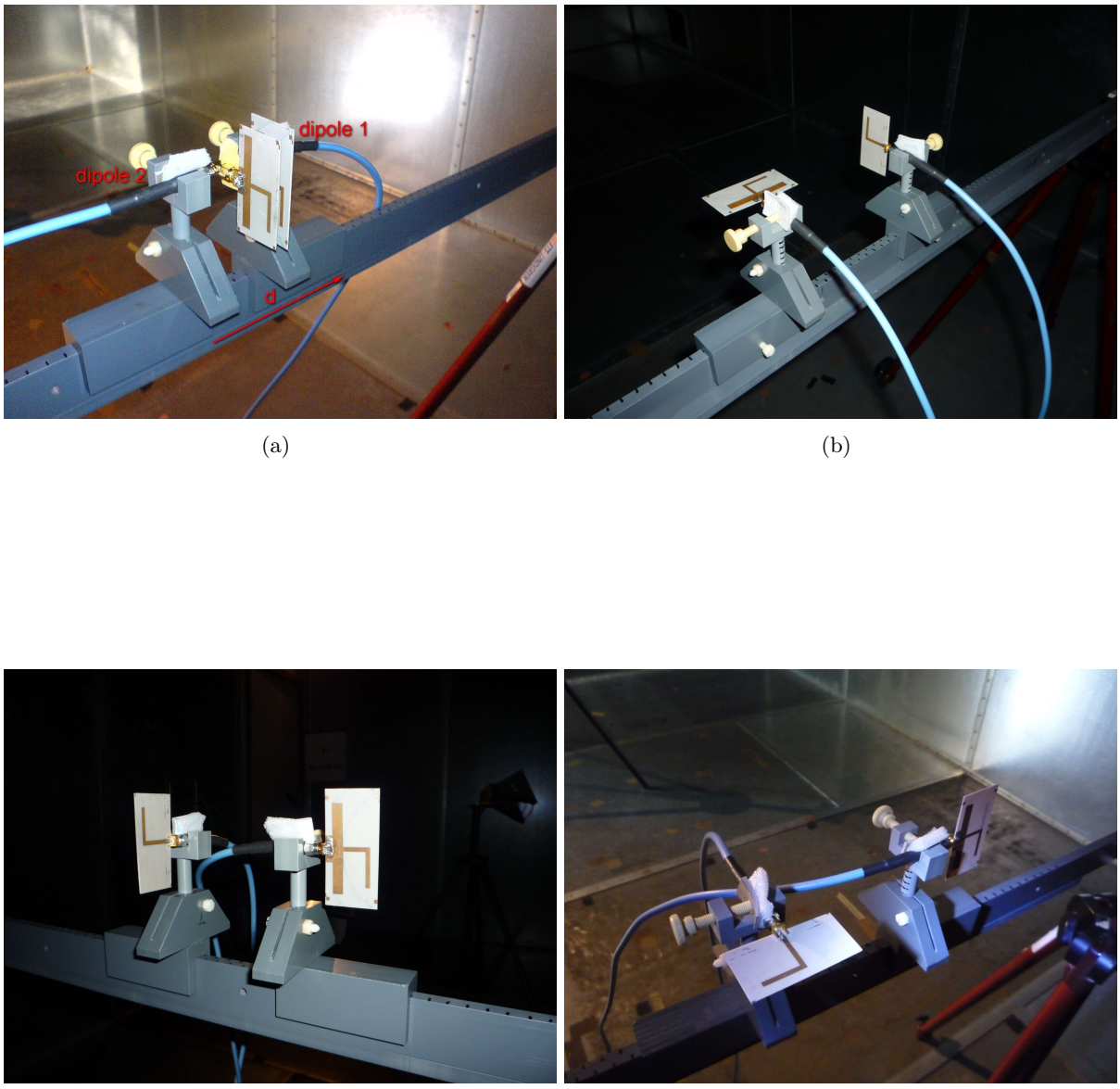

(a) (b)

(c) (d)

Figure 7.9: Non-line-of-sight configurations: spatial diversity (a), polarization diversity (b), pattern diversity (c), pattern and polarization diversity (d).

complex voltage transfer function between x and y ports of the VNA is defined as:

$$H_{xy} = \frac{S_{xy}}{\sqrt{1-|\overline{S_{xx}}|^2}\sqrt{1-|\overline{S_{yy}}|^2}}, \tag{7.33}$$

We measure three functions of this kind: H_{12}, H_{13} and H_{23} (i.e., two transfer functions from horn antennas to dipole antennas and one transfer function from one dipole to the other dipole antenna). As presented before, the number of independent experiments for one complete stirrer position is around 100. To have a better estimation of the diversity gain we chose to increase the number of experiments by mixing samples with different frequencies. In this way, the sample size is increased from 100 to 10 000 experiments when mixing data for 100 frequencies (representing a bandwidth of 20 MHz). This approach does not affect the stirred components except that when unstirred components exist a higher attention must be paid [33]. This is due to the fact that the phase of the unstirred components changes linearly with frequency and it depends on the traveled distance. For a better explanation, we consider the simple situation when we have only the direct unstirred component. The phase of the complex rectangular components of the unstirred component which changes with the distance and frequency is expressed as:

$$\theta(L, f) = 2\pi\frac{Lf}{c}, \tag{7.34}$$

where

- L is the propagation distance;
- f is the frequency of the signal;
- c is the speed of light.

The unstirred components are extracted by averaging the complex voltage transfer function H_{xy} over the stirrer positions [34]. When making the average in frequency domain the averaged phases $E[\cos\theta]^2$ or $E[\sin\theta]^2$ may go to zero. In these conditions, due to the averaging in a frequency range $[f_1, f_2]$ the unitary envelope of the direct unstirred component is attenuated with:

$$\begin{aligned}\sqrt{E[\cos\theta]^2 + E[\sin\theta]^2} = &\sqrt{\left[\frac{c}{\pi L(f_2-f_1)}\sin\frac{L\pi(f_2-f_1)}{c}\cos\left(\frac{L\pi}{c}(f_1+f_2)\right)\right]^2 \cdots} \\ &\overline{\cdots + \left[\frac{c}{\pi L(f_2-f_1)}\sin\frac{L\pi(f_2-f_1)}{c}\sin\left(\frac{L\pi}{c}(f_1+f_2)\right)\right]^2} \\ = &\frac{c}{\pi L(f_2-f_1)}\sin\frac{L\pi(f_2-f_1)}{c},\end{aligned} \tag{7.35}$$

and has a phase shift equal with:

$$\theta = \arctan\frac{\frac{c}{\pi L(f_2-f_1)}\sin\frac{L\pi(f_2-f_1)}{c}\sin\left(\frac{L\pi}{c}(f_1+f_2)\right)}{\frac{c}{\pi L(f_2-f_1)}\sin\frac{L\pi(f_2-f_1)}{c}\cos\left(\frac{L\pi}{c}(f_1+f_2)\right)} = \frac{L\pi}{c}(f_1+f_2). \tag{7.36}$$

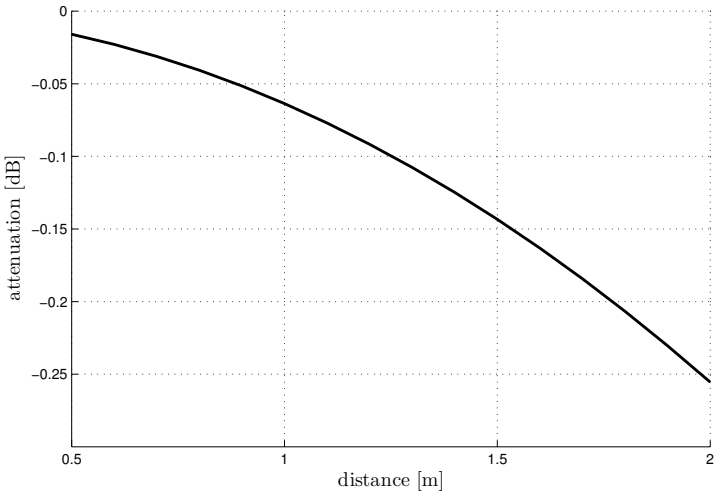

Figure 7.10: Line-of-sight attenuation due to stirring frequencies.

From (7.35) the attenuation of the envelope of unstirred component with the propagation distance between 50 and 200 cm for a stirring bandwidth of 20 MHz is presented in Fig. 7.10. For a maximum distance between horn and antenna array of 2 m the maximum attenuation of the direct unstirred power is around 0.25 dB (which can be later corrected). Also, with the increase of the distance between horn and dipole antennas secondary unstirred components reflected by walls but not by the stirrer may appear. As for the direct unstirred component, their phases change too with the frequency and distance. Because the traveled distance of these components is longer, their attenuation is much higher when averaging in frequency domain. It results that their influences to the total unstirred energy decrease even more. So, the limit presented in Fig. 7.10 is a minimum attenuation of the total unstirred power due to stirring frequencies (which increases with the distance). In other words, we can see the frequency averaging as a way to reduce the secondary unstirred components whereas the attenuation of the direct unstirred component is correctable.

Antennas mismatches, S_{11}, S_{22}, and S_{33} are estimated directly from measurements in reverberation chamber(by averaging measured mismatch parameters over 100 stirrer positions) and validated with measurements in near field chamber. Fig. 7.11 presents the mismatch for dipole antenna in the bandwidth 2.7 – 3.2 GHz, separated by a distance of 10 cm for which there is a small mutual coupling between them. Even though the two dipoles are supposed to be the same, there is a small shift of minimum of mismatch between them.

The efficiencies of antennas are estimated using the method presented in [35]. The main advantage of this method is that the efficiency can be extracted directly from the measured transfer functions between antennas without knowing any reference efficiency. The main disadvantage is the use of several estimated parameters in time and in frequency domains which may bias the result. For example, beside the complex voltage transfer function of the channel it is also necessary to estimate the time decay of the chamber. In our measurements, the decay constant is estimated in subbandwidths of 150 MHz from the averaged power delay profile over 100 experiments. Our tests show that a smaller bandwidth (i.e., until 50 MHz) will only increase the confidence interval of this parameter. Fig. 7.12(a) and 7.12(b) present respectively the radiation efficiencies and the total efficiencies averaged over a frequency window of

50 MHz of the horn and two dipole antennas when the separation distance between them is 10 cm. Due to estimation uncertainties and high values of radiation efficiencies of the dipole antennas in the tested bandwidth, we have obtained values higher than 100%. As the estimated values of efficiencies have to be used in our calculus later we have limited the obtained values to 100%. Beside antenna mismatches and efficiencies, which change with the distance between dipoles, we evaluate several other parameters for both line-of-sight and non-line-of sight configurations. The K-factor for a non-line-of-sight configuration between the horn and the dipole antennas as well the one between dipole antennas when the distance between them is 10 cm is presented in 7.13. This parameter is computed from 10 000 realizations obtained by mixing samples with different frequencies. As presented before this will slightly reduce the direct unstirred component, Fig. 7.10, while secondary unstirred components will be reduced

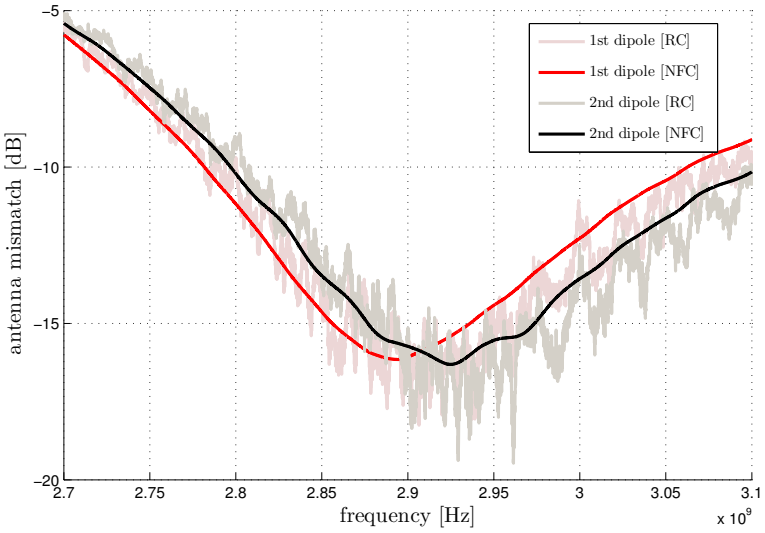

Figure 7.11: Mismatches of dipole antennas separated by a distance of 10 cm.

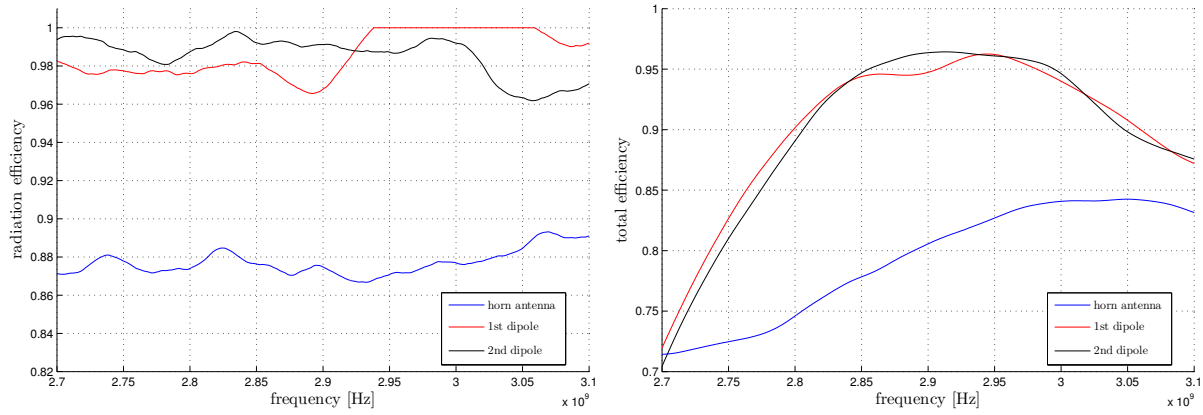

(a) (b)

Figure 7.12: Radiation efficiency (a) and Total Efficiency (b) of two dipole antennas when the distance between them is 10 cm measured in reverberation chamber.

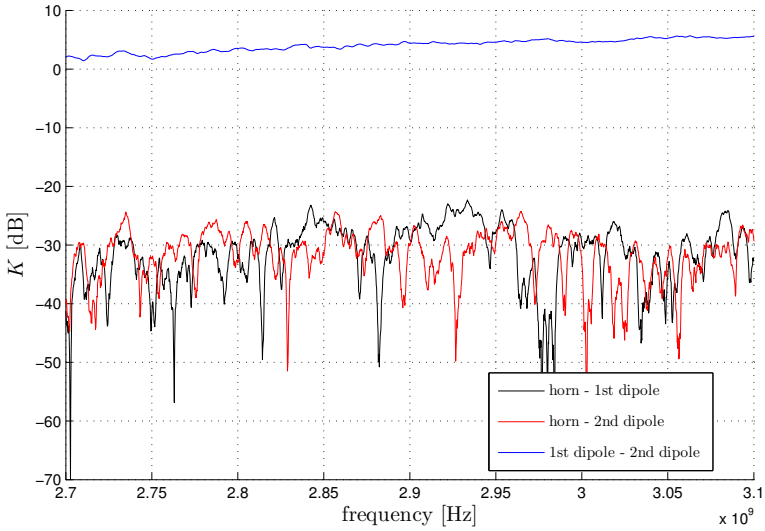

Figure 7.13: K-factor for the non-line-of-sight when the dipoles are separated by 10 cm.

even more (due to longer propagation distances). It means that the value of the estimated K-factor is below the real value (this error increasing with the increase of the distance between antennas due to emergence of secondary unstirred components). We accept this compromise as for the diversity gain we want to characterize the parameters of a distribution defined by those 10 000 experiments and the maximum distance between antennas is 2 m (i.e., resulting a small estimation error of the total power of unstirred components).

Analyzing the received power, Fig. 7.14 presents the mean received power by each antenna and the mean power at the output of diversity combiner when using maximal-ratio combining, selection-combining and equal-gain combining. As we can see from this figure, it is possible to have a lower average power at the output of combiner compared with the power of input signals (i.e., for the equal-gain combiner). The estimated power imbalance between branches with the frequency is not presented as it is very low.

Having computed the CDFs at the input of the combiner (with both keeping and removing the measured antenna efficiencies) and at the output of the combiner (when using different combination techniques), we estimate the apparent and the effective diversity gain. In Fig. 7.15 are presented diversity gains plotted in dB at a 1% probability level when using different techniques and when the dipole antennas are 10 cm apart. This situation corresponds to a low mutual coupling, a low total power imbalance and a low correlation between branches. As expected, the maximal-ratio combining offers the best improvement compared with the other techniques. All the other three configurations in Fig. 7.9 ((b), (c), (d)) give results in the same ranges. This is due to the fact the separation distance between antennas is high enough to have a low mutual coupling, and because there is no line-of-sight and the antennas have almost the same efficiency the power imbalance is quite reduced.

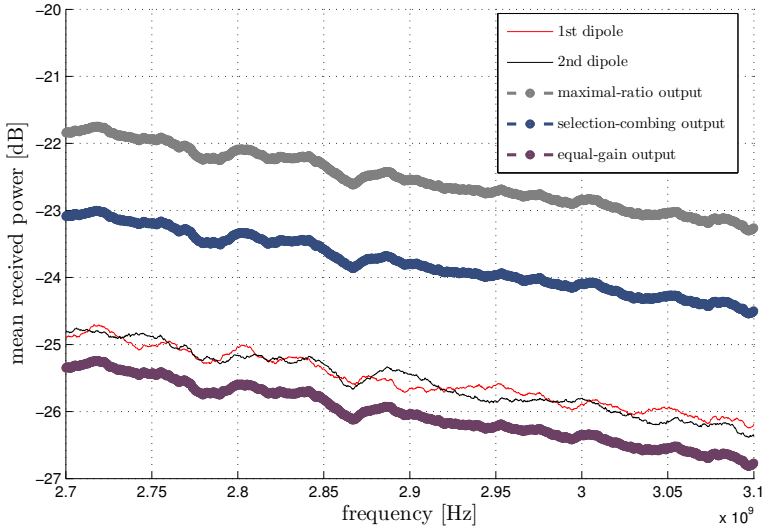

Figure 7.14: Average Received Power of two dipole antennas when the distance between them is 10 cm.

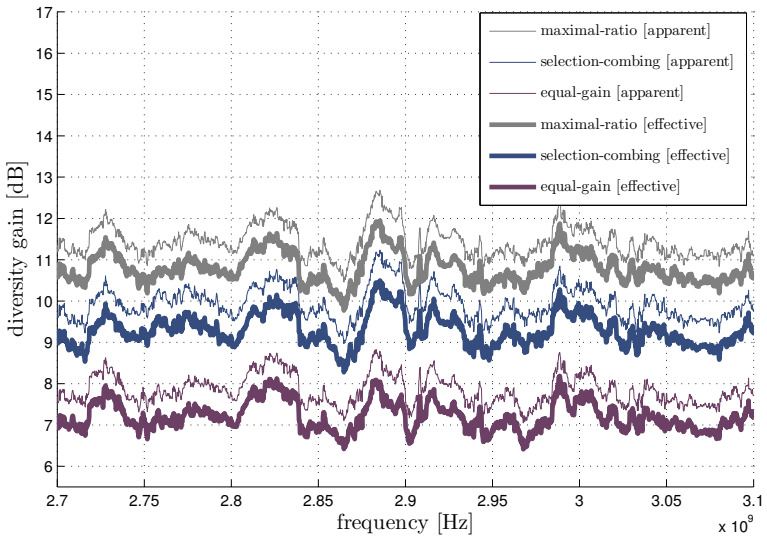

Figure 7.15: Diversity Gain for several diversity techniques for a distance between antennas of 10 cm estimated at 1 % level of reliability.

7.7.2.1 Variation with antenna spacing distance for the non-line-of-sight configuration

Until now we have shown some results when the dipole antennas have a small mutual coupling between each other (i.e., the separation distance between them is almost $1\,\lambda$). Now, we analyze the situation when the distance between antennas is reduced, which mainly change the antenna coupling (i.e., the mismatch and efficiency) and the correlation level. A first measured parameter is antenna mismatch, Fig. 7.16. We present the mismatch with the variation of the separation distance when the signals are measured in near-field chamber (the results measured in RC lead to the same conclusions but with a higher fluctuation level). The oscillations of the mismatches are due to pattern correlation of antennas [36, 37].

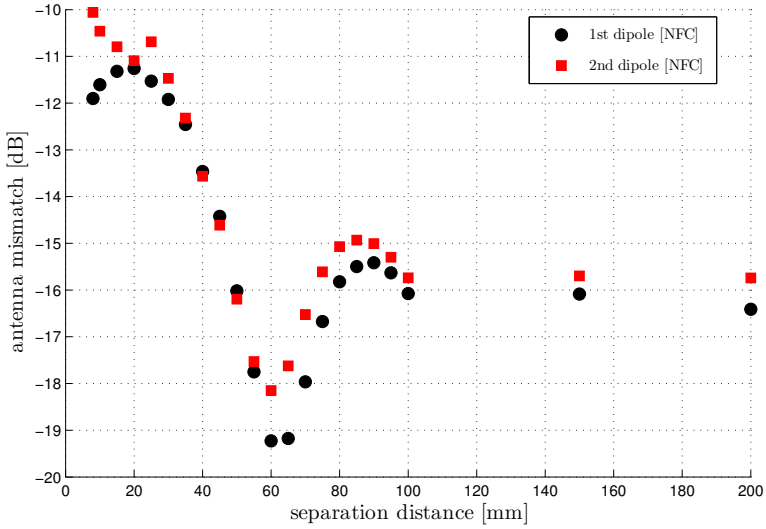

Figure 7.16: Dipole antenna mismatches with the separation distance between them at a frequency of 2.9 GHz.

As the distance between dipoles decreases the mutual coupling increases and the radiation efficiency, Fig. 7.17(a), and the total efficiency, Fig. 7.17(b), decrease. The fluctuations presented in 7.16 are not visible in the total efficiency, therefore the mismatch plays a smaller role in the total efficiency compared with the radiation efficiency.

Analyzing the power received by the two dipoles, Fig. 7.18(a) presents the average power while in Fig. 7.18(b) is presented the power imbalance. Due to an increase of losses, the average power decreases in the same way as the antenna efficiency. Moreover, due to the fact that for both antennas the efficiency is almost the same and since we are in a non-line-of-sight configuration (i.e., very small unstirred power and almost identical stirred power), the power imbalance is very small ($\leq 0.25\,\mathrm{dB}$)

Another factor of interest is the signal correlation between branches. We present both complex Fig. 7.19(a) and envelope/power correlation in Fig. 7.19(b). Also, these results are compared with the theoretical ones estimated with equations in (7.12), (7.13) and (7.14), respectively using (7.18) to estimate $\rho_{\mathrm{pwr,\,omni}}$, $\rho_{\mathrm{pwr,\,iso}}$ and $\rho_{\mathrm{pwr,\,E_Z}}$. None of the chosen theoretical correlations follow the measured values. First, because the antenna patterns of the dipole antennas are not the same as those used in these models. The antennas used in these experiments are very different compared to the ideal receivers in the models presented in 7.6.4.

Second, for the smallest distance between antennas (i.e., 8 mm) the maximum measured complex correlation is only 0.75 (and 0.57 for the envelope/power correlation). An explanation for these values may be the distortion of antenna patterns with regard to the free-space pattern due to the proximity of an antenna to the other. For short separation distances between antennas, their patterns turn to different directions and the incoming multipath components are weighted differently for each antenna. It results that the total signals received by the two antennas become less correlated than expected. It also means that even though we want to measure the influence of only the separation distance between antennas, indirectly, for these types of dipole antennas and for short distances between them our space diversity is also influenced by a pattern diversity.

The final set of results of this analysis are represented by the diversity gain. Fig. 7.20 presents both apparent and effective diversity gains for three diversity combining techniques: maximal-ratio, equal-gain and selection combining. Due to the decrease of antenna radiation efficiency (Fig. 7.17) and increase of correlation(Fig. 7.19) below a distance of 3 cm the diversity gains start to decrease. For the minimum distance between dipole antennas (i.e., 8 mm), the effective diversity gains decrease as low as: 6.8 dB (from a maximum value of 10.65 dB) for maximal-ratio, 5.3 dB (from a maximum value of 9.3 dB) for selection-combining and 3.12 dB (from a maximum value of 6.95 dB) for equal-gain combining.

7.7.2.2 Influence of unstirred components

As already discussed, in 7.6.4 and in 7.7.1, the unstirred components influence both the envelope/power correlation and the diversity gain. The effects are even more important if there is a power imbalance due to these components. We control the level of unstirred components by changing the distance between the horn and the antenna array. Because the separation distance between dipole antennas remains constant (i.e., 10 cm), the total efficiencies of dipole antennas do not change during measurements. The complex correlation between the measured signals by these antennas remains constant with the variation of the distance and it has a low value (i.e., the separation distance between dipoles is high enough to receive different

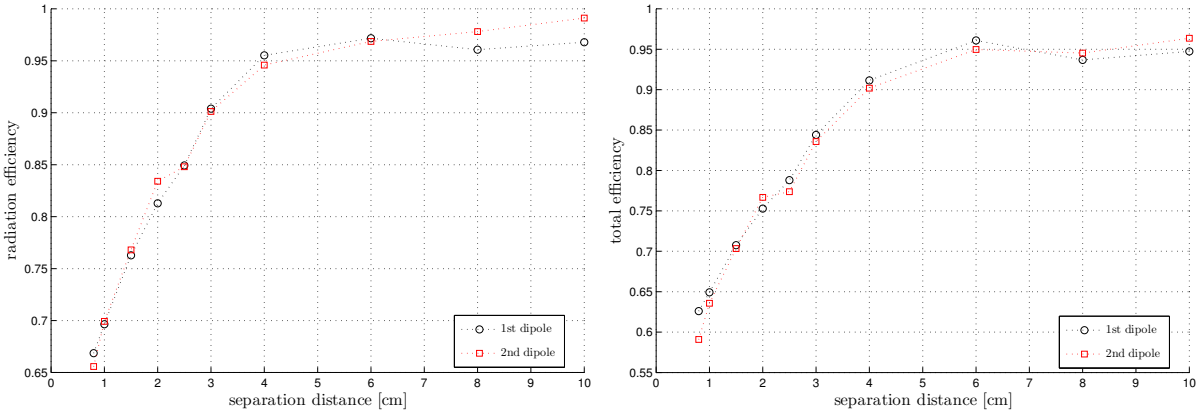

(a) (b)

Figure 7.17: Radiation Efficiency (a) and Total Efficiency (b) with the distance between dipole antennas at 2.9 GHz.

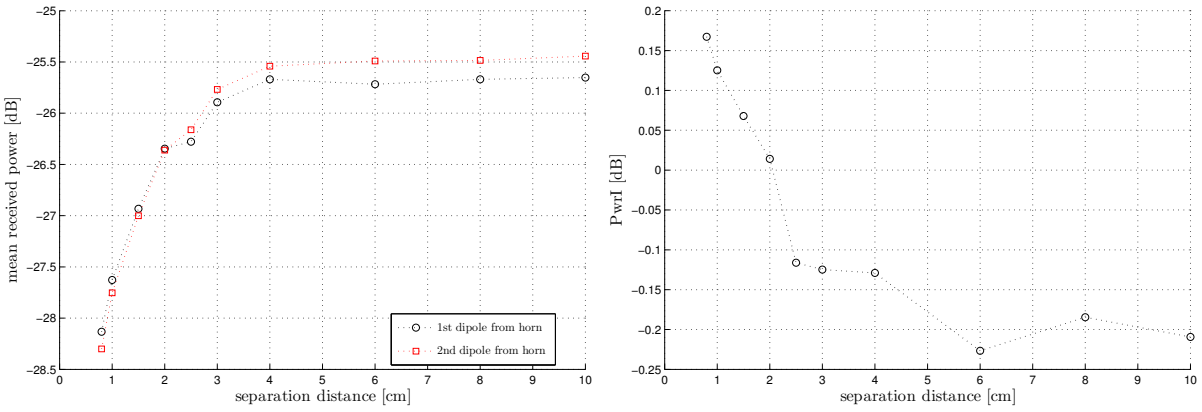

(a) (b)

Figure 7.18: Average Received Power (a) and Power Imbalance between the two antenna branches (b) with the distance between dipole antennas at 2.9 GHz.

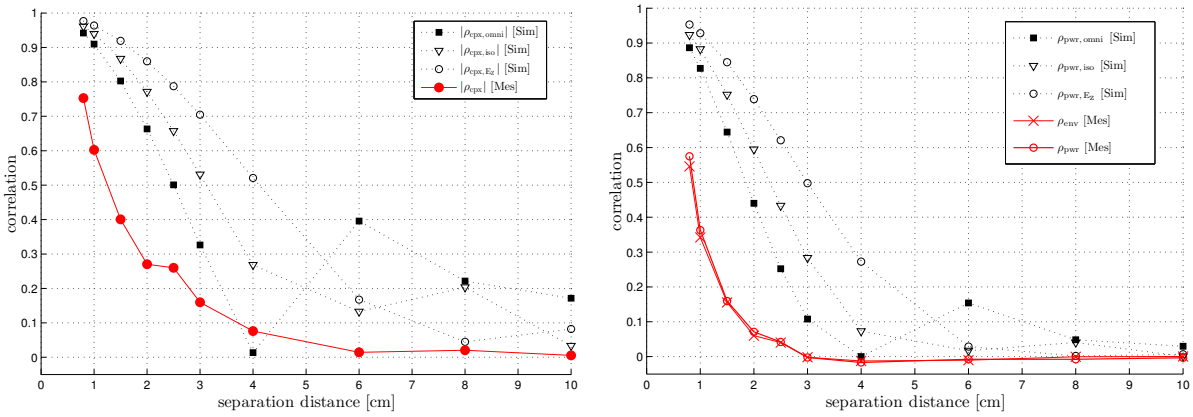

(a) (b)

Figure 7.19: Complex (a), and envelope/power correlations (b) between the signals measured on dipole antennas for a frequency of 2.9 GHz with the separation distance. Comparisons with the correlations provided by two models are provided.

propagation channels between each dipole and horn antenna). From the analysis in 7.6.4 only the envelope and power correlations are affected by the presence of unstirred components, and they decrease even more when the powers of unstirred components arriving on the two antennas are not equal (which corresponds to a higher power imbalance), Fig. 7.21.

Next, we analyze in Fig. 7.22, the average received power and power imbalance, (a) and (b). We do not expect a high imbalance due to the fact that the dipoles are directed to horn antenna in the same manner, the distances from each dipole to the horn antenna are small, and at 2.9 GHz this antenna has an horizontal an vertical half power beamwidth of 45 °. The maximum detected power imbalance is −1 dB.

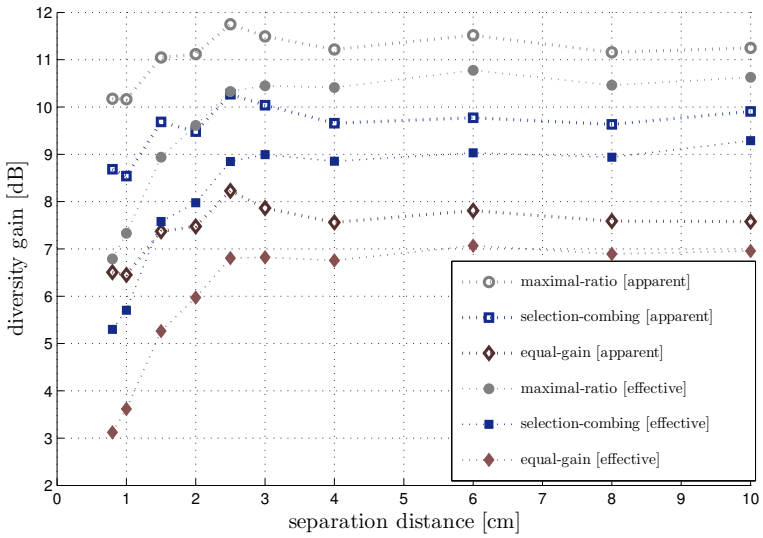

Figure 7.20: Diversity Gain for several diversity techniques with the separation distance between antennas, at 2.9 GHz.

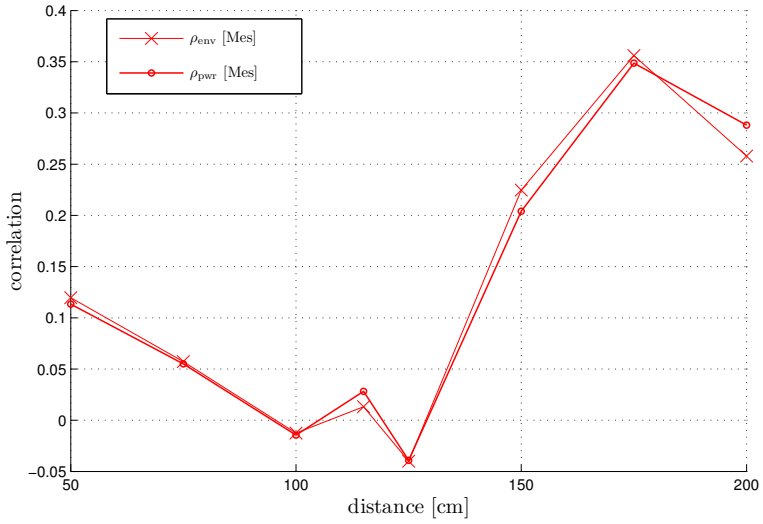

Figure 7.21: Envelope and Power correlation between antenna branches when changing the distance between the horn and dipole array.

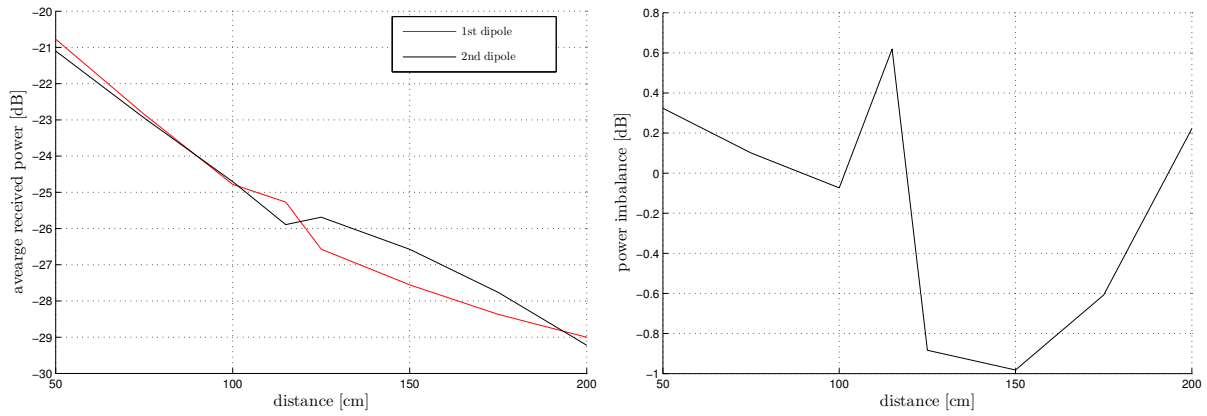

(a) (b)

Figure 7.22: Average Received Power (a) and Power Imbalance between the two branches (b) of two dipole antennas with the variation of the distance between horn and dipole antennas at 2.9 GHz.

The K-factor is presented in Fig. 7.23. As the distance increases, the power of unstirred components decreases, and so the K-factor between the horn and dipole antennas (between 11 dB and $-1, -3$ dB depending on dipole antenna).

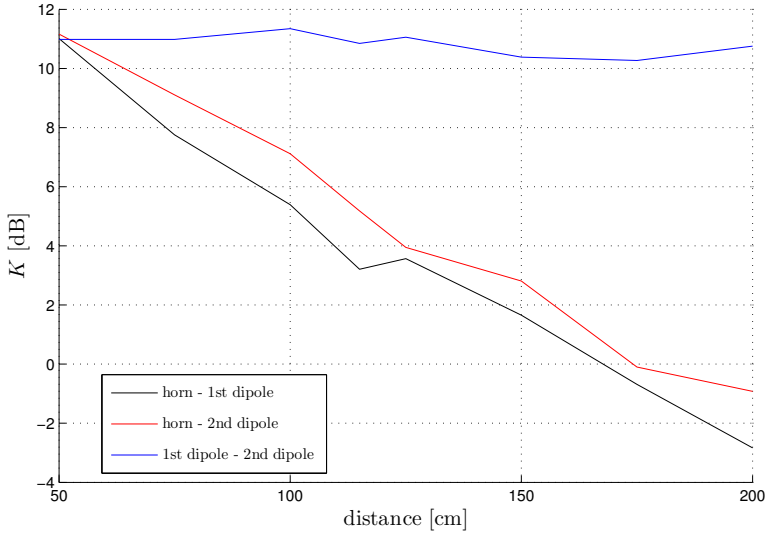

Figure 7.23: K-factor for the line-of-sight configuration with the distance between horn and antenna array.

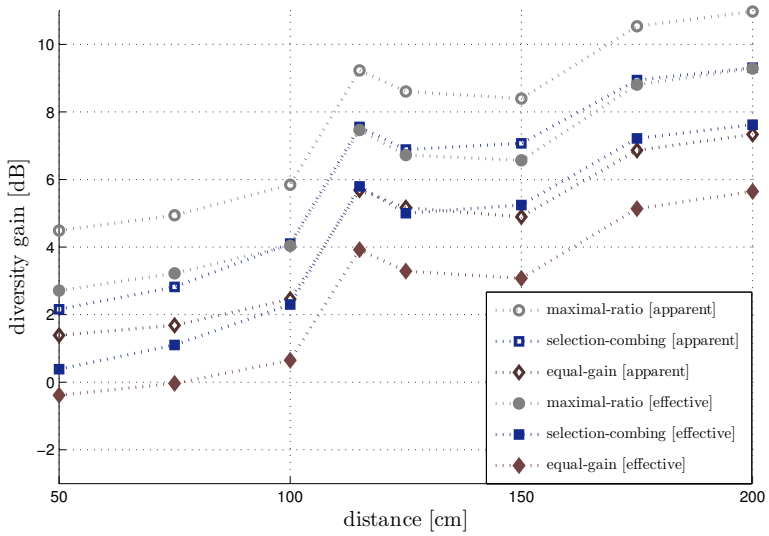

Figure 7.24: Diversity Gain for several diversity techniques with the distance between horn and dipole antennas at 2.9 GHz.

In Fig. 7.24 is presented the diversity gain with the variation of the distance between horn and dipole antennas which mainly affects the unstirred power. As it is expected, with the emergence of unstirred components the diversity gains decrease. We can notice a negative diversity gain for the equal-gain technique. This is due to the definition of effective diversity gain. For that particular distance the unstirred power drops so much the diversity gain that when the dipole antenna efficiency is removed (which does not change with the distance between horn and antenna array) the resulted value (in dB) becomes negative.

7.7.3 Diversity gain in simulations and measurements

Until now we have presented what are the maximum limits of diversity gains depending on different factors in section 7.7.1, and some measurements results in section 7.7.2. Here we compare the results of diversity gain obtained from measurements, Fig. 7.20 and 7.24, with those obtained from statistical simulations (based on the method used in section 7.7.1). The input parameters for simulations: the unstirred and stirred components power, the complex correlation and the radiation efficiencies, are evaluated from measurements. As these values are affected by uncertainties and the simulations are not based on an exact model of the real environment there are some slight differences between the measured and the estimated diversity gains. Fig. 7.25(a) presents the comparison for the non-line-of-sight configuration, while the results for line-of-sight are shown in Fig. 7.25(b). For both situations, there are some differences between measurements and simulations, but all in all the results are in agreement.

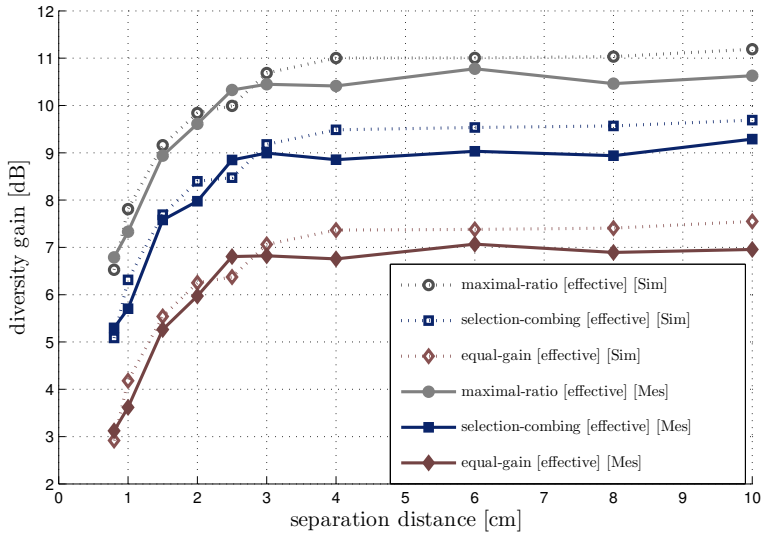

(a)

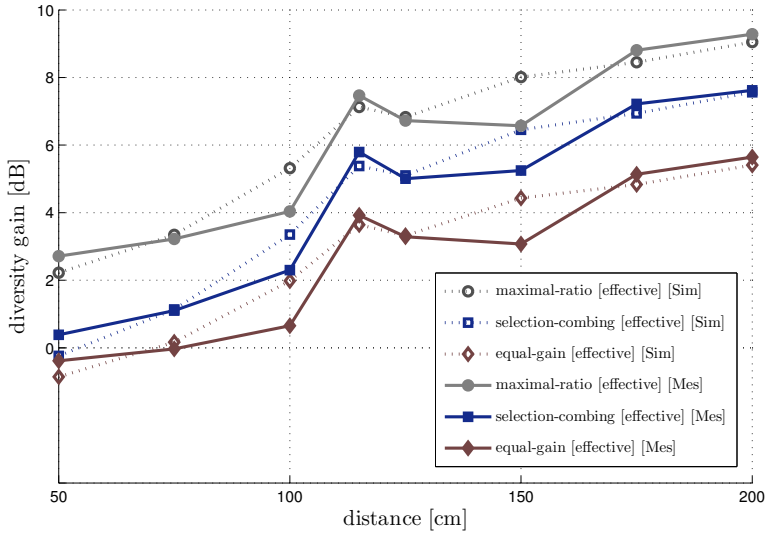

(b)

Figure 7.25: Comparison between the measured and simulated diversity gains for (a) non-line-of-sight configuration when changing the separation distance between dipole antennas and (b) for line-of-sight configuration when changing the propagation distance between horn and antenna array at a frequency of 2.9 GHz.

7.8 Conclusions

In this chapter an analysis of different diversity gain techniques evaluated in reverberation chamber is presented. Depending on how the reference CDF is chosen there are three definitions for diversity gain. In general, the maximal-ratio technique provide a better diversity gain compared with the selection-combining, which in turn provides a higher diversity compared with equal-gain. There are several factors which may influence diversity gain: antenna total efficiency, correlation, level of unstirred components and power imbalance.
From the above simulations and measurements we can extract the following conclusions: The power imbalance can be separated in three factors: associated with discrepancies of antenna total efficiencies, stirred components and unstirred components as seen by both antennas. The envelope and power correlation are lower than the complex correlations and depend on the latter and the K-factors on antenna branches. When the two K-factors on the two branches are not identical, then these correlations are even lower. The received power on antennas decrease due to the losses and coupling between them, influencing the effective diversity gain. Moreover, diversity gain decreases with the increase of the correlation between the signals arriving on antenna array. The use of power correlation or envelope correlation in a Rician environment to characterize the diversity (without taking into account other parameters) is not recommended as it may bias the conclusions. With the increase of K-factor (due to an increase of unstirred power), the diversity gain decreases. When the K-factors on different branches are not identical the diversity gain decreases even more. Several Monte Carlo simulations show the limits of diversity gain in different conditions (i.e., levels of K-factors, power imbalances due to unstirred powers, complex correlations). We increase the sample size by mixing data measured at several frequencies. The effects on the power level of unstirred components and how they can be diminished are discussed. We evaluate the diversity gain when changing the separation distance between dipole antennas and the distance between horn and antenna array and then using statistical simulations we compare the measured diversity gain with the simulated values and the results are in accordance.

Bibliography

[1] W. C. Jakes, *Microwave mobile communications.* New York, USA: IEEE Press, 1974.

[2] W. C. Y. Lee, *Mobile Communication Engineering: Theory and Applications.* New York: McGraw-Hill, 1998.

[3] P.-S. Kildal and K. Rosengren, "Correlation and capacity of MIMO systems and mutual coupling, radiation efficiency, and diversity gain of their antennas: simulations and measurements in a reverberation chamber," *IEEE Communications Magazine*, vol. 2, pp. 104–112, Dec. 2004.

[4] P. Kildal and K. Rosengren, "Electromagnetic characterization of MIMO antennas including coupling using classical embedded element pattern and radiation efficiency," in *Antennas and Propagation Society International Symposium, 2004. IEEE*, vol. 2, Jun. 2004, pp. 1259–1262.

[5] M. Schwartz, W. R. Bennett, and S. Stein, *Communication systems and techniques.* McGraw-Hill, New York, 1966.

[6] A. Turkmani, A. Arowojolu, P. Jefford, and C. Kellett, "An experimental evaluation of the performance of two-branch space and polarization diversity schemes at 1800 MHz," *Vehicular Technology, IEEE Transactions on*, vol. 44, no. 2, pp. 318–326, May 1995.

[7] M. Simon and M.-S. Alouini, "A unified performance analysis of digital communication with dual selective combining diversity over correlated Rayleigh and Nakagami-m fading channels," *Communications, IEEE Transactions on*, vol. 47, no. 1, pp. 33–43, Jan. 1999.

[8] J. Shao, M.-S. Alouini, and A. Goldsmith, "Impact of fading correlation and unequal branch gains on the capacity of diversity systems," in *Vehicular Technology Conference, 1999 IEEE 49th*, vol. 3, Jul. 1999, pp. 2159–2163.

[9] A. Annamalai, C. Tellambura, and V. Bhargava, "Equal-gain diversity receiver performance in wireless channels," *Communications, IEEE Transactions on*, vol. 48, no. 10, pp. 1732–1745, Oct. 2000.

[10] H. T. Hui, "The performance of the maximum ratio combining method in correlated Rician-fading channels for antenna-diversity signal combining," *Antennas and Propagation, IEEE Transactions on*, vol. 53, no. 3, pp. 958–964, Mar. 2005.

[11] M. Stoytchev and D. Wittwer, "Simulations of diversity gains of multiple omni and directive antennas in Rician channel with varying K-factor," in *Wireless Communications and Applied Computational Electromagnetics, 2005. IEEE/ACES International Conference on*, Apr. 2005, pp. 454–457.

[12] W. Lee, "Antenna spacing requirement for a mobile radio base-station diversity," *Bell Syst. Tech. J.*, vol. 50, pp. 1859–1876, Aug. 1971.

[13] D. Cox, "Antenna diversity performance in mitigating the effects of portable radiotelephone orientation and multipath propagation," *Communications, IEEE Transactions on*, vol. 31, no. 5, pp. 620–628, May 1983.

[14] P.-S. Kildal and C. Carlsson, "Detection of a polarization imbalance in reverberation chambers and how to remove it by polarization stirring when measuring antenna efficiencies," *Microwave And Optical Technology Letters*, vol. 34, no. 2, pp. 145–149, Jul. 2002.

[15] P. Kildal, *Foundations of antennas-A unified approach.* Studentlitteratur, Sweden, 2000.

[16] P.-S. Kildal, K. Rosengren, J. Byun, and J. Lee, "Definition of effective diversity gain and how to measure it in a reverberation chamber," *Microwave and Optical Technology Letters*, vol. 34, pp. 56–59, Jul. 2002.

[17] F. Adachi, M. Feeney, and J. Parsons, "An evaluation of specific diversity combiners using signals received by vertically-spaced base-station antennas," *Electronic and Radio Engineers, Journal of the Institution of*, vol. 57, no. 6, pp. S218–S224, Nov. 1987.

[18] J. Winters, J. Salz, and R. Gitlin, "Adaptive antennas for digital mobile radio," in *Adaptive Antenna Systems Symposium, 1992., Proceedings of the IEEE Long Island Section*, Nov. 1992, pp. 81–86.

[19] J. C. B. Dietrich, K. Dietze, J. R. Nealy, and W. Stutzman, "Spatial, polarization, and pattern diversity for wireless handheld terminals," *IEEE Transactions on Antennas and Propagation*, vol. 49, no. 9, pp. 1271–1281, Sep. 2001.

[20] R. G. Vaughan and N. L. Scott, "Closely spaced monopoles for mobile communications," in *Radio Science*, vol. 28, Nov. 1992, pp. 1259–1266.

[21] K. Anim-Appiah, "Complex envelope correlations for non-isotropic scattering," *Electronics Letters*, vol. 34, no. 9, pp. 918–919, 1998.

[22] R. Clarke, "A statistical theory of mobile-radio reception," *Bell Syst. Tech. J.*, vol. 47, pp. 957–1000, Aug. 1968.

[23] D. A. Hill and J. M. Ladbury, "Spatial-correlation functions of fields and energy density in a reverberation chamber," *IEEE Transactions on Electromagnetic Compatibility*, vol. 44, no. 1, pp. 95–101, Feb. 2002.

[24] Y. Karasawa and H. Iwai, "Modeling of signal envelope correlation of line-of-sight fading with applications to frequency correlation analysis," *Communications, IEEE Transactions on*, vol. 42, no. 6, pp. 2201–2203, Jun. 1994.

[25] J. Pierce and S. Stein, "Multiple diversity with nonindependent fading," *Proceedings of the IRE*, vol. 48, no. 1, pp. 89–104, Jan. 1960.

[26] N. Beaulieu, "Generation of correlated Rayleigh fading envelopes," *Communications Letters, IEEE*, vol. 3, no. 6, pp. 172–174, Jun. 1999.

[27] B. Natarajan, C. Nassar, and V. Chandrasekhar, "Generation of correlated Rayleigh fading envelopes for spread spectrum applications," *Communications Letters, IEEE*, vol. 4, no. 1, pp. 9–11, Jan. 2000.

[28] J. Wallace, H. Ozcelik, M. Herdin, E. Bonek, and M. Jensen, "Power and complex envelope correlation for modeling measured indoor MIMO channels: a beamforming evaluation," in *Vehicular Technology Conference, 2003. VTC 2003-Fall. 2003 IEEE 58th*, vol. 1, Oct. 2003, pp. 63–67.

[29] K. Baddour and N. Beaulieu, "Accurate simulation of multiple cross-correlated Rician fading channels," *Communications, IEEE Transactions on*, vol. 52, no. 11, pp. 1980–1987, Nov. 2004.

[30] L. Tran, T. Wysocki, J. Seberry, and A. Mertins, "A generalized algorithm for the generation of correlated Rayleigh fading envelopes in radio channels," in *Parallel and Distributed Processing Symposium, 2005. Proceedings. 19th IEEE International*, Apr. 2005, p. 8 pp.

[31] J.-M. Floc'h, J.-M. Denoual, and K. Sallem, "Design of printed dipole with reflector and multi directors," in *Antennas Propagation Conference, 2009. LAPC 2009. Loughborough*, Nov. 2009, pp. 421–424.

[32] C. Lemoine, P. Besnier, and M. Drissi, "Estimating the effective sample size to select independent measurements in a reverberation chamber," *IEEE Transactions on Electromagnetic Compatibility*, vol. 50, no. 2, pp. 227–236, 2008.

[33] G. Lerideau, E. Amador, P. Besnier, and C. Lemoine, "Quantifying stirred and unstirred components in reverberation chamber with appropriate statistics," in *Electromagnetic Compatibility, 2009. EMC 2009. IEEE International Symposium on*, Austin, TX, 2009, pp. 182–186.

[34] C. Holloway, D. Hill, J. Ladbury, P. Wilson, G. Koepke, and J. Coder, "On the use of reverberation chambers to simulate a Rician radio environment for the testing of wireless devices," *Antennas and Propagation, IEEE Transactions on*, vol. 54, no. 11, pp. 3167–3177, Nov. 2006.

[35] C. Holloway, H. Shah, R. Pirkl, W. Young, D. Hill, and J. Ladbury, "Reverberation chamber techniques for determining the radiation and total efficiency of antennas," *Antennas and Propagation, IEEE Transactions on*, vol. 60, no. 4, pp. 1758–1770, Apr. 2012.

[36] I. Salonen, C. Icheln, and P. Vainikainen, "The dependency of pattern correlation on mutual coupling and losses in antenna arrays," *Microwave and Optical Technology Letters*, vol. 47, no. 2, pp. 145–147, 2005. [Online]. Available: http://dx.doi.org/10.1002/mop.21106

[37] ——, "Pattern correlation and mismatch in two-element antenna arrays," *Microwave and Optical Technology Letters*, vol. 48, no. 1, pp. 41–43, 2006. [Online]. Available: http://dx.doi.org/10.1002/mop.21254

Part IV

Conclusions and future work

CHAPTER 8

General conclusion and future work

8.1 General Conclusion

In most of the cases, a wireless channel signal is affected by the fading phenomenon, which influences its quality, bitrate and other parameters. A successful implementation of an integrated communication system requires both the testing and the optimization of the system. The testing of wireless devices can be done using numerical simulations or channel sounders. Reverberation chamber is an environment, which although not reflecting a real transmission environment may be appropriately modified to emulate one.

The control of transmission can be done based on various parameters, and over our thesis work we analyzed and implemented several techniques to measure and control these parameters inside reverberation chambers.

A first parameter we have analyzed is the K-factor. This parameter is obtained by applying different methods whose results could be influenced by several factors, among them being the rate of correlation between outputs, the stability and independence of samples, the channel noise, etc. Depending on the methods to calculate K-factor, the obtained results are more or less usable (i.e., an I/Q method works fine, but it is necessary to know the signal phase; the envelope method is more simple, gives faster results, but for small values of K-factor this method cannot be used properly, because the results are not only biased, but also some estimators appear as complex values). We analyze several estimators and identify the useful limits in which they can be used. Also, as the envelope-based estimators are the most affected by uncertainties we propose two new estimators which improves the useful detectable range of values while keeping a simple mathematical formulation.

One of the way to control a propagation channel inside reverberation chamber is by modifying the degree of absorption. This will change the quality factor of the chamber and in consequence the decay constant of the environment. This parameter is easily evaluated from measurements of the coherence bandwidth using a single antenna. For simple parallelepiped absorbers and absorbers with simple geometries, the average absorbing cross section is evaluated both by simulations and measurements.

Emulating propagation channels in reverberation chamber requires the knowledge of interrelations between different parameters. Using a statistical model based on the power profile of a pulse modulated sinewave several parameters (i.e., K-factor, average absorbing cross section and different time parameters) are computed. K-factor is described as a function of time moments and the normalized level of the power of envelope. Analytically relations for τ_{μ} and τ_{rms} are presented. The absorbing cross section is estimated with regard to K. We also discuss the dispersion of unstirred secondary components with the time and the effects on this model. Simulations and measurements validate and show the utility of this method.

If it is necessary to measure an antenna, it is possible to do this directly in reverberation chamber. We show that by using a time filtering, several antenna parameters can be directly evaluated. This method is not new but we extend the measurements to the whole antenna pattern. We discuss the evaluation errors due to evaluation of the free space propagation distance, as well of the distance inside antenna. We present results for antenna mismatch, antenna pattern and half power beamwidth and we compare them with those evaluated in a near field chamber.

In the end, we extend our work to antenna arrays and their improvements on the transmission due to diversity. We evaluate the maximum limits of the diversity gain for different combining techniques in several configurations. We discuss especially the situation when unstirred components exist and we show that depending on the level of these components and the ratio between their levels at different branches the diversity gain can be affected. Moreover, we show that when the unstirred components appear and there is a high power imbalance due to these components the power and the envelope correlations may have very low values even though the signal on different branches is highly correlated.

8.2 Future work

8.2.1 Better separation between the direct unstirred components and secondary unstirred components

Beside the direct unstirred component between the transmitting and receiving antenna there are several other secondary unstirred components. These are reflections with the wall but not with the stirrer. A better separation between these components can help for both characterizing the stirring quality in the chamber and also for a better prediction of unstirred energy. A solution may be to make this analysis based on the signal phase in frequency domain.

8.2.2 Shadowing control in reverberation chamber

The shadowing was not introduced in reverberation chamber as it represents a secondary slow fading. We think that it may be important to introduce this aspect directly in measurements as the real propagation channel is in generally affected by this phenomenon. One simple way is to introduce this factor post-measurements but it may be more interesting to be included physically directly in the measured channel. This may be useful to be study once the separation between the direct unstirred component and secondary unstirred components is done.

8.2.3 Clusters control in reverberation chamber

Solutions for the taps clustering were proposed in literature by an artificial modification of the input signal. Nonetheless, this method is far from the true creation of clustering. One solution is to modify with appropriate scatterers and to use the chamber over some suitable directions.

8.2.4 Methodology for a complete communication link testing in reverberation chamber

Compared with what it was proposed before starting this thesis, an important step - a methodology for a complete communication link in reverberation chamber could not be completed. It may be interesting to detail the steps necessary to implement different kinds of communication links and to compare the results in reverberation chamber with measurements in real environments.

Publications

Journaux internationaux avec comité de lecture

M. I. Andries, P. Besnier, and C. Lemoine, "Estimating K-factor and time spread parameters from a transient response of a pulse modulated sine wave in reverberation chamber", IEEE Transactions on Antennas and Propagation, vol. 61, no. 1, pp. 380-389, Jan. 2013.

M. I. Andries, P. Besnier, and C. Lemoine, "Simple approximation for envelope based K estimator", Electronics Letters, vol. 47, no. 3, pp. 222-223, Mar. 2011.

Conférences internationales avec comité de lecture

M. I. Andries, C. Lemoine, and P. Besnier, "On the prediction of the average absorbing cross section of materials from coherence bandwidth measurements in reverberation chamber", Proceedings of the International Symposium on Electromagnetic Compatibility (EMC EUROPE), Rome, Italy, pp. 1-6, Sept. 2012.

E. Amador, M. I. Andries, C. Lemoine, and P. Besnier, "Absorbing material characterization in a reverberation chamber", Proceedings of the International Symposium on Electromagnetic Compatibility (EMC EUROPE), York, UK, pp. 117-122, Sept. 2011.

M. I. Andries, P. Besnier, and C. Lemoine, "Rician channels in a RC: Statistical uncertainty of K estimations versus K fluctuations due to unstirred paths", Proceedings of the 5th European Conference on in Antennas and Propagation (EUCAP), Rome, Italy, pp. 1758-1762, Apr. 2011.

Conférence nationale avec comité de lecture

P. Besnier, C. Lemoine, E. Amador, M. I. Andries, "Extraction de l'onde cohérente d'une mesure en chambre réverbérante. Principe et applications potentielles", 17^e journée nationales microondes (JNM), Brest, France, May 2011.

Communication nationale sans actes

M. I. Andries, P. Besnier, C. Lemoine, "Quantification du facteur K caractéristique des canaux de propagation reproduits en chambre réverbérante à brassage de modes", Journées Scientifiques du Club EEA, GDR ONDES, Rennes, France, Oct. 2010.

Appendix

APPENDIX A

About random variables and some distribution functions.

The probability density function f (pdf) is a statistical measure that defines a probability distribution for of a continuous random variable X [1]. The cumulative distribution function F (CDF) of the random variable X represents the probability that the realizations of the random variable do not exceed a specified value X [1]. It is defined as the integral of its density over the set of possible values:

$$F(x) = \Pr(X \leq x) = \int_{-\infty}^{x} f(v)\,\mathrm{d}\,v \tag{A.1}$$

from which the probability for a variable to be in the range $(x_1, x_2]$ results:

$$\Pr[x_1 \leq X \leq x_2] = F(x_2) - F(x_1). \tag{A.2}$$

while $\lim_{x\to-\infty} F(x) = 0$ and $\lim_{x\to+\infty} F(x) = 1$.

The moments of a pdf

For a continuous function $f(x)$ the nth moments of the probability density function about a value m are given by:

$$\mu_n = \int_{-\infty}^{\infty} (x-m)^n f(x)\,\mathrm{d}\,x = \int_{-\infty}^{\infty} (x-m)^n\, dF(x) \overset{\Delta}{E}\left[X^n\right]. \tag{A.3}$$

When the parameter $m = 0$ these moments are named "moments about zero", "raw moments" or "crude moments". If the parameter m is the mean of $f(x)$ (which characterizes the first order raw moment) these moments are called central moments.
Another usual parameter which represents the second order central moment is the variance σ^2 (respectively standard deviation σ) characterizing the fluctuations of the random variable:

$$\sigma^2 = E[x^2] - E^2[x] = \int_{-\infty}^{\infty} x^2 f(x)\,\mathrm{d}\,x - \mu_1. \tag{A.4}$$

Quantiles

A quantile q_α is defined as

$$F(q_\alpha) = \alpha, \tag{A.5}$$

where α represents the percentage of the values X smaller than q_α.
For a Gaussian distribution, the quantiles at 2.5% and 97.5% levels of uncertainties, the variance and the mean are related as follows:

$$\begin{cases} q_{2.5} = E[X] - 1.96\sqrt{\mathrm{Var}(X)}, \\ q_{97.5} = E[X] + 1.96\sqrt{\mathrm{Var}(X)}. \end{cases} \tag{A.6}$$

In the following lines we describe different pdfs used in this thesis [2, 3] for a measured complex signal in reverberation chamber in the form (see chapter 2):

$$R(p) = r(p)e^{j\Theta(p)} = R_{\mathrm{I}}(p) + jR_{\mathrm{Q}}(p) = R_{\mathrm{sp}}(p) + R_{\mathrm{sc}}(p). \tag{A.7}$$

A.1 The joint probability density function of the fading envelope and the fading phase

The joint probability density function of the fading envelope and the fading phase of a non stationary channel is given by [2]:

$$f(r, \Theta/A, \sigma) = \frac{r}{2\pi\sigma^2} e^{-\frac{r^2 + A^2 - 2rA\cos(\Theta - \theta_0 - \omega_d t)}{2\sigma^2}}. \tag{A.8}$$

For a stationary channel (as the one in reverberation chamber when measuring it in stepped mode) the parameter $\omega_d = 0$.

A.2 The probability density function of the fading phase

The pdf of the fading phase is obtained by integrating the joint pdf presented above over r:

$$\begin{aligned} f(\Theta/A, \sigma) =& \frac{1}{2\pi} e^{-\frac{A^2}{2\sigma^2}} \left[1 + \mathrm{erf}\left(\frac{A\cos(\Theta - \theta_0 - \omega_d t)}{\sigma\sqrt{2}} \right) \right] \\ & \cdot \left[1 + \sqrt{\frac{\pi}{2}} \cdot \frac{A\cos(\Theta - \theta_0 - \omega_d t)}{\sigma} e^{\frac{A^2\cos^2(\Theta - \theta_0 - \omega_d t)}{2\sigma^2}} \right] \\ =& \frac{e^{-K}}{2\pi} + \frac{\sqrt{K}\cos(\Theta - \theta_0 - \omega_d t)}{2\sqrt{\pi}} e^{-K\sin^2(\Theta - \theta_0 - \omega_d t)} \mathrm{erfc}\left(-\sqrt{K}\cos(\Theta - \theta_0 - \omega_d t) \right). \end{aligned} \tag{A.9}$$

If $K \to 0$ the phase becomes uniformly distributed in the interval $[-\pi, \pi)$ having the mean 0. Consequently, the pdf of the fading phase becomes:

$$f(\Theta) = \frac{1}{2\pi}. \tag{A.10}$$

If $K > 1$ then the phase is given by the phase distribution of the dominant component. Integrating the joint pdf of the fading envelope and the fading phase over the fading phase Θ it results a pdf of the fading envelope. Next, we present the pdfs corresponding to the Rayleigh and Rician distributions.

A.3 Rayleigh distribution

The Rayleigh distribution has a pdf given by:

$$f(r/\sigma) = \frac{r}{\sigma^2} e^{-\frac{r^2}{2\sigma^2}}, \quad r \geq 0, \tag{A.11}$$

while its CDF is:

$$F(r/\sigma) = 1 - e^{-\frac{r^2}{2\sigma^2}}, \quad r \geq 0. \tag{A.12}$$

The moments about zero are computed with:

$$\mu_n = E[r^n] = 2^{n/2}\sigma^n \Gamma(1 + n/2) L_{n/2}(0), \tag{A.13}$$

where the operator Γ is the Gamma function presented in section C.2. The mean μ of the Rayleigh distribution is given by:

$$\mu = \mu_1 = \sigma\sqrt{\frac{\pi}{2}} L_{1/2}(0) = \sigma\sqrt{\frac{\pi}{2}} = 1.2533\sigma, \tag{A.14}$$

and the variance $\widetilde{\sigma}$ is:

$$\widetilde{\sigma} = \mu_2 - (\mu_1)^2 = \frac{4-\pi}{2}\sigma^2 \approx 0.4292\sigma^2. \tag{A.15}$$

A.4 Rician distribution

In reverberation chamber, the fast varying amplitude of the received envelope $r(p)$ is described by the Rician distribution [4] whose pdf is:

$$\begin{aligned} f(r/A,\sigma) &= \frac{r}{\sigma^2} e^{-\frac{r^2+A^2}{2\sigma^2}} I_0\left(\frac{rA}{\sigma^2}\right) = \frac{2r(K+1)}{\Omega} e^{-K - \frac{(K+1)r^2}{\Omega}} I_0\left(2r\sqrt{\frac{K(K+1)}{\Omega}}\right) \\ &= \underbrace{\frac{2r10^{K/10}}{A^2} e^{-\frac{10^{K/10}}{A^2}(r^2+A^2)} I_0\left(\frac{2r10^{K/10}}{A}\right)}_{\text{expressed in term of } K[\text{dB}]}, \quad r \geq 0. \end{aligned} \tag{A.16}$$

If A goes to zero (which corresponds to $K \to 0$ or $A^2/2\sigma^2 << r^2/2\sigma^2$), the specular component is eliminated and the envelope distribution becomes Rayleigh distributed $K[\text{dB}] \to -\infty$ (see A.3). If $K >> 1$ then the envelope distribution becomes Gaussian with a mean value given

by A (see A.7).
The CDF of Rician distribution is given by:

$$F\left(r/A,\sigma\right)=1-Q_1\left(\frac{A}{\sigma},\frac{r}{\sigma}\right),\quad r\geq 0, \tag{A.17}$$

where

- $Q_1\left(m_1,m_2\right)=\int_{m_2}^{\infty}xe^{-(x^2+m_1^2)/2}I_0\left(m_1x\right)\mathrm{d}\,x$ is a particularly Marcum function.

The moments about zero are computed as:

$$\mu_n=E\left[r^n(p)\right]=2^{n/2}\sigma^n\Gamma\left(1+n/2\right)L_{n/2}\left(-\frac{A^2}{2\sigma^2}\right), \tag{A.18}$$

The first moment of r is:

$$\mu_1=\mu=E\left[r\right]=\sigma\sqrt{\pi/2}L_{1/2}\left(-\frac{A^2}{2\sigma^2}\right), \tag{A.19}$$

while the second moment is:

$$\mu_2=E\left[r^2\right]=A^2+2\sigma^2. \tag{A.20}$$

The variance $\widetilde{\sigma}$ of the Rician distribution is then given by:

$$\widetilde{\sigma}=2\sigma^2+A^2-\left(\pi\sigma^2/2\right)L_{1/2}^2\left(-A^2/2\sigma^2\right). \tag{A.21}$$

A.5 The probability density function of the fast varying instantaneous power

The squared-envelope follows a non-central chi-square distribution with two degrees of freedom. From [4], using the pdf of the Rician distributed fading envelope f_r, the pdf f of the fast varying instantaneous power of the received signal $p=r^2$ is estimated as:

$$f(p/A,\sigma)=f_r(r)\frac{\mathrm{d}\,r}{\mathrm{d}\,p}\bigg|_{r=\sqrt{p}}=f_r\left(\sqrt{p}\right)\frac{1}{\sqrt{p}}=\frac{1}{\sigma^2}e^{-\frac{p+A^2}{2\sigma^2}}I_0\left(\frac{\sqrt{p}A}{\sigma^2}\right),\quad p\geq 0. \tag{A.22}$$

A.6 The probability density function of the shadowing fading envelope

Due to the potential variations in the obstructions between the transmitter and the receiver the average of the envelope of the signal may vary in time. This phenomenon represents the slow fading or shadowing effect [4]. When both multipath fading and shadowing are present the envelope of the composite signal is no longer Rician distributed. It is not naturally found in reverberation chamber and it has to be introduced artificially or using a supplementary slow speed stirrer. It is possible to use a filter to remove the shadowing effect but it will also filter the unstirred components. The Rician-Nakagami pdf assumes Rayleigh distribution for

the envelope of the scatter component and Nakagami distribution for the amplitude of the specular component [5]:

$$f(r/A,\sigma,m) = \underbrace{\frac{r}{\sigma^2}e^{-\frac{r^2}{2\sigma^2}}\left(\frac{2\sigma^2 m}{2\sigma^2 m + A^2}\right)^m}_{\text{Rayleigh distribution}} \underbrace{{}_1F_1\left(m;1;\frac{A^2r^2}{2\sigma^2\left(A^2+2\sigma^2 m\right)}\right)}_{\text{Nakagami distribution}}, \quad r \geq 0, \tag{A.23}$$

where $m = \dfrac{\left(E\left[r^2\right]\right)^2}{\mathrm{Var}\left[r^2\right]} = \dfrac{\mu_2^4}{\mu_4^2 - \mu_2^4}$ is the parameter of shadowing. When shadowing is absent $(m \to \infty)$ the distribution f becomes Rician.
The general form of the nth order moments about zero is:

$$\mu_n \triangleq \left(\frac{m}{m+K}\right)^m \left(2\sigma^2\right)^{n/2} \Gamma\left(\frac{n}{2}+1\right) {}_2F_1\left(\frac{n}{2}+1, m; 1; \frac{K}{m+K}\right). \tag{A.24}$$

A.7 Gaussian Distribution

The pdf of the normal (or Gaussian) distribution is defined with:

$$f(R_\star/\sigma) = \frac{1}{\sigma\sqrt{2\pi}} e^{-\frac{1}{2}\left(\frac{R_\star - \mu}{\sigma}\right)^2}, \tag{A.25}$$

where $\star$ can corresponds to real (R) or imaginary component (I) (e.g., in reverberation chamber, the rectangular component of the electric field). In this pdf, the parameters μ and σ are respectively the mean and the standard deviation.
The cumulative distribution function is then given by:

$$F(R_\star) = \frac{1}{2}\left[1 + \mathrm{erf}\left(\frac{R_\star - \mu}{\sigma\sqrt{2}}\right)\right], \tag{A.26}$$

where erf is the Gauss error function as presented in section C.3.

A.8 Weibull Distribution

For a Weibull distribution, its pdf is defined with:

$$f(r/\alpha,\beta) = \frac{\alpha}{\beta}\left(\frac{r}{\beta}\right)^{\alpha-1} e^{-(r/\beta)^\alpha}, \quad r \geq 0. \tag{A.27}$$

The mean and variance of a Weibull random variable are defined with:

$$\mu = \beta\,\Gamma\left(1 + \frac{1}{\alpha}\right), \tag{A.28}$$

and

$$\widetilde{\sigma} = \beta^2\left[\Gamma\left(1+\frac{2}{\alpha}\right) - \left(\Gamma\left(1+\frac{1}{\alpha}\right)\right)^2\right], \tag{A.29}$$

where the parameters α and β are respectively the shape parameter and the scale parameter.
The CDF for the Weibull distribution is:

$$F(r/\alpha,\beta) = 1 - e^{-(r/\beta)^\alpha}, \quad r \geq 0. \tag{A.30}$$

A.9 Chi-square Distribution

A noncentral chi-square with n degrees of freedom is defined as [6]:

$$f(x) = \frac{1}{2\lambda}\left(\frac{x}{s^2}\right)^{(n-2)/4} e^{-(s^2+x)/(2\lambda)} I_{n/2-1}\left(\frac{\sqrt{xs^2}}{\lambda}\right), \quad x \geq 0. \tag{A.31}$$

where

- s^2 is the noncentrality parameter;
- λ represents the scale parameter.

The central chi-square with n degrees of freedom is simpler given by:

$$f(x) = \frac{1}{(2\lambda)^{n/2}\,\Gamma\left(\frac{n}{2}\right)} x^{n/2-1} e^{-x/(2\lambda)}, \quad x \geq 0. \tag{A.32}$$

When $n = 2$ the chi-square distribution becomes an exponential distribution.

A.10 F-distribution

The F-distribution corresponds to the ratio of two independently distributed noncentral chi-squared variables $\chi^2_{n_1}(s_1)$ and $\chi^2_{n_2}(s_2)$ having respectively the degrees of freedom n_1 and n_2, and the non-centrality parameters s_1 and s_2:

$$F = \frac{\chi^2_{n_1}(s_1)/n_1}{\chi^2_{n_2}(s_2)/n_2}. \tag{A.33}$$

For instance, a parameter which has a F distribution is the K-factor. In this case the parameters $s_1 \neq 0$ and $s_2 = 0$, the F distribution becoming singly non central defined with:

$$F = \frac{\chi^2_{n_1}(s_1)/n_1}{\chi^2_{n_2}(0)/n_2}. \tag{A.34}$$

A.11 Relations between distributions

In the table A.1 we present several relations between different statistical distributions [7], which are used to characterize different parameters in this thesis.

Table A.1: Relations between distributions.

If initial random variable(s) ···	**then ···**
$X_{\mathcal{U}} \sim$ Uniform	$\sigma\sqrt{-2\ln\left(1-X_{\mathcal{U}}\right)} \sim$ Rayleigh
$X_{\mathcal{E}} \sim$ Exponential(λ)	$\sqrt{2X_{\mathcal{E}}\sigma^2\lambda} \sim$ Rayleigh
$X_{\mathcal{N},1}\left(0,\sigma^2\right)$ and$X_{\mathcal{N},2}\left(0,\sigma^2\right) \sim$ Gaussian	$\sqrt{X_{\mathcal{N},1}^2 + X_{\mathcal{N},2}^2} \sim$ Rayleigh
$X_{\mathcal{N},1}\left(0,\sigma^2\right)$ and$X_{\mathcal{N},2}\left(0,\sigma^2\right) \sim$ Gaussian	$X_{\mathcal{N},1} \cdot X_{\mathcal{N},2} \sim$ Gaussian
$X_{\mathcal{N},1}\left(0,\sigma^2\right)$ and$X_{\mathcal{N},2}\left(0,\sigma^2\right) \sim$ Gaussian	$X_{\mathcal{N},1} \star X_{\mathcal{N},2} \sim$ Gaussian
$X_{\mathcal{N},1}\left(A\cos\theta_0,\sigma^2\right)$ and$X_{\mathcal{N},2}\left(A\sin\theta_0,\sigma^2\right) \sim$ Gaussian	$\sqrt{X_{\mathcal{N},1}^2 + X_{\mathcal{N},2}^2} \sim$ Rician (A,σ)
$X_{\mathcal{R}} \sim$ Rayleigh (σ)	$X_{\mathcal{R}}^2/\sigma^2 \sim \chi_2^2\left(s^2=0\right)$
$X_{\mathcal{R}} \sim$ Rician (A,σ)	$X_{\mathcal{R}}^2/\sigma^2 \sim \chi_2^2\left(s^2=\sigma^2\right)$
$X_{\mathcal{N},i}\left(m_i,\dfrac{\sigma^2}{N}\right) \sim$ Gaussian, $i \in [1,N]$	$\sum_{i=1}^{N} X_{\mathcal{N},i}^2 \sim \chi_N^2\left(s^2=\sum_{i=1}^{n} m_i^2, \lambda=\dfrac{\sigma^2}{N}\right)$
$X_{\mathcal{N},i}\left(0,\dfrac{\sigma^2}{N}\right) \sim$ Gaussian, $i \in [1,N]$	$\sum_{i=1}^{N} X_{\mathcal{N},i}^2 \sim \chi_N^2\left(s^2=0, \lambda=\dfrac{\sigma^2}{N}\right)$
$X_{\chi_N^2,i} \sim \chi_N^2\left(s^2,\lambda_i\right), i \in [1,N]$	$\sum_{i=1}^{M} X_{\chi_N^2,i} \sim \chi_{M\times N}^2$

The operator $\star$ represents the convolution.

APPENDIX B

Basic elements of the statistical estimation

B.1 Correlation and covariance

This parameter quantifies the degree of similarity between several input signals. Various definitions of correlation are in use. In this thesis we use the linear correlation (also named as the Pearson product moment correlation coefficient). The cross-correlation ρ_{XY} of two repeatable random processes X and Y at two discrete moments t_1 and $t_2 = t_1 + \tau$ is computed by subtracting their average values μ_X and μ_Y and dividing by their standard deviations σ_X and σ_Y:

$$\rho_{XY}(\tau) = \frac{E\left[(X_{t_1} - \mu_X)(Y_{t_1+\tau} - \mu_Y)^H\right]}{\sigma_X \sigma_Y} = \frac{\widetilde{\rho}_{XY}(\tau) - \mu_X \mu_Y}{\sigma_X \sigma_Y} = \frac{\mathcal{C}_{XY}(\tau)}{\sigma_X \sigma_Y}, \tag{B.1}$$

In the above definitions, the operator ^{H} indicates the Hermitian transpose, $\mathcal{C}$ represents the covariance between the signals, and $\widetilde{\rho}_{XY}(\tau) = E[X_{t_1} Y_{t_1+\tau}]$. The parameter τ represents the lag between the two random processes. The autocorrelation for the random processes X is defined as:

$$\rho_{XX}(\tau) = \frac{E\left[(X_{t_1} - \mu_X)(X_{t_1+\tau} - \mu_X)^H\right]}{\sigma_X^2} = \frac{\widetilde{\rho}_{XX}(\tau) - \mu_X^2}{\sigma_X^2} = \frac{\mathcal{C}_{XX}(\tau)}{\sigma_X^2}. \tag{B.2}$$

where $\widetilde{\rho}_{XX}(\tau) = E\left[XX^H\right]$.
When the signals are identical the correlation coefficient is 1 (or −1 when the phase is shifted with π). When they are totally different the correlation coefficient is 0. It means that they do not have a linear relationship but it does not mean that the signals are statistically independent. When the correlation coefficient is positive an increase in the value of a input signal corresponds to an increase in the value of the other signal(s). When the correlation coefficient is negative an increase of a signal will most probably correspond to a decrease of the other signal. The procedure to compare two or more different input signals is named cross-correlation (named in this thesis correlation). When the same signal is compared to the phase shifted copies of itself the procedure is known as autocorrelation. The latter technique

is useful for finding repeating patterns in a signal, identifying the fundamental frequency of a signal, etc. [8].

Some properties of autocorrelation

- the autocorrelation is maximum for zero lag between input signals: $|\rho_{XX}(\tau)| \leq \rho_{XX}(0) = 1$;
- the autocorrelation of a real function is an even function: $\rho_{XX}(-\tau) = \rho_{XX}(\tau)$;
- the autocorrelation of a complex function is an Hermitian function: $\rho_{XX}(-\tau) = \rho_{XX}^{H}(\tau)$;
- the autocorrelation of a periodic function has the same period as the function;
- the power spectral density can be computed from autocorrelation using the Wiener-Khinchin theorem: $S(f) = \int_{-\infty}^{\infty} \rho_{\mathrm{XX}}(\tau)\, e^{-j2\pi f\tau}\, \mathrm{d}\tau$.

B.2 Central Limit Theorem

Considering N random variables X_i associated with N independent realizations following a $\mathcal{L}(\mu, \sigma^2)$, the central limit theorem (CLT) states that, when N is high, the sum between these N random, normalized and independent variables, follows a normal distribution.

$$\text{If} X_i \sim \mathcal{L}\left(\mu, \sigma^2\right) \text{then} \begin{cases} \sum_{i=1}^{N} X_i \sim \mathcal{N}\left(\mu, N\sigma^2\right), \\ \text{and} \\ \dfrac{\sum_{i=1}^{N} X_i}{N} \sim \mathcal{N}\left(\mu, \dfrac{\sigma^2}{N}\right). \end{cases} \tag{B.3}$$

When the above variables are correlated, the variance of mean depends on correlation factor ρ between the variables and changes from σ^2/N to [9]:

$$\widetilde{\sigma}^2 = \begin{cases} \dfrac{\sigma^2}{N}\sqrt{\dfrac{1+\rho(0)}{1-\rho(0)}}, & \text{for } \rho(0) \leq 0.55, \\ \dfrac{\sigma^2}{N}\sqrt{\dfrac{1+\rho(0)-\rho(1)}{1-\rho(0)+\rho(1)}}, & \text{for } \rho(0) > 0.55, \end{cases} \tag{B.4}$$

where $\rho(0)$ and $\rho(1)$ are respectively the first and the second order correlation coefficients.

B.3 Independent variables

Two random variables X and Y are considered to be independent when the joint probability density function can be separated as the product between the individual probability density functions:

$$f_{X,Y}(x,y) = f_X(x) f_Y(y) \tag{B.5}$$

Form (B.4) the number of independent realizations N_I can be estimated as a function of the total number of samples N, and the first and second order correlation coefficients as:

$$N_I = \begin{cases} N\dfrac{1-\rho(0)}{1+\rho(0)}\left(\dfrac{\sigma_{\text{th}}}{\mu_{\text{th}}}\right)^2\left(\dfrac{\mu_{\text{mes}}}{\sigma_{\text{mes}}}\right)^2, & \rho(0) \le 0.55, \\ N\dfrac{1-\rho(0)-\rho(1)}{1+\rho(0)-\rho(1)}\left(\dfrac{\sigma_{\text{th}}}{\mu_{\text{th}}}\right)^2\left(\dfrac{\mu_{\text{mes}}}{\sigma_{\text{mes}}}\right)^2, & \rho(0) > 0.55, \end{cases} \tag{B.6}$$

where $\sigma_{\text{th}}/\mu_{\text{th}}$ represents the theoretical ratio between the standard deviation and the mean and $\sigma_{\text{exp}}/\mu_{\text{exp}}$ is the measured ratio.

The number of realizations and the time for measurements

The number of independent realizations during a measurement depends on several parameters. One kind of parameter is the duration of time during which the measurement is made. The number of independent realizations influences the confidence interval of estimated parameters. During a measurement in tuned-mode, when the time between two consecutive measurements is sufficiently high (comparing with the decay constant of the environment) there is a high probability that successive realizations are uncorrelated. If the measurement frequency decreases, the correlation between realizations generally increases, the effective information content of the measurement decreasing.

B.4 Biased/Unbiased estimators

An estimated is unbiased if the expected value of the estimate $\widehat{x}$ equals the true value x:

$$E\left[\widehat{x}\right] = x, \tag{B.7}$$

with the normalized error given by:

$$\xi = \left|\frac{x-\widehat{x}}{x}\right| \tag{B.8}$$

Otherwise the estimate is said to be biased.

B.5 (Root) Mean Squared Error

Mean squared error (MSE) represents a performance parameter of an estimator in terms of variance and bias. The MSE of an estimator $\widehat{x}$ with respect to the true value x of a parameter is the sum of the variance and the squared-norm of the bias:

$$MSE\left(\widehat{x}\right) = E\left[\left(\widehat{x}-x\right)^2\right] = \text{Var}\left(\widehat{x}\right) + \left[\mathcal{B}\left(\widehat{x},x\right)\right]^2, \tag{B.9}$$

for which the operator Var is the variance of the estimator and $\mathcal{B}\left(\widehat{x},x\right) = \widehat{x}-x$ is the bias between the estimated and the true value of the estimator.

B.6 Asymptotic Variance of an Estimator

The asymptotic variance is used to study the relative efficiency of an estimator for a number of realizations which goes to infinity [10]. Among the many definitions, one standard definition is given by:

$$AsV(x) = \frac{1}{N} \lim_{N\to\infty} E\left[\left(x - \lim_{N\to\infty} E(x)\right)^2\right]. \tag{B.10}$$

B.7 Cramer-Rao bound

Cramer Rao lower bound (CRLB) [11, 12] is used to obtain the smallest total variance of any unbiased estimator. It represents the lower bound of the variance of estimators of a deterministic parameter. Accepting an increase of the bias of the estimator, the variance can be made smaller. It is possible to use the Cramer-Rao theorem to determine the limit of the variance of biased estimators.

B.8 Maximum Likelihood Estimation

The maximum likelihood estimation (MLE) is a technique to estimate the parameters of a statistical model from a measured data. When the size of the measured sample is high enough ($N \to \infty$) the estimators using this method converges to their true values.

APPENDIX C

Standard Functions

C.1 Bessel Functions

Bessel functions of the first kind J_α

These functions represents the solutions of the Bessel's equation defined with:

$$J_\alpha(x) = \sum_{p=0}^{\infty} \frac{(-1)^p}{p!\Gamma(p+\alpha+1)} \left(\frac{x}{2}\right)^{2p+\alpha}, \tag{C.1}$$

with the properties:

- when α integer

$$J_{-\alpha}(x) = (-1)^\alpha J_\alpha(x); \tag{C.2}$$

- when α is not integer $J_\alpha(x)$ and $J_{-\alpha}(x)$ are linearly independent;
- $J_0(0) = 0$;
- $\lim_{x\to\infty} J_\alpha(x) = 0$;
- $J_\alpha(x)$ can be written as recurrence identities between consecutive and distant neighbors.

Bessel functions of the second kind Y_α

These functions are the solutions of the Bessel equation:

$$\begin{cases} Y_\alpha(x) = \dfrac{J_\alpha(x)\cos(\alpha\pi) - J_{-\alpha}(x)}{\sin(\alpha\pi)}, & \text{for non-integer} \alpha \\ Y_\beta(x) = \lim\limits_{\alpha\to\beta} Y_\alpha(x), & \text{for integer} \beta. \end{cases} \tag{C.3}$$

Modified Bessel function of the first kind $I_\alpha(x)$

The solutions of the Bessel's equation when the argument x is purely imaginary represent the modified Bessel functions. The modified Bessel function of the first kind is then defined as:

$$I_\alpha(x) = j^{-\alpha} J_\alpha(jx) = \sum_{p=0}^{\infty} \frac{1}{p!\Gamma(p+\alpha+1)} \left(\frac{x}{2}\right)^{2p+\alpha}, \tag{C.4}$$

with the properties:

- $I_\alpha(0) = 0$;
- $I_0(0) = 1$;
- $\lim_{x\to\infty} I_\alpha(x) = \infty$.

Modified Bessel function of the second kind $K_\alpha(x)$

The modified Bessel function of the second kind is defined with:

$$\begin{cases} K_\alpha(x) = \dfrac{\pi}{2} \dfrac{I_{-\alpha}(x) - I_\alpha(x)}{\sin(\alpha\pi)}, & \text{for non-integer} \alpha \\ K_\beta(x) = \lim\limits_{\alpha\to\beta} K_\alpha(x), & \text{for integer} \beta. \end{cases} \tag{C.5}$$

C.2 Gamma Function

This function is defined for all positive values as:

$$\begin{cases} \Gamma(n) = (n-1)!, & \text{when} n \text{is a positive integer,} \\ \Gamma(n) = \int\limits_0^\infty t^{n-1} e^{-t}\, \mathrm{d}t, & \text{when} n \text{is complex.} \end{cases} \tag{C.6}$$

Some properties of Gamma function:

- $\Gamma(1) = 1$;
- $\Gamma\left(\frac{1}{2}\right) = \sqrt{\pi}$;
- $\Gamma\left(\frac{3}{2}\right) = \frac{1}{2}\sqrt{\pi}$;
- $\Gamma(z+1) = z\Gamma(z)$;
- $\Gamma(1-z)\,\Gamma(z) = \dfrac{\pi}{\sin(\pi z)}$.

C.3 Gauss error function

This function is defined as:

$$\operatorname{erf}(x) = \frac{2}{\sqrt{\pi}} \int_0^x e^{-t^2} \, \mathrm{d}\, t = \frac{2x}{\sqrt{\pi}} {}_1F_1\left(\frac{1}{2}; \frac{3}{2}; -x^2\right) = \frac{2xe^{-x^2}}{\sqrt{\pi}} {}_1F_1\left(1; \frac{3}{2}; x^2\right). \tag{C.7}$$

The complementary error function $\operatorname{erfc}[\square]$ is then defined as:

$$\operatorname{erfc}[x] = 1 - \operatorname{erf}(x) = \frac{2}{\sqrt{\pi}} \int_x^\infty e^{-t^2} \, \mathrm{d}\, t. \tag{C.8}$$

In these equations ${}_1F_1$ is the Kummer confluent hypergeometric function whose general definition is:

$${}_pF_q(a_1, \cdots a_p; b_1, \cdots b_q; x) = \sum_{k=0} c_k x^k, \quad c_0 = 1, \tag{C.9}$$

for which the coefficients are extracted from:

$$\frac{c_{k+1}}{c_k} = \frac{P(k)}{Q(k)} = \frac{(k+a_1)\cdots(k+a_p)}{(k+b_1)\cdots(k+b_p)\,(k+1)}. \tag{C.10}$$

C.4 Laguerre polynomials

The solutions of Laguerre differential equation are named Laguerre polynomials. The Rodrigues representation of a Laguerre polynomial is given by:

$$L_n(x) = \frac{e^x}{n!} \frac{\mathrm{d}^n\left(x^n e^{-x}\right)}{\mathrm{d}\, x^n} = {}_1F_1(-n; 1; x). \tag{C.11}$$

Some Laguerre polynomials:

- $L_n(0) = 1$;
- $L_0(x) = 1$;
- $L_1(x) = -x + 1$;
- $L_2(x) = \frac{1}{2}\left(x^2 - 4x + 2\right)$;
- $L_3(x) = \frac{1}{6}\left(-x^3 + 9x^2 - 18x + 6\right)$.

and the identities:

- $L_n(x) = \frac{2n+3-x}{n+1} L_{n+1}(x) - \frac{n+2}{n+1} L_{n+2}(x)$;
- $L_{1/2}(x) = {}_1F_1\left(-\frac{1}{2}; 1; x\right) = e^{x/2}\left[(1-x)\, I_0\left(-\frac{x}{2}\right) - x I_1\left(-\frac{x}{2}\right)\right]$.

APPENDIX D

Frequency to time transformation

D.1 Basics of samplings in frequency and time domain

Let consider a time vector described by a set of N_t discrete time values. A signal with this kind of temporal axis can be measured with a DSO. The maximum duration of this time vector is:

$$t_{\max} = \frac{N_t - 1}{\Delta f} = (N_t - 1)\Delta t, \tag{D.1}$$

where Δf represents the sampling frequency in time domain (Δt the time resolution), for which to recover the analog signal it must be $\Delta f \geq 2 f_{\max}$ (due to Nyquist condition). The parameter $f_{\max}$ represents the highest frequency in the bandwidth of transmitted signal.

When the signal is measured in frequency domain in the range $[f_{\min}; f_{\max}]$ (i.e., by using a VNA) for a number of bins (i.e., frequency points) equal with N_b, the bin resolution is:

$$\Delta bin = \frac{f_{\max} - f_{\min}}{N_b - 1}. \tag{D.2}$$

Making an inverse transform to time domain of this signal (e.g., applying an inverse Fast Fourier Transform (FFT)), the maximum time duration of the signal $t_{\max}$ is:

$$t_{\max} = \frac{1}{\Delta bin} = \frac{N_b - 1}{f_{\max} - f_{\min}}. \tag{D.3}$$

It results that the minimum time resolution is:

$$\Delta t = \frac{t_{\max}}{N_t - 1} = \frac{N_b - 1}{N_t - 1} \frac{1}{f_{\max} - f_{\min}}. \tag{D.4}$$

D.2 Inverse CZT transform function

The chip z-transform (CZT) is a computational algorithm for numerically evaluating the z-transform at M points of a signal whose length is N in the z-plane [13]. Both parameters N

and M are arbitrary integers. This technique is generally used for time to frequency domain transformations and vice versa due the rapidity of estimation and possibility to implement the CZT on a digital signal processor (DSP) for any length N.

Utility and advantages

This technique is implemented in different measurement devices to transform the signal from/to time domain to/from frequency domain. For example, the vector network analyzer (Agilent N5230A) used in this thesis has the capacity to transform the measured signal from frequency to time domain using an inverse CZT transform.
We use this transform to increase the resolution in time domain (which is useful for time interpolations applied for time convolutions), as well as to estimate different time windows of the signal rather than to estimate the signal for all the time vector. We can use the signal already measured and transformed directly by the VNA, but the time to export the data from the VNA takes to much time and it depends on the desired length of the signal. For example a measurement takes 40 min for a complete rotation of the stirrer in frequency domain when the length of the signal is 20 µs which for 20001 points results a frequency resolution of $\Delta f = 1\,\mathrm{Gs}$. If we want to obtain directly with the VNA a frequency resolution of 10 Gs for the same time duration (of 20 µs), we need to concatenate 10 transformations whose time durations are 2 µs. The total duration for saving and concatenate these values for a complete stirrer position is more than 6 h. The solution to reduce this duration is to save the signal in frequency domain, and then offline to transform in time domain (which takes a time between some seconds to minutes, depending on the computational speed).
Comparing with the FFT transform, which requires to make the transformation over all the unit circle $[0; 2\pi)$ for a transformation from 0 Hz to the sampling frequency Δf, the CZT transform can be done over an arc of the unit circle. An illustration of the utility of CZT transform is presented in Fig. D.1. Using this technique is possible to specify the transformation bandwidth, $f_2 - f_1$, and also the number of bins contained in that bandwidth. It results that is possible to evaluate high resolution narrow frequency bandwidth. When using the FFT transform, this requires a very large number N of bins. Another useful utility of CZT transform is the time interpolation or, equivalent, the change of sample rate in time domain.

Mathematical description

The discrete z transform can be written as:

$$X[z] = \sum_{n=0}^{N_t-1} x[n]\, z^{-n}, \tag{D.5}$$

where $x[k]$ is a discrete signal sequence in time domain. While for the discrete Fourier transform the parameter $z = e^{j2\pi kn/N}$, for the CZT transform this parameter can have a more general form: $z = AW^{-k}$. The parameters A and W are arbitrary complex numbers and the factor k is the index in frequency domain of frequency transformed signal X. It results that

$$A^{-n}W^{nk} = A^{-n}e^{-j2\pi kn/N}. \tag{D.6}$$

Using the separation of the product kn as in Bluestein's algorithm:

$$kn = \frac{k^2}{2} + \frac{n^2}{2} - \frac{(k-n)^2}{2}, \tag{D.7}$$

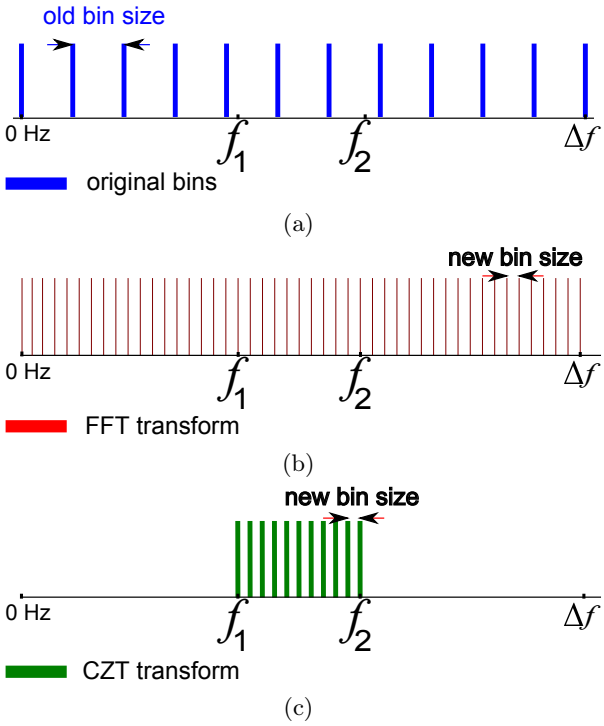

Figure D.1: Comparison between the FFT (b) and the CZT transform (c).

it results that (D.6) can be written as:

$$A^{-n}W^{kn} = A^{-n}W^{k^2/2}W^{n^2/2} \cdot W^{-(k-n)^2/2} \tag{D.8}$$

The CZT transform is defined as:

$$X[k] = \underbrace{W^{k^2/2}}_{\text{step C}} \underbrace{\sum_{n=0}^{N-1} \underbrace{x[n]\, A^{-n}W^{n^2/2}}_{\text{step A}} W^{-(k-n)^2/2}}_{\text{step B}}. \tag{D.9}$$

for which the complex chirps functions are defined as:

$$\begin{cases} W & = e^{-j2\pi/N}, \\ W^{k^2/2} & = e^{-j\pi k^2/N}, \\ W^{n^2/2} & = e^{-j\pi n^2/N}, \\ W^{-(k-n)^2/2} & = e^{-j\pi (k-n)^2/N}. \end{cases} \tag{D.10}$$

From (D.9) it results that the CZT transform has three steps:

- first multiply the input signal by a chirp (step A);
- then convolve with a chirp (which corresponds to a multiplication of the FFT of step A and of a chirp function and then IFFT of this product (step B);
- and at the end multiply by a chirp function (step C).

The inverse CZT

An algorithm for the inverse-transform can be done as in [14]. Much easier we can use the direct CZT transform, which is already implemented in Matlab to estimate the inverse CZT. Comparing with the direct transform we need to make the following modifications to estimate the inverse CZT transform:

- conjugate the argument of CZT function;
- conjugate again the result;
- define correctly the chirp W and parameter A which depend on time limits (not on frequency limits).

The CZT transform requires the knowledge of several parameters:

- identifying the number of zeros necessary to complete the frequency vector;
- computing the number of bins and the actual bin resolution (which represents the maximum time duration);
- establishing the requested time resolution and computing the corresponding length of time vector;
- estimating the chirp w and parameters A;
- creating the time vector.

The Matlab code used for this inverse and direct transformation when the input signal is the complex transfer parameters denoted "S21cpx" (i.e., a matrix whose dimensions are: "Nb" the number of frequencies and "Sp" the number of stirrer positions), measured with a VNA, over a frequency vector denoted "fX" is presented in the following lines:

```
% The parameter S21cpx and fX should be loaded previously
[Nb Sp]=size(S21cpx); % dimensions: Nb - frequencies, Sp - stirrer positions
Z=length(0:fX(2)-fX(1):fX(1))-1; % zeros to complete the frequency vector

% A) Transformation in Time Domain
% Kaiser Filter
betta=6; % Kaiser Bessel function window b value
KA=kaiser(Nb, betta); % Kaiser Bessel function window
kfact=Nb/sum(KA); % Kaiser Bessel function normalization
S21cpxmod=repmat(KA, 1, Sp).*S21cpx*kfact;

% Frequency/Time Domain Info
binRes=(fX(end)-fX(1))/(Nb-1); % bin resolution
disp(['Bin resolution of the signal ' num2str(binRes/1E3) ' [kHz/bin]']);
afs=(Nb-1)*(fX(2)-fX(1)); % actual sampling frequency in time domain
disp(['Actual sampling frequency in time domain ' num2str(afs/1E9) ' [GS]']);
Nt=floor(fs/(fX(2)-fX(1))+1); % the required number of samples (to have "fs")

% Applying the Inverse-CZT
S21cpxmod=[zeros(Z, Sp); S21cpxmod]; % re-creating the entire spectrum
 t1=0; % first limit - corresponding to 0 sec
 t2=(Nb-1)/(fX(end)-fX(1)); % second limit- corresponding to maximum duration
```

```
w=exp(-1i*2*pi*afs*(t2-t1)/((Nt-1)*(Nb-1)));
a=exp(1i*2*pi*afs*t1/(Nb-1));
IRcpx=conj(czt(conj(S21cpxmod),Nt-1,w,a))/(Nb-1); % iCZT+scalling

tIRend=t2; % time vector
tIR=tIRend*linspace(0, 1, Nt-1);

figure(1);
plot(tIR and IRcpx);

% B) Transformation in Frequency Domain
f1=fX(1); % first limit
f2=fX(end); % second limit
w=exp(-1i*2*pi*(f2-f1)/fs/(Nb-1));
a=exp(1i*2*pi*f1/fs);

S21cpxNew=czt(IRcpx, Nb-1,w,a)./(repmat(KA, 1, Nb).*kfact)* (Nb-1)/(Nt-1); % CZT+
    scalling

figure(2);
plot(fX, 20*log10(abs(S21cpxNew)));
```

Listing D.1: Matlab inverse-CZT and CZT code.

The role of Kaiser filter

As it can be seen in the above code we also use a Kaiser window to control the fluctuations in the transformed signal with the cost of interferences between the neighboring taps. This kind of filter is controlled by the parameter $\beta = 1, 2, \ldots 13$. It is defined as [15]:

$$w_n = \begin{cases} \dfrac{I_0\left(\pi\alpha\sqrt{1-\left(\dfrac{2n}{M}-1\right)^2}\right)}{I_0(\pi\alpha)}, & 0 \le n \le M, \\ 0, & \text{otherwise}, \end{cases} \tag{D.11}$$

where

- α is an arbitrary real number that determines the shape of the window. In the frequency domain, it determines the trade-off between main-lobe width and side lobe level, which is a central decision in window design. We have the relationship $\pi\alpha = \beta$;
- M is an integer, and the length of the sequence is $N = M + 1$.

Different other types of filters can be used: Bartlett, Blackman, Chebyshev, etc.

APPENDIX E

3D generation of the absorbers

The simulation of the parallelepiped absorbers Fig E.1 is done by creating a 3D structure using Matlab. A functional code is presented in the following lines:

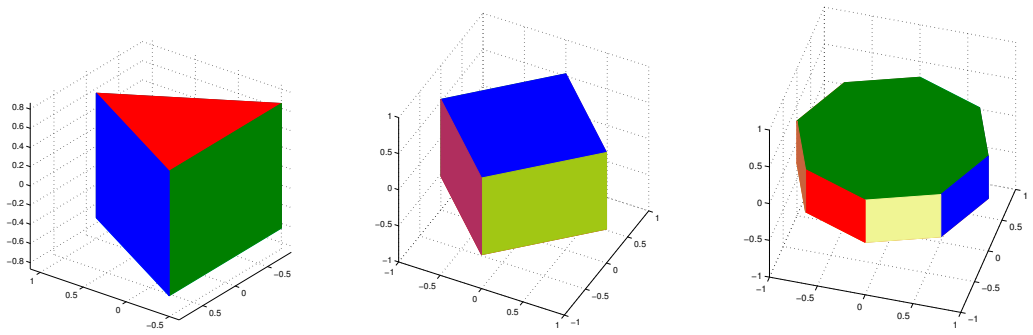

(a) (b) (c)

Figure E.1: Different 3D absorbers shapes: (a) triangular prism, (b) parallelepiped, (c) octagonal prism.

```
clear
clc
close all

% Type of geometry
versionGEN=1; % "1" any number of edges, e.g., L xL xl/ "2" only 4 edges L xL2 xl

% Number of edges/or angles
noEDG=3; % the number of edges of the TOP/BOTTOM polygon when versionGEN==1
 ang=360/noEDG;

% Number of absorbers
noABS=1; % the absorbers are identical whose height is "1"
```

```
% Geometrical Dimensions of one absorber
l=0.45; % [m] (for version 1&2) - (height)
L=0.6; % [m] (for version 1&2) - (lenght)
L2=0.6; % [m] (for version 2) - (the second lenght in a rectangle)

% Colors of the Faces
cl=1; % 0-monochrome (only one color)/1-colored, each face has another color
no=1; % 0-only bottom face remains /1- all the faces remains

% Creating DATA - Horizontal plates
switch versionGEN
    case 1
        disp('Version =1= : any numbers of equal edges (e.g., for parallelepiped:
            LxLxl)')
        L2=L;
        theta=(0:ang:360)/180*pi;
        % 1 (bottom)
        x1=cos(theta);
        y1=sin(theta);
        z1=zeros(size(x1))- l*(2*sin(ang/2*pi/180))/L*noABS/2;
        % 2 (top)
        x2=cos(theta);
        y2=sin(theta);
        z2=zeros(size(x1))+ l*(2*sin(ang/2*pi/180))/L*noABS/2;

    case 2
        disp('Version =2= : 4 edges: (only parallelepiped: LxL2xl)')
        % 1 (bottom)
        x1=L/2*[1 1 -1 -1 1];
        y1=L2/2*[-1 1 1 -1 -1];
        z1=zeros(size(x1))- l/2*noABS;
        % 2 (top)
        x2=L/2*[1 1 -1 -1 1];
        y2=L2/2*[-1 1 1 -1 -1];
        z2=zeros(size(x1))+ l/2*noABS;
    otherwise
        disp('Unknown version')
 return
end
% Creating DATA - Vertical edges
I=1:length(x1)-1;
X = [x1(I); x1(I+1); x2(I+1); x2(I)];
Y = [y1(I); y1(I+1); y2(I+1); y2(I)];
Z = [z1(I); z1(I+1); z2(I+1); z2(I)];

% Preparing a figure
fig=1;
figure(fig);
clf(fig);
ax=axes('parent',fig);
% Display format: Coloring/Resizing/Correcting errors of the figure because of Matlab
    glitches
set(fig,'Color','white'); %color of border
hold(ax,'on');
axis(ax,'off');
```

```
switch versionGEN
    case 1 % Version =1= : any numbers of equal edges (for parallelepiped: LxLxl)
        view(ax,[0 45]);
        axis(ax,'normal');
        axis(ax,'vis3d');
    case 2 % Version =2= : 4 edges: (only parallelepiped: LxL2xl)
        view(ax,[45 45]);
        axis(ax,'normal');
        axis(ax,'vis3d');
    otherwise
        disp('Unknown version')
    return
end
camproj('orthographic'); %orthographic and perspective

% Creating the 3D object and colouring it
TMPcolor=[1 1 1]; % white temp color
switch cl % 0-monochrome/1-colored
    case 0 % All edges have the same color
        % Defining the colors of object (all black)
        colorBOTTOM=1*[0 0 0];
        colorTOP=(no)*[0 0 0]+(1-no)*TMPcolor;
        colorEDGES=(no)*[0 0 0]+(1-no)*TMPcolor;
        % Horizontal plates (creation and colouring)
        patch(x1,y1,z1,colorBOTTOM,'EdgeColor',colorBOTTOM,'Parent',ax); % Top
        hold on
        patch(x2,y2,z2,colorTOP,'EdgeColor',colorTOP,'Parent',ax); % Bottom
        % Vertical edges (creation and colouring)
        patch(X,Y,Z,colorEDGES,'EdgeColor',colorEDGES, 'Parent',ax);
        % Number of colors for edges
        ED=1;
    case 1 % Each side has another color
        % Defining the colors of object
        colorBOTTOM=round(rand(1, 3)*100)/100; % random color
        colorTOP=(no)*round(rand(1, 3)*100)/100+(1-no)*TMPcolor; % random color
        % Horizontal plates (creation and colouring)
        patch(x1,y1,z1,colorBOTTOM,'EdgeColor',colorBOTTOM,'Parent',ax); % Top
        hold on
        patch(x2,y2,z2,colorTOP,'EdgeColor',colorTOP,'Parent',ax); % Bottom
        % Vertical edges (creation and colouring)
        [ANG, ED]=size(X);
        for ed=1:ED
            colorEDGES(ed, :)=(no)*round(rand(1, 3)*100)/100+(1-no)*TMPcolor; %
                random color
            patch(X(:,ed),Y(:,ed),Z(:,ed),colorEDGES(ed, :),'EdgeColor',colorEDGES(
                ed, :), 'Parent',ax);
        end
    otherwise
        disp('Color distribution Unknown')
    return
end
```

Listing E.1: Matlab 3D absorber code.

Bibliography

[1] A. Papoulis, *Probability, Random Variables, and Stochastic Processes*. New York, USA: McGraw-Hill Book Company, 1965.

[2] J. D. Parsons, *The Mobile Radio Propagation Channel, 2nd*. New York: John Wiley & Sons, 2000.

[3] A. Papoulis and S. Pillai, *Probability, random variables, and stochastic processes*, ser. McGraw-Hill electrical and electronic engineering series. McGraw-Hill, 2002. [Online]. Available: http://books.google.fr/books?id=YYwQAQAAIAAJ

[4] G. L. Stüber, *Principles of Mobile Communication (2nd Edition)*. Boston: Kluwer Academic, 2001.

[5] A. Naimi and G. Azemi, "Moment-based Ricean K-factor estimation in the presence of shadowing," in *Signal Processing and Its Applications, 2007. ISSPA 2007. 9th International Symposium on*, Sharjah, 2007, pp. 1–4.

[6] J. G. Proakis, *Digital Communications (4th Edition)*. New York: McGraw-Hill, 2001.

[7] R. Hogg and A. Craig, *Introduction to Mathematical Statistics, 4th*. New York: Prentice-Hall, 1978.

[8] R. Kanthavel, K. Ganesh, and J. Premalatha, "Correlation based effective periodic pattern extraction from multimedia data," *IJCA Proceedings on International Conference in Recent trends in Computational Methods, Communication and Controls (ICON3C)*, no. 3, 2012.

[9] C. Lemoine, "Contribution à l'analyse statistique des mesures en chambre réverbéranteà brassage de modes," Ph.D. dissertation, IETR Rennes, France, 2008.

[10] W. H. Greene, *Econometric Analysis*. Upper Saddle River, NJ: Prentice Hall, 1997.

[11] H. Cramer, *Mathematical Methods of Statistics*, N. P. U. Press, Ed. Princeton, 1946.

[12] H. V. Poor, *An Introduction to Signal Detection and Estimation (2nd Edition)*. New York: Springer-Verlag, 1994.

[13] L. Rabiner, R. Schafer, and C. Rader, "The chirp z-transform algorithm," *Audio and Electroacoustics, IEEE Transactions on*, vol. 17, no. 2, pp. 86–92, Jun. 1969.

[14] R. Mersereau, "An algorithm for performing an inverse chirp z-transform," *Acoustics, Speech and Signal Processing, IEEE Transactions on*, vol. 22, no. 5, pp. 387–388, Oct. 1974.

[15] S. Salivahanan and A. Vallavaraj, *Digital Signal Processing*. McGraw Hill, 2001. [Online]. Available: http://books.google.fr/books?id=5zO6An_g-AgC

List of Figures

2.1 Bello's diagram (i-T: inverse transform, d-T: direct transform). . . . 14
2.2 Reverberation chamber stirrer. . . . 17
2.3 Reverberation chamber components: (a) unstirred components, (b) unstirred secondary components, (c) stirred components. . . . 19
2.4 The received signal amplitude r in steady state (a) and its phase Θ (b) for 100 stirrer positions. 20
2.5 Relative fluctuation of the amplitude for a complete stirrer rotation (i.e., 100 stirrer positions). 21
2.6 The fitting distribution for a non-line-of-sight configuration (a), and for a line-of-sight configuration (b). The number of realizations is 100. . . . 22
2.7 Examples of the transient and steady state regimes of the signal for two different stirrer positions. 22
2.8 100 impulse responses of the reverberation chamber when measuring the signal using the DSO. 23
2.9 Transfer functions of the propagation channel for 100 stirrer positions. . . . 23
2.10 Example of the measured normalized power delay profile for a loaded (top) and an empty chamber (bottom) in the same line-of-sight configuration. . . . 24
2.11 Decay constant of the chamber τ with the quantity of absorbers (a). Reverberation chamber configuration when using absorbers (b). . . . 25
2.12 Definitions of excess delays extracted from normalized power delay profile (estimated from measurements in reverberation chamber). . . . 25

3.1 Rejection rate, bias and confidence interval to characterize K-factor. . . . 38
3.2 Rejection rate over the variation of K-factor using Monte Carlo simulations. . . . 38
3.3 Comparison between the biases of different estimations of K-factor using Monte Carlo simulations. . . . 39
3.4 Comparison between the CI of different estimations of K-factor using Monte Carlo simulations. 40
3.5 Reverberation chamber measurement configuration. . . . 41
3.6 The effect of the frequency sweep duration on the estimated value of K-factor. . . . 42
3.7 Experimental results for K-factor computed at a distance of 1 and 4 m; reverberation chamber is not loaded with absorbers. . . . 43
3.8 Measured horn antenna gain model 3115 in near-field-chamber. . . . 43
3.9 The specular phase, for distances between antennas of 1 m (top) and 4 m (bottom); reverberation chamber is not loaded with absorbers. . . . 44
3.10 Experimental results for K-factor computed at a distance of 1 and 4 m; reverberation chamber is loaded with absorbers. . . . 44
3.11 The specular phase, for distances between antennas of 1 m (a) and 4 m (b); reverberation chamber is loaded with absorbers. . . . 45
3.12 Measured K-factor in reverberation chamber for a distance between antennas of 0.5 m and loading the chamber (a) and for a distance between antennas of 6 m without loading the chamber (b). . . . 46
3.13 Variation of the true and the estimated power of specular and scattered components. . . . 48
3.14 Comparison between different rejection rates of K-factor (Monte-Carlo simulation). . . . 49
3.15 Comparison between different confidence intervals at 95% of K-factor (Monte-Carlo simulation). 50
3.16 Comparison between different biases of K-factor (Monte-Carlo simulation). . . . 50
3.17 Comparisons of K-factors estimators in terms of bias. . . . 53
3.18 The 95% confidence intervals associated with K-factor estimators. . . . 54
3.19 Comparisons of K-factor estimators in terms of rejection rates. . . . 54
3.20 The RMSE associated with K-factor estimators. . . . 55
3.21 Comparison of biases with the variation of SNR (for $K = 10$ dB). . . . 56

3.22 Comparison of 95% confidence intervals with the variation of SNR (for $K = 10\,\text{dB}$). 57
3.23 Comparison of biases with the variation of the sample size (for $K = 10\,\text{dB}$). 57
3.24 Comparison of 95% confidence intervals with the variation of sample size (for $K = 10\,\text{dB}$). . . . 58
3.25 Measured K-factors in reverberation chamber using absorbers and horn antennas placed in line-of-sight at a distance of 1 m (a) and a distance of 4 m (b). 59

4.1 Frequency flat (a) and frequency selective (b) channel. 66
4.2 Projected Surface. 70
4.3 Matlab 3D simulation of the parallelepiped absorber. 72
4.4 Absorbing surface approximation (top side view). 73
4.5 RC measurement configuration. 74
4.6 Coherence Bandwidths computed between $2 - 3\,\text{GHz}$ in sub-bandwidths of 10 MHz each with a step between two consecutive sub-bandwidths of 1 MHz. 75
4.7 Transmitted signal as percentage of the incidence signal for the absorber P150. 76
4.8 Measured and simulated average absorbing cross section as a function of the number of absorbers in the frequency bandwidth $2 - 3\,\text{GHz}$ for P150 absorbers:
(a) when using (4.24) and (b) when using (4.28) to simulate the average absorbing cross section. 78
4.9 Coherence Bandwidth as function of the Average Absorbing Cross Section for P150 absorbers, at a central frequency of 2.5 GHz. 79

5.1 Decay constant of a impulse response sent in reverberation chamber. 84
5.2 The power profile of the total envelope. 84
5.3 The percentage of erroneous values of K-factor as a function of N for $\alpha = 0.95$. 86
5.4 Simulation and measurement scenario (example). 92
5.5 Schematic Description of inverse transform and envelope extraction:
(a) examples of transfer functions of the channel, (b) examples of impulse responses of the channel, (c) examples of resulted convolved signals, (d) examples of extracted power delays profiles, (e) averaged power delay profile. 93
5.6 Example of the measured unstirred power delay profile for two different separation distances between antennas (1 m and 3.5 m). 95
5.7 Variation of the estimated decay constant τ of the chamber. The distance between antennas changes from 0.5 to 4 m (empty chamber). 97
5.8 Variation of K-factor obtained from time parameters. The distance between antennas changes from 0.5 to 4 m (empty chamber). 98
5.9 Variation of τ_μ and τ_{rms}. The distance between antennas changes from 0.5 to 4 m (empty chamber). 98
5.10 Variation of the estimated decay constant of the chamber with the number of absorbers; $d = 1.5$ and 2.5 m. 99
5.11 Variation of detectable average absorbing cross section, $\hat{\sigma}_{\text{A}}$, with the number of absorbers; $d = 1.5$ and 2.5 m. 100
5.12 Variation of K-factor obtained from time parameters with the number of absorbers; $d = 1.5$ and 2.5 m. 100
5.13 Variation of τ_μ and τ_{rms} with the number of absorbers; $d = 1.5$ m. 101

6.1 Free-space propagation distances when antenna turns for $\theta \in [0, 2\pi)$. 110
6.2 Comparison between the estimation of the antenna distance d_{a} when applying the inverse CZT to one filtered pulse and when applying the inverse CZT to a renormalized pulse whose energy is equal to the energy of the filtered pulse. 112
6.3 Antenna measurement configuration in reverberation chamber (a), and antenna polar coordinate system-θ and φ (b). 114
6.4 Example of the time response of the channel obtained from S_{11} measurement. Antenna mismatch is not removed. 115
6.5 Antenna mismatches: [RC, 1] - using average over several measurements, [RC, 2] - using time filtering, [NFC] - measurement made in NFC. 115
6.6 Comparison between measured transfer functions in direction ($\theta = 0$, $\varphi = 0$) in near-field chamber and in reverberation chamber. For reverberation chamber the free space transfer function is computed for different truncation intervals: (a) $[7\,\text{ns}, t_{\max}]$, (b) $[7\,\text{ns}, t_{\max} + 1\,\text{ns}]$, (c) $[7\,\text{ns}, t_{\max} + 2\,\text{ns}]$, (d) $[7\,\text{ns}, t_{\max} + 4\,\text{ns}]$. 116

6.7 Relative error of the guided antenna propagation distance d_a; (X) - f_s sampling frequency, (Y) - $2d_a$ two times propagation distance in antenna, (Z) - percentage of the propagation distance relative error. . . . 117
6.8 Relative error of the guided antenna propagation distance d_a; (X) - 1-γ ratio between antenna gains of two consecutive measurements, (Y) - $2d_a$ is two times propagation distance in antenna, (Z) - percentage of the propagation distance relative error. . . . 118
6.9 Antenna gain offset relative error with the variation of azimuthal angle θ at a frequency of 2.5 GHz; here, this *relative error* represents $1-\gamma$ from the previous figure. . . . 119
6.10 Comparison between measured gain in direction ($\theta = 0$, $\varphi = 0$) in NFC and in RC. . . . 120
6.11 Relative difference (%) of normalized gain for H plane (a), and for V plane (b) of the values measured in reverberation chamber over the values measured in NFC. . . . 121
6.12 Comparison between H plane antenna patterns, in dB, measured in near-field chamber and in reverberation chamber for $f = 3$ GHz (a), and for $f = 5$ GHz (b). . . . 122
6.13 Comparison between V plane antenna patterns, in dB, measured in near-field chamber and in reverberation chamber for $f = 3$ GHz (a), and for $f = 5$ GHz (b). . . . 122
6.14 Antenna half power beamwidth for H plane (a), and V plane (b) estimated in near-field chamber and RC. . . . 124
6.15 Relative difference of antenna half power beamwidth measured in reverberation chamber over value measured in near-field chamber for H plane (a), and for V plane (b). . . . 124

7.1 Computing the diversity gain from the CDF of the signals. . . . 129
7.2 Example of the CDF of the reference received signal and the combined signal. . . . 131
7.3 Maximum Power Correlation, ρ_{pwr}. . . . 137
7.4 Stages of simulation algorithm. . . . 138
7.5 Diversity gain when $\rho_{cpx} = 0$:
(a) Maximal-Ratio method, (b) Selection-Combining method, (c) Equal-Gain method. . . . 141
7.6 Diversity gain for $PI_K = 0$ dB:
(a) Maximal-Ratio method, (b) Selection-Combining method, (c) Equal-Gain method. . . . 142
7.7 Diversity gain when the minimum K-factor of one antenna is -20 dB:
(a) Maximal-Ratio method, (b) Selection-Combining method, (c) Equal-Gain method. . . . 143
7.8 Non-Line-of-Sight (a), and Line-of-Sight (b) configuration. . . . 144
7.9 Non-line-of-sight configurations: spatial diversity (a), polarization diversity (b), pattern diversity (c), pattern and polarization diversity (d). . . . 145
7.10 Line-of-sight attenuation due to stirring frequencies. . . . 147
7.11 Mismatches of dipole antennas separated by a distance of 10 cm. . . . 148
7.12 Radiation efficiency (a) and Total Efficiency (b) of two dipole antennas when the distance between them is 10 cm measured in reverberation chamber. . . . 148
7.13 K-factor for the non-line-of-sight when the dipoles are separated by 10 cm. . . . 149
7.14 Average Received Power of two dipole antennas when the distance between them is 10 cm. . . . 150
7.15 Diversity Gain for several diversity techniques for a distance between antennas of 10 cm estimated at 1 % level of reliability. . . . 150
7.16 Dipole antenna mismatches with the separation distance between them at a frequency of 2.9 GHz. 151
7.17 Radiation Efficiency (a) and Total Efficiency (b) with the distance between dipole antennas at 2.9 GHz. . . . 152
7.18 Average Received Power (a) and Power Imbalance between the two antenna branches (b) with the distance between dipole antennas at 2.9 GHz. . . . 153
7.19 Complex (a), and envelope/power correlations (b) between the signals measured on dipole antennas for a frequency of 2.9 GHz with the separation distance. Comparisons with the correlations provided by two models are provided. . . . 153
7.20 Diversity Gain for several diversity techniques with the separation distance between antennas, at 2.9 GHz. . . . 154
7.21 Envelope and Power correlation between antenna branches when changing the distance between the horn and dipole array. . . . 154
7.22 Average Received Power (a) and Power Imbalance between the two branches (b) of two dipole antennas with the variation of the distance between horn and dipole antennas at 2.9 GHz. . . . 155
7.23 K-factor for the line-of-sight configuration with the distance between horn and antenna array. 155

7.24 Diversity Gain for several diversity techniques with the distance between horn and dipole antennas at 2.9 GHz. 156
7.25 Comparison between the measured and simulated diversity gains for (a) non-line-of-sight configuration when changing the separation distance between dipole antennas and (b) for line-of-sight configuration when changing the propagation distance between horn and antenna array at a frequency of 2.9 GHz. 157

D.1 Comparison between the FFT (b) and the CZT transform (c). 191

E.1 Different 3D absorbers shapes: (a) triangular prism, (b) parallelepiped, (c) octagonal prism. . 195

List of Tables

1.1 Statistical distributions of several electric field components and their pdf measured in reverberation chamber in an EMC configuration. 8

2.1 Excess delays when the PDP is evaluated for each stirrer position (a), and excess delays when the PDP is evaluated as an average over all 100 stirrer positions when the chamber is loaded with 15 canisters with salty water and 5 foam absorbers (b). 26
2.2 Excess delays with the absorbing quantity. 27

3.1 Useful K-factor intervals for 10% rejection rate, 3 dB bias, and 6 dB confidence interval. 40
3.2 Useful K intervals at 10% rejection rate, 3 dB bias, and 6 dB confidence interval. 55

6.1 Gain relative differences (see Fig. 6.11(a) and 6.11(b)). 120

A.1 Relations between distributions. 179

INSA de RENNES
Service des Formations

AVIS DU JURY SUR LA REPRODUCTION DE LA THESE SOUTENUE

Titre de la thèse:
Recherche de méthodes expérimentales de simulation de canaux de propagation en chambre réverbérante à brassage de modes

Nom Prénom de l'auteur : ANDRIES MIHAI IONUT

Membres du jury :
- Madame LIENARD Martine
- Monsieur LUXEY Cyril
- Madame SEETHARAMDOO Divitha
- Monsieur LEMOINE Christophe
- Monsieur UGUEN Bernard
- Monsieur BESNIER Philippe

- Monsieur ARVAUT Luc, invité

Président du jury : Bernard UGUEN.

Date de la soutenance : 04 Avril 2013

Reproduction de la these soutenue

☒ Thèse pouvant être reproduite en l'état
☐ Thèse pouvant être reproduite après corrections suggérées

Fait à Rennes, le 04 Avril 2013

Signature du président de jury

Le Directeur,

M'hamed DRISSI

Résumé

Les tests de dispositifs de communication sans fil peuvent être réalisés en utilisant des simulations numériques ou des sondeurs de canaux. Bien que ne reflétant pas un environnement électromagnétique réaliste, une chambre réverbérante peut néanmoins émuler un canal de propagation comparable à un cas réel si l'on modifie convenablement ses propriétés. Les propriétés des signaux générés dans une chambre réverbérante sont fonction de différents paramètres. Au cours des trois années de thèse, nous avons analysé et mis en œuvre plusieurs techniques pour mesurer et contrôler ces paramètres à l'intérieur d'une chambre réverbérante.

D'abord, différents estimateurs du facteur *K* sont testés et leurs propriétés sont évaluées. Nous présentons les limites de fonctionnement utiles dans lesquelles différents estimateurs peuvent être utilisés. Ensuite, nous proposons deux nouveaux estimateurs qui utilisent comme données d'entrée seulement l'enveloppe du signal. Ils apportent en outre des améliorations sur la gamme des valeurs détectables du facteur *K*.

Une des possibilités pour contrôler un canal de propagation à l'intérieur d'une chambre réverbérante est d'utiliser des matériaux absorbants. Nous présentons une méthode pour estimer la surface équivalente moyenne d'absorption en utilisant une seule antenne. Cette méthode exploite la mesure de la bande de cohérence du canal de propagation. Ensuite, nous étendons notre analyse à la prédiction de la surface équivalente moyenne d'absorption lorsque les dimensions géométriques et les propriétés électromagnétiques des absorbants sont connues.

On crée ensuite un modèle de canal de propagation en exploitant les régimes transitoire et permanent du signal. Avec ce modèle, selon les informations disponibles, on peut extraire le facteur *K*, la surface équivalente moyenne d'absorption et différents paramètres temporels (i.e., profil de l'étalement des retards).

Nous poursuivons avec deux applications possibles des chambres réverbérantes. Tout d'abord, on évalue le gain d'une antenne à partir de mesures du coefficient de réflexion de cette antenne. Nous étendons notre analyse à l'évaluation du diagramme de rayonnement de l'antenne et de son erreur d'estimation. Nous estimons aussi la désadaptation de l'antenne et son ouverture à 3 dB.
La deuxième application porte sur l'évaluation du gain de diversité dans la chambre réverbérante. Nous isolons les influences des efficacités des antennes, des puissances des composantes brassées, et des facteurs *K* sur l'évaluation du gain de diversité. On obtient une relation simple de la corrélation de puissance en fonction de la corrélation complexe lorsque les facteurs *K* sur différents branches ne sont pas identiques. Nous montrons que lors d'un fort déséquilibre de facteur *K* il est impossible de conclure sur le gain de diversité à partir de la seule évaluation de la corrélation d'enveloppe ou de puissance. À l'aide de simulations statistiques on compare le gain de diversité mesuré avec les valeurs simulées.

Abstract

The testing of wireless devices is generally done using numerical simulations or channel sounders. Though a reverberation chamber does not reflect a real transmission environment, its properties can also be appropriately modified to emulate one. This emulation may be achieved thanks to various parameters. Our PhD thesis has been devoted to analyze and implement several techniques to measure and control these parameters inside reverberation chambers.

First we evaluate different *K*-factor estimators and their capabilities. We present the useful limits in which several complex, phase and envelope *K*-factor estimators can be used. Then, we propose two new envelope-based estimators improving the useful range of detectable values of *K*-factor.

One of the possibilities to control a propagation channel inside a reverberation chamber is to use absorbing materials. We present a method to estimate the average absorbing cross section by using only one antenna. This is done with measurements of coherence bandwidth of the channel. Then, we extend our analysis to predict the average absorbing cross section when we know the physical dimensions of a parallelepiped absorber as well its electromagnetic properties.

Next, we create a model of the reverberation chamber propagation channel using the transient regime and steady state of the signal. With this model, depending on the available information, we can extract the *K*-factor, the average absorbing cross section and different time spreads parameters (i.e., mean delay spread and the root mean square delay spread).

We continue with two possible applications of the reverberation chamber. First, we evaluate the gain of an antenna from only the measurement of reflection coefficient. We extend our analysis to the evaluation of antenna pattern and its estimation errors. We also estimate the antenna mismatch and half power beamwidth.
The second application deals with the evaluation of the diversity gain in reverberation chamber. We isolate the effects on the diversity gain due to different antenna efficiencies, stirred powers and *K*-factors. Then, we estimate a simple relation of the power correlation as a function of the complex correlation when the *K*-factors on different branches are not identical. We show that using an envelope/power correlation as a criterion to characterize the diversity may bias the conclusions without taking into account other parameters. Using statistical simulations we compare the measured diversity gain with the simulated values.

N° d'ordre : 13ISAR 08 / D13 - 08

Institut National des Sciences Appliquées de Rennes
20, Avenue des Buttes de Coësmes . CS 14315 . F-35043 Rennes Cedex
Tel : 02 23 23 82 00 – Fax : 02 23 23 83 96